N°d'ordre NNT: **2017LYSEI105**

THESE de DOCTORAT DE L'UNIVERSITE DE LYON
Opérée au sein de
INSA Lyon

Ecole Doctorale: MEGA EDA162
Ecole doctorale des sciences pour l'ingénieur de Lyon:
Mécanique, Energétique, Génie Civil, Acoustique
Spécialité/ discipline de doctorat: Génie Mécanique

Soutenue publiquement le 10/11/2017, par :
Marie-Pierre Noutary

A robust Reynolds solver for textured surfaces in the piston-ring cylinder liner contact

---

Devant le jury composé de:

Tanguy, Anne	Professeur, INSA Lyon	Présidente
Dini, Daniele	Professeur, Imperial College, London	Rapporteur
Fillon, Michel	Directeur de recherche, Université de Poitiers	Rapporteur
Tian, Tian	Principal Research Engineer, M.I.T., Boston	Examinateur
Biboulet, Nans	Maître de Conférences, INSA Lyon	Examinateur
Lubrecht, Antonius	Professeur, INSA Lyon	Directeur de Thèse

Département FEDORA – INSA Lyon - Ecoles Doctorales – Quinquennal 2016-2020

SIGLE	ECOLE DOCTORALE	NOM ET COORDONNEES DU RESPONSABLE
CHIMIE	**CHIMIE DE LYON** **http://www.edchimie-lyon.fr** Sec : Renée EL MELHEM Bat Blaise Pascal 3^e^ etage secretariat@edchimie-lyon.fr Insa : R. GOURDON	M. Stéphane DANIELE Institut de Recherches sur la Catalyse et l'Environnement de Lyon IRCELYON-UMR 5256 Équipe CDFA 2 avenue Albert Einstein 69626 Villeurbanne cedex directeur@edchimie-lyon.fr
E.E.A.	**ELECTRONIQUE, ELECTROTECHNIQUE, AUTOMATIQUE** **http://edeea.ec-lyon.fr** Sec : M.C. HAVGOUDOUKIAN Ecole-Doctorale.eea@ec-lyon.fr	M. Gérard SCORLETTI Ecole Centrale de Lyon 36 avenue Guy de Collongue 69134 ECULLY Tél : 04.72.18 60.97 Fax : 04 78 43 37 17 Gerard.scorletti@ec-lyon.fr
E2M2	**EVOLUTION, ECOSYSTEME, MICROBIOLOGIE, MODELISATION** **http://e2m2.universite-lyon.fr** Sec : Sylvie ROBERJOT Bât Atrium - UCB Lyon 1 04.72.44.83.62 Insa : H. CHARLES secretariat.e2m2@univ-lyon1.fr	M. Fabrice CORDEY CNRS UMR 5276 Lab. de géologie de Lyon Université Claude Bernard Lyon 1 Bât Géode 2 rue Raphaël Dubois 69622 VILLEURBANNE Cédex Tél : 06.07.53.89.13 cordey@univ-lyon1.fr
EDISS	**INTERDISCIPLINAIRE SCIENCES-SANTE** **http://www.ediss-lyon.fr** Sec : Sylvie ROBERJOT Bât Atrium - UCB Lyon 1 04.72.44.83.62 Insa : M. LAGARDE secretariat.ediss@univ-lyon1.fr	Mme Emmanuelle CANET-SOULAS INSERM U1060, CarMeN lab, Univ. Lyon 1 Bâtiment IMBL 11 avenue Jean Capelle INSA de Lyon 696621 Villeurbanne Tél : 04.72.68.49.09 Fax :04 72 68 49 16 Emmanuelle.canet@univ-lyon1.fr
INFOMATHS	**INFORMATIQUE ET MATHEMATIQUES** **http://edinfomaths.universite-lyon.fr** Sec :Renée EL MELHEM Bat Blaise Pascal, 3^e^ étage Tél : 04.72. 43. 80. 46 Fax : 04.72.43.16.87 infomaths@univ-lyon1.fr	M. Luca ZAMBONI Bâtiment Braconnier 43 Boulevard du 11 novembre 1918 69622 VILLEURBANNE Cedex Tél :04 26 23 45 52 zamboni@maths.univ-lyon1.fr
Matériaux	**MATERIAUX DE LYON** **http://ed34.universite-lyon.fr** Sec : Marion COMBE Tél:04-72-43-71-70 –Fax : 87.12 Bat. Direction ed.materiaux@insa-lyon.fr	M. Jean-Yves BUFFIERE INSA de Lyon MATEIS Bâtiment Saint Exupéry 7 avenue Jean Capelle 69621 VILLEURBANNE Cedex Tél : 04.72.43 71.70 Fax 04 72 43 85 28 Ed.materiaux@insa-lyon.fr
MEGA	**MECANIQUE, ENERGETIQUE, GENIE CIVIL, ACOUSTIQUE** **http://edmega.universite-lyon.fr/** Sec : Marion COMBE Tél:04-72-43-71-70 –Fax : 87.12 Bat. Direction mega@insa-lyon.fr	M. Philippe BOISSE INSA de Lyon Laboratoire LAMCOS Bâtiment Jacquard 25 bis avenue Jean Capelle 69621 VILLEURBANNE Cedex Tél : 04.72 .43.71.70 Fax : 04 72 43 72 37 Philippe.boisse@insa-lyon.fr
ScSo	**ScSo*** **http://ed483.univ-lyon2.fr/** Sec : Viviane POLSINELLI Brigitte DUBOIS Insa : J.Y. TOUSSAINT Tél : 04 78 69 72 76 viviane.polsinelli@univ-lyon2.fr	M. Christian MONTES Université Lyon 2 86 rue Pasteur 69365 LYON Cedex 07 Christian.montes@univ-lyon2.fr

*ScSo : Histoire, Géographie, Aménagement, Urbanisme, Archéologie, Science politique, Sociologie, Anthropologie

Acknowledgments

It would not have been possible for me to achieve this work without the help of many people and I would like to express here my gratitude.
First of all I want to express my gratitude to my supervisor Pr. Ton Lubrecht who believed in me at a time when I thought that science was not for me. I have also discovered, thanks to him, that many things remain possible even when one starts getting old. Finally, I have learned, through him, that one little step after the other, it is possible to achieve more that one thought.
I am also very indebted to Dr Nans Biboulet for his guidance and fruitful advices. They were very precious.
I am very grateful to the jury members: Pr. Daniele Dini, (Imperial college, London) and Dr. Michel Fillon (CNRS, Institut Pprime, Poitiers) for accepting to review my work and for their relevant comments, Pr. Anne Tanguy (INSA Lyon) for accepting to preside the jury and Dr. Tian Tian (Sloan Automotive Laboratory, MIT) for coming from the USA to examine my work.
I would also like to express particular thanks to Pr. Carole Plossu and Pr. Catherine Verdu, former and present directors of the 1st cycle department, for allowing me to reduce my teaching duties by 50% during my thesis. Without this opportunity, it would not have been possible to complete this work.
I am thankful to the LaMCoS laboratory and in particular to the SMC team for accepting me amongst them with a special mention for Sophie de Oliveira who was very helpful in practical matters.
I must not forget all the members of the ”Pôle de Mathématiques” for their support and kindness. A particular thank you to Bernard with whom I have been sharing an office for many years now and for staying kindly and supportive even when I was rather moody. A thank you to Adrien for his friendly advice and thank you to everyone at the ”pôle”. I do not mention any name because I am afraid that I may forget someone but I am very grateful to each of you. However, I must mention Sandrine who was very helpful during the last days before the thesis defense.
Thank you very much to Christine, Claire, Cécile, Martine, Florence, Dominique for their friendship during those days.
Thank you to Anne, Marie-Laure and Edmond.
And finally I dedicate this work to Julien, Lisa, Jeanne, Sophie and Lauren. I want you to remember that at any age, many opportunities are offered that are worth being explored.

Abstracts

Abstract: The piston ring cylinder liner (PRCL) contact is essential in the CO_2 and pollutant emission reduction in internal combustion engine. These two constraints being antagonistic, a compromise has to be found and it is necessary to study the microgeometry influence in order to find new PRCL contact architectures. As experimental study can be very expensive, modeling PRCL contact performance becomes crucial. Multigrid methods allow a huge reduction of the computational time. Unfortunately, in presence of texture, classical multigrid efficiency decays significantly and it is not usable. A new algorithm based on an approach developed by Alcouffe et al. was designed that allows the study of the hydrodynamic lubrication of this contact even in the case of a highly varying geometry due to the texture. The obtained code was validated by comparison with a 1D analytical model, its performance was evaluated and a first study of an analytic cross hatched geometry parameter influence on the load carrying capacity was completed. The code was modified to include flow conservation. A relaxation process closer to the physics phenomenon is used. The code efficiency is not the one that is expected from multigrid methods. However its convergence is sufficiently fast to study the dimple influence for the oil control ring and show the importance of partial texturing. Finally the transient term of the Reynolds equation is accounted for. In the case of a parabolic ring and for a cross hatched liner, the influence of the groove parameters (depth, width, distance and groove angle) on the average minimum film thickness with respect to the smooth case is analyzed.

Keywords: Multigrids – Reynolds Equation – Hydrodynamic lubrication – Piston ring cylinder liner contact – Texture.

Résumé: Le contact Segment-Piston-Chemise (SPC) est essentiel pour la réduction des émissions de CO2 et de polluants dans les moteurs automobile. Pour optimiser ces deux contraintes antagonistes, il est nécessaire d'étudier l'influence de la micro-géométrie afin de trouver de nouvelles architectures de ce contact. L'étude expérimentale étant très coûteuse, il est impératif de pouvoir modéliser les performances du contact SPC. Les méthodes multigrilles permettent de réduire considérablement les temps de calcul. Pour le contact SPC, les méthodes multigrilles classiques perdent leur efficacité en présence de texture. Un nouvel algorithme, basé sur des idés développées par Alcouffe et al. a été con cu qui permet l' étude du contact hydrodynamique en présence de texturation importante. Il a été validé par comparaison avec un modèle analytique 1D, ses performances ont été étudiées et une première étude de línfluence des paramètres sur la portance pour une surface striée a été faite. L'algorithme a ensuite été modifié pour imposer la conservation des flux. Un processus de relaxation plus proche de la physique du phénomène est utilisé. Le code obtenu n'atteint pas l'efficacité multigrille optimale. Cependant sa convergence est suffisamment rapide pour étudier l'influence de pores pour le segment plat et montrer l'importance d'une texturation partielle. Pour finir, le terme transitoire de l'équation de Reynolds est pris en compte. Pour un segment parabolique et une chemise striée, l'influence des paramètres des stries (profondeur, largeur, distance et angle des stries) sur la variation moyenne de la hauteur de film par rapport à une surface lisse est analysée.

Mots clés: Multigrilles – Equation de Reynolds – Lubrification Hydrodynamique – Contact Segment Piston Chemise – Texturation.

Contents

Notations

a	Groove depth or dimple depth[m]
d	Distance between grooves or dimples [m]
d_1	Distance between groove crossovers in sliding direction [m]
e	Ring half width [m]
h	Geometry height [m]
$hoil$	Film thickness, $hoil = \theta h$ [m]
h_0	Clearance or x_0^2/R_x(Chapter 6)[m]
h_m	Minimum film thickness (Chapter 6) [m]
h_x	Fine grid space step in the x-direction
h_y	Fine grid space step in the y-direction
h_t	Fine grid time step,
p	Pressure[Pa]
p_{amb}	Ambient pressure[Pa]
R_x	Reduced radius in direction of sliding [m]
x	Coordinate in direction of sliding [m]
x_a, x_b	Domain size in direction of sliding [m]
x_g	Groove position on the central line [m]
x_0	Ring half width (chapters 5, 6) [m]
y	Coordinate perpendicular to direction of sliding [m]
y_a, y_b	Domain size in direction perpendicular to direction of sliding sliding [m]
t	Time [s]
u_m	Mean surface velocity [m/s]
v_p	Piston velocity [m/s]
w	Load carrying capacity[N]
α	Angle between groove and Y axis
η	Fluid viscosity [Pa.s]
λ	Groove width [m]
ρ	Fluid density [kg/m^3]
θ	Oil film ratio
ω	Piston angular velocity[s^{-1}]

A	Dimensionless groove or dimple depth
D	Dimensionless distance between grooves or dimples
D_1	Dimensionless distance between crossovers in sliding direction
E	Dimensionless ring half width
H	Dimensionless geometry
$Hoil$	Dimensionless equivalent oil film thickness, $Hoil = \theta H$
H_m	Dimensionless minimum film thickness (Chapter 6)
H_x	Coarse grid space step in the X-direction
H_y	Coarse grid space step in the Y-direction
H_t	Coarse grid time step
LCC	Dimensionless load carrying capacity
P	Dimensionless pressure
P_{amb}	Dimensionless ambient pressure
R	Dimensionless dimple radius (Chapters 4,5) or surface roughness
X	Dimensionless coordinate in direction of sliding
X_0	Dimensionless ring half width (Chapters 5, 6)
X_g	Dimensionless groove position on the central line
Y	Dimensionless coordinate perpendicular to direction of sliding
T	Dimensionless time
U_m	Dimensionless mean surface velocity
V	Dimensionless piston velocity
W	Dimensionless load
Λ	Dimensionless groove width

BDC	Bottom Dead Center
BTU	British Thermal Unit
EU	European Union
FMG	Full MultiGrid
HL	Hydrodynamic Lubrication
HC	HydroCarbons
IC	Internal Combustion
LCC	Load Carrying Capacity
NMHC	Non Methane HydroCarbons
NOx	Mono Nitrogen oxides
PM	Particulate Matter
PN	Particulate Number
PRCL	Piston Ring Cylinder Liner
TDC	Top Dead Center
Wu	Work unit

Introduction

Contents

Environmental issues

Energy resources and environmental issues have become priorities of our societies. Transport being one of the world largest energy consumer, this sector is submitted to increasing constraints. Worldwide two major problems are connected to the massive use of motor vehicles:

- an important production of CO_2 which is a major greenhouse gas and henceforth an important contributor to global warming.
- pollutant emission: carbon monoxide CO, nitrogen oxides NOx, hydrocarbons HC and particles

Because of a general increasing environmental awareness, automotive constructors are required to substantially diminish those emissions. It has become a major issue for the automotive industry. Carbon dioxide and pollutant emissions as well as fuel cost are directly related to vehicle fuel consumption. The pollution standards in European legislation are more and more coercive as shown in Table 1. They strongly regulate the emissions of NOx, CO, HC, non-methane hydrocarbons (NMHC), particulate matter and number (PM and PN). Certification is obtained through laboratory emission testing and does not rely on real driving conditions. As a consequence of the recent scandals where some constructors had adapted their cars to the test cycle, there was a discrepancy between test results and reality. The European Union has validated a new test for September 2017. However as in automotive industry new cars are designed long before they are put on the market, EU allows constructors a compliance factor until 2021. It is 2.1 up to 2019 and of 1.5 afterwards so that they have to adapt. Therefore, between 2019 and 2021, a car should not pollute more than 50% more than required by the Euro 6 norm.

Besides customers also demand for safe and reliable cars. Henceforth research is conducted to build safer, cleaner and more economic vehicles, trying to find compromises between sometimes conflicting requirements.

Currently, such research focuses on hybrid or electric cars. Nowadays the precious metal resources needed to build the batteries are not sufficient to change the whole park into an

Diesel	Euro1 Oct. 1994	Euro 2 Jan. 1998	Euro 3 Jan. 2000	Euro 4 Sept. 2009	Euro 5 Sept.2011	Euro 6b Sept.2015
NOx(mg/km)	–	–	500	250	180	80
CO(mg/km)	2720	1000	640	500	500	500
HC(mg/km)	–	–	–	–	–	–
NMHC(mg/km)	–	–	–	–	–	–
HC+NOx (mg/km)	970	900	560	300	230	170
PM(mg/km)	140	100	50	25	5	4.5
PN(Nb/km)	–	–	–	–	6×10^{11}	6×10^{11}
Gasoline	Euro1 Oct. 1994	Euro 2 Jan. 1998	Euro 3 Jan. 2000	Euro 4 Sept. 2009	Euro 5 Sept.2011	Euro 6b Sept.2015
NOx(mg/km)	–	–	150	80	60	60
CO(mg/km)	2720	2200	2200	1000	1000	1000
HC(mg/km)	–	–	200	100	100	100
NMHC(mg/km)	–	–	–	–	68	68
HC+NOx (mg/km)	–	–	–	–	–	–
PM(mg/km)	–	–	–	–	5	4.5
PN(Nb/km)	–	–	–	–	–	6×10^{11}

Table 1: Passenger car European Emission Standards (Quoted from Wikipedia)

electric one. Batteries are heavy, battery autonomy is still low and their charging time may be a problem for long journeys. The number of charge cycles they can undergo may also be a problem. Besides energy sources are needed to supply electricity. To get clean energy, it may necessitate more nuclear power plants which are not very popular. Green electricity is still limited and coal and natural gas are going to remain the main sources of electricity generation for the coming years. Natural gas is the least CO_2 emitting fossil energy but it also involves the development of shale gas. For generating electricity many efforts are made on renewable energy sources, natural gas or nuclear power but coal remains one of the main sources. It is expected that renewable generation will only surpass coal generation in 2040.
Hybrid engines offer an intermediate solution. Their technology is based on an optimization of the internal combustion (IC) engine. Their development is complex and it will probably not be everyone's car for the next coming 20 years. Figure 1(a) quoted from "International Energy Outlook 2016", shows the projections to 2040 of the energy source distributions for transportation. It includes all kinds of transportation but, as shown in Figure 1(b) passenger cars constituted in 2012 the main part of the transportation energy consumption and it should still be the case in 2040.

It seems clear that traditional IC (internal combustion) engines still have a future and improving their performance remains a major investment for the automotive industry.

To reduce car consumption various options can be considered. For instance it is possible

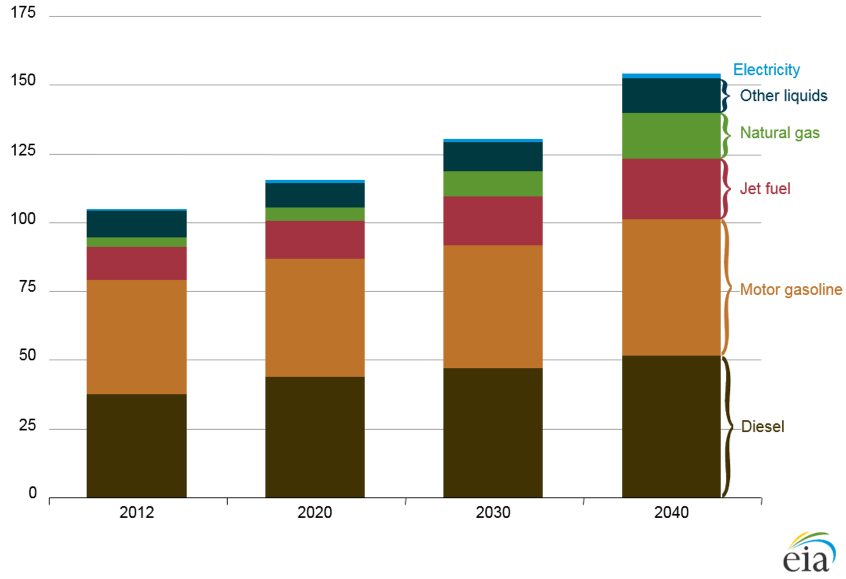

(a)

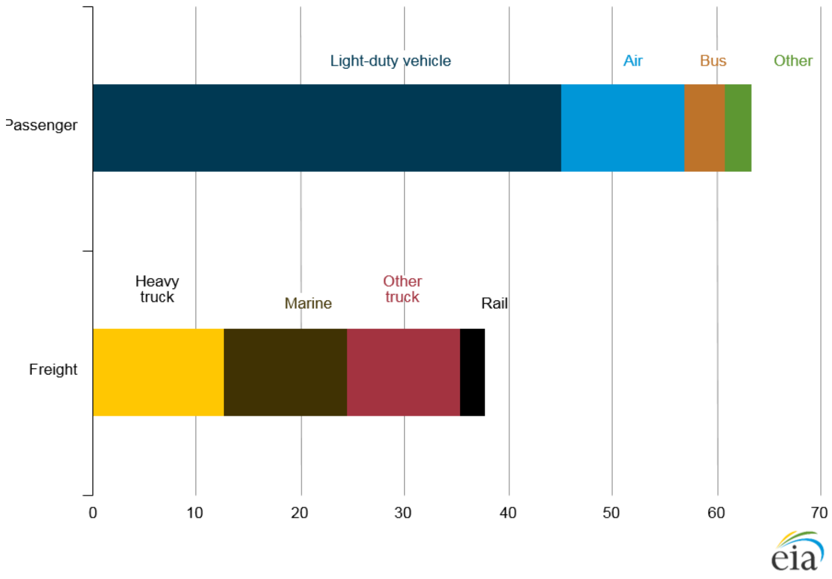

(b)

Figure 1: (a) World transportation energy consumption (quadrillon BTU) by source, 2012-2040 (b) World transportation energy consumption(quadrillon BTU) by mode, 2012. (Quoted from "International Energy Outlook 2016")

to build lighter vehicles. However, nowadays most people want power steering and air conditioning systems, ... and these are heavy devices. So the current trend is not lighter but heavier vehicles. An other possibility consists in improving the engine trying to get an optimal consumption, reducing energy losses with an engine as small and light as possible. For a modern fired engine only 38 to 41% of the energy is effectively used, the other part is lost. Mechanical friction consumes between 4 to 15% of the energy and about half of this loss is due to the piston-assembly system. Figure 2 shows how fuel is spent in en engine car. More details can be found in [1].

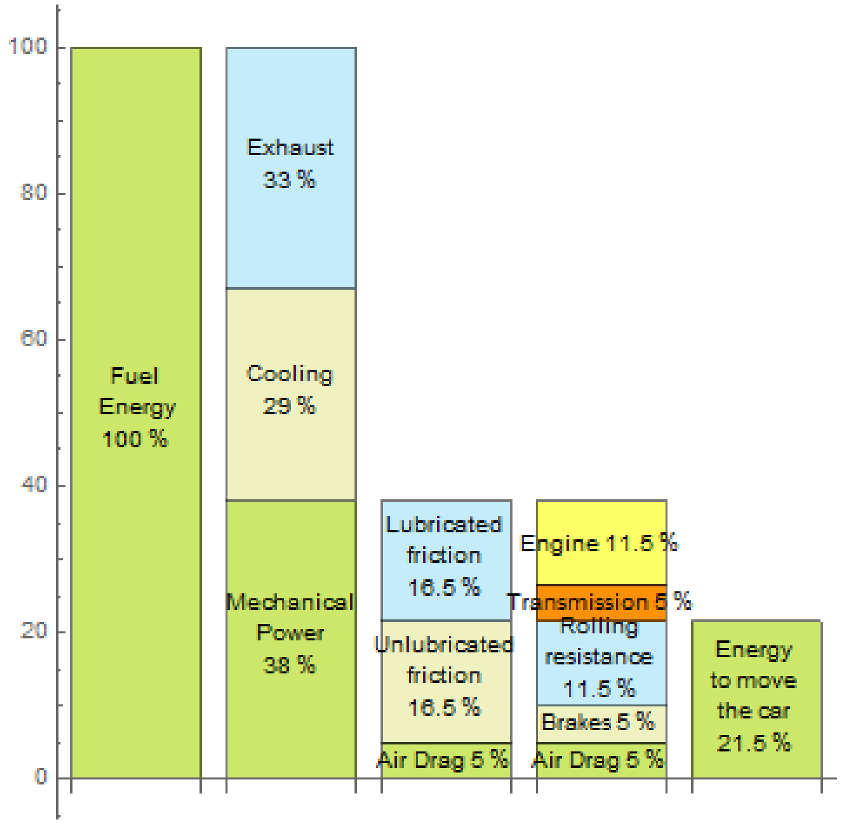

Figure 2: Fuel energy distribution in a passenger car. (Based on [1])

Therefore, improving lubrication and reducing friction in the piston pack remain important domain of research since, considering the whole transportation sector, even a small gain in fuel consumption induces a significant environmental improvement.
In the piston-assembly system the piston ring pack is a key factor for those environmental issues. For instance the combustion chamber crevices such as in the piston top-land are responsible for unburned fuel and particle emissions and will emit HC at exhaust. Lubricant is used to diminish the friction between moving parts of an engine and therefore reduce energy losses, fuel consumption and CO_2 emissions. Besides oil consumption has to be limited. Here again, the piston ring cylinder pack plays a central part because of the oil degradation and possible leakage into the combustion chamber creating pollutant emissions while burning. Therefore a compromise must be found between friction reduction and oil consumption. The lubricant amount should be sufficient to reduce friction and CO_2 emissions by ensuring a good lubrication of all moving parts but should not be too high to limit oil leakage into the combustion chamber. These constraints

being antagonistic, it is necessary to find new architectures for the PRCL contact. For instance the choice of a good liner texturing may be interesting. It is also possible to work on the lubricant chemical structure by the use of additives and improve its lubricity to reduce lubricated friction losses. Used lubricant are not easy to dispose of and they decompose very slowly. Thus manufacturers have to strive to significantly increase the time intervals between oil services for modern cars.
Experimental studies are difficult and expensive because building prototypes is long and expensive. Therefore the development of the numerical modeling has become an important part of current research. In this work a geometrical multigrid code that allows to study the hydrodynamic lubrication of the PRCL contact in presence of very rough textured liners is developed.

Lubrication

Lubricant is essential to reduce friction. Lubricant also limits wear, corrosion and heat generation. It keeps the surfaces clean by removing small debris that could damage the system. It also absorbs shocks and vibrations.
The friction coefficient depends on the minimum film thickness. It can be improved by adequate texturing or coating of the surfaces. For a given lubricated contact several lubrication regimes can exist. They can be described by a Stribeck curve. An example is given in Figure 3. Depending on the oil viscosity, the load and the velocity of the surfaces in the contact, three different lubrication regimes exist. For low viscosity, small velocity or high load, it is the boundary regime. It is a dry contact and the friction coefficient is determined by the characteristics of the 2 surfaces. For high viscosity, high velocity or low load, it is the hydrodynamic regime. Both surfaces are perfectly separated by an oil film. The friction mainly depends on the lubricant. In between, is the mixed regime. The film does not completely separate the 2 surfaces. The friction is defined by the surfaces and the lubricant. According to the regime different models of the contact must be considered. PRCL contacts operate in the mixed lubrication or hydrodynamic lubrication regime. This study focuses on hydrodynamic lubrication of textured contacts.

It will be assumed that the film behavior is governed by the Reynolds equation. Therefore it will be considered that:

- the flow is laminar
- the fluid is newtonian
- fluid inertia forces are negligible
- pressure variations across the film are negligible.

It will also be assumed that the surfaces are rigid since we only study the hydrodynamic contact. The fluid will be considered isoviscous and incompressible. The Reynolds equation that describes the contact reads:

$$\frac{\partial}{\partial x}\left(\frac{\rho h^3}{12\eta}\frac{\partial p}{\partial x}\right)+\frac{\partial}{\partial y}\left(\frac{\rho h^3}{12\eta}\frac{\partial p}{\partial y}\right)-u_m\frac{\partial(\rho h)}{\partial x}-\frac{(\partial \rho h)}{\partial t}=0 \tag{1}$$

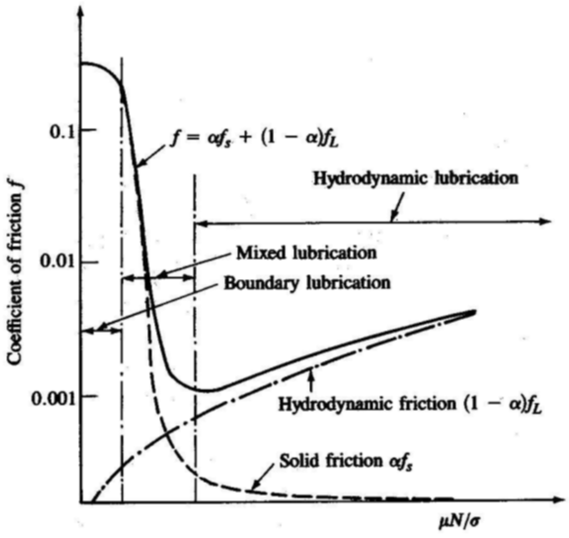

Figure 3: Example of a Stribeck Curve, from [2]

In this equation p is the fluid pressure assumed to be constant across the film height, h represents the film thickness, u_m is the mean velocity of the surfaces, ρ is the fluid density (for us it will be constant since the fluid is assumed incompressible) and η is the fluid viscosity that will also be assumed constant. The first two terms constitute the Poiseuille terms. They describe the flow generated by the pressure gradient. The third term is the wedge or Couette term due to the surface velocities and subsequent fluid displacement. The last term is the squeeze flow due to the variation of the film height with time.

Piston ring cylinder liner pack

The piston system is composed of the piston, piston rings, connecting rods and bearings. It induces three main types of friction: piston skirt against the liner, piston rings against liner and bearing surfaces, more details can be found in [3]. Figure 4 (a) presents a general view of the piston assembly and Figure 4 (b) gives a sketch of the ring-pack liner subsystem.

The ring pack usually consists of three rings that have sealing and lubricating functions. Lubrication is needed to reduce friction during the piston course and the rings maintain the right amount of oil in the contact. But no unburned fuel or exhaust gas should enter the crankcase and degrade the lubricant. Besides oil leakage into the combustion chamber should also be limited. The three rings are the following:

- Top ring or first ring or compression ring: it is mostly used for sealing the combustion chamber. It also increases the combustion pressure and efficiency.
- Second ring or scraper ring: it has a sealing function and also scrapes the lubricant.
- Third ring or oil control ring: it controls and regulates the oil distribution between the crankcase and the cylinder wall. It also has a sealing role.

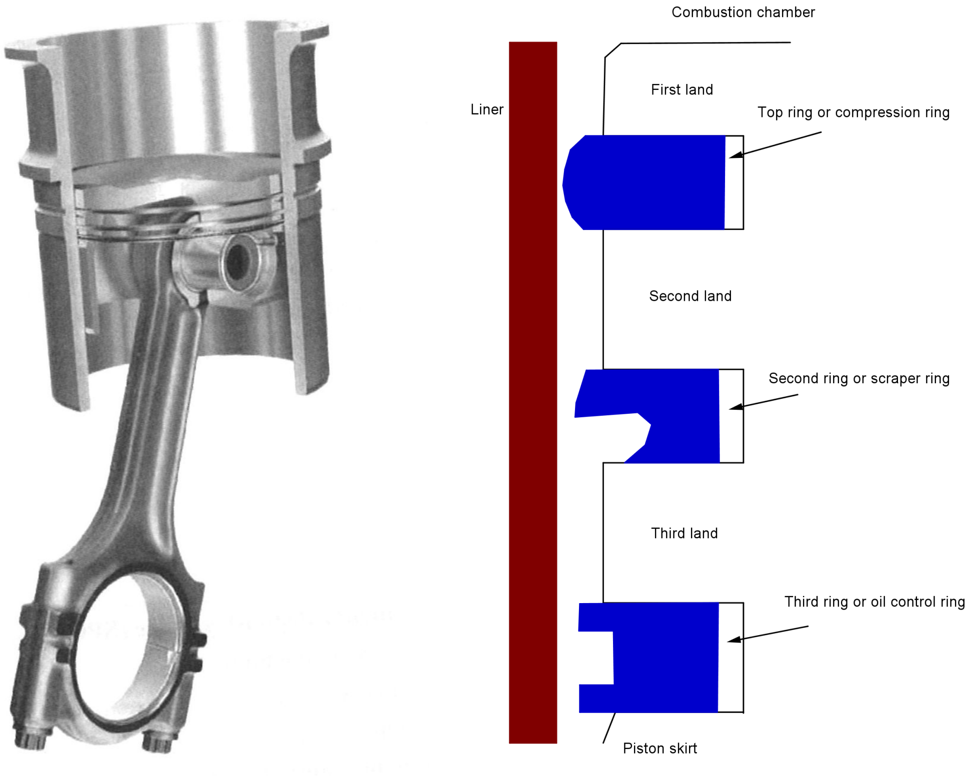

(a) (b)

Figure 4: Piston Pack (a) global view (b) piston rings - liner

The friction induced by the piston ring subsystem in reciprocating motion along the liner represent 28 to 45% of the piston assembly friction. Figure 5 shows the friction power loss per ring. Losses due to the second ring are much less important than for the other two rings. For the top ring the losses are more important when the piston reaches its highest position (top dead center) at the end of the compression phase. Otherwise all rings present local loss peaks at mid-stroke when the piston velocity is highest. These peaks are most important for the oil control ring.

Thesis structure

The purpose of the current research is to write an efficient code to solve the Reynolds equation in the hydrodynamic case in presence of surface texture in order to study the minimum film thickness behavior in the PRCL contact. The code that has been written is a multigrid algorithm based on some ideas developed by Alcouffe et al. [4].

- Chapter 1: the algorithm is described. At this stage mass conservation is not accounted for and the squeeze term is not considered.

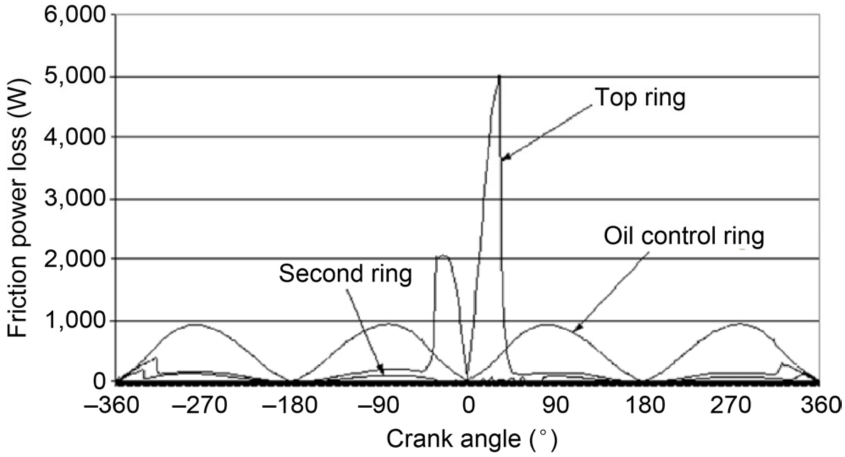

Figure 5: friction power loss contribution in the piston ring pack at 1,800 rpm full load (taken from [3].)

- Chapter 2: results are shown and a comparison is made with the standard geometrical multigrid algorithm presented in [5].
- Chapter 3: the code is validated by comparison with 1D analytical results obtained by Biboulet and Lubrecht [6] and the influence of the groove parameters for a cross-hatched textured liner is studied.
- Chapter 4: the algorithm is modified to include flow conservation.
- Chapter 5: although the code performance is not optimal, it can be used to study the influence of dimples for flat ring lubrication.
- Chapter 6: the algorithm without flow conservation is modified to include the squeeze term and used to study the behavior of the minimum film thickness in the PRCL close to top and bottom dead centers.

Chapter 1

Algorithm

Contents

1.1 Introduction

We want to build an efficient algorithm to study the lubricated piston ring cylinder liner contact. The smooth contact problem converges using classical algorithms (see for instance [5]). Deep grooves show divergence. A more robust algorithm is therefore needed that accounts for the liner roughness. The algorithm that we have developed is based on ideas of Alcouffe, Brandt, Dendy and Painter that were expressed in [4]. In this chapter after a rapid survey of the general principles of multigrid techniques, the Alcouffe algorithm as applied to the Reynolds equation, is described.

1.2 Multigrid principles

The first multigrid scheme was developed by R.P. Fedorenko [7, 8] in the early 60's and was extensively studied and developed by Brandt in the late 70's [9]. Their efficiency in accelerating convergence for elliptic partial differential equations as well as the multigrid integration make them particularly interesting in lubrication problems in particular for solving the Reynolds equation (see [5]). The main principles on multigrid techniques are described in [5, 9, 10].
The partial differential equation to be solved is discretized on the target grid h and the problem reads:

$$L^h u^h = f^h$$

where u^h is the unknown discretized function, L^h the discretized operator and f^h the discretized right hand side of the equation. The letter h refers to the space step of the grid h. A relaxation process is used to solve the discretized problem. It has to be a good smoother meaning that it must rapidly suppress the high frequency components of the error $e^h = u^h - \tilde{u}^h$ where $\tilde{u}^h$ is an approximation of u^h. If this is actually the case, it is achieved using very few pre-relaxations on the target grid. The Gauss-Seidel scheme is often chosen. To estimate the error e^h, since u^h is not known, the residual $r^h = f^h - L^h \tilde{u}^h$ of the equation is considered. The problem is solved when $r^h = 0$ since then $\tilde{u}^h = u^h$.
When the error is very smooth, the relaxation process is no longer efficient on the fine grid and the remaining components of the error will be more efficiently eliminated on a coarser grid H. Usually one takes $H = 2 \times h$ meaning that the space step in any direction is doubled although this is not mandatory (see Figure 1.1).

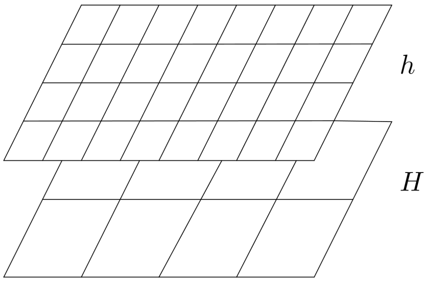

Figure 1.1: Fine grid and coarse grid

In the linear case a Correction Scheme (in short CS) is used. For a linear operator we get $L^h e^h = r^h$. Since e^h is smooth, this problem is more efficiently solved using a coarser grid. It is transferred to the coarse grid H and becomes $L^H e^H = I_h^H r^h$ where L^H is a coarse grid approximation of the operator L^h, I_h^H is a restriction operator from grid h to grid H and e^H a coarse grid approximation to the error e^h. Once the problem is solved on the coarse grid, the solution e^H is interpolated to the fine grid with an interpolation operator I_H^h and added to the fine grid approximation $\tilde{u}^h$ to correct it. This process induces high frequency errors that can be eliminated using very few post-relaxations on the fine grid h.
For a non linear case a Full Approximation Scheme (in short FAS) is used. We no longer have

$L^h e^h = r^h$. As it is the error that is smooth and therefore can be represented on the coarse grid, another way of estimating it on the coarse grid must be found. One has $L^h(\tilde{u}^h + e^h) = L^h\tilde{u}^h + r^h$ since $u^h = \tilde{u}^h + e^h$ and $f^h = L^h(\tilde{u}^h + e^h)$. The coarse grid problem is then $L^H\hat{u}^H = \hat{f}^H$ with $\hat{u}^H = I_h^H(\tilde{u}^h + e^h) = I_h^H(\tilde{u}^h) + e^H$ and $\hat{f}^H = L^H(I_h^H(\tilde{u}^h)) + I_h^H(r^h)$. The coarse grid problem is solved and the interpolated error $I_H^h(e^H)$ that is to say $I_H^h(\tilde{u}^H - I_h^H(\tilde{u}^h))$ is added to the previous fine grid approximation $\tilde{u}^h$ to get a new fine grid approximation.

The choice of the relaxation scheme that must be a good smoother, the choice of the restriction and interpolation operators, I_h^H and I_H^h, and of the coarse grid operator L^H are essential to the efficiency of the process. This chapter will focus on these operators to get good convergence for the hydrodynamic lubrication of the piston ring for textured liners.

The numbers ν_1 and ν_2 of pre and post-relaxations have to be small. Typical values are $\nu_1 = 2$ and $\nu_2 = 1$. The process can be repeated recursively to solve the coarse grid problem. This corresponds to $V(\nu_1, \nu_2)$-cycles see figure 1.2. On the coarsest grid, the problem is solved using ν_0 relaxations. If the coarsest grid is very coarse, $\nu_0 = 10$ is sufficient. Since this work only uses V-cycles, other options are not discussed. A few cycles, ncy, have to be used to reach the discretization error.

To speed up the process, one may solve the initial problem on a grid H, interpolate the solution u^H to the next fine grid in order to get a better starting solution on the next fine grid. This is called: Full MultiGrid scheme and is referred as FMG.

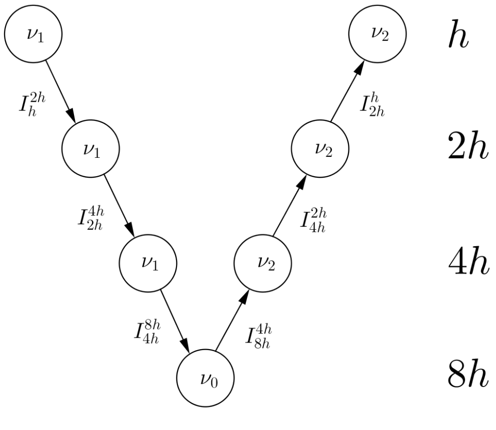

Figure 1.2: V-cycle for 4 levels.

1.3 Equations

Before adapting the ideas presented by Alcouffe et al. in [4] to the PRLC lubrication and the Reynolds equation, we present what they propose for the diffusion equation with strongly discontinuous coefficients. Our purpose is to explicit the required operators (interpolation, restriction, fine grid and coarse grid operators) in order to be able to code them for the piston ring hydrodynamic lubrication. The notations used mostly correspond to Alcouffe's paper notations. The problem that they considered is a problem of the following form:

$$-\nabla\cdot(D(x,y)\nabla U(x,y)) + \sigma(x,y)U(x,y) = f(x,y) \qquad (x,y)\in\Omega, \tag{1.1a}$$

$$-\nu\cdot(D(x,y)\nabla U(x,y)) + \gamma(x,y)U(x,y) = 0 \qquad (x,y)\in\partial\Omega, \tag{1.1b}$$

where Ω is a bounded region of $\mathbb{R}^3$ of boundary $\partial\Omega$. The functions σ and γ are nonnegative. The functions D, σ, f can have discontinuities on some internal line Γ in Ω. The function ν is the outer normal to $\partial\Omega$. Moreover it is assumed that:

$$U \text{ and } \mu\cdot(D\nabla U) \text{ are continuous almost everywhere on } \Gamma \tag{1.2}$$

where μ represents a normal to Γ.

In the case when D has strong discontinuities on Γ, it is important to have a good representation of the problem on the coarse grids and thus, the interpolation, restriction and coarse grids operators have to be carefully designed. To build the interpolation operator, the continuity of $D\cdot\nabla U$ has to be taken into account instead of just the continuity of ∇U which does not hold. It corresponds to a flow continuity.

1.4 Volume discretization

We assume that the domain Ω is a rectangle $[x_a, x_b]\times[y_a, y_b]$ covered with a grid made of straight lines parallel to the coordinate axes.

$$\{x_a = x_0 < x_1 < \ldots < x_n = x_b\} \times \{y_a = y_0 < y_1 < \ldots < y_m = y_b\} \tag{1.3}$$

Set $h_i = x_{i+1} - x_i$ and $k_i = y_{i+1} - y_i$. Usually the steps will be taken constant in each direction and may be called h_x and h_y and often, but not necessarily, $h_x = h_y$.
Integrate equation 1.1 over the domain Ω using Green-Riemann on each cell, Δ, represented in figure 1.3(a). Set $G = (G_1, G_2)$ with $G_1 = D\partial U/\partial x$ and $G_2 = D\partial U/\partial y$.
Using Green's theorem to convert the integral of 1.1 over the cell Δ, one gets :

$$\iint_\Delta -\nabla G\,\mathrm{d}x\mathrm{d}y = \int_{M_1}^{M_2} G_2\,\mathrm{d}x + \int_{M_3}^{M_4} G_2\,\mathrm{d}x - \int_{M_2}^{M_3} G_1\,\mathrm{d}y - \int_{M_4}^{M_1} G_1\,\mathrm{d}y \tag{1.4}$$

Besides, the midpoint rule gives:

$$\int_{M_1}^{M_2} G_2\,\mathrm{d}x \approx G_2(x_i, y_j - \frac{k_{j-1}}{2})\frac{h_{i-1}+h_i}{2} = D(x_i, y_j - \frac{k_{j-1}}{2})\frac{\partial U}{\partial y}(x_i, y_j - \frac{k_{j-1}}{2})\frac{h_{i-1}+h_i}{2}. \tag{1.5}$$

Denote $G_{i,j} = G(x_i, y_j)$ and $G_{i+\frac{1}{2},j+\frac{1}{2}} = G(x_i + h_i/2, y_j + k_j/2)$ for any function G .
One has

$$D\Big(x_i, y_j - \frac{k_{j-1}}{2}\Big) \approx \frac{1}{2}(G_{i-\frac{1}{2},j-\frac{1}{2}} + G_{i+\frac{1}{2},j-\frac{1}{2}}) \tag{1.6}$$

$$\frac{\partial U}{\partial y}\Big(x_i, y_j - \frac{k_j}{2}\Big) \approx \frac{U_{i,j} - U_{i,j-1}}{k_{j-1}} \tag{1.7}$$

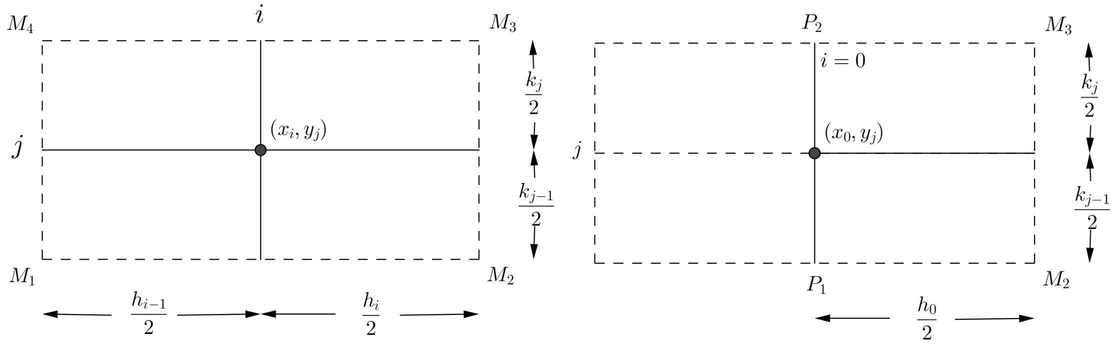

(a) (b)

Figure 1.3: (a) Elementary cell Δ (b) Example of boundary cell.

and so on...
With these approximations, we derive Alcouffe formulas:

$$\iint_\Delta -\nabla(D \cdot \nabla U)\,\mathrm{d}x\mathrm{d}y = -A_{i,j+\frac{1}{2}}(U_{i,j+1}-U_{i,j}) - A_{i,j-\frac{1}{2}}(U_{i,j-1}-U_{i,j}) - B_{i+\frac{1}{2},j}(U_{i+1,j}-U_{i,j}) - B_{i-\frac{1}{2},j}(U_{i-1,j}-U_{i,j}) \tag{1.8}$$

with

$$A_{i,j+\frac{1}{2}} = \frac{1}{2}(D_{i+\frac{1}{2},j+\frac{1}{2}} + D_{i-\frac{1}{2},j+\frac{1}{2}})\frac{h_{i-1}+h_i}{2k_j}$$

and

$$B_{i+\frac{1}{2},j} = \frac{1}{2}(D_{i+\frac{1}{2},j+\frac{1}{2}} + D_{i+\frac{1}{2},j-\frac{1}{2}})\frac{k_{j-1}+k_j}{2h_i}$$

which simply reads for constant steps $h_i = h_x, k_j = h_y$ as will be the case:
$A_{i,j+\frac{1}{2}} = \frac{1}{2}(D_{i+\frac{1}{2},j+\frac{1}{2}} + D_{i-\frac{1}{2},j+\frac{1}{2}})h_x/h_y$ and $B_{i+\frac{1}{2},j} = \frac{1}{2}(D_{i+\frac{1}{2},j+\frac{1}{2}} + D_{i+\frac{1}{2},j-\frac{1}{2}})h_y/h_x$.
For a boundary cell as shown in figure 1.3(b), these formulas remain valid setting the function D to 0 outside the domain Ω.

Remark:
From now on, we write $A_{i,j}$, $B_{i,j}$ and $D_{i,j}$ instead of $A_{i,j+\frac{1}{2}}$,$B_{i+\frac{1}{2},j}$ and $D_{i+\frac{1}{2},j+\frac{1}{2}}$.
The numbers $A_{i,j}$ and $B_{i,j}$ can be viewed as diffusion coefficients or conductances between the nodes (i, j) and $(i, j + 1)$ and between the nodes (i, j) and $(i + 1, j)$. This is represented in figure 1.4.
The right hand side is discretized as follows:

$$\iint_\Delta f(x,y)\,\mathrm{d}x\mathrm{d}y \approx \frac{1}{4}(h_{i-1}+h_i)(k_{j-1}+k_j)f_{i,j} = F_{i,j} \tag{1.9}$$

It would be more consistent to take
(1.10)

$$\iint_\Delta f(x,y)\,\mathrm{d}x\,\mathrm{d}y \approx \frac{1}{4}(h_{i-1}k_{j-1}f_{i-\frac{1}{2},j-\frac{1}{2}} + h_i k_{j-1} f_{i+\frac{1}{2},j-\frac{1}{2}} + h_{i-1}k_j f_{i-\frac{1}{2},j+\frac{1}{2}} + h_i k_j f_{i+\frac{1}{2},j+\frac{1}{2}})$$

In our applications the function σ will be zero and therefore we skip the treatment of the integral of $\sigma(x, y)U(x, y)$ over a cell. Further details can be found in Appendix A, section A.1.

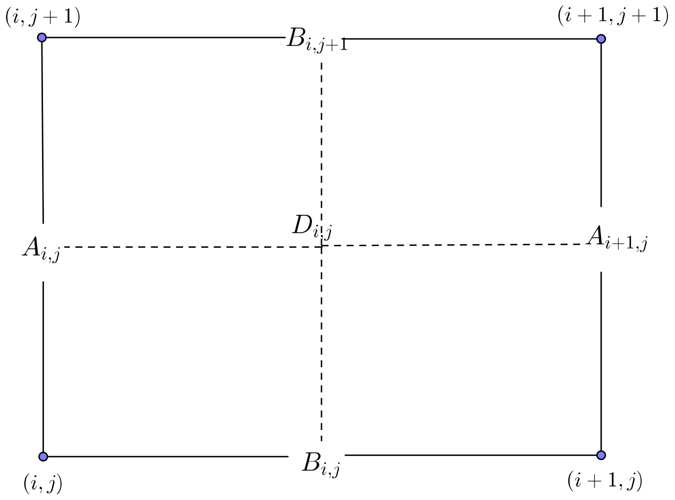

Figure 1.4: Cell coefficients

1.5 Coarse grid coefficients

It is now assumed that for all i, $h_i = h_x$ and $k_i = h_y$. We use a superscript k to denote the various coefficients and functions of the k^{th} level grid. It may be referred to as the fine grid k and the next coarser grid (level $k-1$) may then be referred to as the coarse grid. A general fine grid cell is represented in figure 1.5 .
The coefficient $D_{i,j}$, corresponding to the value of the function D at the cell middle point, is only defined on the finest grid. It enables us to calculate the coefficients $A^k_{i,j}$ and $B^k_{i,j}$ on the very finest grid by the above derived formulas:

$$A^k_{i,j} = \frac{(D_{i-1,j} + D_{i,j})}{2} \frac{h_x}{h_y} \tag{1.11a}$$

$$B^k_{i,j} = \frac{(D_{i,j-1} + D_{i,j})}{2} \frac{h_y}{h_x} \tag{1.11b}$$

The evaluation of the coarse grid coefficients from the fine grid coefficients is now explained. A coarse grid cell is plotted in figure 1.5.
In figure 1.5, the indices on the coarse grid are denoted by (i_C, j_C) and indices of the fine grid corresponding cell by (i_F, j_F). In general $i_C = 2i_F$ and $j_C = 2j_F$.
We must explain how the coefficients $A^{k-1}_{i_c,j_c}$ and $B^{k-1}_{i_c,j_c}$ are calculated.

As previously mentioned the coefficients A and B can be viewed as conductances. Therefore it seems appropriate to calculate the equivalent conductance between the nodes (i_C, j_C) and

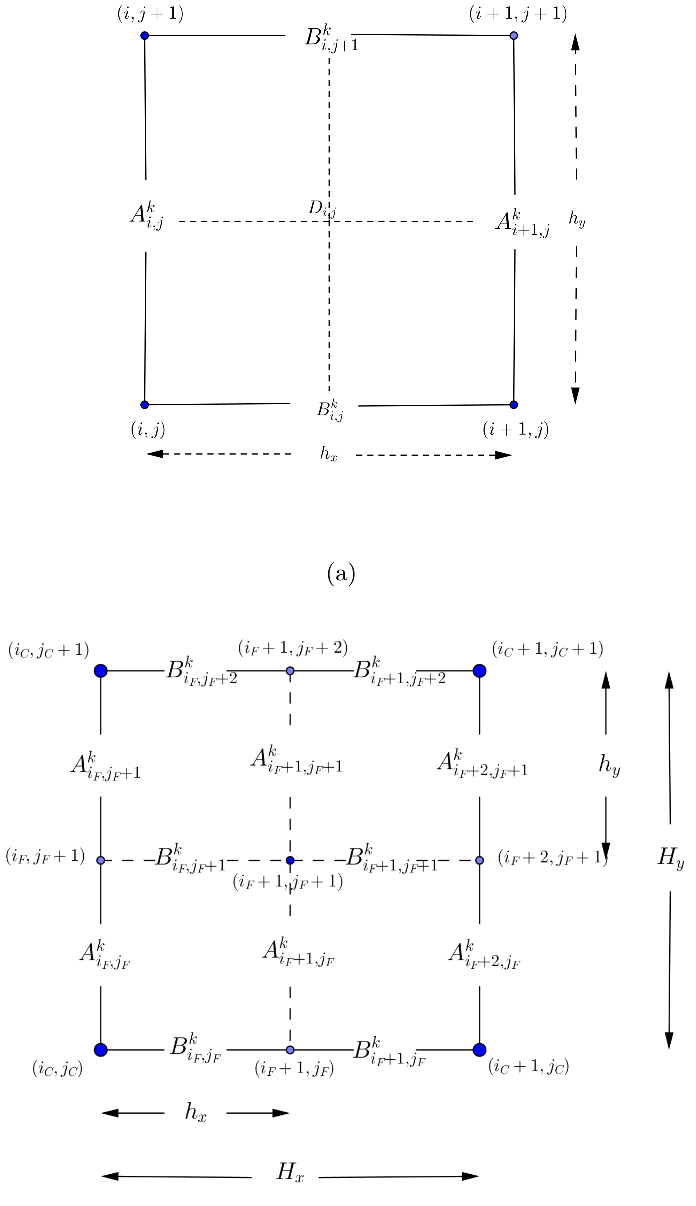

(a)

(b)

Figure 1.5: (a) Fine grid cell (b) Coarse grid cell.

(i_C, j_C+1) on one hand and between the nodes (i_C, j_C) and (i_C+1, j_C) on the other hand by:

$$\begin{aligned}
A^{k-1}_{i_c,j_c} &= \frac{1}{2}\delta(A^k_{i_F,j_F}, A^k_{i_F,j_F+1}) + \frac{1}{4}\delta(A^k_{i_F+1,j_F}, A^k_{i_F+1,j_F+1}) + \frac{1}{4}\delta(A^k_{i_F-1,j_F}, A^k_{i_F-1,j_F+1}) \\
B^{k-1}_{i_c,j_c} &= \frac{1}{2}\delta(B^k_{i_F,j_F}, B^k_{i_F+1,j_F}) + \frac{1}{4}\delta(B^k_{i_F,j_F+1}, B^k_{i_F+1,j_F+1}) + \frac{1}{4}\delta(B^k_{i_F,j_F-1}, B^k_{i_F+1,j_F-1})
\end{aligned} \tag{1.12}$$

with

$$\delta(x,y) = \frac{1}{\frac{1}{2}\left(\frac{1}{x}+\frac{1}{y}\right)} \tag{1.13}$$

This can be improved by better accounting for those "conductances" with the following formulas:

$$\begin{aligned} A^{k-1}_{i_c,j_c} = \frac{1}{2}\delta(A^k_{i_F,j_F}, A^k_{i_F,j_F+1}) &+ \frac{1}{4}\delta(B^k_{i_F,j_F}, A^k_{i_F+1,j_F}, A^k_{i_F+1,j_F+1}, B^k_{i_F,j_F+2}) \\ &+ \frac{1}{4}\delta(B^k_{i_F-1,j_F}, A^k_{i_F-1,j_F}, A^k_{i_F-1,j_F+1}, B^k_{i_F-1,j_F+2}) \end{aligned} \tag{1.14}$$

accounting for conductances along the 3 following paths from node (i_C, j_C) to node (i_C, j_C+1): the direct path, the path passing through nodes (i_F+1, j_F) and (i_F+1, j_F+2) and the path through nodes (i_F-1, j_F) and (i_F-1, j_F+2). And similarly:

$$\begin{aligned} B^{k-1}_{i_c,j_c} = \frac{1}{2}\delta(B^k_{i_F,j_F}, B^k_{i_F+1,j_F}) &+ \frac{1}{4}\delta(A^k_{i_F,j_F}, B^k_{i_F,j_F+1}, B^k_{i_F+1,j_F+1}, A^k_{i_F,j_F+2}) \\ &+ \frac{1}{4}\delta(A^k_{i_F,j_F-1}, B^k_{i_F,j_F-1}, B^k_{i_F+1,j_F-1}, A^k_{i_F+2,j_F-1}) \end{aligned} \tag{1.15}$$

In these formulas one has:

$$\delta(x,y,z,t) = \frac{1}{\frac{1}{4}\left(\frac{1}{x}+\frac{1}{y}+\frac{1}{z}+\frac{1}{t}\right)} \tag{1.16}$$

1.6 Interpolation: part 1

In this section the interpolation operator, I^h_H or I^k_{k-1} from the coarse grid, level $k-1$, to the fine grid, level k, is built.
The coarse grid solution u^{k-1} is denoted u and the fine grid interpolated solution v^k is denoted v. As before, if (i_C, j_C) are the indices of a coarse grid point the fine grid indices of the corresponding point are denoted (i_F, j_F).

$$v = I^k_{k-1} u$$

- **Injection at the coarse grid points** (i_F, j_F) :
  The interpolated value v_{i_F,j_F} is simply given by injection.

  $$v_{i_F,j_F} = u_{i_C,j_C} \tag{1.17}$$

- **Interpolation at non coarse grid points** (i_F+1, j_F) **or** (i_F, j_F+1) :
  The continuity of $D\partial U/\partial x$ which corresponds to a flow conservation is used to determine the interpolated value of v_{i_F+1,j_F}. At the node (i_F+1, j_F) of the fine grid, $D\partial U/\partial x$ is

approximated by $B^k_{i_F+1,j_F}(v_{i_F+2,j_F} - v_{i_F+1,j_F})/h_{i_F+1}$ on the left and by $B^k_{i_F,j_F}(v_{i_F+1,j_F} - v_{i_F,j_F})/h_{i_F}$ on the right. These 2 values must be equal. It yields:

$$B^k_{i_F+1,j_F}\frac{v_{i_F+2,j_F} - v_{i_F+1,j_F}}{h_{i_F+1}} = B^k_{i_F,j_F}\frac{v_{i_F+1,j_F} - v_{i_F,j_F}}{h_{i_F}} \tag{1.18}$$

When $h_{i_F+1} = h_{i_F}$ as it will be the case for us and assumed from now on, one gets:

$$B^k_{i_F+1,j_F}(v_{i_F+2,j_F} - v_{i_F+1,j_F}) = B^k_{i_F,j_F}(v_{i_F+1,j_F} - v_{i_F,j_F}) \tag{1.19}$$

Because of the injected values at points of the fine grid that also belong to the coarse grid, it reads:

$$B^k_{i_F+1,j_F}(u_{i_C+1,j_C} - v_{i_F+1,j_F}) = B^k_{i_F,j_F}(v_{i_F+1,j_F} - u_{i_C,j_C}) \tag{1.20}$$

Hence, the interpolated value at the node (i_F+1, j_F) is given by:

$$v_{i_F+1,j_F} = \frac{B^k_{i_F+1,j_F}u_{i_C+1,j_C}+B^k_{i_F,j_F}u_{i_C,j_C}}{B^k_{i_F+1,j_F}+B^k_{i_F,j_F}} \tag{1.21}$$

Please note that it is a weighted average of u_{i_C,j_C} and u_{i_C+1,j_C} with respective weights B_{i_F,j_F} and B_{i_F+1,j_F}, the "diffusion coefficients".

Similarly, the continuity of $D\partial U/\partial y$ yields:

$$A^k_{i_F,j_F+1}(u_{i_C,j_C+1} - v_{i_F,j_F+1}) = A^k_{i_F,j_F}(v_{i_F,j_F+1} - u_{i_C,j_C}) \tag{1.22}$$

and thus:

$$v_{i_F,j_F+1} = \frac{A^k_{i_F,j_F+1}u_{i_C,j_C+1}+A^k_{i_F,j_F}u_{i_C,j_C}}{A^k_{i_F,j_F+1}+A^k_{i_F,j_F}} \tag{1.23}$$

Again it is a weighted average of u_{i_C,j_C} and u_{i_C,j_C+1} with respective weights A_{i_F,j_F} and A_{i_F,j_F+1}.

- **Interpolation at non coarse grid points** (i_F+1, j_F+1) :
  Still using the continuity of $D\partial U/\partial x$ and $D\partial U/\partial y$, it can be written that

$$B^k_{i_F+1,j_F+1}(v_{i_F+2,j_F+1} - v_{i_F+1,j_F+1}) = B^k_{i_F,j_F+1}(v_{i_F+1,j_F+1} - v_{i_F,j_F+1}) \tag{1.24}$$

$$A^k_{i_F+1,j_F+1}(v_{i_F+1,j_F+2} - v_{i_F+1,j_F+1}) = A^k_{i_F,j_F+1}(v_{i_F+1,j_F+1} - v_{i_F+1,j_F}) \tag{1.25}$$

Adding those two relations, we obtain:

(1.26)

$$v_{i_F+1,j_F+1} = \frac{A^k_{i_F+1,j_F+1}v_{i_F+1,j_F+2} + A^k_{i_F+1,j_F}v_{i_F+1,j_F} + B^k_{i_F+1,j_F+1}v_{i_F+2,j_F+1}+B^k_{i_F,j_F+1}v_{i_F,j_F+1}}{A^k_{i_F+1,j_F}+A^k_{i_F+1,j_F+1} + B^k_{i_F+1,j_F+1}+B^k_{i_F,j_F+1}}$$

And then the interpolated values of v_{i_F+1,j_F} and v_{i_F,j_F+1} previously computed can be used. Using simplified notations, the final result will be given in section 1.8.

1.7 Restriction

In this section the restriction operator, I_h^H or I_k^{k-1} from the fine grid, level k, to the coarse grid level $k-1$, is built. It is defined as the transpose of the interpolation operator. Its stencil at the coarse grid point (i_C, j_C) is explicited.

$$I_h^H = (I_H^h)^T \text{ or } I_k^{k-1} = (I_{k-1}^k)^T. \tag{1.27}$$

If f and g are two functions defined on the domain Ω, their dot $< f|g >$ product is defined by

$$< f|g >= \iint f(x,y)g(x,y)\,\mathrm{d}x\,\mathrm{d}y. \tag{1.28}$$

Its discretized version on grid k becomes

$$< f|g >= h_x h_y \sum_{i,j} f_{i,j} g_{i,j} \tag{1.29}$$

On the grid k we use the orthogonal basis $(e_I^k)_I$ where e_I^k represents the function that has the value 1 at the node $I_F = (i_F, j_F)$ and 0 at the other nodes. Its squared norm is then $< e_I^k|e_I^k >= h_x h_y$. If $W^k = \sum_I W_I^k e_I^k$ is a function discretized on grid k, its restriction to the coarse grid $k-1$ is

$$I_k^{k-1} W^k = \sum_{I_C} (I_k^{k-1} W^k)_{I_C} e_{I_C}^{k-1} \tag{1.30}$$

with

$$(I_k^{k-1} W^k)_{I_C} = \frac{< I_k^{k-1} W^k | e_{I_C}^{k-1} >}{< e_{I_C}^{k-1} | e_{I_C}^{k-1} >} = \frac{< W^k | I_{k-1}^k e_{I_C}^{k-1} >}{< e_{I_C}^{k-1} | e_{I_C}^{k-1} >} = \sum_I E_{I_C,I} W_I^k \tag{1.31}$$

where

$$E_{I_C,I} = \frac{< e_I^k | I_{k-1}^k e_{I_C}^{k-1} >}{< e_{I_C}^{k-1} | e_{I_C}^{k-1} >} \tag{1.32}$$

Hence we must find the component along each vector e_I^k of $I_{k-1}^k e_{I_C}^{k-1}$. This can be done by applying the interpolation formulas previously computed to $u = e_{I_C}^{k-1}$ where $I_C = (i_C, j_C)$ is a coarse grid node. Denoting $v = I_{k-1}^k e_{I_C}^{k-1}$, the components of v can be obtained by substituting in the results of section 1.6 to $u = e_{I_C}^{k-1}$ that is to say to the u defined on the coarse grid by $u_{i_C,j_C} = 1$ and $u_{i,j} = 0$ otherwise. Figure 1.6 represents the points of the fine grid that have a non zero contribution to the restricted value. In this picture $I_C = (i_F, j_F)$ is the point of the fine grid k coinciding with the coarse grid point $I_C = (i_C, j_C)$, $I_N = (i_F, j_{F+1})$, $I_{NE} = (i_{F+1}, j_{F+1})$, etc... One obtains

$$I_{k-1}^k e_{I_C}^{k-1} = (NW e_{I_{NW}}^k + N e_{I_N}^k + NE e_{I_{NE}}^k + W e_{I_W}^k + C e_{I_C}^k + E e_{I_E}^k + SW e_{I_{SW}}^k + S e_{I_S}^k + SE e_{I_{SE}}^k) \frac{H_x H_y}{h_x h_y} \tag{1.33}$$

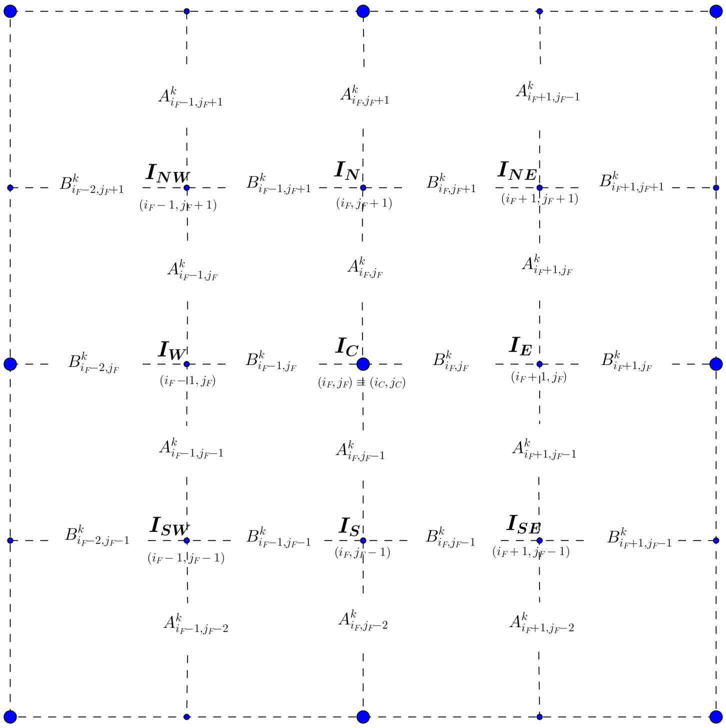

Figure 1.6: Fine grid points involved in the restricted value at the point I_C and useful coefficients.

With, the following values computed by the formulas obtained in the previous section 1.6 for $u^{k-1} = e^{k-1}_{I_C}$,

$$
\begin{aligned}
&C = 1 \\
&N = \frac{A^k_{i_F,j_F}}{A^k_{i_F,j_F} + A^k_{i_F,j_F+1}} \qquad S = \frac{A^k_{i_F,j_F-1}}{A^k_{i_F,j_F-2} + A^k_{i_F,j_F-1}} \\
&W = \frac{B^k_{i_F-1,j_F}}{B^k_{i_F-2,j_F} + B^k_{i_F-1,j_F}} \qquad E = \frac{B^k_{i_F,j_F}}{B^k_{i_F,j_F} + B^k_{i_F+1,j_F}}
\end{aligned}
\tag{1.34}
$$

And

$$
\begin{aligned}
NW &= \frac{N\,B^k_{i_F-1,j_F+1} + W\,A^k_{i_F-1,j_F}}{A^k_{i_F-1,j_F} + A^k_{i_F-1,j_F+1} + B^k_{i_F-2,j_F+1} + B^k_{i_F-1,j_F+1}} \\
NE &= \frac{N\,B^k_{i_F,j_F+1} + E\,A^k_{i_F+1,j_F}}{A^k_{i_F+1,j_F} + A^k_{i_F+1,j_F+1} + B^k_{i_F,j_F+1} + B^k_{i_F+1,j_F+1}} \\
SW &= \frac{S\,B^k_{i_F-1,j_F-1} + W\,A^k_{i_F-1,j_F-1}}{A^k_{i_F-1,j_F-2} + A^k_{i_F-1,j_F-1} + B^k_{i_F-2,j_F-1} + B^k_{i_F-1,j_F-1}} \\
SE &= \frac{N\,B^k_{i_F,j_F-1} + E\,A^k_{i_F+1,j_F-1}}{A^k_{i_F+1,j_F-2} + A^k_{i_F+1,j_F-1} + B^k_{i_F,j_F-1} + B^k_{i_F+1,j_F-1}}
\end{aligned}
\tag{1.35}
$$

It corresponds to a weighting with the diffusion coefficients around each point.
Henceforth, because of the linearity of the restriction operator and if $v^{k-1} = I_k^{k-1}(u^k)$, we can write that:

$$\begin{aligned} v^{k-1}_{i_C,j_C} = (&NW\, u^k_{i_F-1,j_F+1} + N\, u^k_{i_F,j_F+1} + NE\, u^k_{i_F+1,j_F+1} \\ &+ W\, u^k_{i_F-1,j_F} + C\, u^k_{i_F,j_F} + E\, u^k_{i_F+1,j_F} \\ &+ SW\, u^k_{i_F-1,j_F-1} + S\, u^k_{i_F,j_F-1} + SE\, u^k_{i_F+1,j_F-1})\, \frac{h_x h_y}{H_x H_y} \end{aligned} \tag{1.36}$$

The stencil of the restriction at the point (i_C, j_C) of the coarse grid coinciding with the point (i_F, j_F) of the fine grid is then given by:

$$I_k^{k-1} = \frac{h_x h_y}{H_x H_y} \begin{bmatrix} NW & N & NE \\ W & C & E \\ SW & S & SE \end{bmatrix} \tag{1.37}$$

For these coefficients, it may be better to write $NW^k_{i_C,j_C}$ instead of NW, etc... These values depend on the point (i_C, j_C) at which the restriction is performed. It may be noted that when the function D is constant equal to 1(Poisson operator) then the following stencil is obtained:

$$I_k^{k-1} = \frac{h_x h_y}{H_x H_y} \begin{bmatrix} 1/4 & 1/2 & 1/4 \\ 1/2 & 1 & 1/2 \\ 1/4 & 1/2 & 1/4 \end{bmatrix} \tag{1.38}$$

which corresponds to the restriction operator used in classical geometrical multigrid.

1.8 Interpolation: part 2

With the notations of the previous section, the interpolation formulas from the coarse grid $k-1$ to the fine grid k, read:

$$\begin{aligned} v^k_{i_F+1,j_F} &= E^k_{i_C,j_C}\, u^{k-1}_{i_C,j_C} + W^k_{i_C+1,j_C}\, u^{k-1}_{i_C+1,j_C} \\ v^k_{i_F+1,j_F} &= N^k_{i_C,j_C}\, u^{k-1}_{i_C,j_C} + S^k_{i_C,j_C+1}\, u^{k-1}_{i_C,j_C+1} \end{aligned} \tag{1.39}$$

and

$$\begin{aligned} v^k_{i_F+1,j_F+1} =& NE^k_{i_C,j_C}\, u^{k-1}_{i_C,j_C} + NW^k_{i_C+1,j_C}\, u^{k-1}_{i_C+1,j_C} \\ &+ SE^k_{i_C,j_C+1}\, u^{k-1}_{i_C,j_C+1} + SW^k_{i_C+1,j_C+1}\, u^{k-1}_{i_C+1,j_C+1} \end{aligned} \tag{1.40}$$

The stencil of the interpolation operator I^k_{k-1} at the point (i_C, j_C) of the coarse grid coinciding with the point (i_F, j_F) is then given by:

$$I^k_{k-1} = \begin{bmatrix} NW^k_{i_C,j_C} & N^k_{i_C,j_C} & NE^k_{i_C,j_C} \\ W^k_{i_C,j_C} & C^k_{i_C,j_C} & E^k_{i_C,j_C} \\ SW^k_{i_C,j_C} & S^k_{i_C,j_C} & SE^k_{i_C,j_C} \end{bmatrix} \tag{1.41}$$

The entries of this stencil give the weight that is attributed to $u^{k-1}_{i_C,j_C}$ in the calculation of the interpolated value at each of the nine points of the fine grid surrounding the point (i_C, j_C) corresponding to (i_F, j_F).

1.9 Grid operators

On grid k the discretized problem to be solved is written:

$$L^k U = F \tag{1.42}$$

The last task that needs to be completed is the definition of the stencils of the operator L^k on each grid.

1.9.1 Finest grid operator

On the very finest grid ($k = k_{max}$), the stencil of the operator L^k at the node (i, j) is directly computed from the discretization that is used. It reads

$$L^k(i,j) = \begin{bmatrix} 0 & A^k_{i,j} & 0 \\ B^k_{i-1,j} & -A^k_{i,j} - A^k_{i,j-1} - B^k_{i,j} - B^k_{i-1,j} & B^k_{i,j} \\ 0 & A^k_{i,j-1} & 0 \end{bmatrix} \tag{1.43}$$

The coefficients A and B were defined by equations 1.11. On the finest grid, the operator L^k is a five points operator.

1.9.2 Coarse grid operators

Knowing the operator L^k on grid k the operator L^{k-1} on grid $k-1$ has to be defined. The Galerkin operator (see [9] or [10]), is used.

$$L^k = I^{k-1}_k \, L^k \, I^k_{k-1}$$

The stencil of this linear operator at the point (i_C, j_C) is determined by finding the image of the basis function $u^{k-1} = e^{k-1}_{i_C,j_C}$ where $e^{k-1}_{i_C,j_C}$ is the coarse grid function that has the value 1 at node (i_C, j_C) and 0 elsewhere. Details are skipped in this section but can be found in Appendix A, section A.2.

1.10 Full multigrid interpolation

In the full multigrid code (FMG), a solution of the problem is computed on the coarse grid $k-1$, it is then interpolated to the grid k and this interpolation is used as an initialization of the solution on grid k. In [4], Alcouffe, Brandt, Dendy and Painter propose a new cubic interpolation that is also based on the continuity of $D\partial U/\partial x$ and $D\partial U/\partial y$. Although they note that classical cubic interpolation is sufficient which can be verified on our problem. Both were tried and it did not lead to significant improvement on the problems studied. Details on their new cubic interpolation can be found in Appendix A, section A.3.

1.11 Reynolds Equation

Our purpose is to find a solution to the Reynolds equation for hydrodynamic lubricated contacts. For an appropriate choice of dimensionless parameters and neglecting the transient term, the corresponding dimensionless equation is

$$\frac{\partial}{\partial X}(H^3\frac{\partial P}{\partial X}) + \frac{\partial}{\partial Y}(H^3\frac{\partial P}{\partial Y}) - \frac{\partial H}{\partial X} = 0 \tag{1.44}$$

This equation is not sufficient to describe the behavior of the pressure since it allows negative pressures. In that case, the fluid evaporates, the pressure is zero. Henceforth, the HL problem to be solved reads:

$$\frac{\partial}{\partial X}(H^3\frac{\partial P}{\partial X}) + \frac{\partial}{\partial Y}(H^3\frac{\partial P}{\partial Y}) - \frac{\partial H}{\partial X} = 0 \quad (X,Y) \in \Omega_1 \tag{1.45a}$$

$$P = 0 \quad (X,Y) \in \Omega_2 \tag{1.45b}$$

An extended Reynolds equation that describes the flow in the complete and incomplete zone can be used and leads to the following complementary problem:

$$\frac{\partial}{\partial X}(H^3\frac{\partial P}{\partial X}) + \frac{\partial}{\partial Y}(H^3\frac{\partial P}{\partial Y}) - \frac{\partial H_{oil}}{\partial X} = 0 \quad (X,Y) \in \Omega \tag{1.46}$$

Where H_{oil}, represents the oil film thickness and H the geometry. When the pressure is positive, H_{oil} is equal to H. Otherwise it is a fraction of H.

$$H_{oil} = \theta H \text{ with } \theta = 1 \text{ if } P > 0 \text{ and } 0 \leq \theta \leq 1 \text{ if } P = 0 \tag{1.47}$$

This model was proposed by Elrod [11] [12].

1.12 Algorithm implementation

In a first step, the cavitation was not taken into account and the previous algorithm is used, taking, in equation 1.1, the function $D = H^3$, $\sigma = 0$ and $f = \partial H/\partial X$. The geometry H is defined by the segment shape and the liner roughness. It is described in section 1.12.1. The previously described algorithm works well for a parabolic segment and for a model roughness with a cross hatched groove pattern and it remains efficient for deep grooves. Then cavitation was accounted for as explained in section 1.12.2.

1.12.1 Geometry

For a parabolic ring see figure 1.7, the geometry that was used is defined by

$$H(X,Y) = 1 + \frac{X^2}{2} + R(X,Y) \tag{1.48}$$

The function R that is defined on Ω describes the roughness of the liner surface.
We first used an analytic model defined by a cross hatched groove pattern for the liner surface as represented in figures 1.8, 1.9 and 1.10 .

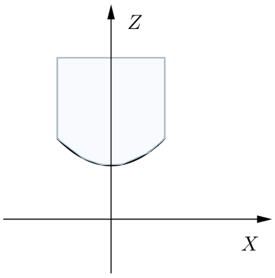

Figure 1.7: Ring shape

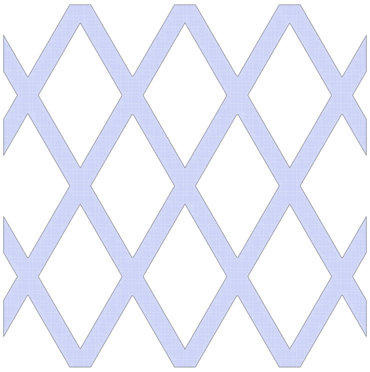

Figure 1.8: Cross hatched groove pattern (projection)

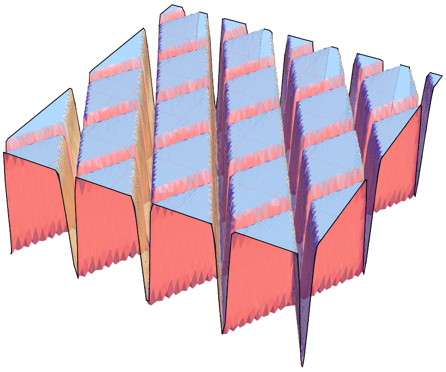

Figure 1.9: Cross hatched groove pattern

To describe the full pattern we need the half angle α, the groove width Λ, the distance between grooves D, the groove depth A. Because of symmetry and periodicity the values of R in the red rectangle shown in 1.10 completely determine R.
In the red rectangle $[0, D/(2\cos\alpha)] \times [0, D/(2\sin\alpha)]$, one gets:

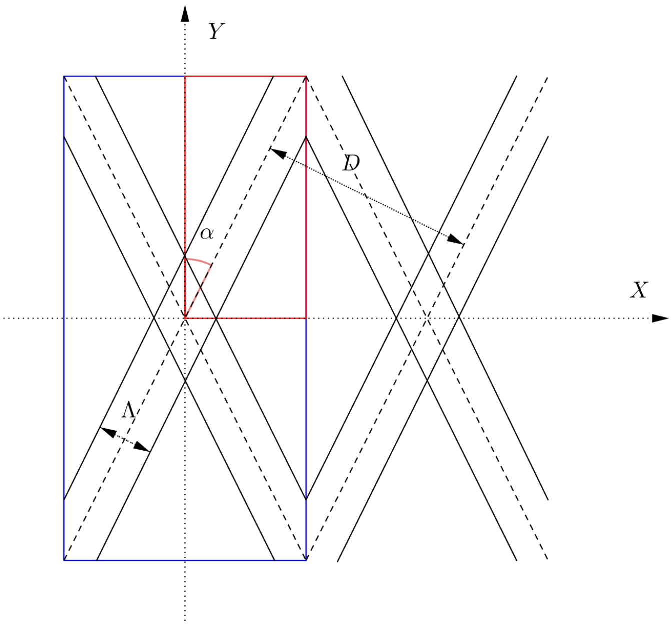

Figure 1.10: Cross hatched groove pattern

$$R(X,Y) = \begin{cases} (1 + A/2\cos(\pi(X\cos\alpha - Y\sin\alpha)) & \text{if } |X\cos\alpha - Y\sin\alpha| \leq \Lambda/2 \\ 0 & \text{otherwise} \end{cases} \tag{1.49}$$

The surface is smooth when $A = 0$.

1.12.2 Cavitation

The implementation of the cavitation proved to be more complex. It was decided that the free boundary defined by the cavitation zone, had to be determined only on the finest grid and only use the coarser grids as convergence accelerators. Therefore it was crucial, in the interpolating process from a coarse grid to the next finer grid, that values in the cavitated zone do not interact with values in the non cavitated zone. In the cavitated zone boundary the residual becomes completely wrong because equation 1.47 is not valid in the cavitation zone. And those residuals must not be used in any way on the finest grid. They introduce huge errors.

In the relaxation process all points are relaxed on the finest grid while on the coarser grids they are relaxed only in the case of a non zero pressure. Each time the pressure becomes negative, it is set to 0. Hence on the fine grid the cavitation boundary can change. But interpolation of the coarse grid may induce new positive pressure on the fine grid within the cavitation area and undo the previous work. This should be avoided.

To achieve this, the interpolation, restriction stencils and hence the coarse grids operators were modified. A very simple idea was used. It consists in cutting all possible communication between the two regions by setting to 0 the coefficients of the restriction and interpolation stencils that lead to interference between the two zones. But this proved to be too simple. This problem has to be carefully addressed as we are now going to try to explain.

Suppose a 1D problem and that on a fine grid there are 9 points labeled x_i for $i \in 0, 1, 2, ..., 8$ and on the next coarser grid there are 5 points X_i for $i \in 0, 1, 2, ..., 4$ as shown in figure 1.11.

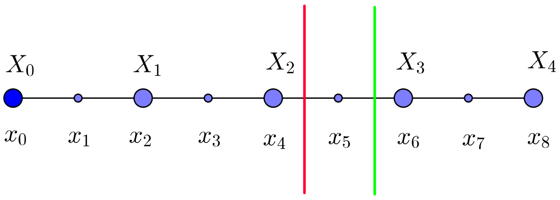

Figure 1.11: 1D cavitation boundary

Call p_i and P_i, the corresponding pressures. The colored line represents the cavitation boundary. The red boundary means that on the fine grid the pressure $p_4 > 0$ and $p_5 = p_6 = p_7 = p_8 = 0$ while the green one means that $p_5 > 0$ and $p_6 = p_7 = p_8 = 0$. These are the two cases of cavitation boundaries that can be encountered in 1D. In both cases, the coarse grid points X_3, X_4 lie in the cavitated zone. Hence $P_3 = 0, P_4 = 0$. When going from the coarse grid to the fine grid, the V-cycle interpolation induces the following pressures, using basic interpolation rules (just to get an idea of what is going on):

$$\begin{aligned}
p_0 &= P_0 \\
p_1 &= \frac{P_0 + P_1}{2} \\
p_2 &= P_1 \\
p_3 &= \frac{P_1 + P_2}{2} \\
p_4 &= P_2 \\
p_5 &= \frac{P_2 + P_3}{2} \\
p_6 &= P_3 \\
p_5 &= \frac{P_3 + P_4}{2} \\
p_8 &= P_4
\end{aligned} \tag{1.50}$$

Hence after interpolation, p_5 may become positive but this does not lead to major changes in the solution and in the cavitation boundary. It can be fixed with one relaxation sweep. For the coarsening steps, the pressure will be restricted according to laws of the following type :

$$\begin{aligned}
P_0 &= 0.5p_0 + 0.25p_1 \\
P_1 &= 0.25p_1 + 0.5p_2 + 0.25p_3 \\
P_2 &= 0.25p_3 + 0.5p_4 + 0.25p_5 \\
P_3 &= 0.25p_5 + 0.5p_6 + 0.25p_7 \\
P_4 &= 0.5p_4 + 0.25p_8
\end{aligned} \tag{1.51}$$

And then a problem at the node X_3 will occur. If p_5 is positive (green cavitation boundary in figure 1.11), then P_3 becomes positive and we extend the non cavitated zone on the coarse grid which was forbidden. But there is a problem that is even worse, we also need to coarsen the residuals of the fine grid with the same rules in order to find the right pressure correction on the coarse grid because all fine grids residuals are completely wrong in the cavitated region. In order to avoid these problems, it was decided to modify the restriction and interpolation stencil as follows.

For the interpolation operators in the refining step:

- The coarse grid points are injected (i.e. no change).
- Fine grid points inside the non cavitated zone: normal procedure (i.e. no change).
- Fine grid points on the cavitation boundary or inside the cavitated zone, they are put to zero pressure. This is done by setting the coefficients of the interpolation stencils of the coarse grid points that contribute to these fine grid points to 0.

For the restriction operators in the coarsening step:

- The coarse grid points that lie in the cavitated zone are injected (only the central coefficient of the restriction stencils is kept, the other are set to 0).
- For the coarse grid points that lie in the non cavitated area normal full weighting procedure (i.e. no change).

Then the coarse grid operator is computed with those stencils.

We can now give some examples of those changes. These examples explain how the restriction and interpolation stencils at coarse grid points near the cavitation frontier for the considered case. In Figures 1.12(a), various configurations that induces changes in the operators at C_1 and C_2 according to the pressure values on the horizontal coarse grid boundary cell $[C_1, C_2]$. Similar cases can be found for the vertical boundaries. In Figures 1.12(b), an example of cell configuration that will induce changes in the operators at C_1, C_2, C_3, C_4.

Consider the figure 1.12(a). In the first case, the restriction stencils at C_1 and at C_2 will be changed to:

$$R_0 = \frac{h_x h_y}{H_x H_y} \begin{bmatrix} 0 & 0 & 0 \\ 0 & 1 & 0 \\ 0 & 0 & 0 \end{bmatrix} \tag{1.52}$$

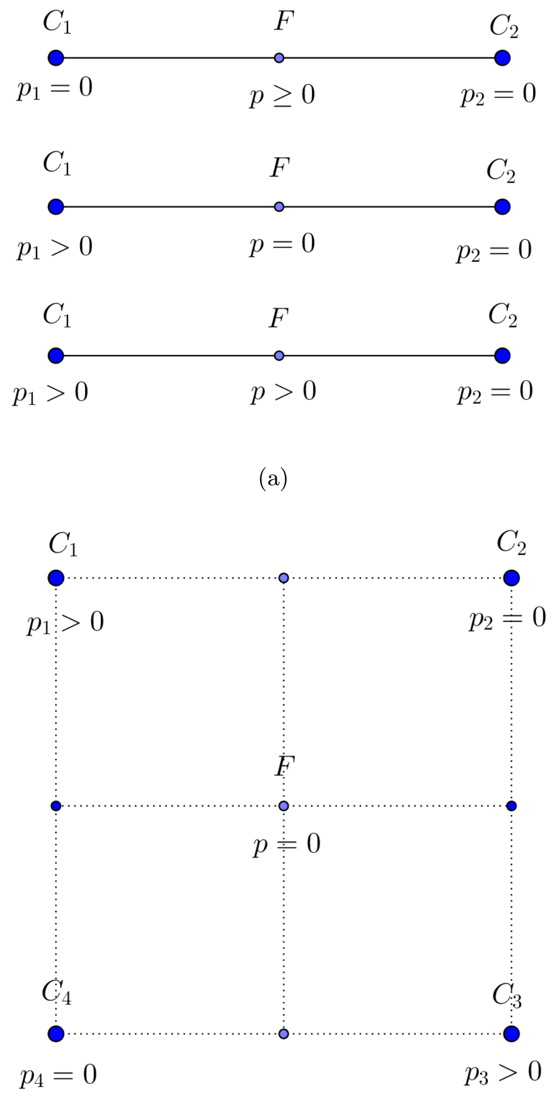

(a)

(b)

Figure 1.12: Stencil modification cases (a) aligned points (b) central fine grid point.

In the second and third cases only the restriction stencils at C_2 are changed into R_0. In the first and second cases the "East" coefficient of the interpolation stencil at C_1 is set to 0 and at C_2, the "West" interpolation coefficient becomes 0. While in the third case no changes are needed. When the fine grid point that is close to the cavitation boundary is a coarse grid cell center as in figure 1.12(b), we similarly modify the restriction and interpolation stencils at the four surrounding coarse grid points. For the example shown in figure 1.12(b), the restriction stencils at points C_1 and C_3 are unchanged while at points C_2 and C_4, they are changed into R_0. The "South-East", "South-West", "North-West" and " North-East" interpolation coefficients respectively at C_1, C_2, C_3 and C_4 are set to zero while the 8 other coefficients remain unchanged.

The coarse grid operators are then recalculated with these new stencils. As computer memory was not an issue, it was decided to store all these stencils, although, by carefully considering what is going on, some memory space could probably have been saved. Finally the standard multigrid algorithm described in [5] is used with the following modifications:

- Calculate the finest grid stencil coefficients: $A_{i,j}^{k_{max}}, B_{i,j}^{k_{max}}$ and the finest grid stencils.
- V-cycle modifications:
  - Calculate all coarser grid stencils.
  - Perform the V-cycle as in [5] modifying the stencils to account for cavitation after the fine grid relaxations and before the coarsening steps.

Algorithm performances are presented in the following chapter.

1.13 Conclusion

In this chapter the main ideas of Alcouffe et al. to recover multigrid efficiency in the case of an elliptic operator with highly varying coefficients have been implemented. The computations of the restriction and interpolation stencils have been fully explained as well as the fine and coarse grid operators. The Galerkin method was used and it was indicated how to calculate the resulting nine grid operator on each coarse grid with further details in Appendix A, section A.2. Finally, it was shown that it could be applied to the Reynolds equation with a special care to deal with the cavitation boundary. It is particularly interesting for a textured liner in the PRLC hydrodynamic contact. In this case the function D being H^3 can undergo large variations and the standard multigrid techniques loose their efficiency. The obtained code leads to a better representation of the equation on the coarse grid since the interpolation formula is based on flow conservation.

Chapter 2

Results

Contents

2.1 Introduction

In this chapter the performance of the Reynolds code with or without cavitation is analyzed. At this stage flow conservation at the cavitation boundary is not considered. The convergence is shown for deep grooves in the case of a cross hatched surface. Its evolution for a wide variety of depths is shown. The performance in terms of work units is studied. The results are also compared with the results that were obtained with the classical HL code developed in [5].

2.2 Pressure and film height

The 2D height distribution with grooves is given by

$$H(X,Y) = 1 + \frac{X^2}{2} + R(X,Y) \quad (X,Y) \in [-10,10] \times [-10,10]. \tag{2.1}$$

Where R represents the roughness as described in section 1.12.1. The parameter A is the groove depth. The case $A = 0$ corresponds to the smooth case. The smooth minimum film thickness is 1. In this chapter, the distance between grooves is set to $D = 2$, their width is $\Lambda = 0.5$ and their angle is 45°. The coarse grid is a 4×4 grid. For grooves of depth $A = 4$, the geometry and the corresponding pressure are shown in Figure 2.1. After running the new FMG code with 20 cycles on 9 levels on the square $[-10, 10] \times [-10, 10]$, the obtained central pressure and geometry on the line $X = -5.0$ are shown in Figure 2.2. A zoom of these curves on the central line is given in Figure 2.3. The pressurized points (in blue) and therefore the cavitation boundary can be seen in Figure 2.4.
Finally, pictures of the residuals are given in figures 2.5.

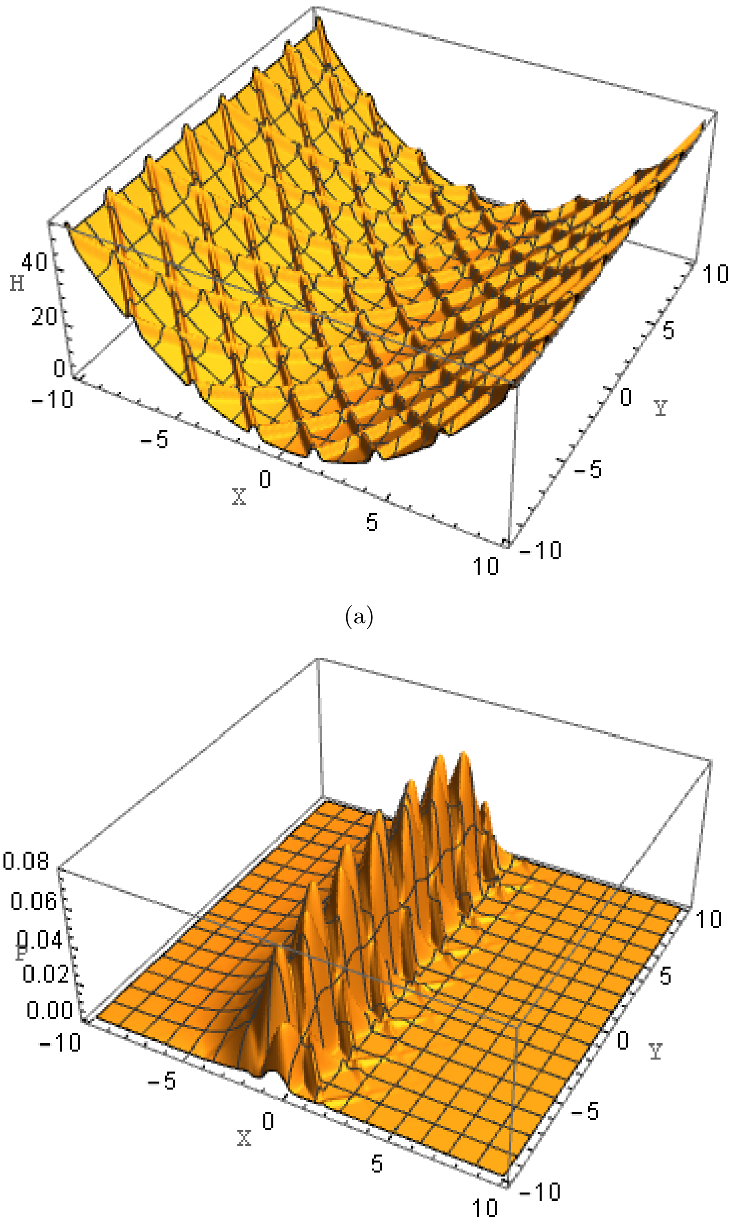

(a)

(b)

Figure 2.1: Geometry (a) and pressure (b) for grooves of depth 4.

Note that the geometry at $Y = 5$ shows the individual grooves section on the corresponding line. Since the grooves cross on the line $Y = 0$, they are regularly spaced on the central line and seem to be fewer than on the line $Y = 5$. The boundary pressure being zero, it is normal to get a maximum pressure at $Y = 5$ lower than the one on the central line. This is also due to the fact that there are more grooves in the central part of the contact where they are the most influential. Figure 2.3 indicates a small positive pressure in the grooves beyond the cavitation boundary. These remaining very small pressures in the grooves also appear in figure 2.4 on the

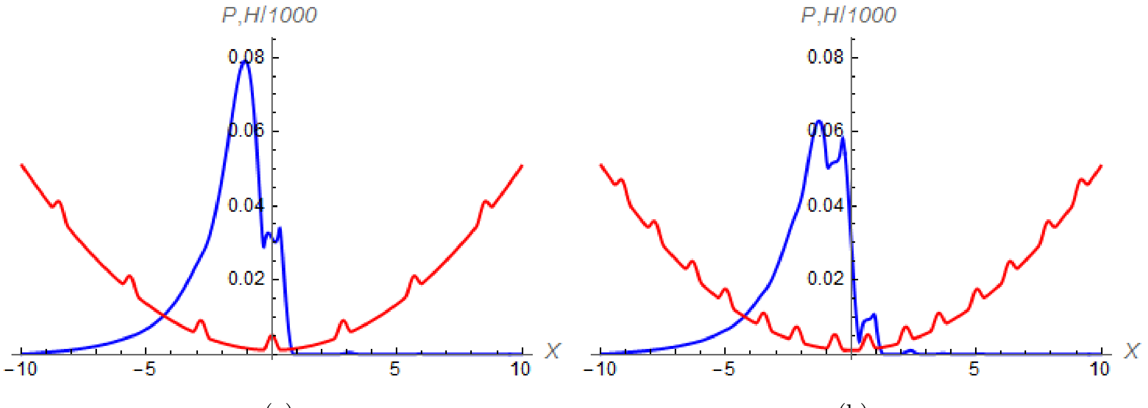

(a)

(b)

Figure 2.2: Converged pressure and geometry on the central line $Y = 0$. (a) and on the line $Y = 5$. (b) for grooves of depth 4.

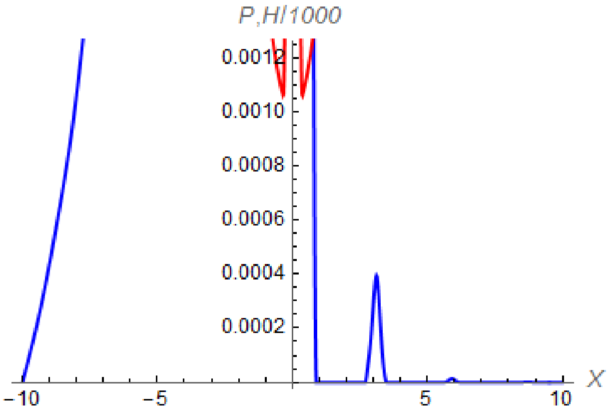

Figure 2.3: Zoom of converged pressure and geometry on the central line for grooves of depth 4.

right half of the picture. The pressures are very small as was pointed out in figure 2.3. At this stage flow conservation is not yet considered and therefore after cavitation the algorithm can be questioned.

Concerning the residuals, figure 2.5 (a) shows that the most important ones are to be found, as expected, near the cavitation boundary. The Reynolds equation is no longer valid in the cavitation zone. The equation that is used does not account for the correct Couette flow at cavitation. When P is set 0, an error is introduced in the residual since the geometry is considered and not the oil level. Besides the zoomed picture (b), shows that the deep grooves also create larger residuals than in the other parts of the domain but they can be rapidly reduced below the discretization error.

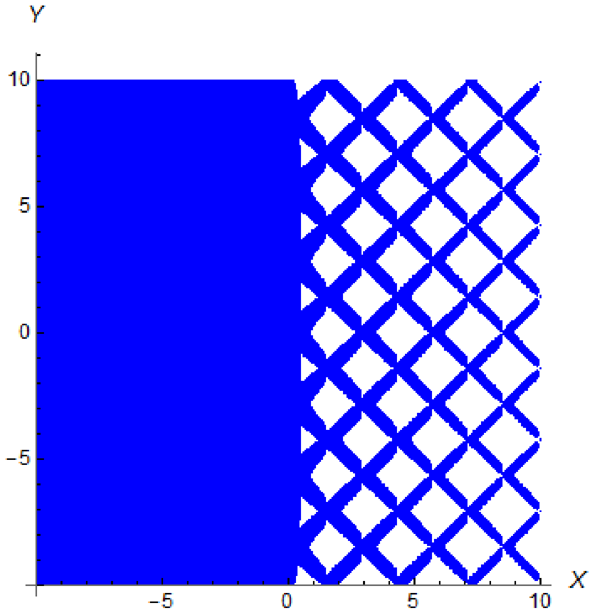

Figure 2.4: Pressurized points (in blue) and cavitation boundary.

2.3 New code results: Residuals and Work Units.

Pictures of the evolution of the residual in terms of work units (Wu) on 9 levels for grooves of depth $A = 0$ to 10. are given in Figure 2.6 using only V-cycles, in Figure 2.7 using FMG and 20 V-cycles and in figure 2.8 using FMG and 10 V-cycles. Considering the first figure, with V-cycles only, initially the residual does not decrease very fast because the cavitation boundary needs to stabilize. Afterwards it decreases rapidly although it becomes more difficult with increasingly deep grooves. The residuals are only evaluated on the finest grid and this explains why, in case of FMG, the curves do not begin at $Wu = 0$. Indeed the problem is solved on each subgrid to get a good starting pressure on the next fine grid, this time has to be considered.

Henceforth, when using FMG, it is a little difficult to use a prescribed number of cycles to evaluate the work that is required to obtain a certain accuracy. Only 10 cycles are sufficient for grooves of depth $A \leq 4$ to reach a very small residual. This figure also shows that FMG diminishes the number of work units that are necessary to obtain a prescribed accuracy. Indeed when it begins solving the problem on a given fine grid, it has already solved it on the previous coarse grid and this solution provides a better starting point. Besides FMG has already localized the cavitation boundary on the coarse grid. Convergence is not so fast for very deep grooves. When using only V(2,1) cycles, the convergence at the beginning is rather slow. The algorithm needs to stabilize the cavitation boundary. Afterwards a linear behavior of $\log_{10}(residual)$ as a function of Wu, the number of work units, is observed with a slope that increases as the grooves get deeper. It means that the residual is divided by a constant factor at every cycles until machine precision is reached. This factor is about 10 for shallow grooves, around 5 for grooves of depth 1 and around 2 for very deep grooves (depth between 10 and 30). It was also tried for grooves of depth 50 and the factor becomes 1.66. These pictures also show that if convergence slows down as A increases,

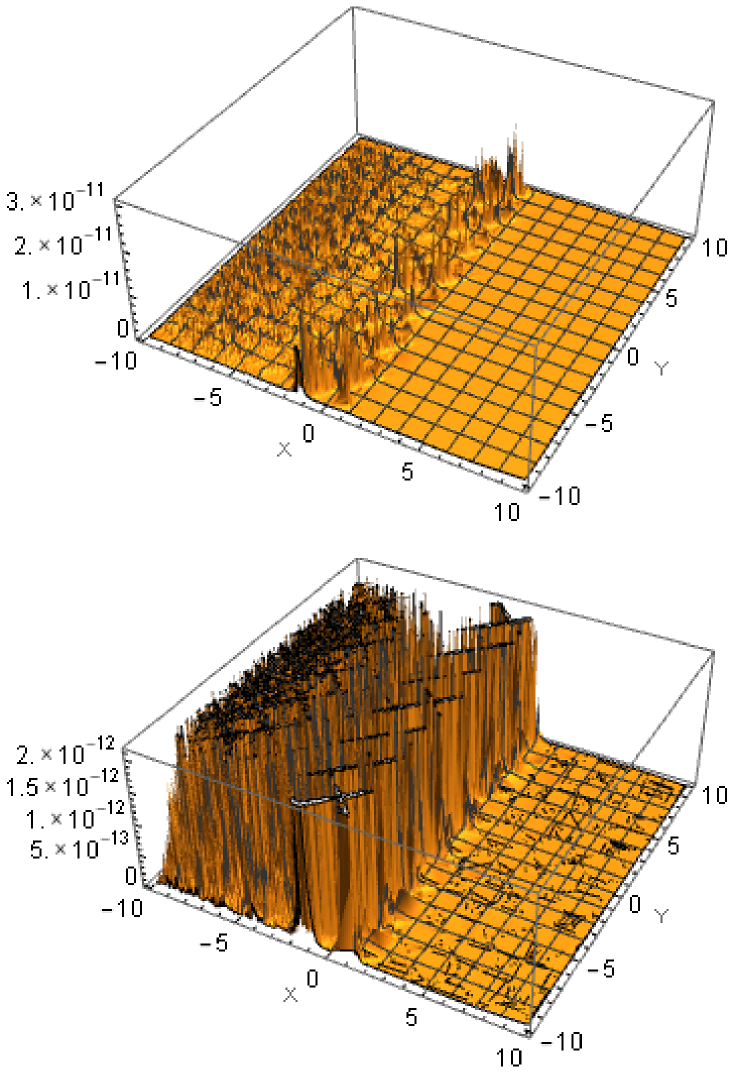

Figure 2.5: (a) Residuals for grooves of depth $A = 4$ for 7 levels, (b) Zoom of the same residuals.

it remains acceptable. Besides by increasing the number of cycles: 30 instead of 10 or 20, very small residuals are obtained for very deep grooves as shown in Figures 2.9 and 2.10 for grooves of depth 10 and 20. At the beginning convergence is fast. For grooves of depth 20, after the first cycle V(2,1) cycle, the residual is divided by ten, then by 5 while for grooves of depth 10, after the first two V(2,1) cycles, the residual is divided by ten and after the third cycle by 5. Afterwards, in both cases, a linear behavior of the logarithm of the residual as a function of the number of work units is observed This factor is roughly 2 for depth of depth 20 and slightly above 2 for grooves of depth 10. Please note that for comparison with classical geometrical multigrid whose discretization is not done by means of volume discretization but finite differences, the residual here is divided by $h_x \times h_y$. This explains why it stabilizes around 10^{-12} for 9 levels. Besides no special prerelaxation is done to find more rapidly the cavitation boundary.
For all these figures only $V(2,1)$ cycles were used. The geometry consists of a cross hatched

pattern with a groove width equal to 0.5, a distance between grooves of 2., an angle $\alpha = \pi/4$ for various values of the grooves depth A (see figure 2.2). The case $A = 0.$ corresponds to the smooth case.

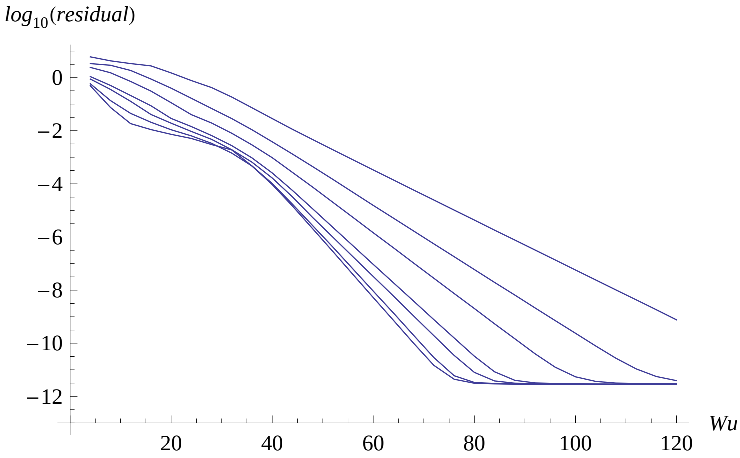

Figure 2.6: Residual evolution as a function of work units using only 30 V-cycles (no FMG), grooves of depth $A = 0, 0.4, 0.8, 1., 2., 4., 10.$ from bottom to top, with cavitation.

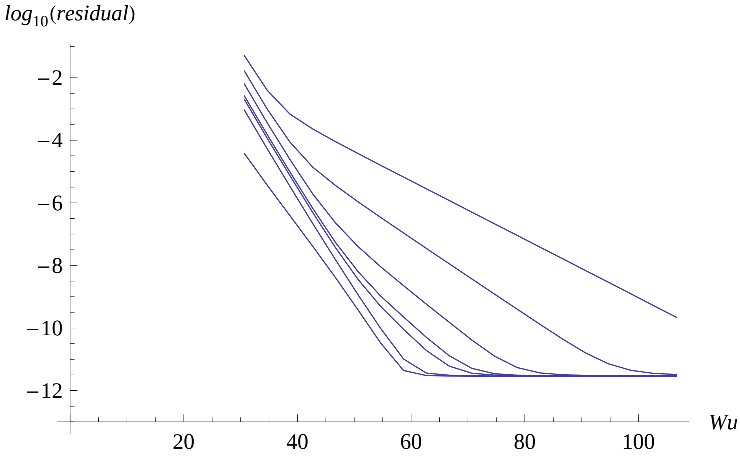

Figure 2.7: Residual evolution as a function of work units using FMG and 20 V-cycles, grooves of depth $A = 0, 0.4, 0.8, 1., 2., 4., 10.$ from bottom to top, with cavitation.

Figures 2.9 and 2.10 show the residual in terms of work units for FMG with nine levels, 30 cycles and grooves of depth 10 and grooves of depth 20. The convergence speed is quite satisfactory since for all these results only $V(2,1)$ cycles are used and the coarsest grid is a 4×4 grid.

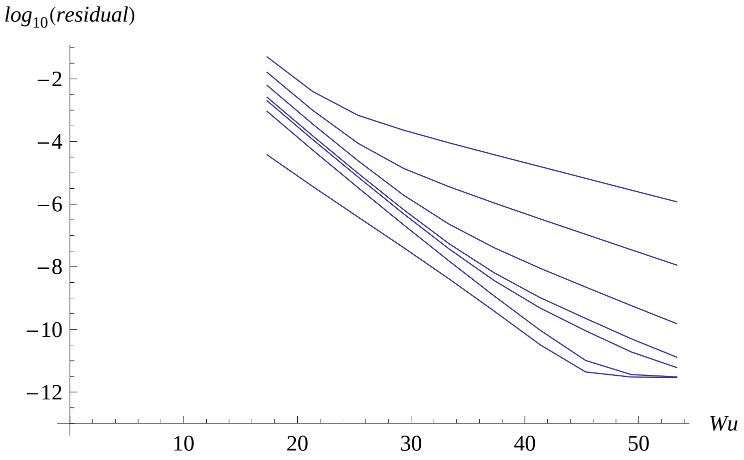

Figure 2.8: Residual evolution as a function of work units using FMG and 10 V-cycles, grooves of depth $A = 0, 0.4, 0.8, 1., 2., 4., 10.$ from bottom to top, with cavitation.

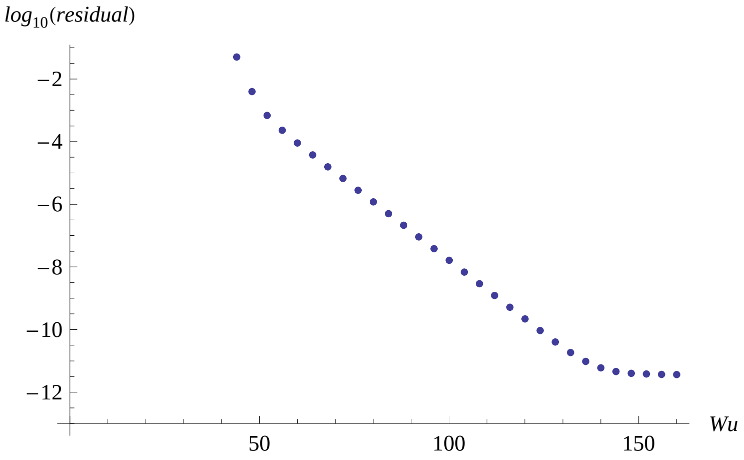

Figure 2.9: Residuals as a function of work units for grooves of depth 10 (FMG, 30 cycles and 9 levels, with cavitation).

2.4 Comparison with classical code

2.4.1 Without cavitation

The classical code is the code "HL2D" that is described in [5] for hydrodynamic lubrication, without cavitation. It was run with a 4×4 coarsest grid and nine levels. The performance of this code is compared with the one of the new code for a cross hatched pattern with a groove width equal to 0.5, a distance between grooves of 2., an angle $\alpha = \pi/4$ and for various values of the grooves depth a. The case $a = 0.$ corresponds to the smooth case. In tables 2.1, only V-cycles were used while in table 2.2, full multigrid, FMG, was used. For both codes, calculations were performed with only V(2,1) cycles. Images of the pressure after 20 cycles and of the geometry on the central line are given for grooves of depth 2.0 in figures 2.11. As cavitation was not

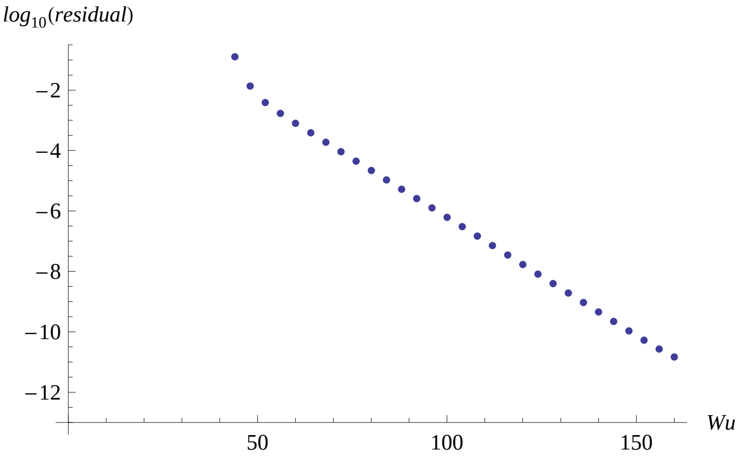

Figure 2.10: Residuals as a function of work units for grooves of depth 20 (FMG, 30 cycles and 9 levels, with cavitation).

taken into account and negative pressures were accepted because of the geometry symmetry an anti-symmetric pressure field is obtained. The convergence problems due to the free cavitation boundary do not occur in this case and therefore a better convergence is observed as can be seen in Table 2.1 (only V(2.1)-cycles) and Table 2.2 (FMG). With only 10 V-cycles, convergence seems to be better in the case of the old code as long as groove depth remains ≤ 1 but for deeper grooves it stops working while the new code keeps similar performance for grooves of depth less than 10. When doubling the number of V-cycles, the new code is clearly more efficient and continues to converges for deep grooves while the first code stops converging for grooves of depth ≥ 2. With FMG with only 10 V(2,1) cycles the new code already proves to be more efficient for deep grooves. Considering the FMG results (Table 2.2) for the non cavitated case, it can be noticed that residual of the same order of magnitude are obtained for grooves of depth $A = 2$ with the classical code and for grooves of depth $A = 10$ with the improved code. In terms of the Reynolds equation, it corresponds to a diffusion coefficient H^3 that is of order 10^3 instead of 8.

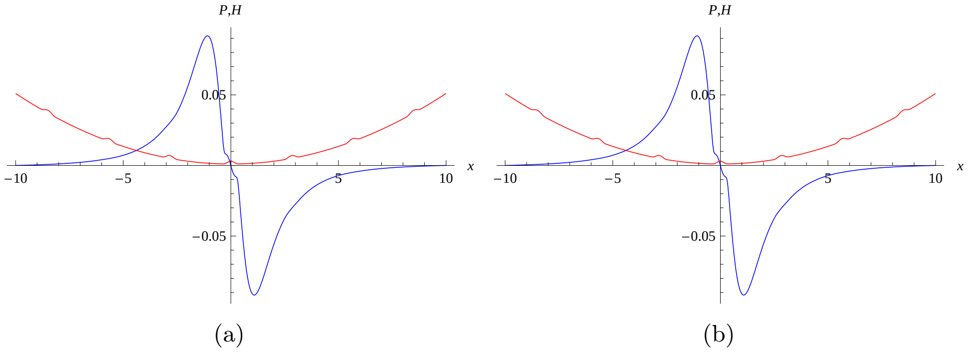

(a)
(b)

Figure 2.11: Non cavitated pressure and geometry on the central line with the old code (a) and and with the new one for grooves of depth 2 (b).

Groove depth	Old code(10)	New Code(10)	Old code(20)	New Code(20)
$A = 0$	$3.45536\,10^{-12}$	$4.54186\,10^{-8}$	$3.18550\,10^{-12}$	$5.65094\,10^{-12}$
$A = 0.2$	$3.63007\,10^{-12}$	$4.56751\,10^{-8}$	$3.19421\,10^{-12}$	$5.65315\,10^{-12}$
$A = 0.5$	$2.20238\,10^{-11}$	$5.03335\,10^{-8}$	$3.20121\,10^{-11}$	$5.64959\,10^{-12}$
$A = 1.0$	$3.62181\,10^{-10}$	$7.39086\,10^{-8}$	$3.22345\,10^{-10}$	$5.68816\,10^{-12}$
$A = 2.0$	$8.26621\,10^{-5}$	$4.72002\,10^{-7}$	$1.56038\,10^{-5}$	$5.85417\,10^{-12}$
$A = 4.0$	–	$2.06547\,10^{-8}$	–	$8.70319\,10^{-11}$
$A = 10.0$	–	$2.27533\,10^{-3}$	–	$3.05718\,10^{-7}$

Table 2.1: Residuals without cavitation after 10 V- Cycles (columns 2 and 3) and after 20 V-Cycles (columns 4 and 5).

Groove depth	Old code(10)	New Code(10)	Old code(20)	New Code(20)
$A = 0$	$3.19117\,10^{-12}$	$8.21423\,10^{-12}$	$3.18425\,10^{-12}$	$5.61320\,10^{-12}$
$A = 0.2$	$3.19082\,10^{-12}$	$8.35724\,10^{-12}$	$3.12200\,10^{-12}$	$5.63743\,10^{-12}$
$A = 0.5$	$3.24179\,10^{-12}$	$9.50510\,10^{-12}$	$3.20156\,10^{-12}$	$5.62231\,10^{-12}$
$A = 1.0$	$5.90107\,10^{-12}$	$1.67512\,10^{-11}$	$3.22519\,10^{-12}$	$5.65955\,10^{-12}$
$A = 2.0$	$2.10552\,10^{-6}$	$4.03689\,10^{-10}$	$3.50085\,10^{-8}$	$5.75466\,10^{-12}$
$A = 4.0$	–	9.7413910^{-9}	–	$6.04012\,10^{-12}$
$A = 10.0$	–	1.3675110^{-6}	–	$3.00429\,10^{-10}$

Table 2.2: Residuals for non cavitated FMG with 10 cycles (columns 2 and 3) and with 20 cycles (columns 4 and 5).

2.4.2 With cavitation

For this the code "HL2D" that is described in [5] is used. Results in terms of residual are presented in Tables 2.3 and 2.4. In this case, because of cavitation, the efficiency of the old code degrades. Without FMG and with 20 V-cycles, it can be observed that even for shallow grooves convergence is not very good and even with FMG, for grooves of depth ≥ 1, it does not converge while the new code, when the cavitation boundary is stabilized (10 V(2,1) cycles without FMG are not sufficient), keeps a similar behavior to the non cavitated case. It is even better in the cavitated case as shown in table 2.4. The convergence of the classical code becomes very slow for $A = 2$ and stops converging for deeper grooves.
After only 10 V-cycles, for shallow grooves, the new code does not seem to be more efficient than the old one, but with more cycles or using FMG, it is much faster and it keeps converging for very deep grooves. At the beginning, because of the free cavitation boundary the residual does not seem to change a lot but afterwards, the algorithm becomes very efficient which is not the case with the old code (see figure 2.12).

In fact, if we only consider up to 10 V-cycles without FMG, the new code does not seem to be better but it does not deteriorate too much. But if we increase the number of V-cycles from 10

Groove depth	Old code(10)	New Code(10)	Old code(20)	New Code(20)
$A = 0$	$4.21049\,10^{-7}$	$9.3649\,10^{-5}$	$1.54652\,10^{-11}$	$3.15071\,10^{-12}$
$A = 0.2$	$1.85151\,10^{-6}$	$9.29645\,10^{-5}$	$3.63546\,10^{-8}$	$3.05494\,10^{-12}$
$A = 0.5$	$1.17584\,10^{-5}$	$1.28189\,10^{-4}$	$4.91446\,10^{-8}$	$4.12592\,10^{-12}$
$A = 1.0$	$4.12544\,10^{-4}$	$2.55260\,10^{-4}$	$2.39287\,10^{-4}$	$3.27813\,10^{-11}$
$A = 2.0$	$6.75510\,10^{-3}$	$9.62750\,10^{-4}$	$3.27918\,10^{-3}$	$2.02697\,10^{-9}$
$A = 4.0$	$6.10157\,10^{-1}$	$3.83358\,10^{-3}$	–	$5.96005\,10^{-8}$
$A = 10.0$	–	$2.86277\,10^{-2}$	–	$4.32911\,10^{-6}$

Table 2.3: Residuals with cavitation after10 V-cycles (columns 2 and 3) and after 20 V-cycles (columns 4 and 5).

Groove depth	Old code(10)	New Code(10)	Old code(15)	New Code(15)
$A = 0$	$7.33557\,10^{-10}$	$2.92645\,10^{-12}$		$2.83849\,10^{-12}$
$A = 0.2$	$2.20751\,10^{-7}$	$3.02393\,10^{-12}$	$4.00056\,10^{-8}$	$2.86069\,10^{-12}$
$A = 0.5$	$2.46322\,10^{-7}$	$3.58037\,10^{-12}$	$1.59958\,10^{-8}$	$2.89432\,10^{-12}$
$A = 1.0$	$2.30557\,10^{-4}$	$1.30786\,10^{-11}$	$2.64162\,10^{-4}$	$2.96992\,10^{-12}$
$A = 2.0$	$2.67886\,10^{-3}$	$1.52475\,10^{-10}$	$3.41708\,10^{-3}$	$3.20307\,10^{-12}$
$A = 4.0$	–	$1.13176\,10^{-8}$	–	$4.41069\,10^{-11}$
$A = 10.0$	–	$1.19284\,10^{-6}$	–	$1.62029\,10^{-8}$

Table 2.4: Residuals for cavitated FMG with 10 cycles (columns 2 and 3) and with 15 cycles (columns 4 and 5)

to 20, the residual of the new code decreases very quickly and the residual reduction remains very good, even for quite deep grooves. For the same running conditions, the old code residual decreases very slowly or oscillates or even diverges. Using full multigrid the new code becomes even better. In terms of work units or even real calculation times, Figures 2.12 or 2.13 in subsection 2.3 as well as table 2.5 show that the new code is quite efficient in spite of the extra work that is required to correctly represent the highly varying flows on the coarse grid and in the relaxation process. For grooves of depth of $A = 4.$, a graph of the residual as a function of work units is plotted in figure 2.12. In red, the residual after running the old code and in blue after running the new code. No FMG is used, only V(2,1) cycles. For grooves of depth of $A = 1.$, a graph of the residual as a function of work units is plotted in figure 2.13. In red, the residual after running the old FMG code with 100 cycles and in blue after running the new FMG code with only 15 cycles. The number of cycles being different the starting point of both curves is different.Those two figures clearly show the divergence of the old code and the very satisfying convergence of the Alcouffe based code. In the classical geometrical multigrid code, the coarse grid is a poor representation of the flows and therefore they do not accelerate convergence and they even deteriorate it. The diffusion coefficients being in H^3, they undergo huge variations in the grooves. Therefore, coarse grid representation remains acceptable for shallow grooves but then the discrepancy is too big.

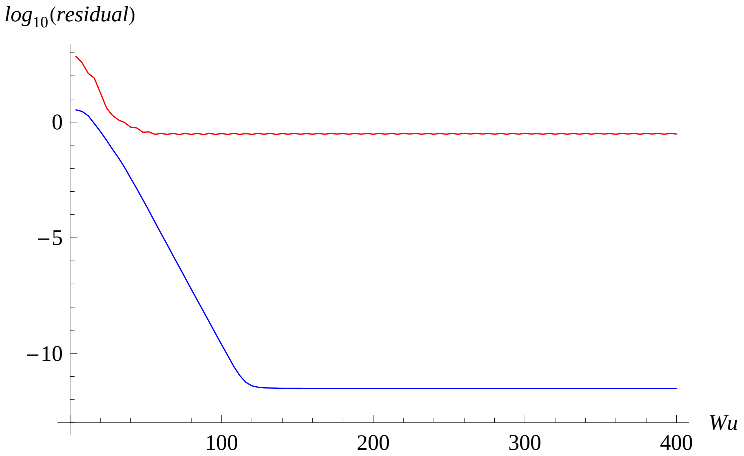

Figure 2.12: New code residuals (blue) and old code residuals (red) in terms of the number of cycles for grooves of depth 4 (no FMG, only V(2,1) cycles).

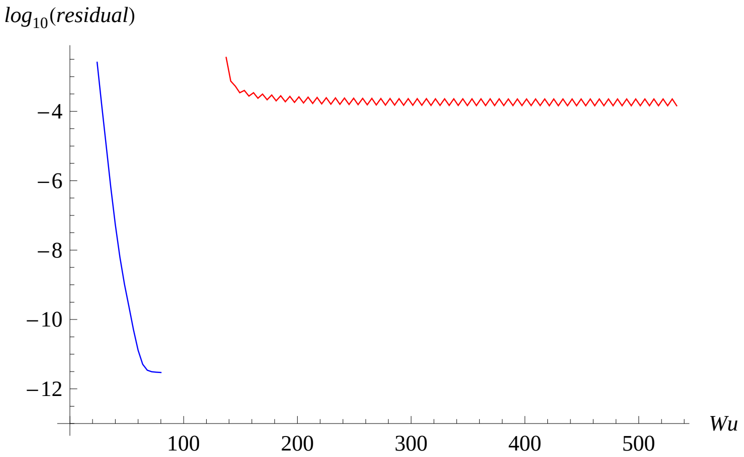

Figure 2.13: Residuals for the FMG codes as a function of work units, for grooves of depth 1., new code in blue (15 V(2,1) cycles) and old code in red (100 V(2,1) cycles).

2.4.3 Computing time

In the new code each cycle requires more time because of the modification of the stencils and their re-initialization at each FMG change of level. Besides the finest grid relaxation routine is more complex in order to better account for the flow equilibrium. Calculation time for the cavitated case has been measured in seconds. All output has been eliminated. The results are given in table 2.5.

Level 8	Old Code	NewCode	Level 9	Old Code	NewCode
$ncy = 1$	≈ 1	≈ 1	$ncy = 1$	≈ 2	≈ 4
$ncy = 2$	≈ 1	≈ 1	$ncy = 2$	≈ 2	≈ 6
$ncy = 4$	≈ 1	≈ 2	$ncy = 4$	≈ 5	≈ 9
$ncy = 10$	≈ 3	≈ 4	$ncy = 10$	≈ 11	≈ 20
$ncy = 20$	≈ 5	≈ 8	$ncy = 20$	≈ 21	≈ 38
$ncy = 50$	≈ 13	≈ 20	$ncy = 50$	≈ 52	≈ 93

Table 2.5: Comparison of FMG computing times in seconds.

2.5 Conclusion

In this chapter the efficiency of the new code is demonstrated. It remains efficient even in the case of deep grooves although it slows down a little for very deep grooves. Of course the computing time increases because of the additional calculation time of the stencils and of the nine point operator. It is not quite doubled, which is not too much, considering the multigrid efficiency of the old code in terms of time saving. In chapter 6 an impact problem is studied. The transient term of the Reynolds equation will have to be added. The stencil will have to be evaluated twice per cycle: at the beginning and after having updated the minimum film thickness. It will not significantly affect the calculation time. In that case since at each time step the solution will be close to the one at the previous time step and therefore not many cycles will be used. The computing time will be more impacted by the required number of time steps.

Chapter 3

Influence of liner groove parameters.

Contents

3.1 Introduction

Concerning both friction reduction and pollution reduction, the piston ring pack plays a crucial part because of its sealing and lubricating functions. Therefore, the piston ring pack has been the subject of many studies. Analysis of the piston-ring pack can be found in [13–16] where the effects of relative ring locations, tension and design of oil-control ring, ring conformability, bore distortion,. . . are investigated.

Cylinder liner texturing is also an important factor to improve load carrying capacity, friction coefficient and oil consumption. They can serve as local pressure generators, lubricant reservoirs or debris traps. Surface texture is necessary to generate pressure in the case of flat rings such as the oil control ring [16–22].

The interest of cross-hatched grooves for good oil redistribution and friction reduction was shown in [23–25]. In [26], the honing process is studied and its effects on the surface topography and henceforth on the PRLC performance are developed. Dynamic effects also play a role in the PRCL contact as studied in [27].

The influence of the groove parameters, density, depth and angle for a cross hatched texture was studied in [18, 28, 29]. In order to obtain a more precise model of the PRCL contact, it is necessary to solve the transient hydrodynamic lubrication problem, requiring millions of points of a measured surface and thousands of time steps. Hence, the use of an efficient and robust solver for the Reynolds equation is a must. Because of the surface roughness, the film thickness cubed term in the Reynolds equation shows huge variations, making the problem difficult to solve. Different approaches have been applied in the past such as the stochastic methods using the Patir and Cheng flow factors [30] or homogenization methods [31–33]. Our approach is based on a deterministic model and measured surfaces. As such a detailed description requires very fine grids, it requires long computing times and therefore multigrid techniques become an obvious choice. The code we have developed is adapted to highly varying coefficients and allows us to quickly solve the problem even in presence of deep grooves. In this chapter, in the case of a parabolic ring, it is validated by comparison with the 1D analytical model presented in [6] and the influence of some groove parameters for a cross-hatched textured liner is studied.

3.2 Notation and dimensionless equations

In this chapter the hydrodynamic lubrication of the piston ring-cylinder liner contact is considered and the following problem is solved on a domain ω:

$$\frac{\partial}{\partial x}(\frac{\rho h^3}{12\eta}\frac{\partial p}{\partial x}) + \frac{\partial}{\partial y}(\frac{\rho h^3}{12\eta}\frac{\partial p}{\partial y}) - u_m\frac{\partial(\rho h)}{\partial x} - \frac{(\partial \rho h)}{\partial t} = 0 \text{ and } p > 0$$

$$\text{or } p = 0$$

Where p is the hydrodynamic pressure, h, the geometry, u_m the mean velocity of the piston ring and liner. The fluid is assumed to be incompressible and isoviscous and therefore the lubricant density, ρ and the viscosity, η are considered constant. The problem is made dimensionless using the following dimensionless parameters. Upper case letters represent dimensionless parameters and R_x is the ring radius of curvature.

A	dimensionless groove depth	$= a/h_0$
D	dimensionless distance between grooves	$= d/\sqrt{h_0 R_x}$
E	dimensionless ring half width	$= e/\sqrt{h_0 R_x}$
H	dimensionless film thickness	$= h/h_0$
P	dimensionless pressure	$= p h_0 \sqrt{h_0}/(12\eta u_m \sqrt{R_x})$
T	dimensionless time	$= u_m t/\sqrt{h_0 R_x}$
W	dimensionless load	$= w h_0/(12\eta u_m R_x)$
X	dimensionless coordinate in direction of sliding	$= x/\sqrt{h_0 R_x}$
Y	dimensionless coordinate in direction perpendicular to sliding	$= y/\sqrt{h_0 R_x}$
α	angle between groove and Y axis	
Λ	dimensionless groove width	$= \lambda/\sqrt{h_0 R_x}$

This yields the following dimensionless problem in a domain Ω:

$$\frac{\partial}{\partial X}(H^3\frac{\partial P}{\partial X}) + \frac{\partial}{\partial Y}(H^3\frac{\partial P}{\partial Y}) - \frac{\partial H}{\partial X} - \frac{\partial H}{\partial T} = 0 \quad \text{and } P > 0$$

$$\text{or } P = 0$$

The geometry H is defined by the macroscopic ring shape and by the liner texture. In this chapter, only analytical models of the cross-hatched surfaces are considered.

$$H(X,Y) = 1 + \frac{X^2}{2} + R(X,Y)$$

where R describes the liner texture. The sliding direction is the X direction. In this work, the transient part is replaced as described in [6] where it is shown that

$$\frac{\partial H}{\partial T} = -2\frac{\partial R}{\partial X}.$$

In dimensionless form, it amounts to solving

$$\frac{\partial}{\partial X}(H^3\frac{\partial P}{\partial X})+\frac{\partial}{\partial Y}(H^3\frac{\partial P}{\partial Y})=\frac{\partial H_1}{\partial X}$$

where

$$H_1(X,Y)=1+\frac{X^2}{2}-R(X,Y).$$

Examples of possible dimensional and associated dimensionless values can be found in Appendix B, section B.1.

3.3 Code validation

The 2D periodic or pseudo periodic code results were compared with results obtained with a 1D analytical model developed in [6]. In this section the geometry H is given by $H(X,Y) = 1+X^2/2+R(X,Y)$ where $R(X,Y)$ corresponds to the description of the grooves. Numerical results are given for a sinusoidal groove shape as shown in figure 2.2, whereas [6] uses a triangular groove shape to derive the analytical pressure distribution. For a smooth liner the pressure distributions on the central line are identical, as can be seen in Figure 3.1.

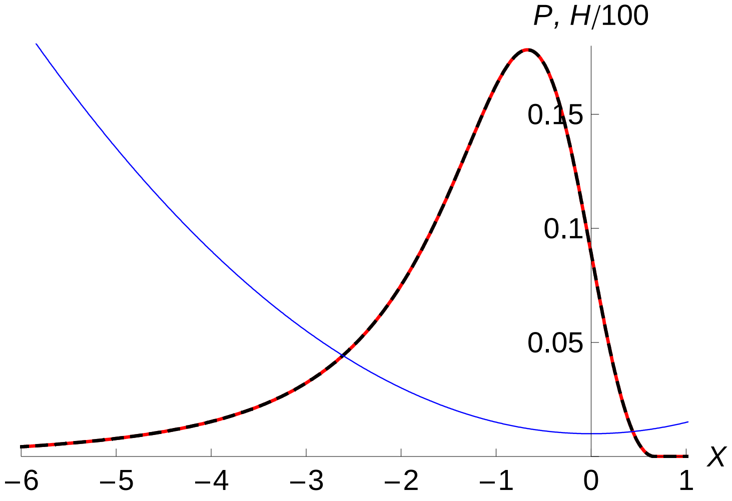

Figure 3.1: Smooth pressure distribution (solid line) and geometry for a dimensionless ring half width $E = 10$ compared with the 1D analytical model [6] (dashed line).

Figure 3.2 shows the results obtained for one single groove of depth $A = 5$ perpendicular to the sliding direction for a groove located at $X_g = -2$. Figure 3.3 is for a groove at $X_g = -1$. The 2D pressure on the central line $Y = 0$ is compared with the 1D analytical pressure (dashed line) for triangular grooves. It can be seen that the two curves are still superimposed for $X_g = -2$ and that the average difference is less than 1%. The maximum pressure difference does not exceed 4%.

Figure 3.4 shows the 2D pressure for multiple grooves of depth $A = 5$, perpendicular to the sliding direction. The solution is compared with the 1D predictions of [6] for grooves that are spaced by

2. Again, there is less than 1% difference for the average pressure. The main differences between the two curves are to be found near the maximum pressure and when a groove approaches the cavitation boundary but they remain small. This difference is probably essentially due to the fact that after the cavitation boundary non physical residual pressures exist. Flow conservation is not considered. It may be noticed that the maximum pressure reduction from the smooth case not only depends on the groove depth but also on the groove location. The maximum reduction is observed when the groove approaches the contact center.

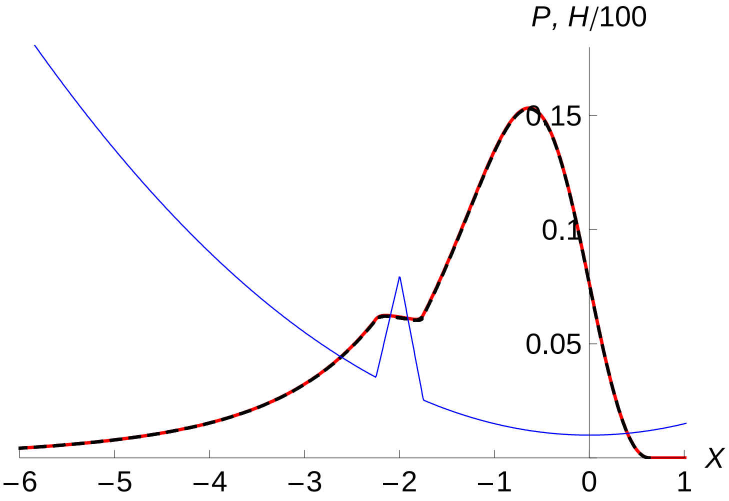

Figure 3.2: Textured pressure distribution (solid line) and geometry for a single groove perpendicular to the sliding direction located at $X_g = -2$ for $A = 5., E = 10, \Lambda = 0.5$ compared with the 1D analytical model [6] (dashed line).

3.4 Groove shape influence

For a single groove perpendicular to the sliding direction, three groove shapes were considered: triangular as in [6], rectangular and sinusoidal shapes as shown in figure 3.5. The pressure on the central line is shown in figure 3.6 together with the smooth pressure and the 1D prediction (dashed line). In this figure the groove depth is $A = 5$ and its location is $X_g = -2$.

The three curves corresponding to the three studied groove shapes are quite close. The lowest one corresponds to the rectangular shape which is larger than the other ones and therefore induces a lower pressure. However, it is not significantly lower. The other curves can hardly be distinguished one from another. Similar results are obtained for other groove locations. When the groove approaches the $X = 0$ location, the difference between the various curves increases a little but not significantly.

From figure 3.7, the same conclusion can be drawn for multiple grooves spaced by $D = 2$. It tends to show that the groove shape is not a major factor influencing the pressure distribution.

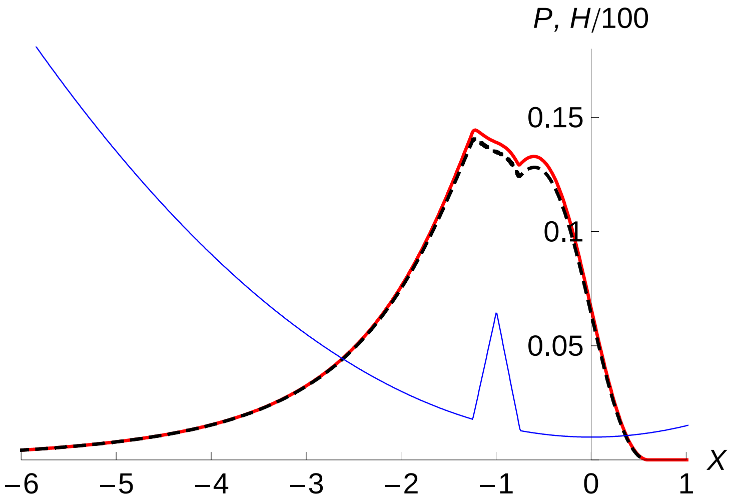

Figure 3.3: Textured pressure distribution (solid line) and geometry for a single groove perpendicular to the sliding direction located at $X_g = -1$ for $A = 5., E = 10, \Lambda = 0.5$ compared with the 1D analytical model [6] (dashed line).

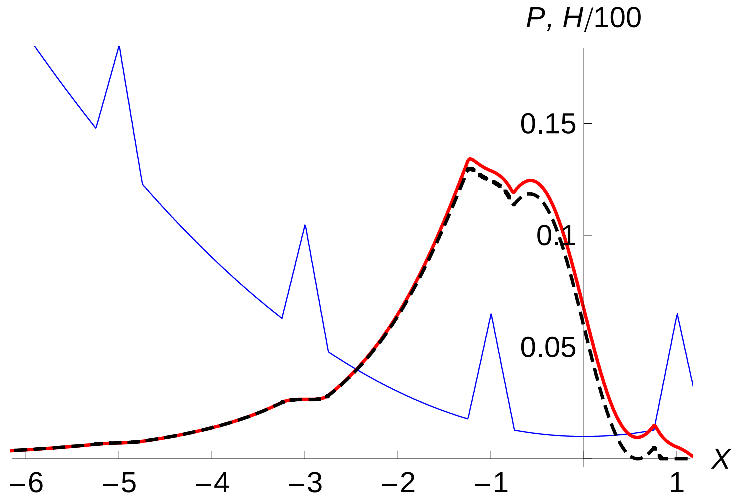

Figure 3.4: Textured pressure distribution (solid line) and geometry for multiple grooves perpendicular to the sliding direction located at $X_g = -9, -7, -5, -3, -1, 1,\ A = 5., E = 10, \Lambda = 0.5$ compared with the 1D analytical model [6] (dashed line).

3.5 Pressure distribution for small angles.

An analytical cross hatched texture is considered with a small angle $\alpha = 5°$. This angle corresponds to the angle between a groove and the Y direction. It is studied on the domain $\Omega = [-10, 2] \times [-0.5D/\sin(\alpha), -0.5D/\sin(\alpha)]$ where D is the dimensionless distance between the grooves. The pressure distribution on the central line $Y = 0$ and on the line $Y = -0.25D/\sin(\alpha)$

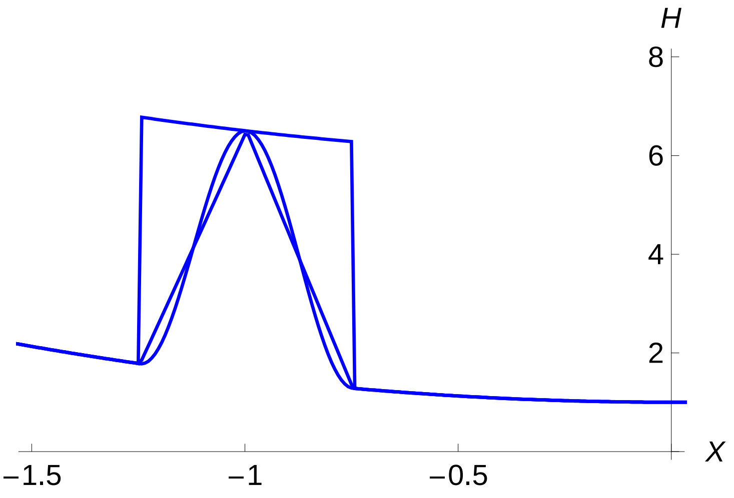

Figure 3.5: Groove shapes: Triangular- Rectangular - Sinusoidal

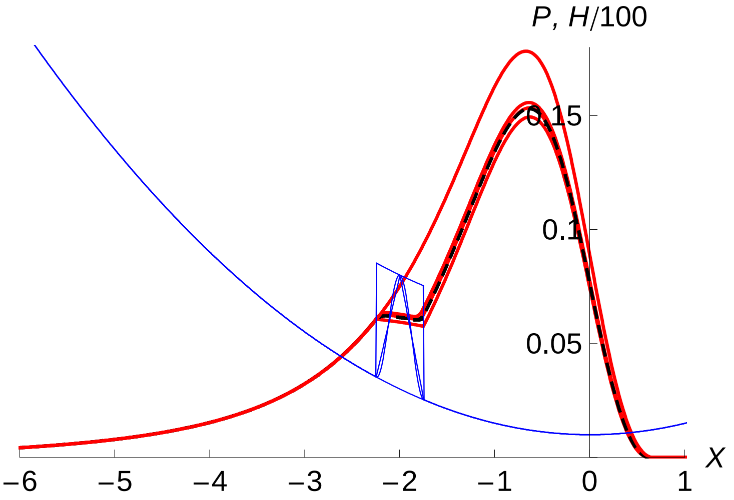

Figure 3.6: Textured pressure distribution and geometry for one groove perpendicular to the sliding direction located at $X_g = -2$ - $A = 5., E = 10, \Lambda = 0.5$ for various groove shapes: rectangular, triangular, sinusoidal, smooth from bottom to top with the 1D analytical model (dashed line).

were drawn for $A = 5$ and $D = 3$. It was compared with a 1D analytic model using the same groove distribution on both lines. Sinusoidal grooves were used with the 2D code and triangular grooves with the 1D analytical prediction.

The curves are quite close in spite of the fact that the 2D geometry and the different groove shapes already induce some differences. This conclusion is only valid for a limited groove depth. On each line parallel to the sliding direction, the pressure seems to be mainly determined by the groove location on this particular line. The results are shown in figures 3.8 and 3.9.

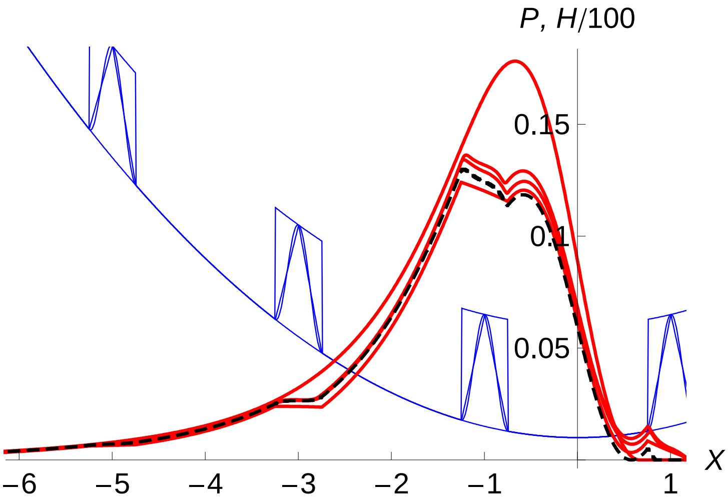

Figure 3.7: Textured pressure distribution and geometry for multiple grooves spaced by 2 perpendicular to the sliding direction located at $X_g = -9, -7, -5, -3, -1, 1$-$A = 5., E = 10, \Lambda = 0.5$ for various groove shapes: rectangular, triangular, sinusoidal, smooth from bottom to top with the 1D analytical model (dashed line).

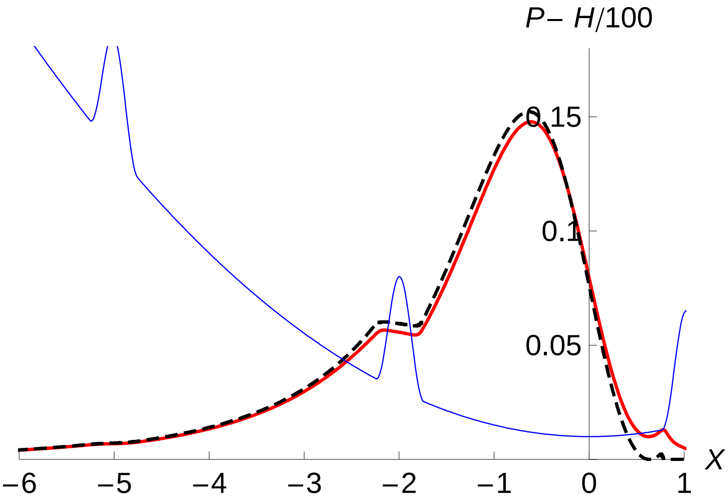

Figure 3.8: Pressure and geometry for a cross hatched liner texture of angle $\alpha = 5°$ for $A = 5., E = 10, \Lambda = 0.5$ on the central line $Y = 0$ and 1D prediction (dashed line) with the same groove distribution.

3.6 Load carrying capacity

Finally, the load carrying capacity for a cross hatched liner texture with the same angle $\alpha = 5°$, groove depth $A = 5$ and groove width $\Lambda = 0.5$ has been studied for two distances between grooves, namely $D = 3$ and $D = 10$ with a dimensionless ring half width $E = 10$. Because of the pattern repetition, it is in fact sufficient to draw them for grooves located between $-D/\cos(\alpha)$

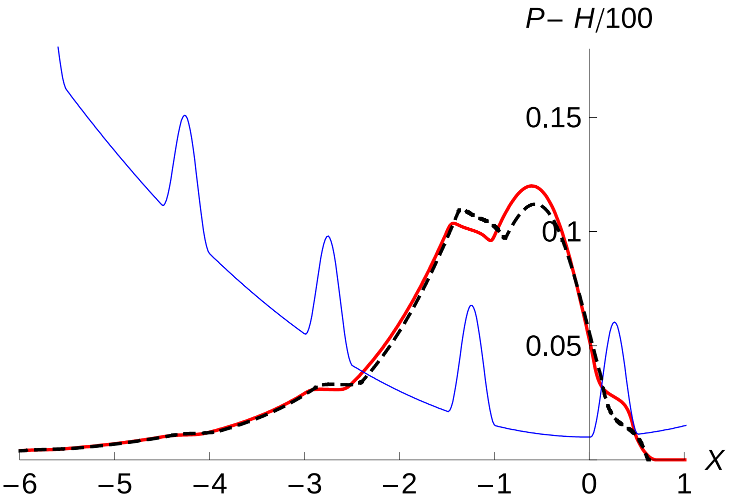

Figure 3.9: Pressure and geometry for a cross hatched liner texture of angle $\alpha = 5°$ for $A = 5., E = 10, \Lambda = 0.5$ on the line $Y = -0.25D/\sin(\alpha)$ and 1D prediction (dashed line) with the same groove distribution.

and 0. The results are given in figures 3.10 and 3.11. In these figures the total load carrying capacity relative to the smooth load carrying capacity, as a function of the groove location is represented. A periodicity $0.5D/\cos(\alpha)$ can be observed. It is a consequence of the chosen pattern. As expected the deeper the grooves and/or the closer the grooves, the lower the load carrying capacity. For $D = 3$, there are 3 times as many grooves in the contact and this explains why the load carrying capacity is lower in this case. Besides in this case there are always a large amount of grooves in the center of the contact where the pressure is most affected by the grooves. The above mentioned periodicity in the load carrying capacity can be better observed for $D = 10$ and deep grooves. In this case, for very deep grooves, one can better observe a variation in the load carrying capacity. It may be due to the distribution of the grooves with respect to the sensitive zone (i.e. the zone where the pressure is most influenced by grooves). For instance for $X_g = -4.5$, the grooves spread more widely on the sensitive part of the contact while for $X_g = -1$ there are more concentrated and therefore influence pressure in a smaller domain as shown in Figures 3.12. On this figure the groove projection is plotted together with a rectangle that roughly corresponding to the sensitive zone. However, these variations are not very important when $D = 3$. When $D = 10$ and for very deep grooves they do not exceed 7%. As the angle α is small, the distance between grooves roughly defines the load carrying capacity periodicity although variations can be observed. The pressure is highest when the distance between grooves is large.

3.7 Conclusion

The multigrid code based on Alcouffe's ideas for the hydrodynamic Reynolds equation in the PRCL contact with a textured liner shows good convergence and robustness, even in presence of very deep grooves. The code is validated by comparison with a 1D model developed by Biboulet,

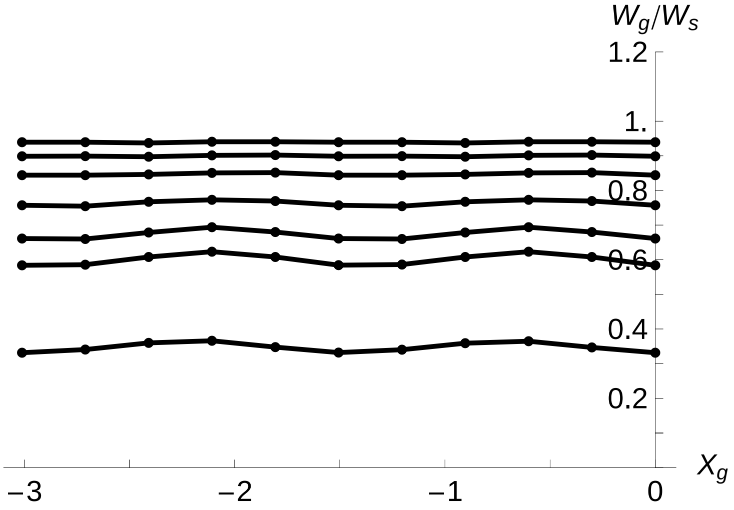

Figure 3.10: Relative textured load carrying capacity $D = 3, E = 10, \Lambda = 0.5, \alpha = 5°$, $A = 0.5, 1, 2, 5, 10, 15, 50$ from top to bottom

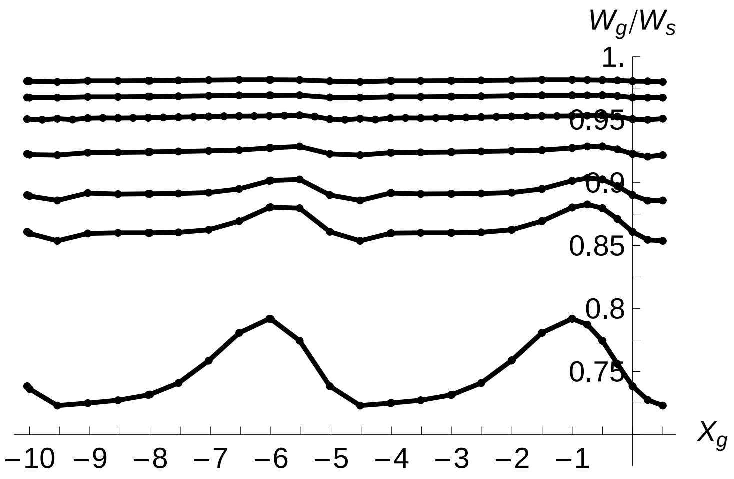

Figure 3.11: Relative textured load carrying capacity $D = 10, E = 10, \Lambda = 0.5, \alpha = 5°$, $A = 0.5, 1, 2, 5, 10, 15, 50$ from top to bottom

in the case of grooves perpendicular to the sliding direction. It is also tested for three different groove shapes and the results confirm that the groove shape has little influence on the pressure distribution. Then a cross hatched texture with a small angle is studied. For a limited groove depth, only a small difference between the 1D and 2D results was obtained. Overall the 1D analytical model can be used to approximate the pressure distribution on each line parallel to the sliding direction for a limited groove depth since it seems to be mainly determined by the location of the grooves on this specific line. Finally, curves of the load carrying capacity as a function of the groove position for various groove depths and groove distances are drawn. They

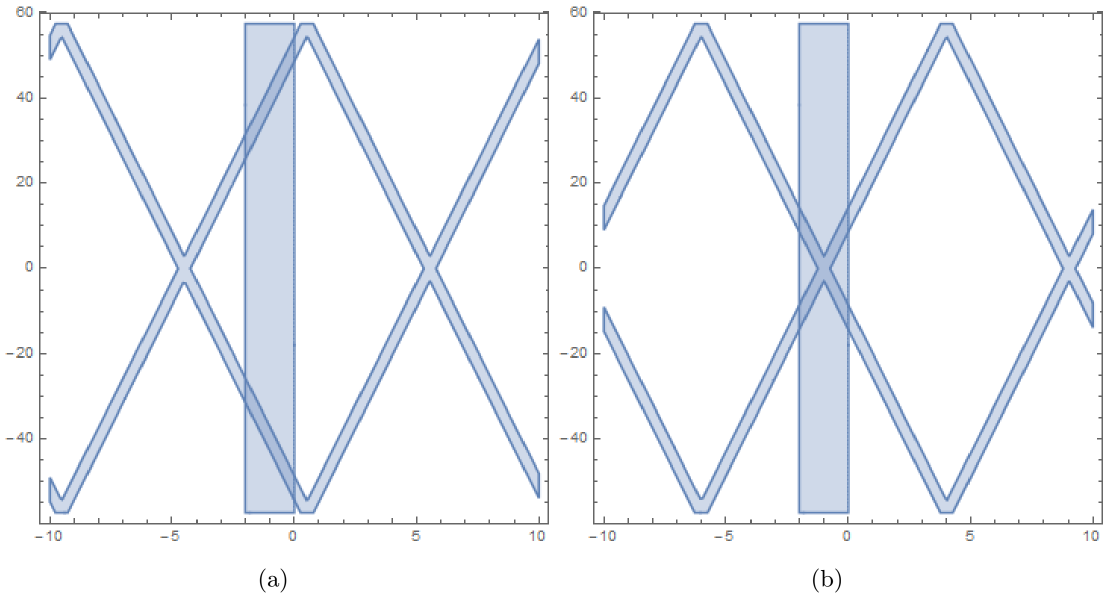

(a) (b)

Figure 3.12: Portion of grooves in the pressure influential zone for $D = 10, E = 10, \Lambda = 0.5, \alpha = 5°$ (a) $X_g = -4.5$ (b) $X_g = -1$.

tend to show that groove depth and density are important factors determining the load carrying capacity, whereas the groove shape has only a small influence. Other groove angles should be considered.

CHAPTER 4

Flow conservation

Contents

4.1 Introduction

The problem of a mass-conserving algorithm has been the topic of many investigations as for instance [31, 34–37]. After applying our algorithm to textured surfaces we were interested in similar questions for indented surfaces. When we started to study dimples for the flat ring, it appeared that it was not sufficient to have built a robust multigrid algorithm but that it was also crucial to construct a mass conserving algorithm or flow-conserving algorithm, since here only incompressible flows are studied.
Henceforth, for the stationary case the equation to be solved is now the complementary problem already mentioned in section 1.11:

$$\frac{\partial}{\partial X}(H^3\frac{\partial P}{\partial X}) + \frac{\partial}{\partial Y}(H^3\frac{\partial P}{\partial Y}) - \frac{\partial H_{oil}}{\partial X} = 0 \quad (X,Y) \in \Omega \tag{4.1}$$

Where H_{oil}, represents the oil film thickness and H the geometry. When the pressure is positive H_{oil} is equal to H. Otherwise it is a fraction of H, this is Elrod's model [11, 12]. The oil level is imposed at the entrance of the domain $\Omega = [X_a, X_b] \times [Y_a, Y_b]$ that is to say on the line $X = X_a$. The pressure is set to zero for $X \leq X_a$ in the periodic case in Y or taken to be 0 outside Ω for the Dirichlet problem.

To account for the flow conservation, it was first decided to modify the Alcouffe based algorithm by implementing a new relaxation scheme based on the physics of the problem.

4.2 Grid configuration

The domain is a rectangle $[X_a, X_b] \times [Y_a, Y_b]$, decomposed into rectangular cells of dimension h_x, h_y by vertical and horizontal equally spaced straight lines. The pressure is evaluated at each node (i, j) that is to say at each point (X_i, Y_j) with $X_i = X_a + i\, h_x$ and $Y_j = Y_a + j\, h_y$. The geometry $H_{i,j}$ or the oil film $Hoil_{i,j}$ are evaluated at the points $(X_{i-1/2}, Y_j)$ with $X_{i-1/2} = X_a + (i - 1/2)\, h_x$ for $0 < i < i_{max}$ and $0 \leq j \leq j_{max}$. On the boundaries $X = X_a$ and $X = X_b$, the film height and the geometry are evaluated at the same point as the pressure.
In Figure 4.1, a fine grid (thin full lines) and the next coarse grid (thick full lines) can be seen. On the fine grid, the dots indicate the points at which the pressure is calculated and the crosses mark the points at which the film height is evaluated except on the 2 lines $i = 0$ and $i = i_{max}$ where they are evaluated at the same points as P. The larger dots indicate the points of the coarse grid where the pressure is evaluated.

4.3 Relaxation scheme

A volume discretization is still used to discretize the problem. Consider a general cell of the finest grid (see Figure 4.2). On the fine grid, the residual at the point $(X_i, Y_j))$ reads:

$$\begin{aligned}&A_{i,j}(P_{i,j+1} - P_{i,j}) + A_{i,j-1}(P_{i,j-1} - P_{i,j}) + B_{i,j}(P_{i+1,j} - P_{i,j}) + B_{i-1,j}(P_{i-1,j} - P_{i,j})\\ &- h_y(Hoil_{i+1,j} - Hoil_{i,j})\end{aligned}$$

where h_y is the step size in the Y-direction and the $A_{i,j}, B_{i,j}$ the Alcouffe coefficients. In this residual the coefficient of $P_{i,j}$ is $C_{i,j} = -(A_{i,j} + A_{i,j-1} + B_{i,j} + B_{i-1,j})$. This coefficient is negative. It represents the flow balance through the domain limited by the red dashed lines that is to say through the domain of frontiers $\partial_w, \partial_s, \partial_e$ and ∂_n surrounding the point (X_i, Y_j). This domain is also indicated in red in Figure 4.1.
Indeed, through a vertical boundary such as for instance ∂_w, the flow is:

$$\Phi_w(i, j) = h_y Hoil_{i,j} - B_{i-1,j}(P_{i,j} - P_{i-1,j})$$

and through a horizontal one such as for instance ∂_s, it is :

$$\Phi_s(i, j) = -A_{i,j-1}(P_{i,j} - P_{i,j-1}).$$

The residual at $(X_i, Y_j))$ then reads

$$res(i, j) = \Phi_w(i, j) - \Phi_e(i, j) + \Phi_s(i, j) - \Phi_n(i, j).$$

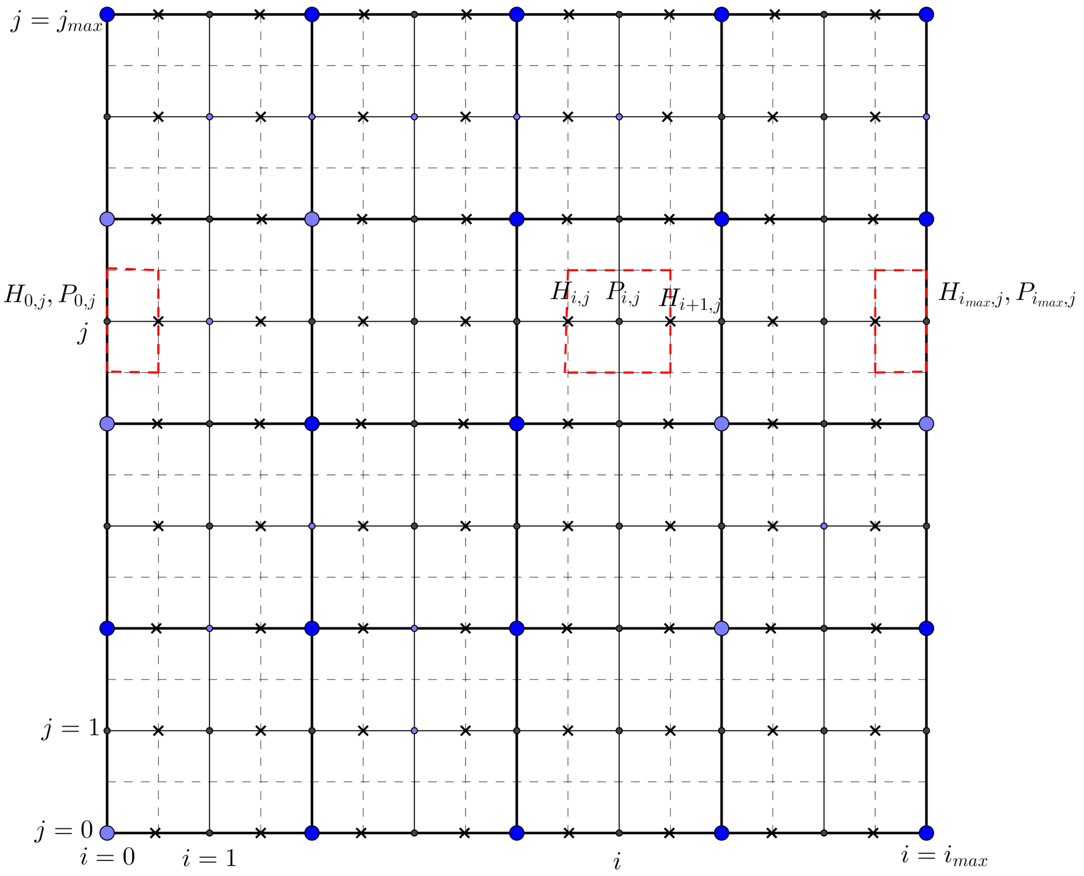

Figure 4.1: 2 grids

To eliminate a positive residual $res(i,j)$, we can increase $Hoil_{i+1,j}$ or decrease $P_{i,j}$ and when it is negative, we can decrease $Hoil_{i+1,j}$ or increase $P_{i,j}$. It is also possible to change $Hoil_{i,j}$ or the pressures surrounding $P_{i,j}$.

Since in the pressurized zone the oil film is complete, when the residual is positive we first increase $Hoil_{i+1,j}$ by $res(i,j)/hy$ and if it reaches the maximum possible value $H_{i+1,j}$ we increase the pressure $P_{i,j}$ by $-res_1(i,j)/C_{i,j}$ to eliminate the remaining part of the residual, $res_1(i,j)$. When the residual is negative, for the same reason we first decrease the pressure $P_{i,j}$ by $-res(i,j)/C_{i,j}$ and if $P_{i,j}$ becomes negative, we set it to zero and then decrease the oil film $Hoil_{i+1,j}$ by $res_2(i,j)/h_y$ where $res_2(i,j)$ is the remaining residual. Henceforth, the following relaxation scheme is used.

- Evaluate the residual res at point (i,j)
- if $res > 0$
  - $Hoil_{i+1,j} \leftarrow Hoil_{i+1,j} + res/hy$
  - if $Hoil_{i+1,j} > H_{i+1,j}$

```
        ∗ $Hoil_{i+1,j} = H_{i+1,j}$
        ∗ Evaluate the remaining residual $res1$ at point $(i,j)$
        ∗ $P_{i,j} \leftarrow P_{i,j} - res1/C_{i,j}$
• if $res < 0$
    – $P_{i,j} \leftarrow P_{i,j} - res1/C_{i,j}$
    – if $P_{i,j} < 0$
        ∗ $P_{i,j} = 0$
        ∗ Evaluate the remaining residual $res2$ at point $(i,j)$
        ∗ $Hoil_{i+1,j} \leftarrow Hoil_{i+1,j} + res2/hy$
```

Remark: $C_{i,j} < 0$.
Another option would consist in making a distributive relaxation on $Hoil$. When the residual is positive, we first increase $Hoil_{i+1,j}$ by $0.5 \times res(i,j)$, if it reaches the maximum possible value $H_{i,j}$ we increase the pressure $P(i,j)$ to eliminate the remaining part of the residual and otherwise we decrease $Hoil_{i,j}$ by $0.5 \times res(i,j)$. When the residual is negative, for the same reason we first decrease the pressure $P_{i,j}$ and if it becomes negative, we set it to be zero and distribute the remaining residual between $Hoil_{i+1,j}$ and $Hoil_{i,j}$.

```
• Evaluate the residual $res$ at point $(i,j)$
• if $res > 0$
    – $Hoil_{i+1,j} \leftarrow Hoil_{i+1,j} + 0.5 * res/hy$
    – if $Hoil_{i+1,j} > H_{i+1,j}$
        ∗ $Hoil_{i+1,j} = H_{i+1,j}$
        ∗ Evaluate the remaining residual $res1$ at point $(i,j)$
        ∗ $P_{i,j} \leftarrow P_{i,j} - res1/C_{i,j}$
    – else $Hoil_{i,j} \leftarrow Hoil_{i,j} - 0.5 * res/hy$
• if $res < 0$
    – $P_{i,j} \leftarrow P_{i,j} - res1/C_{i,j}$
    – if $P_{i,j} < 0$
        ∗ $P_{i,j} = 0$
        ∗ Evaluate the remaining residual $res2$ at point $(i,j)$
        ∗ $Hoil_{i+1,j} \leftarrow Hoil_{i+1,j} + 0.5 * res2/hy$
        ∗ $Hoil_{i,j} \leftarrow Hoil_{i,j} - 0.5 * res2/hy$
        ∗ if $Hoil_{i,j} > H_{i,j}$ then $Hoil_{i,j} = H_{i,j}$
```

Special care has to be taken for the cells $i = 0$ and $i = i_{max}$ since there, the configuration is not the same (see figure 4.1).

It was also decided that the free boundaries between the pressurized zone and the cavitated areas were going to be only determined/modified on the fine grid.

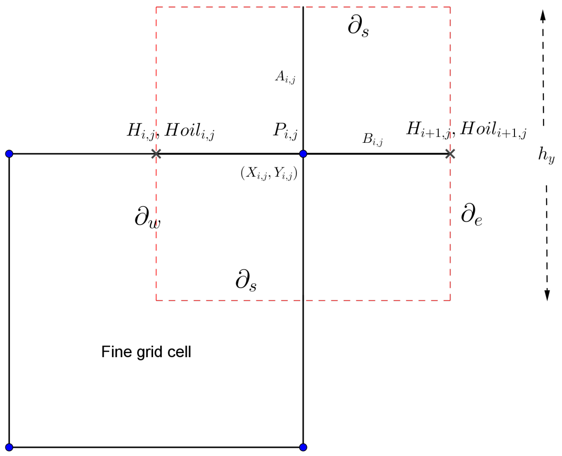

Figure 4.2: Fine cell configuration

4.4 Multigrid difficulties

When using multigrid techniques, the problem to be solved is written as

$$Lu = f.$$

Here, we have two options.

- Option 1: set $f = 0$ and the unknown vector u contains P and $Hoil$.
- Option 2: set $f = \partial Hoil/\partial X$ which means that the Couette part of the flow is put in the right hand side of the equation.

In the first case we need to define coarsening and refining procedures for $Hoil$ as well as for P while in the second case this is not needed but it will be necessary to update the right hand side f on the finest grid of each V-cycle each time the value of $Hoil$ is changed. The coarsening routines for f should induce the correct right-hand side for the coarse grid equations.
In both cases an interpolation of $Hoil$ will be needed if FMG is used.
Option 2 is the simplest one. In that case it was also decided not to change the free boundaries on the coarser grids. Henceforth, the coarse grid relaxation will consist in only changing the pressure in the pressurized zone as follows $P_{i,j} \leftarrow P_{i,j} - res/C_{i,j}$ and set it to 0 if it becomes negative.
This option was the first one to be tried. This way, a code was obtained that converges in the fully flooded case. In partially starved contacts, the convergence is more difficult. To check that the flow conservation is indeed satisfied a periodic code in the Y-direction was also written. In this case the value of the flow calculated along different lines will also tell us something about the quality of the obtained results.

4.5 FMG interpolation

For the pressure, we keep the previously used interpolation. For the film height, the following simple interpolation is first used:

$$\begin{aligned}
&Hoil(2i,2j) = 0.75Hoil_c(i,j) + 0.25Hoil_c(i+1,j)\\
&Hoil(2i-1,2j) = 0.75Hoil_c(i,j) + 0.25Hoil_c(i-1,j)\\
&Hoil(2i,2j-1) = 0.5(Hoil(2i,2j) + Hoil(2i,2j-2))\\
&Hoil(2i-1,2j-1) = 0.5(Hoil(2i-1,2j) + Hoil(2i-1,2j-2)).
\end{aligned}$$

In these formulas $Hoil$ and $Hoilc$ are respectively the fine grid and coarse grid oil levels. They are shown in Figure 4.3. These formulas need to be adapted near the boundaries because, on the lines $X = X_a$ and $X = X_b$, the film height is evaluated at the same point as the pressure. On the line $X = X_a$, that is to say $i = 0$, no change because there $Hoil$ is defined by the initial condition but on the next vertical line $i = 1$ we cannot use the same formulas as above.

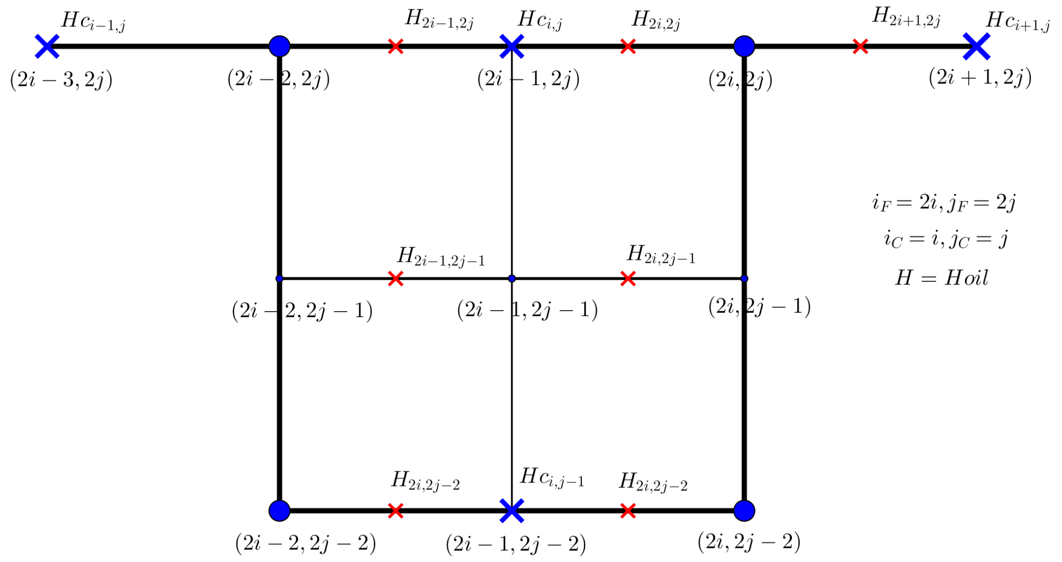

Figure 4.3: Fine cell and coarse configuration for oil film interpolation.

$$\begin{aligned}
&Hoil(1,2j) = 0.5Hoil_c(0,j) + 0.5Hoil_c(1,j)\\
&Hoil(1,2j-1) = 0.5(Hoil(1,2j) + Hoil(1,2j-2)).
\end{aligned}$$

For the Dirichlet case, there is a problem on the lines $Y = Y_a$ or $Y = Y_b$. Because of the Dirichlet conditions, the values on these lines are not relaxed and the definition of the oil level on these lines is not clear. The corresponding value at $X = X_a$ was taken on these two lines. In the periodic case, this is no longer a difficulty.

4.6 Couette flow in the right hand side: numerical results

4.6.1 Groove geometry

The geometry is defined by $H(X,Y) = 1 + 0.5X^2 + \Psi(X,Y)$. The domain is a square $[-10,10] \times [-10,10]$. The function $\Psi(X,Y)$ describes the roughness of the surface. As previously, a cross hatched pattern is used. The distance between grooves is $D = 2$, their width is $\Lambda = 1$ and the angle between the grooves is $\alpha = 45°$. This geometry can be seen in figure 4.4.

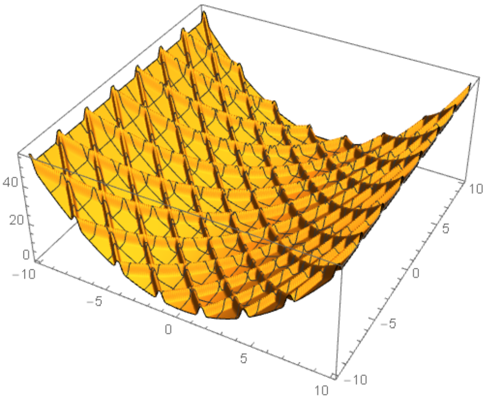

Figure 4.4: Groove geometry

The relaxation process that is used on the finest grid is the first one and on the coarse grid, only the pressure is relaxed and only in the pressurized zone.

4.6.1.1 Dirichlet code

In the fully flooded case the associated pressure and oil film distributions are shown in figure 4.5. In the same figure, the evolution of the residual in terms of work units is shown. The fine grid is a 1024×1024 grid. The code was run with 9 levels.
As before convergence slows down with deeper grooves. However convergence is still good. For deep grooves the stabilization of the free cavitation boundaries takes time and no special prerelaxation is used and only V(2.1)-cycles are used. Finally, for fully flooded conditions, results are satisfactory.
Afterwards the algorithm was tested on partially starved contacts. This will be crucial for dimples and the flat ring because, inside the dimples, we have cavitation and oil film re-formation. Results are shown in figures 4.6. Surprisingly in that case, convergence seems to be more difficult in the case of smoother surfaces and is not at all good in the smooth case!!!

4.6.1.2 Periodic code

Here special care to the choice of the domain has to be taken. We need a domain that allows a periodicity of the surface with respect to the Y-direction. As the angle between the grooves was chosen to be 45°, we can still work on the same domain $[-10,10] \times [-10,10]$ if the chosen

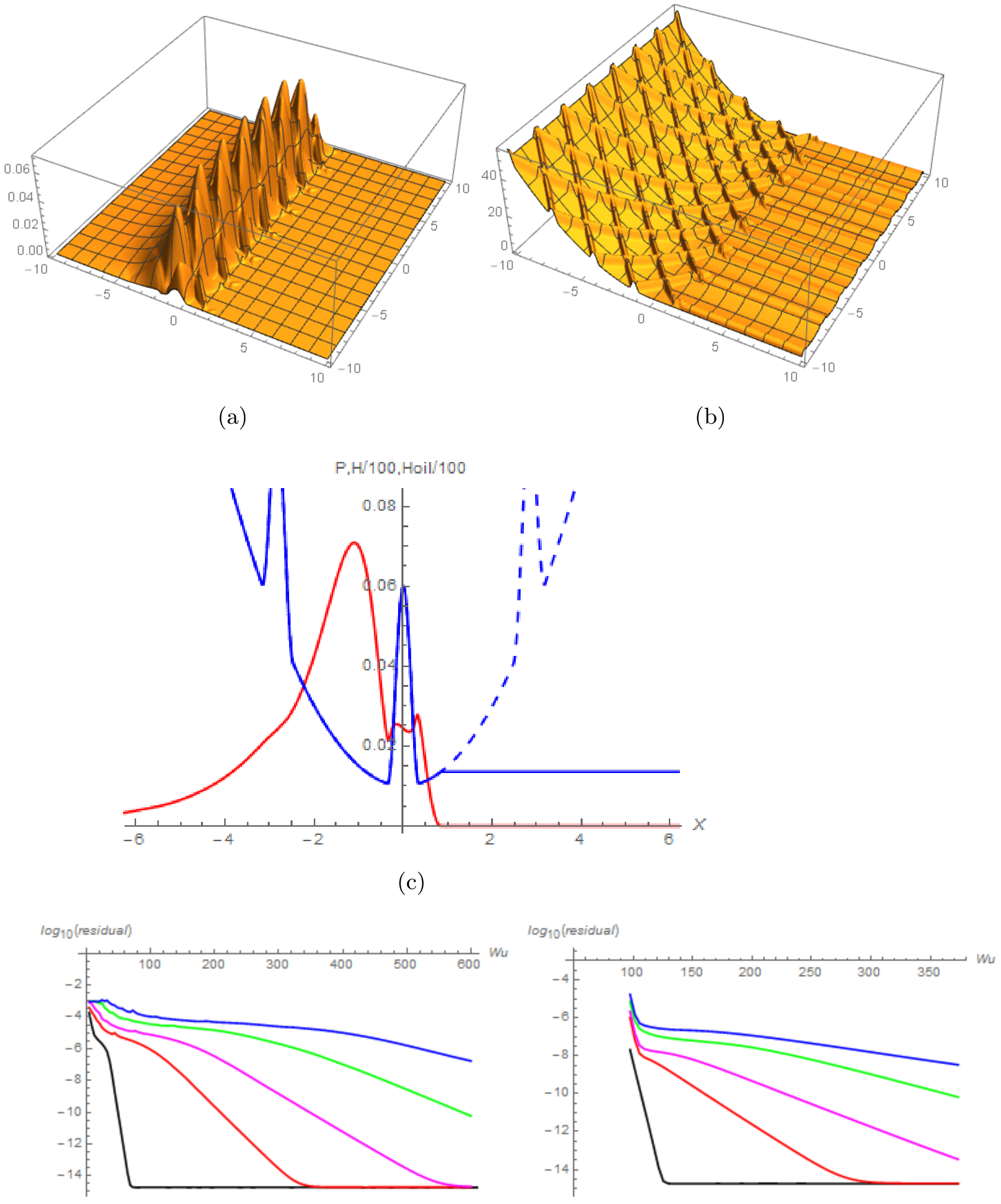

(a)

(b)

(c)

(d)

(e)

Figure 4.5: Fully flooded case - Dirichlet conditions - Cross-hatched groove pattern of depth A. For $A = 5$ (a) pressure (b) film height (c) pressure, geometry and oil film on the line $Y = 0$. Residual in terms of work units for eight levels for grooves of depth 0 (black), 1 (red), 2 (pink), 5 (green), 10 (blue) from bottom to top (d) 150 V(2,1) cycles (e) FMG with 70 V(2,1) cycles.

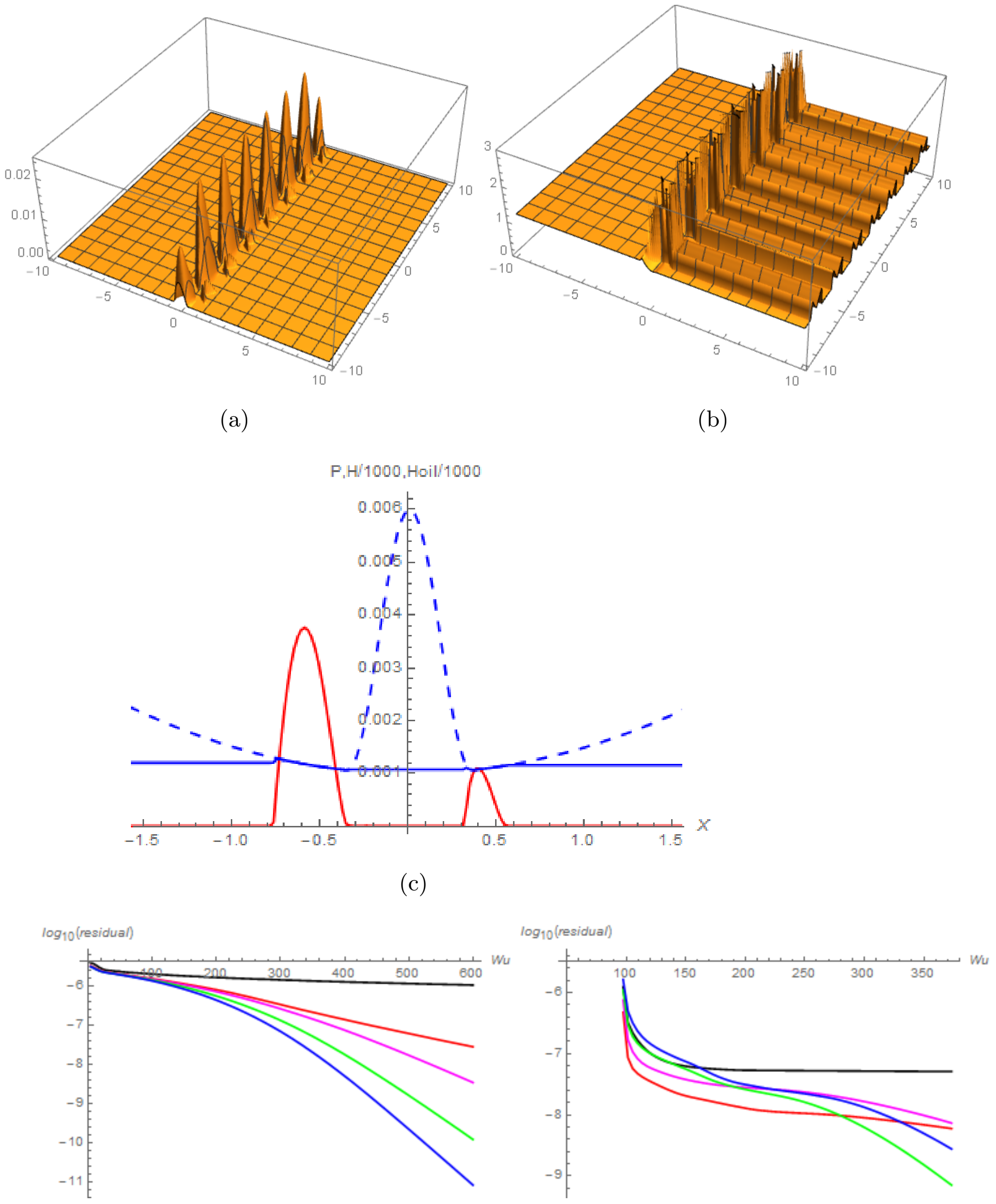

(a) (b)

(c)

(d) (e)

Figure 4.6: Starved case (initial oil level: $Hoil = 1.2$ on $X = X_a = -10$ - Dirichlet conditions - Cross-hatched groove pattern of depth A.
For $A = 5$ (a) pressure (b) film height (c) pressure, geometry and oil film on the line $Y = 0$.
Residual in terms of work units for eight levels for grooves of depth 0 (black), 1 (red), 2 (pink), 5 (green), 10 (blue) (d) 150 V(2,1) cycles (e) FMG with 70 V(2,1) cycles.

distance between grooves is $D = \sqrt{2}$ and their width $\Lambda = 1$.

In the fully flooded case, results can be seen in Figures 4.7. Similar conclusions as in the Dirichlet case can be drawn. In this case, it was also possible to check the mass conservation through each vertical line of the domain. This may also give a means of checking the quality of the convergence.

Results in the partially starved contact were also calculated and they can be seen in figures 4.8. Again the convergence is very slow in the smooth case. However if the initial oil level is larger than the limit value (about 1.225), the code converges to the fully flooded case, although a little slowly when the initial oil level is close to the limit value (for instance 1.3). In case of grooves, it works better. Why? Maybe this can be explained by the fact that at the film formation, the inlet meniscus position has to be determined by the code. This seem to be a rather slow process and it is longer in the smooth case since the flow must recede more in that case. It was also noticed that once the inlet position is found, the residuals at those points diminish rather slowly. A possible explanation may be that the relaxation process and the code probably do not correctly account for the phenomenons that occur at the inlet. It is a continuity for the Poiseuille flow that is considered with Alcouffe 's ideas. The cavitation boundary is not a difficulty since at cavitation there is no jump in $Hoil$. However, at the film formation this jump can be huge and this is particularly true in the smooth case.

4.6.2 Numerical results: Dimple geometry

Since in the next chapter this algorithm will be used to study the influence of dimples for a flat ring in the piston ring liner contact, it may be interesting to consider the behavior of the code in such a case. Here a single dimple of radius 1 and depth A is considered. It is located at the center of a square domain $\Omega = [-5, 5] \times [-5, 5]$. The geometry H, shown in figure 4.9, is defined as follows:

$$H(X, Y) = 1 + \Psi(X, Y)$$

with

$$\Psi(X, Y) = \frac{A}{2}(1 + \cos(\frac{\pi}{R}\sqrt{X^2 + Y^2}))$$

if there is a dimple of depth A and radius R centered at $(0, 0)$ and if $(X^2+Y^2 \leq 1$ and $\Psi(X, Y) = 0$ otherwise. Only Dirichlet conditions are considered. In the given results, the cavitation pressure is set to 0 and the ambient pressure is taken as $Pamb = 0.01$. For $A = 1$ and $R = 1$, the pressure distribution and oil film are shown in figure 4.10.

The code still converges in that case. However, the convergence becomes very slow with increasing depth. It was noticed that the problem mainly arises at the film re-formation boundary. As previously mentioned, here too it was noticed that the frontiers between the pressurized and non-pressurized zones stabilize after a some cycles and then residual very slowly diminish at the film re-formation. For deep dimples the discontinuity in $Hoil$ becomes large (see figure 4.10) and is not well accounted for by the code. With FMG, the frontiers need less cycles to stabilize which may explain the acceleration of convergence for the first V-cycles at the beginning of the

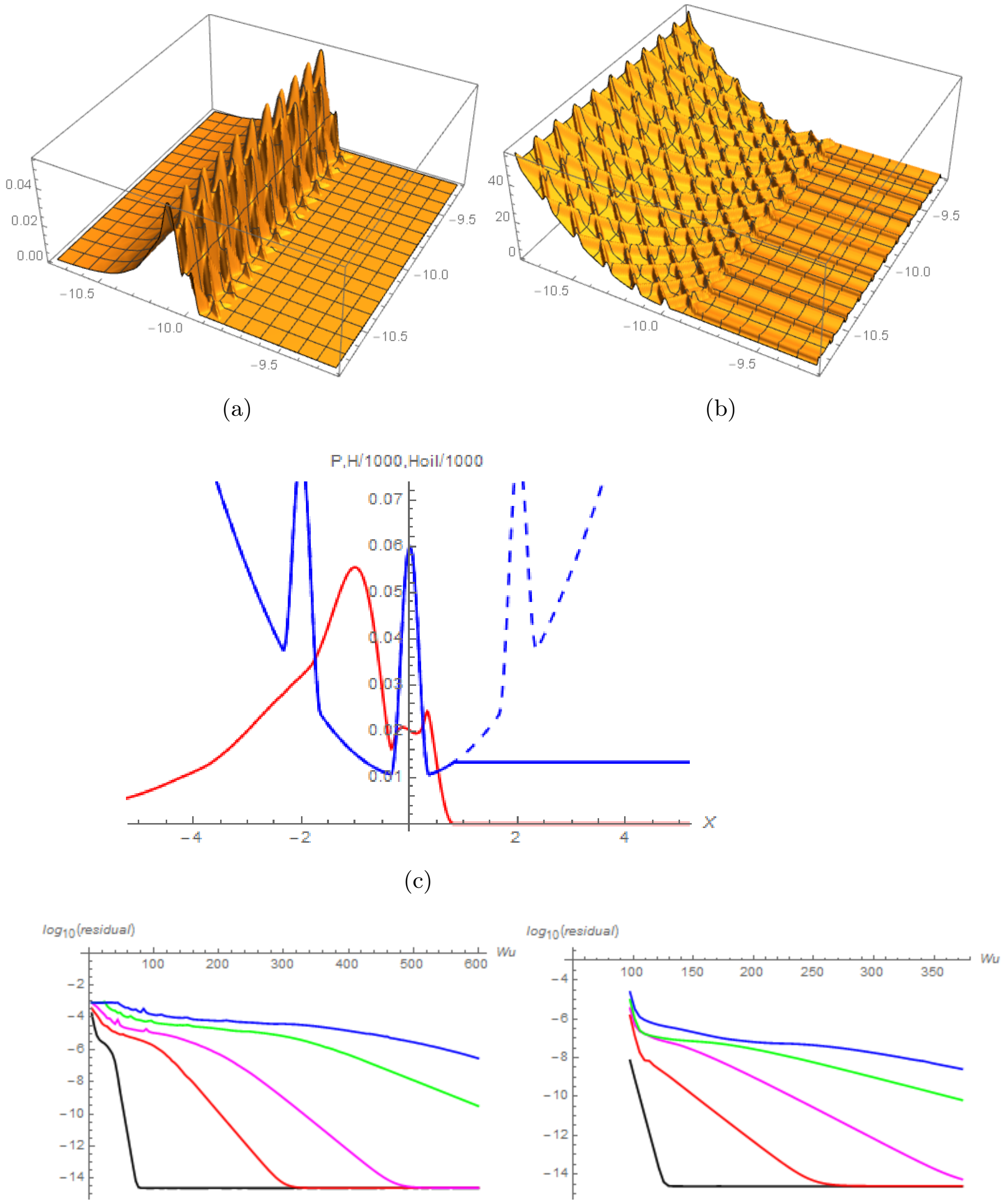

(a) (b)

(c)

(d) (e)

Figure 4.7: Periodic fully flooded case - Cross-hatched groove pattern of depth A
For $A = 5$ (a) pressure (b) film height (c) pressure, geometry and oil film on the line $Y = 0$.
Residual in terms of work units for eight levels for grooves of depth 0 (black), 1 (red), 2 (pink), 5 (green), 10 (blue): (d) 150 V(2,1)-cycles-(e) FMG with 70 V(2,1)-cycles.

process on the finest grid. This becomes more difficult with increasing depth because the $Hoil$ jump is becoming larger. As shown the convergence is not very satisfactory, however it converges and sufficiently fast to study the hydrodynamic lubrication in the case of parallel surfaces with dimples. As shown in Table 4.1, with a 10 × 10 coarse grid and 6 levels, we were able to reach

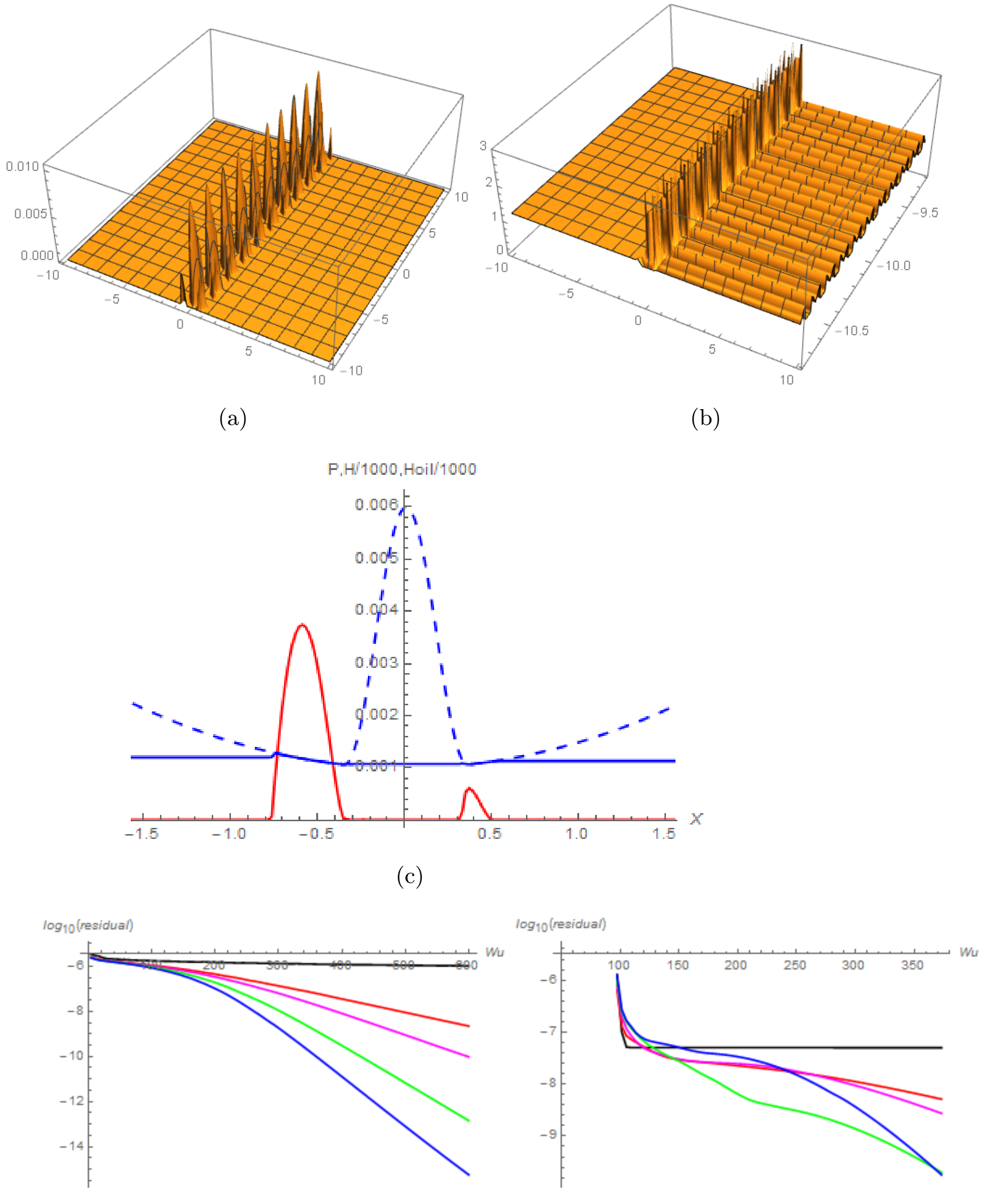

(a) (b)

(c)

(d) (e)

Figure 4.8: Periodic partially starved conditions - Initial oil level $Hoil = 1.2$ on the line $X = X_a = -10$ - Cross-hatched groove pattern of depth A with $H(X,Y) = 1 + 0.5X^2$ - Pressure, geometry and oil film on the line $Y = 0$ (a) for $A = 1$ (b) for $A = 5$ c) pressure, geometry and oil film on the line $Y = 0$ - Residual in terms of work units for eight levels for grooves of depth 0 (black), 1 (red), 2 (pink), 5 (green), 10 (blue): (d) 150 V(2,1)-cycles-(e) FMG with 70 V(2,1)-cycles.

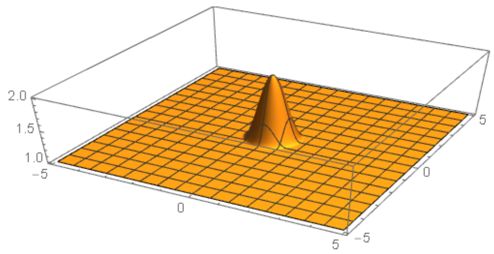

Figure 4.9: Dimple geometry.

an accuracy that was sufficient to study the influence of dimples in a reasonable computational time. To obtain this table the code was run with 2000 V(10,5) cycles (!) on 8 levels to ensure very good convergence on the finest grid. To obtain the same accuracy on level 6 fewer cycles are needed and the computing time is about 3 minutes. In those calculations the dimple depth was $A = 2$ which is the most difficult one among the studied depths. For other depths convergence can be achieved more rapidly.

Level	Residual	Load Carrying Capacity	Δ LCC	Maximum Pressure	ΔP_{max}
Level 1	$6.35102\,10^{-17}$	$-1.00000\,10^{-2}$	-	$2.76492\,10^{-2}$	-
Level 2	$2.09152\,10^{-18}$	$-1.94861\,10^{-2}$	$9.5\,10^{-3}$	$4.34372\,10^{-2}$	$1.6\,10^{-2}$
Level 3	$1.98892\,10^{-18}$	$-1.68488\,10^{-2}$	$2.6\,10^{-3}$	$3.43925\,10^{-2}$	$9.0\,10^{-3}$
Level 4	$1.82116\,10^{-18}$	$-1.69852\,10^{-2}$	$1.4\,10^{-3}$	$3.66619\,10^{-2}$	$2.3\,10^{-3}$
Level 5	$1.69281\,10^{-18}$	$-1.70794\,10^{-2}$	$9.4\,10^{-5}$	$3.62509\,10^{-2}$	$4.1\,10^{-4}$
Level 6	$1.55315\,10^{-18}$	$-1.71136\,10^{-2}$	$3.4\,10^{-5}$	$3.64604\,10^{-2}$	$2.1\,10^{-4}$
Level 7	$8.24906\,10^{-18}$	$-1.71084\,10^{-2}$	$5.2\,10^{-6}$	$3.64659\,10^{-2}$	$5.5\,10^{-6}$
Level 8	$2.15277\,10^{-15}$	$-1.71068\,10^{-2}$	$1.6\,10^{-6}$	$3.64642\,10^{-2}$	$1.7\,10^{-6}$

Table 4.1: Residual, Load carrying capacity, Load Carrying Capacity difference with the previous level, maximum pressure and maximum pressure difference with the previous level for one dimple according to the level. (FMG with 8 levels on $\Omega = [-5, 5] \times [-5, 5]$, with one dimple of radius 1 and depth 2 at the center of the domain.

4.7 Second multigrid option

It was decided to also try the first option mentioned in section 4.4. The problem is written as $Lu = f$, with $f = 0$ on the finest grid. The unknown vector u contains P and $Hoil$. Coarsening and refining routines are now required for $Hoil$ as well as for P. Besides now in the cavitated area, the following non-elliptic equation: $\partial Hoil/\partial X$ has to be solved. As a distributive relaxation of this equation yields an elliptic operator, it was decided to use the distributive relaxation on $Hoil$.

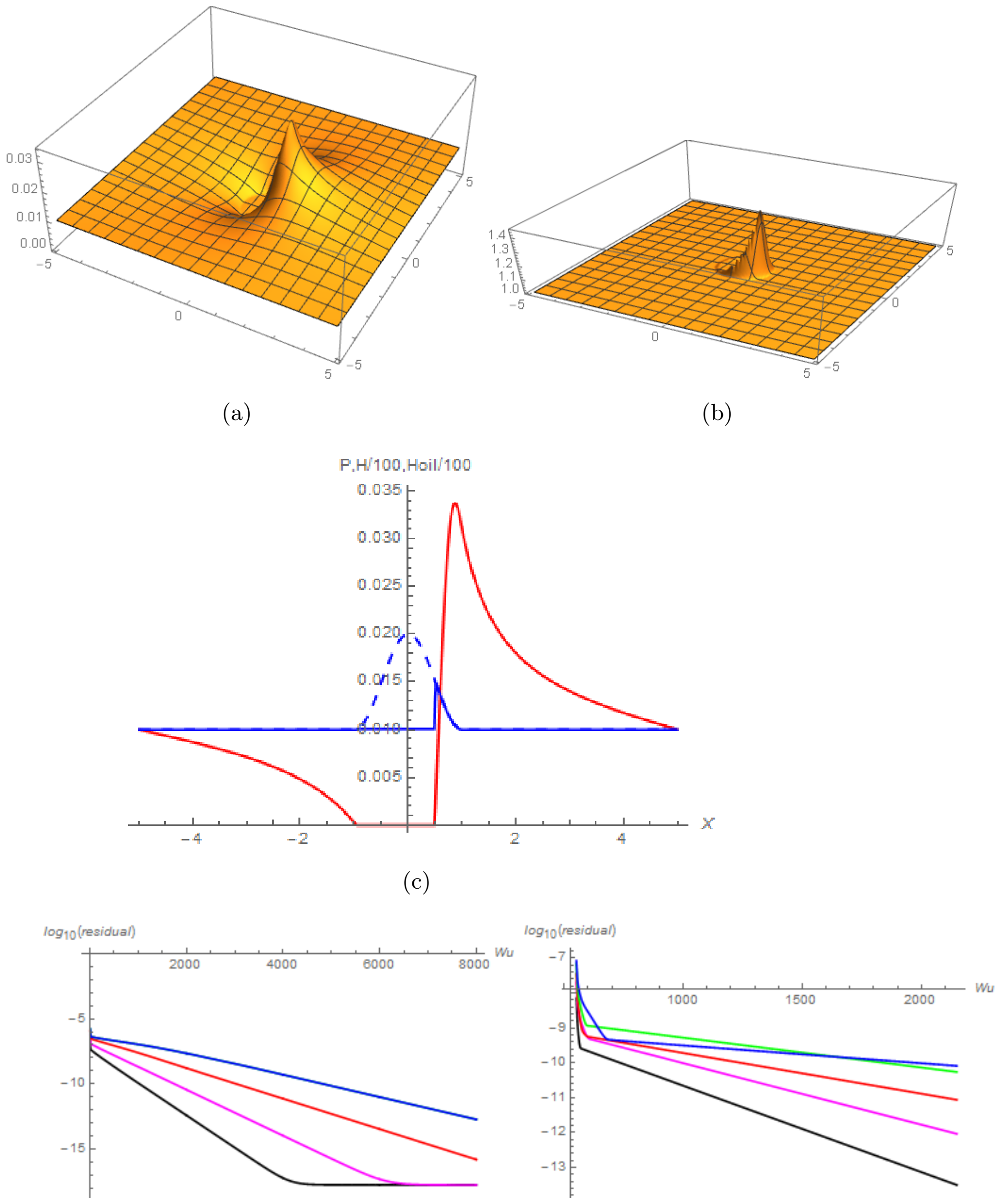

(a) (b)

(c)

(d) (e)

Figure 4.10: Dimple of depth $A = 1$ - Dirichlet conditions .
(a) pressure (b) film height (c) pressure, geometry and oil film on the line $Y = 0$.
Residual in terms of work units for eight levels for one dimple of depth 0.1 (black), 0.2 (red), 0.5 (pink), 1 (green), 2 (blue) (d) 2000 V(2,1) cycles (e) FMG with 400 V(2,1) cycles.

4.7.1 Coarsening routine

The pressure coarsening routines are not changed. For the oil film, a simple geometrical restriction is used.

$$\begin{aligned}Hoil_c(i,j) =& 1/8(Hoil(2i,2j+1)+Hoil(2i-1,2j+1))+\\ & 1/4(Hoil(2i,2j)+Hoil(2i-1,2j))+\\ & 1/8(Hoil(2i,2j-1)+Hoil(2i-1,2j-1)).\end{aligned}$$

This was for $1 \leq i \leq ii_c, 0 \leq j \leq jj_c$ where ii_c, jj_c represents the maximum i, j indices on the coarse grid. This gives an exact representation of the Couette flow on the coarse grid around $P_c(i,j)$.

4.7.2 Refining routine

Here again for the pressure the refining routines are not changed. The values of $Hoil(i,j)$ on the fine grid are corrected as follows:

$$\begin{aligned}&Hoil(2ic,2jc)+=\delta(ic,jc), && (1 \leq ic \leq iic, 0 \leq jc \leq jjc)\\ &Hoil(2ic-1,2jc)+=\delta(ic,jc), && (1 \leq ic \leq iic, 0 \leq jc \leq jjc)\\ &Hoil(2ic,2jc-1)+=0.5(\delta(ic,jc-1)+\delta(ic,jc)), && (1 \leq ic \leq iic, 1 \leq jc \leq jjc)\\ &Hoil(2ic-1,2jc-1)+=0.5(\delta(ic,jc-1)+\delta(ic,jc)), && (1 \leq ic \leq iic, 1 \leq jc \leq jjc).\end{aligned}$$

In these formulas, $\delta(ic,jc) = Hoil_c(ic,jc) - Hoil_{co}(ic,jc)$ where $Hoil_{co}(ic,jc)$ represents the value of the film height just after the coarsening steps in the cycle and $Hoil_c(ic,jc)$ its value just before the refining step to the next fine grid.

4.7.3 Right hand side coarsening routine

Here we encounter a major difficulty. On the finest grid, the right hand side f represents the flow balance in the dashed cell around $P(i,j)$ (see figures 4.11). And therefore a good representation of the flow is needed on the coarse grids. For the pressure, the Alcouffe representation was a good choice but for the film height, the following one is more appropriate because it corresponds to an exact representation of the Couette flow around $P_c(i,j)$.

On the fine grid, we have $Lu(P, Hoil) = f$ and on the next coarse grid $Lu_c(P, Hoil) = f_c$, with f_c computed as follows in the non pressurized zone:

$$f_c(i,j) = Lu_c(P_c, Hoil_c, i, j) + (0.25(rnw + rne + rsw + rse) + 0.5(rw + re + rs + rn) + rc)$$

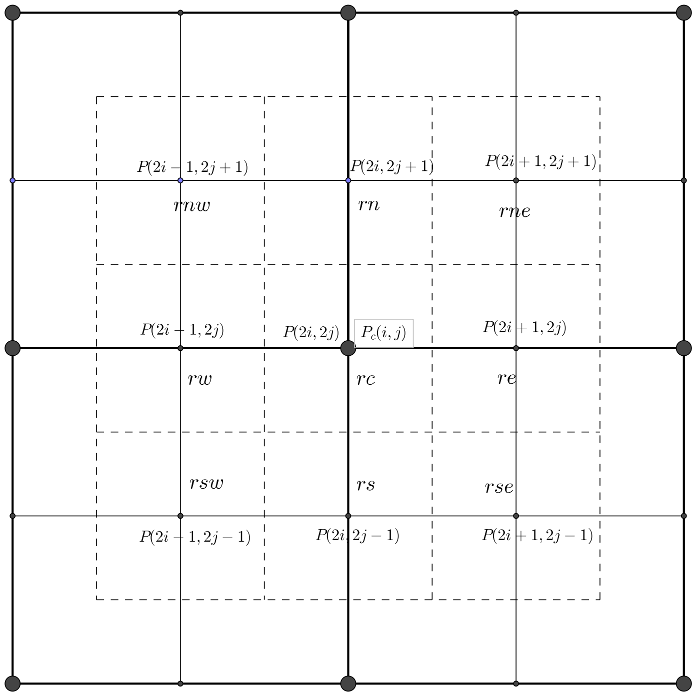

Figure 4.11: Coarse cell and associated fine cells

with

$$
\begin{aligned}
rnw &= f(2i-1,2j+1) - Lu(P,Hoil,2i-1,2j+1)\\
rne &= f(2i+1,2j+1) - Lu(P,Hoil,2i+1,2j+1)\\
rsw &= f(2i-1,2j-1) - Lu(P,Hoil,2i-1,2j-1)\\
rse &= f(2i+1,2j-1) - Lu(P,Hoil,2i+1,2j-1)\\
rn &= f(2i,2j+1) - Lu(P,Hoil,2i,2j+1)\\
rs &= f(2i,2j-1) - Lu(P,Hoil,2i,2j-1)\\
rw &= f(2i-1,2j) - Lu(P,Hoil,2i-1,2j)\\
re &= f(2i+1,2j) - Lu(P,Hoil,2i+1,2j)\\
rc &= f(2i,2j) - Lu(P,Hoil,2i,2j)
\end{aligned}
$$

Note that because of the coarse grid definition of $Hoil$, in the non pressurized zone we could take $F_c = 0$ because it is an exact description of the coarse Couette flow.
For the pressurized zone, the coefficients that are used for the fine grid cell residuals contributing to the coarse grid residual at (i,j) are the Alcouffe coefficients. In the parts between cavitation and pressure, we choose one coefficient or the other according to whether the fine grid corresponding pressure is 0 or not. But this is not satisfactory. It was not found how to precisely represent the 2 flows on the coarse grid.

4.7.4 Results

The single grid algorithm converges. For the periodic case, the multigrid algorithm converges in the completely starved case but in the general case it does not work.

4.8 Conclusion

The convergence was not always satisfactory and sometimes very far from the expected convergence of a multigrid code. Of course this may be partly due to the fact that nothing special was done to localize the free boundaries more rapidly which is always a difficult task in multigrid. With Alcouffe's ideas we are however able to get mass conserving codes that can deal with a rough geometry. It was noticed that the most crucial difficulties are located at the oil film formation or re-formation boundary. The fact that the pressure P and the film height $Hoil$ are not calculated at the same point may be a difficulty that is hard to overcome in multigrid in the presence of free boundaries. We have not been able to include the oil film in the left hand side of the equation of the code previously developed. The different treatments of the oil film and of the pressure are difficult to combine in order to have a good representation of the flow on coarser grids. In order to solve this problem, or at least better understand it, and because with partially starved condition the worst convergence is obtained with a smooth surface, it was decided to consider a simpler problem. Many attempts were tried and not all successful. A multigrid 1D code was written that works. It was transformed into a 2D code that still works without the Y-Flow but its performance diminishes a little when considering the Y-flow. This work is presented in Appendix C. The treatment of $P - \theta$ proposed in [36] could be a solution to this.
However, the code we have obtained and presented in this chapter can be used to study the influence on dimples on parallel surfaces in the hydrodynamic lubrication regime. This is the subject of the next chapter.

Chapter 5

Dimple influence for parallel surfaces.

Contents

5.1 Introduction

The flow conserving algorithm, explained in chapter 4, is used to study hydrodynamic lubrication of textured parallel surfaces and henceforth to study the flat ring in the PRLC contact.

The use of textured surfaces to improve contact performance is of great importance for lubricated contacts. In the case of parallel surfaces without texture, no load carrying capacity is generated. Texture can be used to create the equivalent of a Raleigh step bearing to generate pressure. Hence, the texture parameters (size, density, texture position) have to be chosen in order to optimize the load carrying capacity and minimize the friction. Besides, the texture can reduce fluid leakage and can act as a fluid reservoir. Micro oil pockets can also trap wear debris. It is also possible that they allow to avoid abnormal temperature rises due to dry contact.
Early research on this topic has been conducted by Etsion, Kligerman, Halperin, Brizmer

(see for instance [38], [39], [40], [41], [42], [43]). They performed many experimental and also analytical investigations and have shown the benefits of surface texturing for the enhancement of lubrication and in particular the benefits of partial texturing for piston rings. In particular in [40] for a simplified model, the distribution of the local pressure was shown in the case of partial texturing in the inlet and in the case of full texturing. They observed that the pressure peak at the dimple exit is higher and higher while moving in the sliding direction. The maximum pressure is obtained at the exit of the last dimple in the X-direction. In the case of full texturing, at each dimple exit, the rise in pressure is the same and they analyze the optimum texturing density to maximize the load carrying capacity for parallel thrust bearings. Tonder (see for instance [44]) introduced the idea that performance improvement can be gained by introducing artificial roughness in the inlet of the contact by means of micro-structures instead of macro-structures, inducing in particular low coefficients of friction coexisting with high hydrodynamic stiffness and damping parameters. Wakuda et al. in [45] experimentally analyses the friction reduction due to surface texturing between ceramic and steel materials, using a pin-on-disk tester and highlight the importance of texturing for friction reduction. The benefits remain even under severe friction conditions and they give some recommendations on the parameter choice. A recent experimental study by Vladescu et al. [46] analyses the influence of texturing in reciprocating contacts for various lubrication regimes. To achieve this, they have built a set up that simulates an automotive piston ring-liner contact. According to the lubrication regime the conclusions are not the same. Surface texture just after reversal helps to build the film and reduces friction. It is better to have texture pockets entirely lying inside the contact zone and no pocket should be at the reversal point. Another recent experimental study of Lu et al. [47] for reciprocating sliding line contacts studies the effects of surface texturing by square dimples in various lubrication regimes. They note a lower friction coefficient in the boundary regime, due to the fact that the dimples act as lubricant reservoirs. They observe that textures at the reversal point can help reducing friction, this is contrary to [46].

Many one-dimensional analytical or numerical studies were conducted to analyze the influence of various parameters using a simpler problem. Using a one-dimensional model Tomanik [48] investigated the influence of laser textured profiles for cylinder bore and rings and particularly on the oil control ring. Fowell et al., in [49], explain the inlet suction phenomenon on a 1D analytical model. In [50] Fowell et al. use a 1D mass conserving numerical model to study the influence of the texture parameters such as texture density, texture location, texture height according to the convergence ratio of the two main surfaces on load support and friction. Pascovci et al. [51] also perform a 1D analysis without cavitation to optimize the texture parameters for parallel sliders and make a comparison with Raleigh step bearings. Rahmani et al. [52] also use an analytical solution of the one dimensional Reynolds equation to optimize micro dimple texture for parallel thrust bearings. They present results to optimize the load carrying capacity and minimize the friction coefficient.

Some numerical results have been questioned because mass-conservation was not always respected. The complex phenomenon of cavitation and film reformation was first studied in the Floberg-Jakobsson-Olsson (JFO) cavitation theory [53, 54]. They considered the mass conservation problem. Elrod and Adams [11], [12] proposed an alternative mass conserving model derived from the Reynolds equation. It was shown by Ausas et al, [34], that it is very important to have a mass-conserving algorithm in order not to underestimate the cavitation area and thus get poor estimates of the pressure. Henceforth the Elrod and Adams model which is mass-conserving has to be considered instead of the simple Reynolds model. Many studies concerning mass-conserving algorithms and their use for textured surfaces can be found in the literature. To study cavitation in dimples, Qiu and Khonsari [37], developped a mass-conservative cavitation multigrid algorithm based on an algorithm developed by Vijayaraghavan and Keith [55], itself based on Elrod's work. Bayada, Martin and Vazquez [31] have developed a mass-conserving algorithm using homogeneization techniques. Using the pressure and the void fraction, Giacoponi et al., [35] developed a mass-conserving complementary formulation of the one-dimensional cavitation problem and Bertocchi et al. [56] extended it to two-dimensional domains and for compressible, piezoviscous and non-Newtonian fluids. They then use finite element methods to numerically solve the problem. Ausas et al. [57] proposed a finite volume implementation of the Elrod-Adams model that is better adapted to the physics of piston ring liner lubrication. An implementation of an element-based finite volume method derived from the $p-\theta$ Elrod-Adams cavitation model model is proposed by Profito et al. [58].

The validity of the Reynolds model was also discussed. Sahlin et al. [59] use a commercial CFD code to solve the Navier-Stokes system for a single micro-groove on one of 2 parallel surfaces. For them, fluid inertia is an important factor for the load carrying capacity. They also show that for deep and wide grooves a vortex occurs that limits the increase in load carrying capacity. Cavitation is not considered. In their sequel, Menon et al. [60] have optimized dimples on one of the 2 parallel surfaces. They decompose their surfaces in repeating cells containing a single dimple, imposing some periodic conditions. They also think that fluid advection is a major factor for generating load carrying capacity and also note the formation of a vortex when the dimple depth approaches its optimum value. Cavitation is not considered. These and other studies in the same vein tend to show that the Reynolds model is not adequate to study those problems. These conclusions were questioned by Dobrica and Fillon. In [61], they study the range of validity of the Reynolds equation also neglecting cavitation. They found that the dimple aspect ratio (dimple depth/dimple width) must be sufficiently small but nevertheless in a range that covers most useful cases and that the Reynolds number must be sufficiently small. They also show that the inertia effects cannot be properly accounted for by using single cell dimple centered textures.

Using a mass-conserving algorithm, Dobrica et al. [21] studied the influence of full and partial texturing for parallel and plane inclined sliders, verifying in particular the benefit of partial texturing in the inlet of the contact and the importance of the cavitation phenomenon to generate load carrying capacity in parallel or nearly parallel structures. They have also shown that the texture parameters can be optimized. Cupillard et al [62, 63] use the full Navier-Stokes equation with a multiphase flow cavitation model to study the performance of a dimple textured journal bearing and analyze the pressure buildup mechanism. They consider the variations in mechanical energy and also the consequence of flow re-circulation when it occurs, according to the dimple positions and size. In [20], Tala-Ighil, Fillon and Maspeyrot analyze the performance of various texture configurations on the performances of a journal bearing. Shen and Khonsari have studied parallel textured surfaces, numerically as well as experimentally. For macroscopic dimples, they studied the influence of the cavitation pressure in steady state lubrication that can experimentally be significantly lower than the ambient pressure and have shown that its choice can influence simulation results [64]. Again, in the case of macroscopic dimples, they have also studied numerically and experimentally the influence of the size and shape of the dimples on the load carrying capacity in hydrodynamic lubrication [65]. They also tried to optimize the texture shape to obtain a maximum load carrying capacity for parallel surfaces [66]. To simplify the calculations, they used the Reynolds equation with a half-Sommerfeld boundary condition, although it is not mass-conserving, and a sequential quadratic programming method. In [67], they experimentally and numerically investigate new texture designs to improve piston ring lubrication. They used lasered pockets with special shape and specific distribution on the piston rings (mesoscopic scale). Gherca et al. [68, 69] have recently developed a mass-conserving algorithm that enables them to study the influence of surface texturing in steady-state but also transient hydrodynamic lubrication of parallel sliders. Another study of transient effects using a mass-conserving solver deduced from [35] for reciprocating textured bearing can be found in [70]. But this last work is only 1D.

The multigrid flow-conserving algorithm based on Alcouffe's paper and presented in chapter 4 does not show full multigrid efficiency. This is probably due to the discontinuities of Poiseuille and Couette flow which were not well accounted for when the pressure builds up again. However, it converges sufficiently fast and is flow conserving. It can therefore be used to study and discuss dimple textured parallel surfaces, even with deep dimples. Woloszynski, Podsiadlo and Stachowiak [36], have reformulated the complementary constraint on $p.\theta = 0, p \geq 0, \theta \geq 0$ by a continuous differentiable system $F(p, \theta) = 0$ to which Newton's method can be efficiently applied and this way they obtain a new solver for the cavitation problem. The code in use here might be improved using their formulation.

5.2 Problem formulation

5.2.1 Mass complementary formulation

The hydrodynamic lubrication of the piston ring-cylinder liner contact can be described by the Reynolds equation. According to Elrod, because of cavitation and in order to have a mass conserving algorithm, the following complementary problem is solved:

$$\frac{\partial}{\partial x}\left(\frac{\rho h^3}{12\eta}\frac{\partial p}{\partial x}\right) + \frac{\partial}{\partial y}\left(\frac{\rho h^3}{12\eta}\frac{\partial p}{\partial y}\right) - u_m\frac{\partial(\rho\theta h)}{\partial x} - \frac{\partial(\rho\theta h)}{\partial t} = 0 \tag{5.1}$$

with

$$(p > p_{cav} \quad \text{and} \quad \theta = 1) \quad \text{or} \quad (p = p_{cav} \quad \text{and} \quad 0 < \theta < 1) \tag{5.2}$$

Where p is the hydrodynamic pressure, h, the geometry, u_m the mean velocity. The lubricant density, ρ and the viscosity, η can be considered constant in the studied regime. Considering $p - p_{cav}$ instead of p, it is assumed that the cavitation pressure p_{cav} is 0. This problem will be solved on a square domain Ω and the pressure on the boundaries is the ambient pressure denoted p_{amb} or rather $p_{amb} - p_{cav}$. Here the generated pressures are not very high because the considered surfaces are mainly parallel. Therefore the difference between the ambient pressure and the cavitation pressure is significant. No pressure would be generated if it were assumed that p_{cav} and p_{amb} are identical as previously done. Indeed, in that case, the solution to our problem would be $p = p_{amb} = p_{cav}$. The pressure would not be able to decrease when entering the dimple and no extra oil would flow inside the dimple. In the cavitated area the fluid becomes a mixture of liquid, vapor and gas and $\theta\rho$ can be viewed as the lubricant density. Here we prefer to consider the variable $h_{oil} = \theta h$, that represents the fluid level or an equivalent of the fluid level in the whole domain $\Omega = [-x_0, x_0] \times [y_0, y_0]$. Hence $h_{oil} = h$ in the pressurized regions and lies between 0 and the geometry h elsewhere. In this section only the stationary case is considered and therefore, we solve the following problem:

$$\frac{\partial}{\partial x}(\frac{\rho h^3}{12\eta}\frac{\partial p}{\partial x}) + \frac{\partial}{\partial y}(\frac{\rho h^3}{12\eta}\frac{\partial p}{\partial y}) - u_m\frac{\partial(\rho h_{oil})}{\partial x} = 0 \tag{5.3}$$

with

$$(p > 0 \quad \text{and} \quad h_{oil} = h) \quad \text{or} \quad (p = 0 \quad \text{and} \quad 0 < h_{oil} < h) \tag{5.4a}$$

$$p = p_{amb} \quad \text{on} \quad \partial\Omega \tag{5.4b}$$

In what follows the fluid will be considered to flow between two parallel surfaces of constant gap h_0. One of the 2 surfaces will be indented by circular dimples of radius r and depth a. For a single dimple, the cross section of the two surfaces by a plane passing through the middle of the dimple is sketched in figure C.1. The geometry h is defined as follows:

$$h(x, y) = h_0 + \phi(x, y)$$

with

$$\phi(x, y) = \frac{a}{2}(1 + \cos(\frac{\pi}{r}\sqrt{(x - x_i)^2 + (y - y_i)^2}))$$

if there is a dimple of depth a centered at (x_i, y_i) and if $(x - x_i)^2 + (y - y_i)^2 \leq r^2$ and $\phi(x, y) = 0$ otherwise.

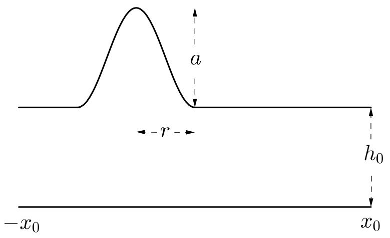

Figure 5.1: Geometry: cross section through the middle of a dimple.

5.2.2 Dimensionless equations

The dimensionless parameters are chosen as follows:
Dimensionless coordinates: $X = x/\lambda$, $Y = y/\lambda$ and the dimensionless radius $R = r/\lambda$ where λ is a reference length. It could be $\lambda = x_0$ or $\lambda = r$.

Dimensionless geometry and film height: $H(X,Y) = h(x,y)/h_0$, $H_{oil}(X,Y) = h_{oil}(x,y)/h_0$.
Dimensionless pressure: $P(X,Y) = p(x,y)/p_0$ with $p_0 = \dfrac{12\eta u_m \lambda}{h_0^2}$.
Dimensionless indent depth: $A = \dfrac{a}{h_0}$.
Dimensionless distance between dimples: $D = d/\lambda$.

With these dimensionless variables the dimensionless Reynolds equation reads:

$$\frac{\partial}{\partial X}(H^3\frac{\partial P}{\partial X}) + \frac{\partial}{\partial Y}(H^3\frac{\partial P}{\partial Y}) - \frac{\partial (H_{oil})}{\partial X} = 0 \tag{5.5}$$

with the following dimensionless complementary and boundary conditions:

$$(P > 0 \quad \text{and} \quad H_{oil} = H) \quad \text{or} \quad (P = 0 \quad \text{and} \quad 0 < H_{oil} < H) \tag{5.6a}$$

$$P = P_{amb} \quad \text{on} \quad \partial\Omega \quad \text{with} \quad \Omega = [-X_0, X_0] \times [-Y_0, Y_0] \tag{5.6b}$$

and

$$H(X,Y) = 1 + \Phi(X,Y)$$

with

$$\Phi(X,Y) = \frac{A}{2}(1 + \cos(\frac{\pi}{R}\sqrt{(X - X_i)^2 + (Y - Y_i)^2})) \tag{5.7}$$

if there is a dimple of depth A centered at (X_i, Y_i) and if $(X - X_i)^2 + (Y - Y_i)^2 \leq R^2$ and $\Phi(X,Y) = 0$ otherwise.
Examples of possible dimensional and associated dimensionless values can be found in Section B.2 of Appendix B.

5.2.3 Generated pressure and oil film

In this section some figures of the pressure and oil film obtained for several dimple configurations are shown. In the chosen examples $P_{amb} = 0.01$.
Figure 5.2 shows the results for a single dimple of depth $A = 1$ and radius $R = 1$ in the domain $\Omega = [-4, 4] \times [-4, 4]$ whose center is located at $(X_i, Y_i) = (-2, 0)$. The geometry is given by the first figure the dimple is located at the center of the first half of the domain. The resulting pressure is given in the third figure. It rapidly decreases towards the cavitation pressure inside the dimple and then at the dimple exit which corresponds to the convergent part of the surfaces, it grows very rapidly to reach its maximum value. On the second figure the oil level is given. In the cavitation zone the representation is not adequate since, in reality, there is a mixture of gas oil and vapor. We have decided to represent an equivalent oil level. The oil flow inside the dimple before cavitation can be viewed. Inside the cavitation zone it remains constant in the X-direction. At the exit of the dimple, where the film reforms, a discontinuity can be observed. The full film zone inside the dimple is narrow around the dimple edges. Figure 5.4 shows the geometry, the oil level and the pressure for a set of nine dimples of depth $A = 1$ and radius $R = 1$ in the domain $\Omega = [-10, 10] \times [-10, 10]$ whose center is located at $(X_i, Y_i) = (-2, 0)$. The dimple pattern is shown in Figure 5.3. In each dimple the pressure shows the same behavior as

in a single dimple but at the exit of the first 2 rows of dimples the pressure does not reach very high values since rapidly it will decrease towards cavitation because of the next row of dimples. The maximum pressure is reached at the exit of the last row of dimples because afterwards no cavitation occurs. Here the limitation is mainly given by the exit boundary condition and therefore depends on the distance to the contact exit. Related results can be seen on the oil film. The last row of dimples is the fullest of the three.

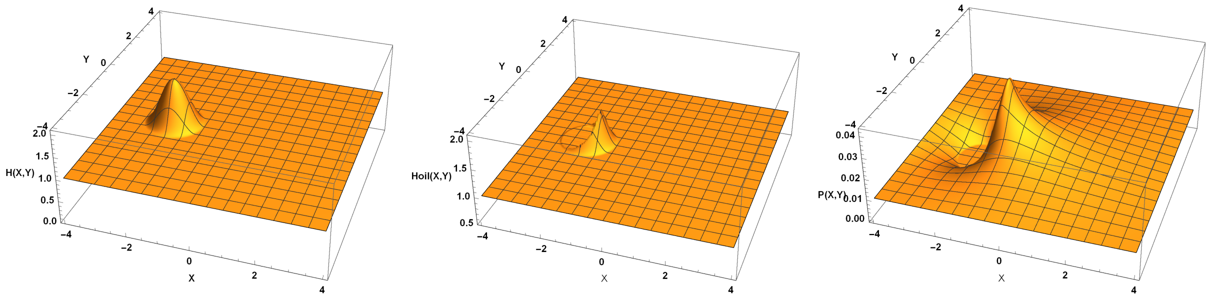

(a) (b) (c)

Figure 5.2: Pressure and oil film generated on $[-4,4] \times [-4,4]$ by a single dimple of depth 1 centered at $(-2,0)$. (a) Geometry, (b) Film height, (c) Pressure.

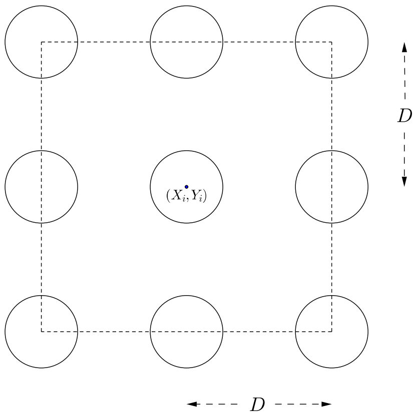

Figure 5.3: Nine dimple pattern

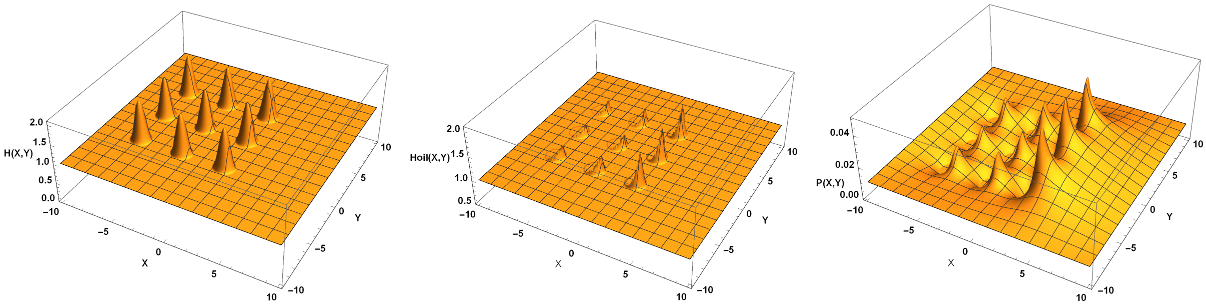

(a) (b) (c)

Figure 5.4: Pressure and oil film generated on $[-10,10]\times[-10,10]$ by a pattern of 9 dimples of depth 1 and spaced by $D = 4$ centered at $(-2,0)$. (a) Geometry (b) Film height (c) Pressure.

5.3 Load carrying capacity

5.3.1 Partial texturing and load carrying capacity

The load carrying capacity is defined as:

$$LCC = \int_{\Omega} (P - P_{amb})\, dX\, dY.$$

When the dimples are near the inlet, the load carrying capacity is positive and then it becomes negative as noticed by many authors. Considering a single dimple, it may be noted that the pressure will first decrease. This decrease will be limited by the cavitation pressure. To conserve the flow, oil must enter the dimple, the "inlet suction" phenomenon. Afterwards, in the convergent part of the dimple, the pressure will rise again starting from a point defined by the extra oil inside the dimple and then it will decrease to reach the ambient pressure at the contact exit. If the dimple is situated near the entrance of the contact, the zone where the pressure is less than the ambient pressure is limited and if it is located near the exit, the zone where it is above the ambient pressure is more limited. Besides, in case of cavitation, the pressure is not anti-symmetric with respect to P_{amb} and if P_{max} denotes the maximum pressure, $P_{max} - P_{amb}$ is usually higher than $P_{amb} - P_{cav}$. This is illustrated in figure 5.5 where the left figure shows the part of the pressure above P_{amb} while the right one shows the part of the pressure below the ambient pressure. In the second figure, to highlight the zone where the pressure is less that the ambient pressure, we have plotted $-P$ and $-Pamb$.

If the texture symmetrically covers the domain the generated load carrying capacity becomes zero in case of no cavitation and negative otherwise. Hence partial texturing is needed to induce a positive load. To illustrate this, rows of three dimples of depth 1 spaced by 4 centered at $X_i = -18, Y_i = 0$, then $X_i = -16, Y_i = 0$, then $X_i = -14, Y_i = 0$, etc... up to $X_i = 18, Y_i = 0$ where they cover the whole domain $\Omega = [-20,20]\times[-20,20]$ in the X-direction were progressively added and the generated load was computed. The pressure distribution can be viewed in figure 5.6. It can be noticed that at the exit of each row the pressure progressively increases except on the last figure where the whole range of values in X is covered. The largest

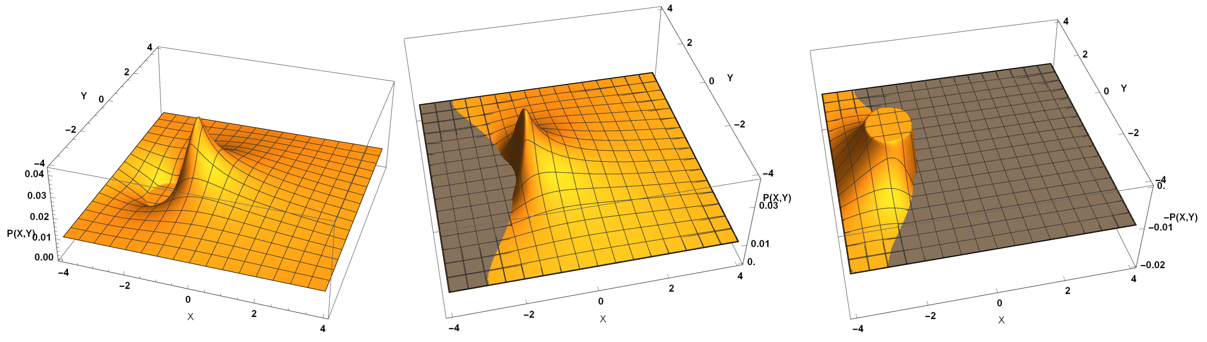

(a) (b) (c)

Figure 5.5: (a) Pressure generated on $[-4,4] \times [-4,4]$ by a single dimple of depth 1 centered at $(-2,0)$. (b) Part above the ambient pressure (c) Part below the ambient pressure (Here $-P$ and $-P_{amb}$ are plotted).

pressures are obtained on the last row of dimples when the dimples remain in the first part of the domain. The load carrying capacity in terms of the number, N, of dimple rows is shown in figure 5.7. The maximum load carrying capacity is obtained with 3 rows of dimples in the inlet of the contact. When adding more rows it rapidly decreases to reach a negative value when the entire domain is covered. When rows are added at the end of the contact, there is always a loss in LCC. The variations in LCC are more limited than when rows are added in the inlet. The behavior of the maximum pressure is also quite different. Considering the different behaviors of the load carrying capacity and of the maximum pressure according to whether the inlet or the outlet is textured (see figures 5.6, 5.7, 5.8), it can be noticed that the loss of load carrying capacity when the outlet is textured is lower than the gain when the inlet is textured. The maximum pressure is much higher if the inlet is textured rather than the outlet and its variations are also less important. For a one-dimensional simple model, Fowell et al. [49] show that $P_{max} \approx P_{amb} L/\Delta$ where L is the contact length and Δ, the distance of the pocket to the inlet. Here it seems that a similar trend can be observed.

Henceforth it may be worth for reciprocating contacts to have partial texture at both ends of the contact. This type of partial texturing for piston ring was experimentally tested by Ryk and Etsion [71] and Etsion and Sher [72]. Tomanik [48] also investigated that kind of partial texturing but using a 1D code without mass-conservation. In 2016, Shen and Khonsari [67] have also conducted experimental as well as numerical studies with a mass-conserving algorithm and for transient lubrication effects on the effects of different positions of pockets (rather patches of micro-dimples) in the inlet and in the outlet for a flat piston ring. Tala-Ighil, Fillon and Maspeyrot [20] have also tested various configurations of patches of dimples but for a hydrodynamic journal bearing. As can be seen in figure 5.9, a positive load carrying capacity is always generated. Its value is indicated in each case on the corresponding image of the pressure distribution. On our example the maximum load carrying capacity is obtained for two rows of indents at both ends.

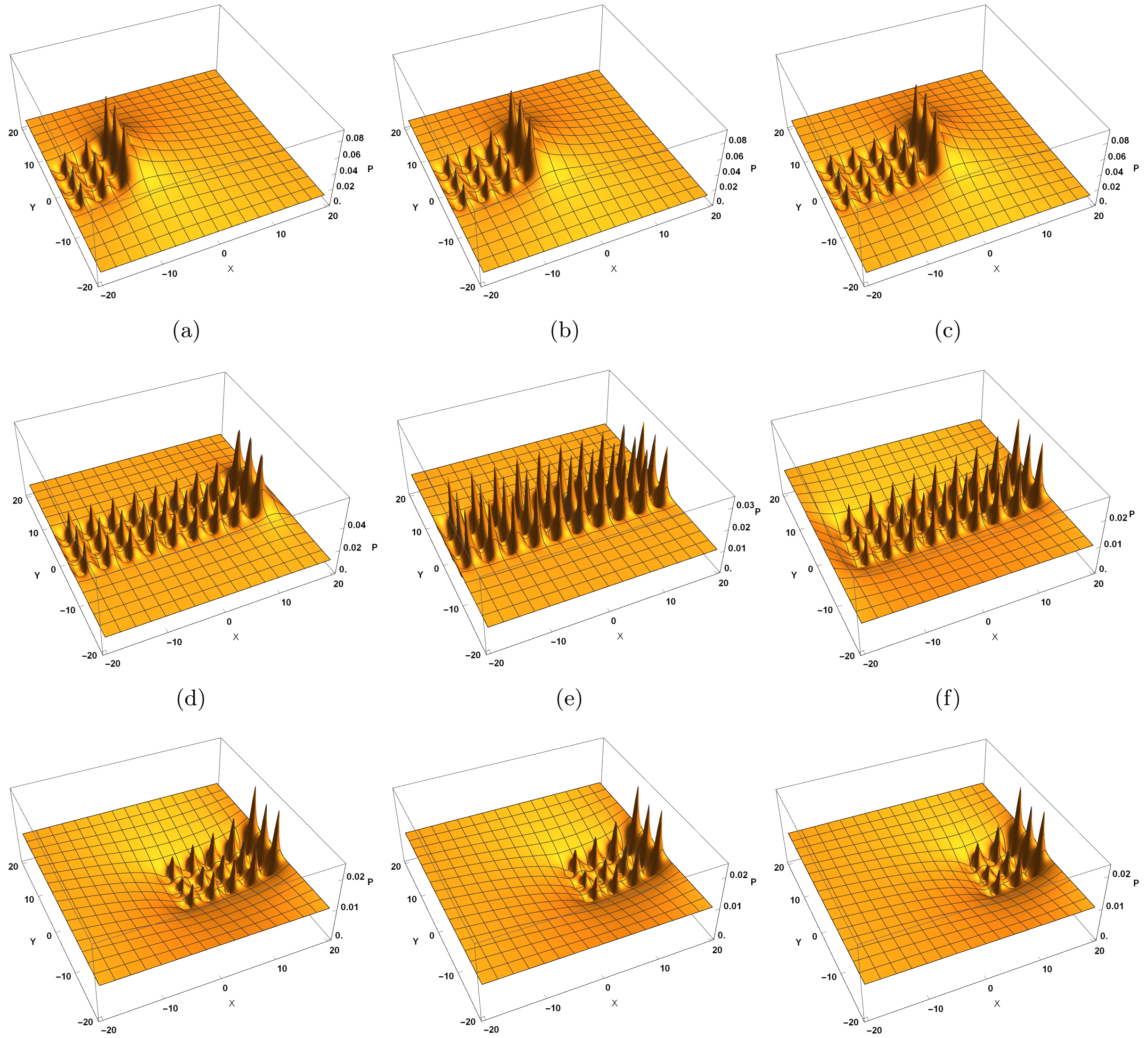

(a) (b) (c)

(d) (e) (f)

(g) (h) (i)

Figure 5.6: Pressure generated on $[-20, 20] \times [-20, 20]$ according to the number of rows of 3 dimples of depth 1 in the inlet or in the outlet. (a) 3 rows in the inlet (b) 4 rows in the inlet (c) 5 rows in the inlet (d) 9 rows in the inlet (e) 10 rows (f) 9 rows in the outlet (g) 5 rows in the outlet (h) 4 rows in the outlet (i) 3 rows in the outlet.

The maximum pressure is obtained at the exit of the last row of indents in the inlet. It will reach a sufficiently high value if the distance between the 2 sets of dimples is large enough and if the inlet set of dimples lies sufficiently near the inlet inducing a total positive load carrying capacity.

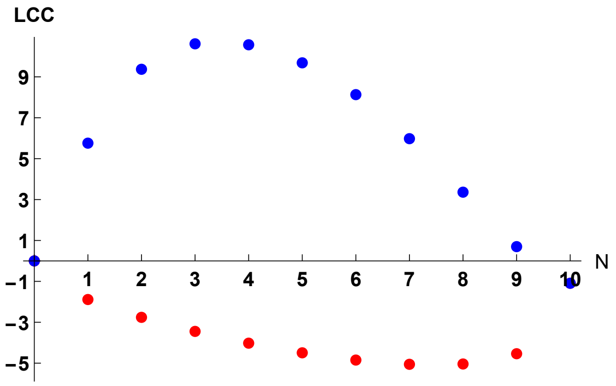

Figure 5.7: Load carrying capacity in terms of the number N of rows of three dimples of depth 1 spaced by $D = 4$ on $\Omega = [-20, 20] \times [-20, 20]$. In blue the first row is located at $(-18, 0)$, in red the last row is located at $(18, 0)$.

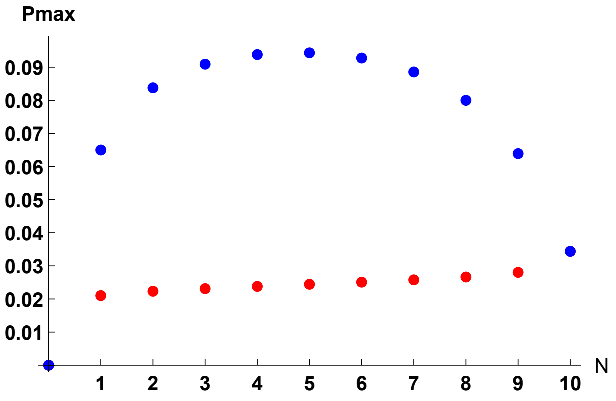

Figure 5.8: Maximum pressure in terms of the number N of rows of three dimples of depth 1 spaced by $D = 4$ on $\Omega = [-20, 20] \times [-20, 20]$. In blue, the first row is located at $(-18, 0)$, in red, the last row is located at $(18, 0)$.

5.3.2 Load carrying capacity in terms of the texture location

The behavior of the load carrying capacity in terms of the position of the set of dimples along the line $Y = 0$ is now studied. In the figure 5.10, the results are shown for $\Omega = [-10, 10] \times [-10, 10]$ and for $\Omega = [-20, 20] \times [-20, 20]$ for a pattern of nine dimples of radius 1, depth 1 and equally spaced by 4. The load carrying capacity becomes negative when the texture approaches the middle of the contact. A linear behavior is observed in the center of the domain although this is less clear on the smaller domain, but in this case the domain is not large enough to ensure that no dimple is close to the inlet or the outlet of the contact. Close to the boundaries and especially near the inlet, the dimple influence becomes non linear. When plotting the curves on the same figure 5.11, they superimpose when the abscissa X_i of the center of the texture is greater than -2. A homothety of ratio 2, corresponding to the ratio between the dimensions of the 2 domains, allows a rather good superposition of the two sets of points. This can be explained by the chosen dimensionless parameters: to fit the domain the parameter λ that is used is modified by the ratio

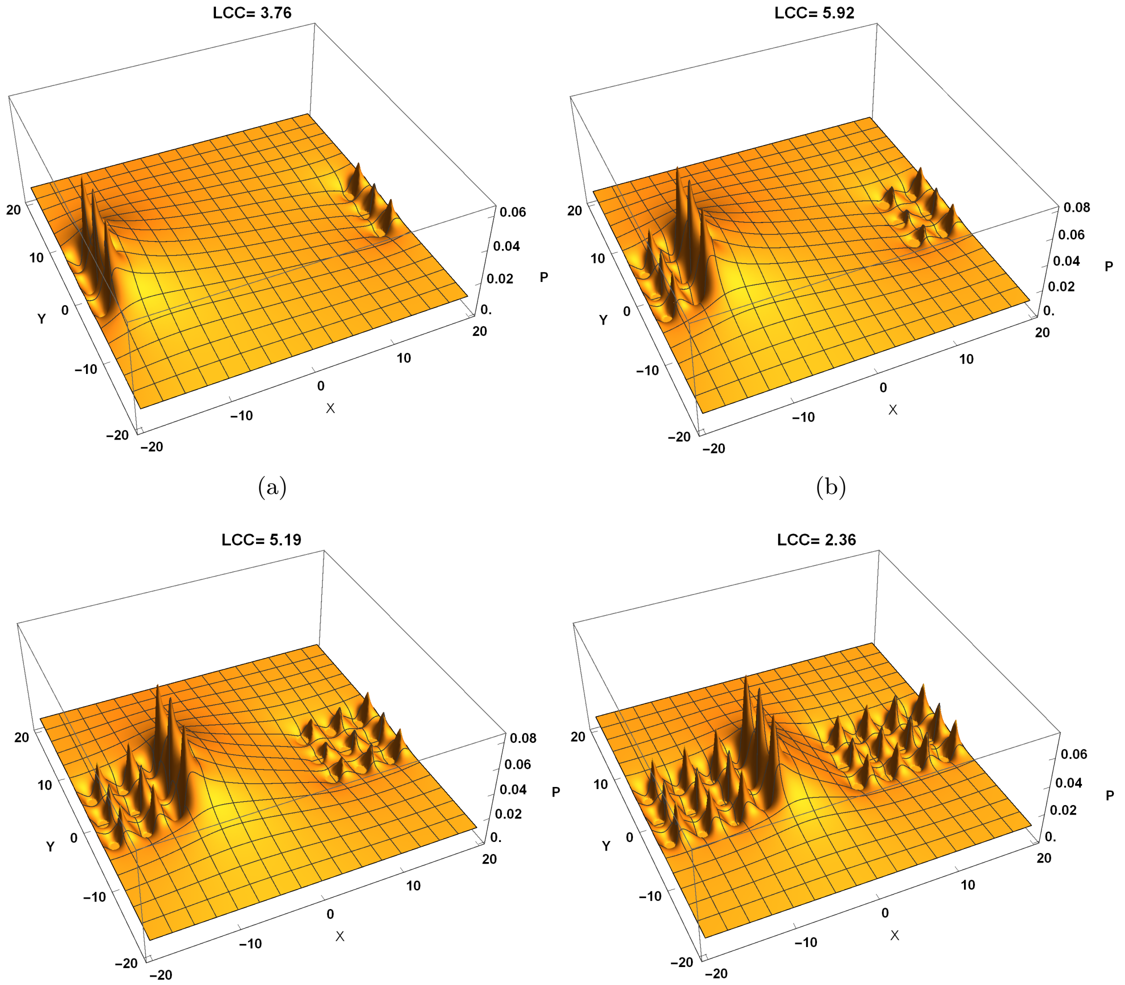

(a) (b) (c) (d)

Figure 5.9: Pressure generated on $[-20, 20] \times [-20, 20]$ with N rows of 3 dimples of depth 1 spaced by 4 at both ends, $P_{amb} = 0.01$.(a) $N = 1$ (b) $N = 2$ (c) $N = 3$ (d) $N = 4$.

of the domain dimensions. It can be observed that when the pattern lies near the center of Ω, the maximum pressure P_{max} is rather similar in both cases. If we now consider P_{max} as a function f_1 of X_i on $[-20, 20] \times [-20, 20]$ and as a function f_2 of $2X_i$ on $[-10, 10] \times [-10, 10]$, the slope of the second function is roughly twice the slope of the first one (see figure 5.12). Again this can be explained by the choice of the dimensionless parameters. The maximum pressure and the extent of the outlet induce the positive part in the load carrying capacity while the cavitation pressure, which is the same in all cases and the extent of the inlet zone determine the negative part.

Finally, an image of the load carrying capacity for a square pattern of 25 dimples of radius 1, depth 1 equally spaced by 4 on $\Omega = [-30, 30] \times [-30, 30]$ is given in figure 5.13. Except at the

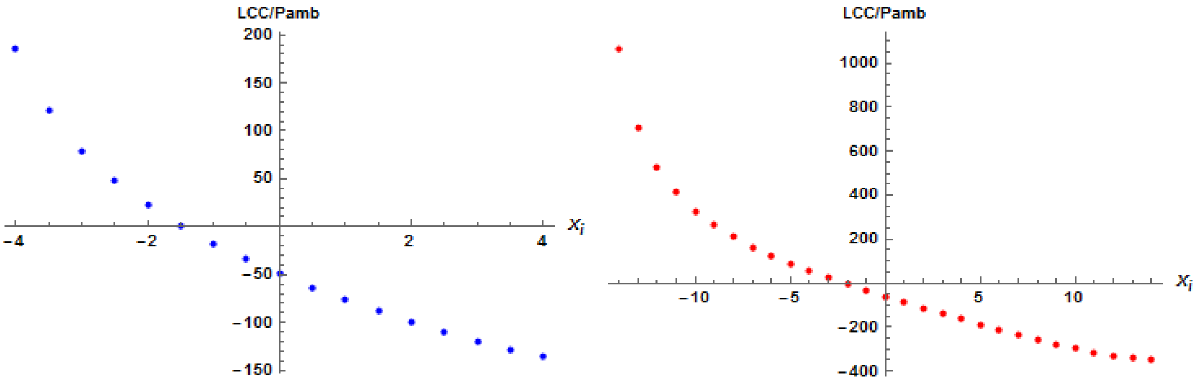

(a) (b)

Figure 5.10: Load carrying capacity generated on Ω by a pattern of nine dimples of depth 1 spaced by 4 as a function of the position of the centre of the pattern on the line $Y = 0$.(a) $\Omega = [-10, 10] \times [-10, 10]$ (b) $\Omega = [-20, 20] \times [-20, 20]$.

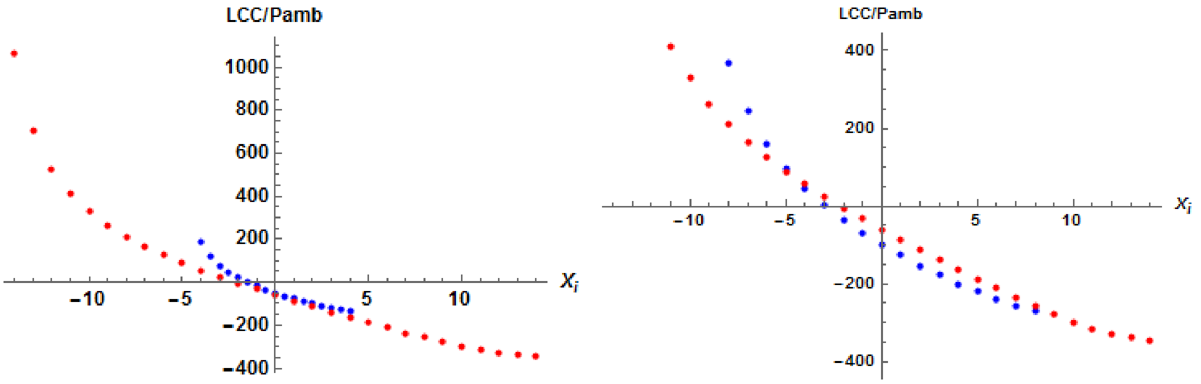

(a) (b)

Figure 5.11: Load carrying capacity generated by a pattern of nine dimples of depth 1 spaced by 4 as a function of the position of the center of the pattern on the line $Y = 0$, on $\Omega = [-10, 10] \times [-10, 10]$ in blue and on $\Omega = [-20, 20] \times [-20, 20]$ in red.(a) the obtained LCC (b) after an homothety of ratio 2 of the results on $\Omega = [-10, 10] \times [-10, 10]$.

beginning of the contact, a linear behavior is again observed. Perhaps it is possible to view the pattern as a single local texture whose influence on the load carrying capacity only depends on its vicinity to the inlet or the outlet of the contact. In the next section, the influence of a dimple pattern will be compared to the one of a single dimple of same volume.

5.3.3 Homogenization

Choosing $\Omega = [-10, 10] \times [-10, 10]$, we tried to replace the previously pattern of nine dimples by a single dimple of same volume or by a square dimple of same volume. The volume of the

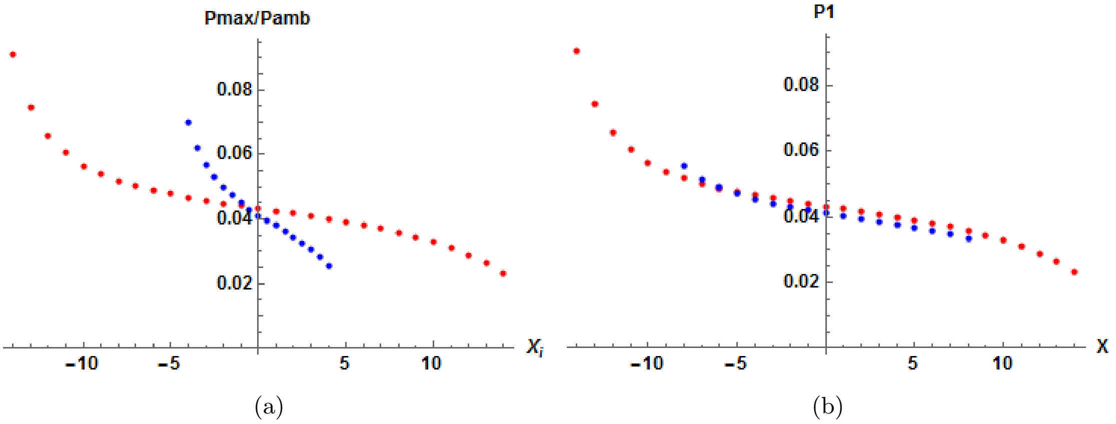

(a) (b)

Figure 5.12: Maximum pressure generated by a pattern of nine dimples of depth 1 spaced by 4 as a function of the position X_i of the center of the pattern on the line $Y = 0$, $\Omega = [-10, 10] \times [-10, 10]$ in blue, $\Omega = [-20, 20] \times [-20, 20]$ in red. (a) Both curves on the same figure, (b) $\Omega = [-20, 20] \times [-20, 20], P_1 = P_{max}/P_{amb}, X = X_i$; $\Omega = [-10, 10] \times [-10, 10], P_1 = Q(0) + 0.5(Q - Q(0))$ with $Q = P_{max}//P_{amb}$, $X = 2X_i$.

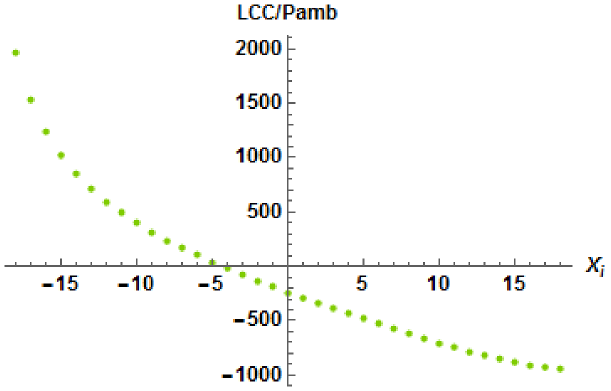

Figure 5.13: Load carrying capacity generated by a pattern made of 5 rows of 5 dimples of depth 1 spaced by 4 as a function of the position of the center of the pattern on the line $Y = 0$, on $\Omega = [-30, 30] \times [-30, 30]$.

chosen dimples (see equation 5.7) of radius R and depth A is given by

$$Vol = AR^2(\frac{\pi}{2} - \frac{2}{\pi}). \tag{5.8}$$

Therefore a dimple of depth 1 and radius 3 was first considered. The curves showing the load carrying capacity do not coincide very well (figure 5.14). For the same position on the X-axis, the geometric variation takes place much farther from the inlet than for the nine dimple pattern. We then tried a single square dimple of same volume and same center as the nine dimples. We had 2 obvious choices for that square: a 10 × 10 square corresponding to the smallest square containing all dimples or a 8 × 8 square passing through the centers of the external dimples. Both were tried and results are shown in figure 5.14. The square of size 10 is the best choice in the inlet while the other square is better in the outlet. Similar trends as for step bearings are observed.

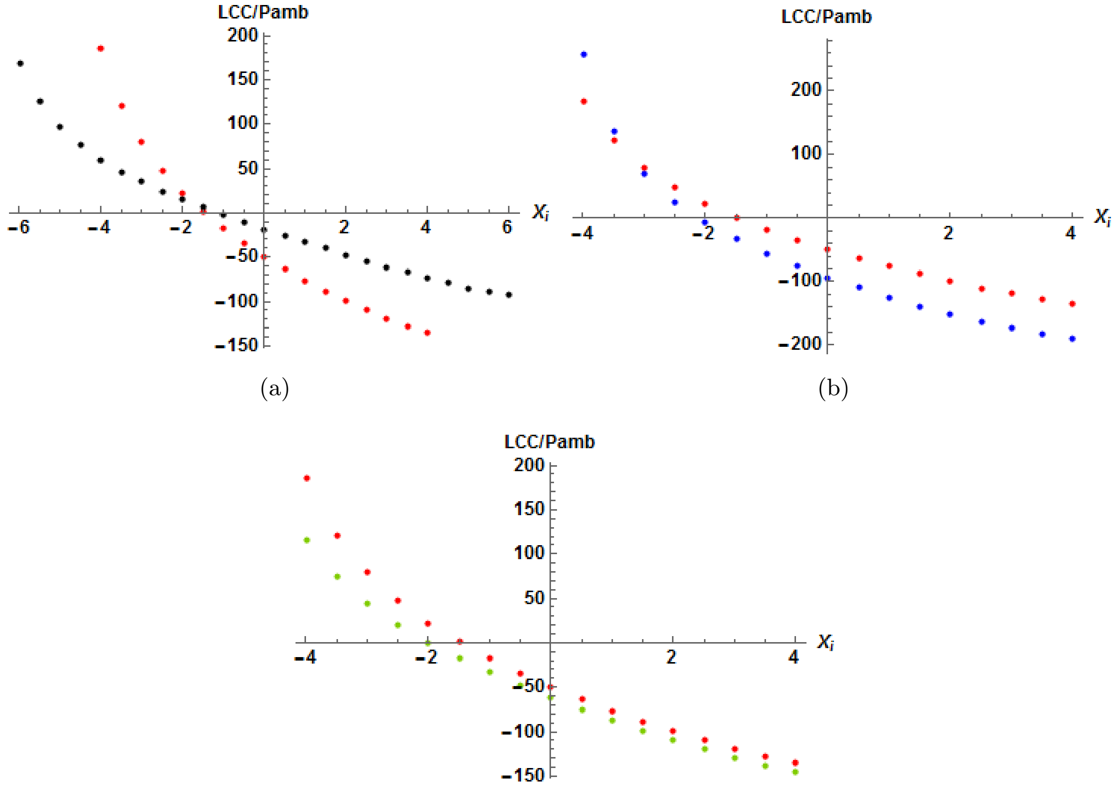

(a) (b)

(c)

Figure 5.14: Load carrying capacity of a single dimple of identical volume as the nine indent pattern compared with the load carrying capacity (in red) of the pattern of nine dimples of depth 1 spaced by 4 on $\Omega = [-10, 10] \times [-10, 10]$, (a) a single dimple of radius 3 and depth 1, (b) a square dimple of size 10, (c) a square dimple of size 8.

5.3.4 Load carrying capacity for a single dimple in terms of the dimple location

For a single dimple, the behavior of the load carrying capacity, presents the same trends as with pattern of dimples. As in section 5.3.2, it can be seen in figure 5.15, that outside the inlet region, the load carrying capacity as a function of the dimple position has a linear behavior. No matter the domain size, the curves overlap in their linear part. Because of the chosen dimensionless parameters, they can be fitted with homotheties of ratio equal to the ratio of the domain sizes.

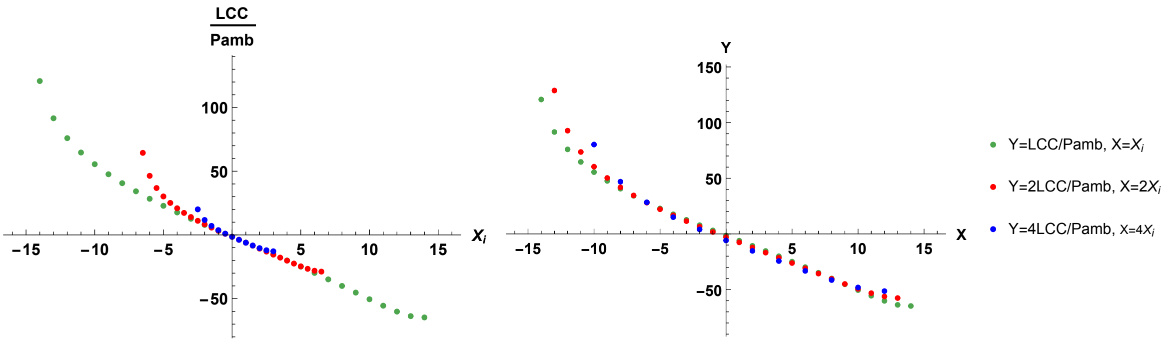

(a) (b)

Figure 5.15: Load carrying capacity generated by a single dimple of depth 1 as a function of the position of the center of the pattern on the line $Y = 0$, on $\Omega = [-4, 4] \times [-4, 4]$ in blue, on $\Omega = [-8, 8] \times [-8, 8]$ in red and on $\Omega = [-16, 16] \times [-16, 16]$ in green.(a) All curves on the same figure, (b) after fitting the 3 curves with homotheties.

5.4 Influence of the different parameters

Since the load carrying capacity trend using a single dimple does not differ substantially from those obtained with a pattern of dimples, an analysis of the LCC and, in particular, an analysis of the influence of the different parameters (depth, radius or domain size, P_{amb} will be conducted considering a single dimple.

5.4.1 One dimple at the center of the domain

The load carrying capacity was computed for various values of P_{amb}, depths A and radii R for a centered dimple. In this case the load is always negative. As shown in Figure 5.16, for small depths no cavitation occurs because the geometry does not decrease sufficiently for the pressure to drop below the cavitation pressure. When P_{amb} is large enough (0.02 or 0.05), for deep dimples no cavitation occurs either (see Figure 5.17). When no cavitation occurs, for a dimple at the center of the domain, $P - P_{amb}$ is anti-symmetric and the load carrying capacity vanishes. For very deep dimples, the H^3 coefficient becomes huge. Thus to conserve the flow the variation of pressure becomes small and when the dimple is deep enough, it does not reach the cavitation pressure in the divergent part of the dimple and no cavitation occurs. Besides for larger values of P_{amb}, in the contact inlet the pressure drop is not sufficient to reach P_{cav} and no cavitation occurs. It can be observed that for larger radii this phenomenon occurs for deeper grooves or higher values of P_{amb}. It should be remembered that P_{amb} in fact represents $P_{amb} - P_{cav}$. Otherwise for smaller values of P_{amb}, the curve of the LCC seems to reach an asymptote when A increases. The pressure can drop below the cavitation pressure in the inlet and oil enters the dimple but the maximum pressure being limited by the outlet pressure, the position of the film reformation moves back or oil flows back inside the dimple and refills it and cavitation stops occurring. The calculation domain is $\Omega = [-8, 8] \times [-8, 8]$. Figure 5.16 shows the evolution of the depth A_{cav} for which cavitation starts in terms of P_{amb}. Calculations have be performed for three dimple radii: $R = 1$ in blue, $R = 2$ in red and $R = 0.5$ in green. For small values of P_{amb}, a linear behavior is observed and the three curves superimpose if we plot A_{cav} as a function of P_{amb}/R. In a 1D case, this linear behavior could be explained as follows: for very shallow dimples one has $H \approx 1$ and therefore

$$\frac{\partial}{\partial X}(\frac{H^3 \partial P}{\partial X}) = \frac{\partial H}{\partial X}$$

roughly leads to

$$\frac{1}{R}\frac{0 - (P_{cav} - Pamb)}{R} \approx \frac{A}{R}$$

and therefore $A \approx P_{amb}/R$. Afterwards, the load carrying capacity in terms of the dimple depth was studied for two radii $R = 1$ (in blue) and $R = 2$ (in red). If we plot $LCC/(P_{amb}R^2)$ in terms of AR the 2 curves superimpose if P_{amb} remains small as shown in figure 5.18 for $P_{amb} = 0.001$. For larger values of P_{amb}, the 2 curves still coincide for shallow dimples and then diverge for $P_{amb} = 0.005$ (see figure 5.18). In this case for $R = 1$, no cavitation occurs for very deep dimples and the load carrying capacity vanishes. Except for this case, all curves show similar trends. At the beginning, a shift can be noted due to the beginning of the cavitation process which is delayed when P_{amb} increases. Figure 5.17 shows the evolution of the depth A_{cav}/R^2 for which cavitation stops in terms of P_{amb}. Calculations have be performed for three dimple radii: $R = 1$ in blue, $R = 2$ in red and $R = 0.5$ in green. It was found that A_{cav}/R^2 varies like $1/P_{amb}^2$ and more precisely in this case $A_{cav}/R^2 \approx 0.016/P_{amb}^2$.

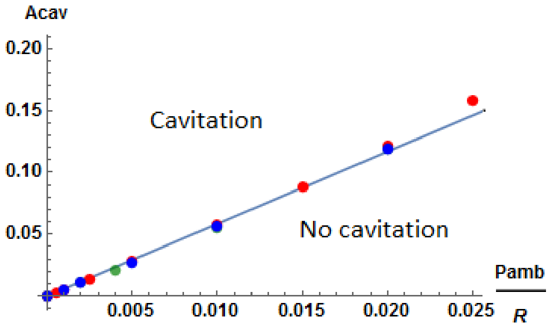

Figure 5.16: Evolution of A_{cav} as a function of P_{amb}/R for three dimple radii: $R = 1$ in blue, $R = 2$ in red and $R = 0.5$ in green in the case of a single dimple at the center of $\Omega = [-8, 8] \times [-8, 8]$ (A_{cav} is the depth value after which cavitation begins).

5.4.2 One dimple in the first quarter of the domain

In this case the load carrying capacity is always positive even when no cavitation occurs. The inlet being closer than the outlet, the zone where the pressure is above P_{amb} dominates. As long as cavitation has not occurred, the LCC and $P_{max} - P_{amb}$ show a linear behavior in the dimple depth A and do not depend on the value of P_{amb} as shown in figure 5.19. Please note that in this case the load carrying capacity is not zero since, because of the non symmetry of

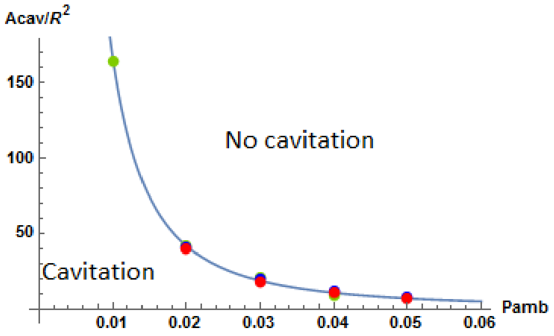

Figure 5.17: Evolution of A_{cav}/R^2 as a function of P_{amb} for three dimple radii: $R = 1$ in blue, $R = 2$ in red and $R = 0.5$ in green in the case of a single dimple at the center of $\Omega = [-8, 8] \times [-8, 8]$ (A_{cav} is the depth value after which cavitation stops).

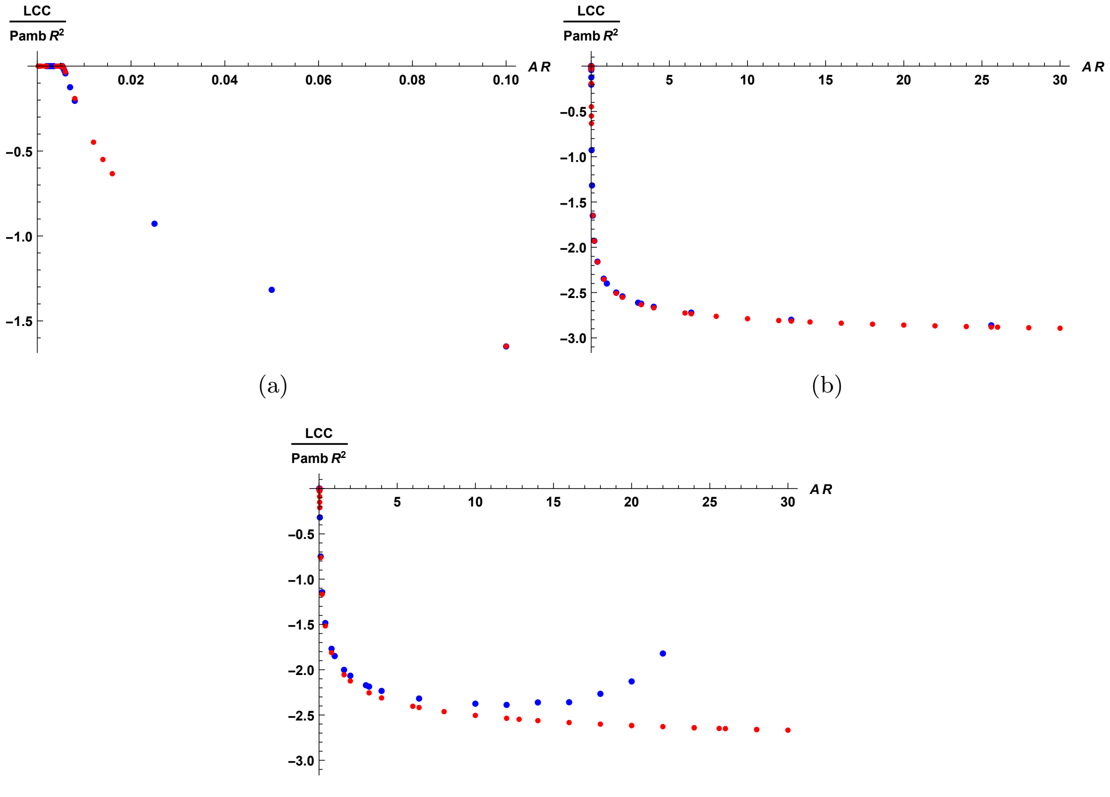

(a)

(b)

(c)

Figure 5.18: Evolution of $LCC/(P_{amb}R^2)$ as a function of AR for two dimple radii: $R = 1$ in blue, $R = 2$ in red in the case of a single dimple at the center of $\Omega = [-8, 8] \times [-8, 8]$. (a) $P_{amb} = 0.001$ (b) $P_{amb} = 0.002$ (c) $P_{amb} = 0.005$.

the geometry, the pressure field is not anti-symmetric. A similar behavior is observed for $R = 2$. In this case also, the starting value of A for which cavitation occurs is proportional to P_{amb} for small values of P_{amb} as shown in figure 5.20. Similarly for large values of P_{amb} and deep dimples, no cavitation occurs.

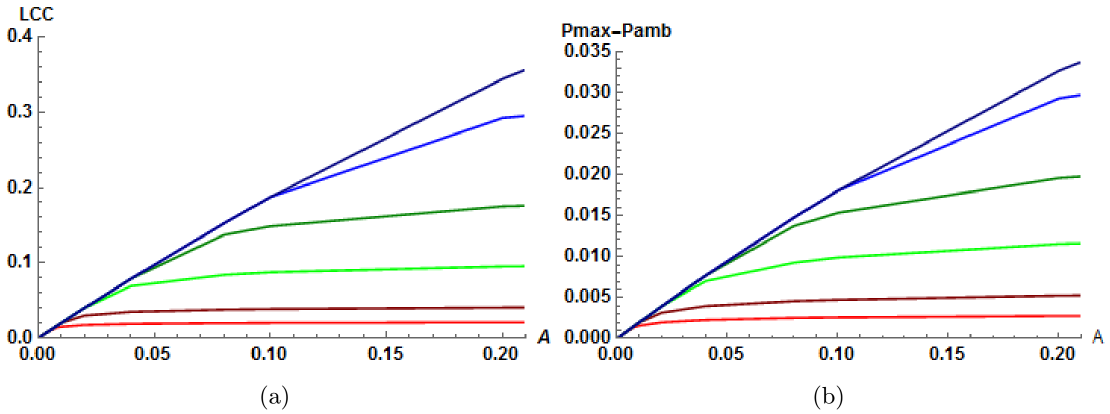

(a) (b)

Figure 5.19: Evolution of the load carrying capacity and of $P_{max} - P_{amb}$ as a function of the dimple depth A for a single dimple of radius $R = 1$ at $(-4, 0)$ in $\Omega = [-8, 8] \times [-8, 8]$ for shallow dimples and for $P_{amb} \in \{0.001, 0.002, 0.005, 0.01, 0.02, 0.05\}$ from bottom to top (a) LCC, (b) $P_{max} - P_{amb}$.

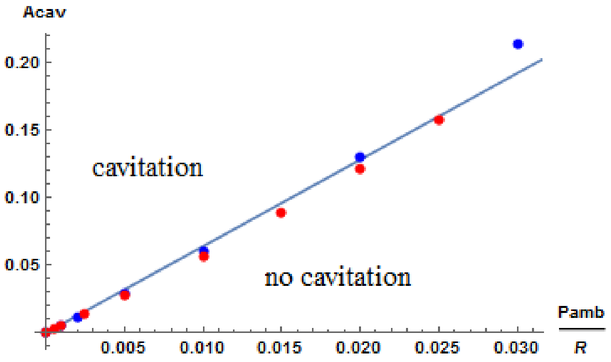

Figure 5.20: Cavitation depth A_{cav} for a single dimple of radius $R = 1$ at $(-4, 0)$ in $\Omega = [-8, 8] \times [-8, 8]$ as a function of P_{amb}/R.

This time the curves of $LCC/(P_{amb}R)$ (and not $LCC/(P_{amb}R^2)$) as a function of AR almost coincide as can be seen in figure 5.21, part (a). Other computations were performed for $P_{amb} = 0.01$ and dimples at $(-2, 0)$ with radii $R = 0.5$, $R = 1$ and $R = 2$ and similar trends are obtained see part (b) of figure 5.21. It is likely that, when the indent is located at the center of the domain, as the distance to the inlet and to the outlet are the same, first order effects cancel and a second order effect emerges.

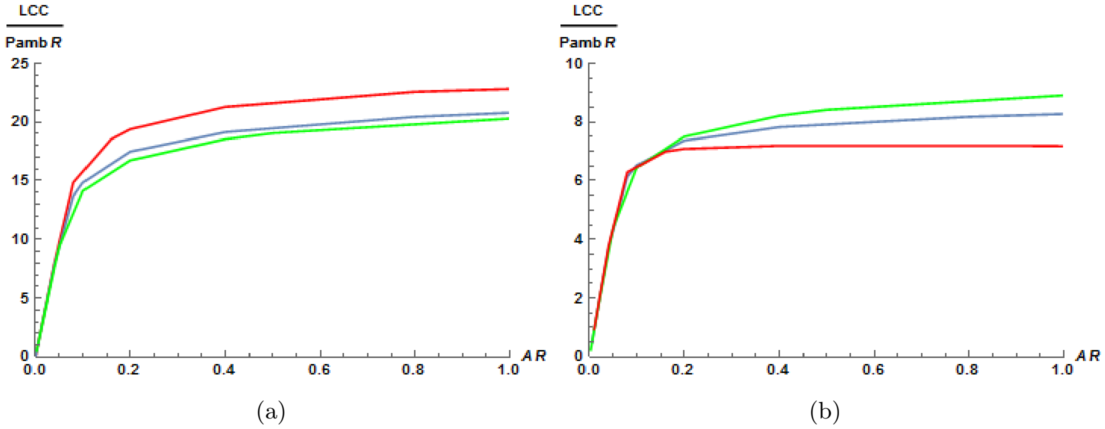

Figure 5.21: Evolution of $LCC/(P_{amb}R)$ as a function of AR for three dimple radii: $R = 0.5$ in green, $R = 1$ in blue and $R = 2$ in red in the case of a single dimple at (a) $(-4, 0)$ (b) $(-2, 0)$ with $\Omega = [-8, 8] \times [-8, 8]$ for $P_{amb} = 0.01$.

5.4.3 Ambient pressure influence on the load carrying capacity

The influence of the value of P_{amb} (or rather $P_{amb} - P_{cav}$) was considered and it was noticed that LCC/P_{amb} as the function of the dimple position on the X-axis is independent of the chosen value for P_{amb} as can be seen in figure 5.22.

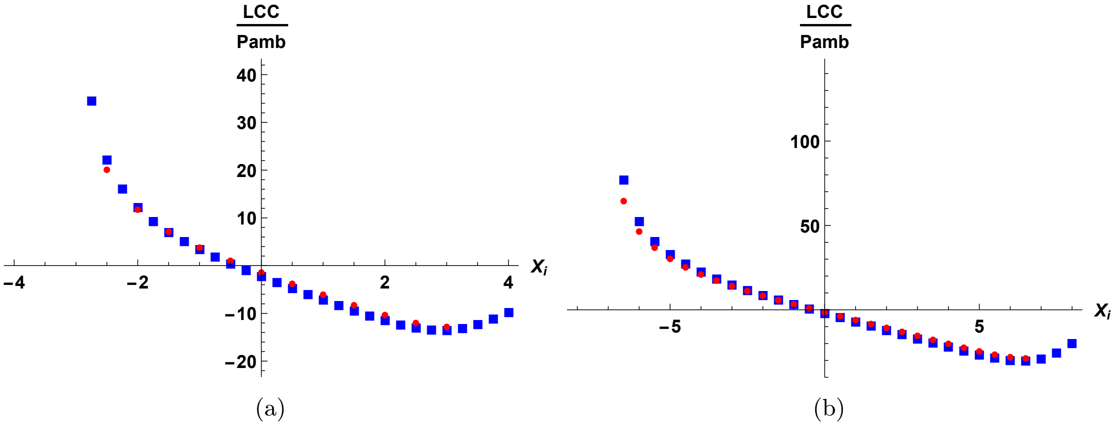

Figure 5.22: Graph of LCC/P_{amb} as a function of X_i position of the dimple of radius 1 and depth 1 on (a) $\Omega = [-8, 8] \times [-8, 8]$ (b) $\Omega = [-4, 4] \times [-4, 4]$, for $P_{amb} = 0.001$ in blue and $P_{amb} = 0.01$ in red

5.4.4 Dimple depth influence on the load carrying capacity

The graph of LCC/P_{amb} as a function of dimple position, X_i, was determined for $P_{amb} = 0.001$ and $A \in \{0.05, 0.1, 0.5, 1, 2\}$, the four curves coincide except when the indent is located close to the inlet as can be seen in figure 5.23. When the dimple is near the inlet, the load carrying

capacity is very dependent on A. It rapidly drops with A. Otherwise, for shallow indents, the linear decrease of the load carrying capacity is slower than for deeper dimples.
Besides for a given radius and ambient pressure, we have seen that the load carrying capacity for a centered dimple or a dimple at the first quarter of the domain usually has an asymptote as A increases which is already reached at $A = 1$ (see figure 5.18 or 5.21). As in figure 5.23, no big difference can be noticed for $A \geq 1.0$ (blue and red squares) (and even for $A = 0.5$ (green squares)) except in the inlet. It seems that this remains true for other dimple positions outside the inlet.

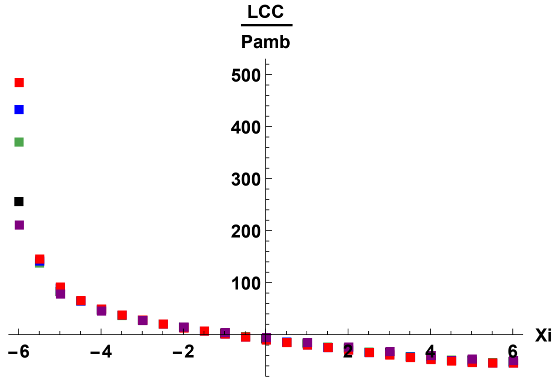

(a) (b)

Figure 5.23: (a)Graph of LCC/P_{amb} as a function of X_i, position of the dimple of radius 2 and depth $A = 0.05$ in purple, $A = 0.1$ in black, $A = 0.5$ in green, $A = 1$ in blue and $A = 2$ in red on $\Omega = [-8, 8] \times [-8, 8]$ and $P_{amb} = 0.001$ (b) Zoom.

5.4.5 Dimple radius influence on the load carrying capacity

The evolution of the load carrying capacity in term of the dimple position was also plotted on a given domain for various values of the dimple radius. It can be noticed that $LCC/(RP_{amb})$ as a function of X_i is independent of R (see figure 5.24) except in the inlet.

5.4.6 Dimple shape influence on the load carrying capacity

The evolution of the load carrying capacity in term of the dimple position was also plotted on a given domain for circular dimples and elliptic dimples of the same volume and the same depth along the sliding direction or perpendicular to the sliding direction. No major difference could be observed as shown in Figure 5.25

5.5 Conclusion

For parallel surfaces in hydrodynamic lubrication, no pressure can be generated without a surface texture. Partial texturing with micro dimples can induce positive pressure when the texture is

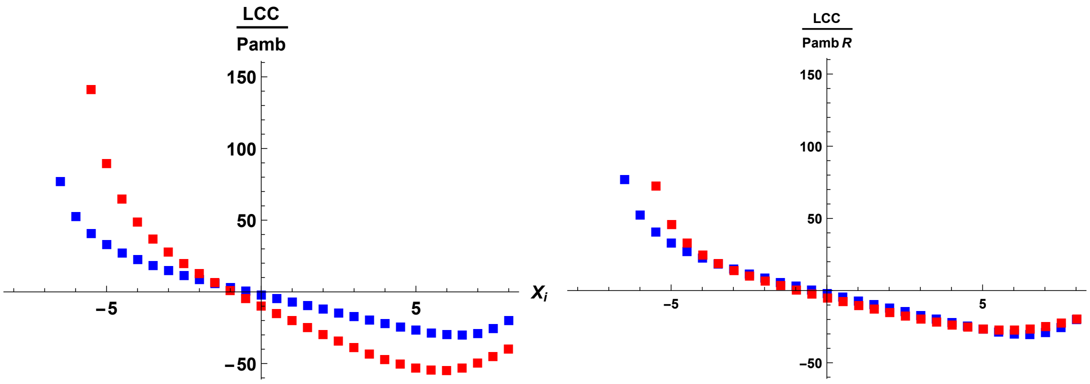

(a)

(b)

Figure 5.24: Curves of (a) LCC/P_{amb} (b) $LCC/(RP_{amb})$ as a function of X_i position of the dimple of depth 1 and radii 1 in blue and 2 in red on $\Omega = [-8, 8] \times [-8, 8]$.

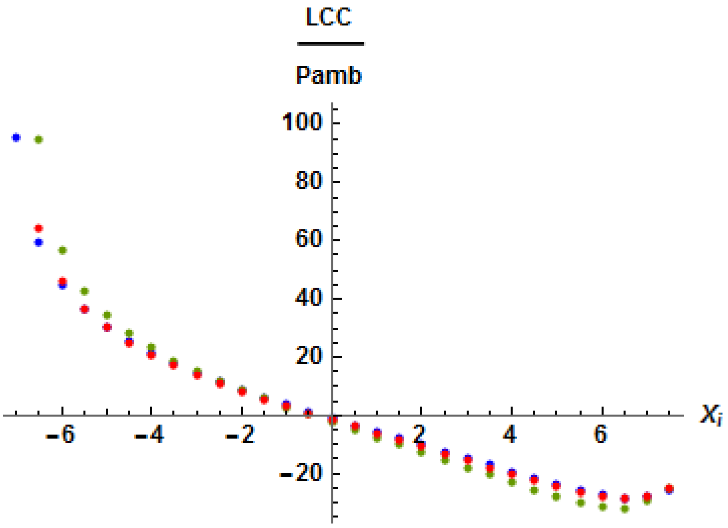

Figure 5.25: Scaled LCC for a circular dent of radius 1 and depth 1 in red and for elliptic dents of same volume and same depth green (perpendicular to the sliding direction) and blue (along the sliding direction) on $\Omega = [-8, 8] \times [-8, 8]$ with $P_{amb} = 0.01$.

located in the contact inlet. It shows a step bearing behavior. However, the loss of pressure is less important for the outlet texture than the gain for the inlet texture. By texturing both contact ends, a positive load carrying capacity is generated which may be useful for reciprocating contacts as for the flat ring in the PRLC contact. The load carrying capacity was examined with respect to the position of the dimples and their dimension. The parameter influence is more sensitive when the texture lies in the inlet. Otherwise, for a single dimple, the load carrying capacity seems to be proportional to its radius and concerning their depth an asymptotic value is reached.

CHAPTER 6

Groove influence on piston ring minimum at TDC and BDC.

Contents

6.1 Introduction

An investigation of the piston ring minimum film thickness in the case of a textured liner is conducted.

The piston ring cylinder liner contact is the principal source of friction and oil consumption. These two phenomena are directly related to the minimum film thickness over an engine cycle. Because of the importance of the influence of cylinder liner texture, piston friction has been studied in detail over the past two decades.

A first publication on the hydrodynamic lubrication of the piston ring cylinder liner (PRCL) contact was by Castleman in 1936 [73] to explain the profile of a worn ring. In 1956, Eilon and Saunders [74] studied the piston-ring lubrication both experimentally and theoretically. They suggested that the oil film thickness is determined by the balance of forces acting on the ring. In 1959 Furuhama [75] published a study of the piston-ring lubrication in which he highlights the importance of the squeeze effect at low speeds near top and bottom dead center (TDC and BDC). More recently, Jeng [76, 77] published a 1D analysis of the piston ring lubrication where he calculates oil film thickness, friction force and power loss for fully flooded and starved conditions. Priest et al. [78] have developed a numerical model that accounts for the dynamic lubrication study of the change in ring profile of wear. Tian et al. [79] created a 1D mixed lubrication model where a ‘film non-separation’ exit condition when squeeze effects are most important. Surface roughness proved to be important for oil transportation. Akalin and Newaz [80] also developed a numerical method to study friction in the mixed lubrication regime. They show that the hydrodynamic lubrication regime occurs over the major part of the stroke. Increase of the friction coefficient near TDC and BDC is due to the mixed lubrication near those points because of low speed and high cylinder pressure. Taylor [81] mentions that the squeeze effect is often omitted in studies of the PRCL contact in spite of its importance near top and bottom dead center where the piston velocity is zero. He developed a 1D model and compares results obtained with or without squeeze effects. He shows that there is no cavitation at reversal when squeeze effects are considered. He also shows that the oil film thickness is very sensitive to the ring radius of curvature near reversal points and that it would be useful to have models that accurately predict that film thickness near TDC and BDC to reduce friction and maintain durability.

Recently, many studies [41, 42, 46, 48, 67, 70, 71, 82–85] about the texture influence on the minimum film thickness have been published. Etsion and co-workers [41, 42, 71] have conducted many experimental studies to investigate the influence of texture on piston ring lubrication or reciprocating automotive components. Medina et al. [70] have developed a 1D numerical mass-conserving solver and compare its performance with experiments to show it suitability in studying fiction in lubricated textured bearings under steady-state and transient configurations. Tomanik [48] built a 1D model to study the dimple effects on the hydrodynamic lubrication of the oil control ring and top ring. Spencer et al. [82] developed a 2D semi deterministic model to analyze the PRCL contact for artificially created real cylinder liner topographies. Gherca et al. in [85] have used a transient mass-conserving code and consider surface roughness and surface texturing on both surfaces of a parallel bearing and their impact on the lubrication under transient conditions. In [67], Shen and Khonsari numerically and experimentally analyze the effect of lasered pockets on the lubrication of a flat ring. They study the influence of pocket shape and depth on the friction force during the piston motion. They show that the pocket area ratio and depth are the major factors. Pocket area ratio or depth should not be too large. Biboulet et al., in [86], have developed an automatic procedure for groove geometry identification of cross hatched surfaces in order to study the micro-geometry evolution and wear. In [46], Vladescu et al. experimentally study friction and power loss in a convergent-divergent bearing under various lubrication regimes with an apparatus that simulates the piston-ring liner contact. They consider various texture patterns (crosshatch, chevron, angular grooves, parallel grooves, transverse grooves) and try to determine their beneficial or detrimental effect according to the lubrication regime. They show that in low film thickness contacts surface texture is beneficial all along the stroke and the best texturing consists of transverse grooves and the most detrimental consists of grooves that are parallel to the sliding direction. Under full film lubrication, texture is detrimental. In the mixed regime surface texture just after reversal helps reducing friction but there should not be pockets at the reversal points. Best textures seem to be transverse grooves or chevrons. In [84], Vladescu et al. show through experimental studies that simulate the piston ring liner motion that the squeeze effect preserves film thickness at reversal. The film is minimal shortly after reversal and there, the friction force is maximum. Under fully flooded conditions texture reduces film thickness and increases friction while under mixed and boundary conditions texture provides a small increase of minimum film thickness that significantly decreases friction. In other recent experimental studies on the textured piston ring liner contact [83], Vladescu et al. try to better understand the effects of cavitation, starvation, texture and their interactions. They observe lubricant replenishment mechanisms. They show that in case of limited oil supply, texture pockets help to get an even distribution of the lubricant on the liner and allow about 33% friction reduction compared to the smooth case and also oil consumption reduction. They also show that immediately after reversal starvation occurs even under fully flooded conditions explaining the high wear often encountered near TDC and BDC. A good choice for the texture pattern is beneficial not only for friction but also for oil consumption.

In the present work, the previous multigrid code is used to study the hydrodynamic lubrication of the PRCL contact over an engine cycle. Consequently, the transient Reynolds term is taken into account. Multigrid techniques allow a significant reduction of the computing time which becomes crucial for this time dependent problem since many time steps are needed. Besides, the code, based on Alcouffe's [4] ideas, enables us to consider highly varying coefficients and henceforth it is adapted to the study of textured liners. For the smooth case results are compared with results found in the literature [81]. Afterwards a 2D analytic model of cross hatched grooves is considered as reference. A minimum film thickness is obtained near the TDC and the BDC. The influence of the groove density, depth and width on those minimum film thicknesses is studied.

6.2 Problem formulation

In this chapter the transient hydrodynamic lubrication of the piston ring-cylinder liner contact is considered and the following problem is solved on a domain Ω:

$$\frac{\partial}{\partial x}\left(\frac{\rho h^3}{12\eta}\frac{\partial p}{\partial x}\right)+\frac{\partial}{\partial y}\left(\frac{\rho h^3}{12\eta}\frac{\partial p}{\partial y}\right)-u_m\frac{\partial(\rho h)}{\partial x}-\frac{(\partial\rho h)}{\partial t}=0 \tag{6.1}$$

Where p is the hydrodynamic pressure, h, the geometry, u_m the mean velocity of the piston ring and liner. The load is imposed, it is defined by the piston ring radial tension and is constant: w_0. Henceforth the minimum film thickness becomes a function of time that has to be evaluated in order to satisfy the force balance equation 6.2:

$$\iint_\Omega p(x,y,t)\,\mathrm{d}x\mathrm{d}y = w_0, \quad \forall t. \tag{6.2}$$

The geometry h is defined as follows:

$$h(x,y,t)=h_m(t)+\frac{x^2}{2R^2}+\phi(x+tv_p(t),y) \tag{6.3}$$

with the roughness ϕ defined by cross hatched grooves. Our task consists in determining $h_m(t)$ as a function of time. This is not exactly the minimum film but it is close to it. In our study

the mass conservation being less important, the pressure is set to 0 if it becomes negative. The fluid is assumed to be incompressible and isoviscous. Henceforth the lubricant density, ρ and the viscosity, η are considered constant. This problem will be solved on a rectangular domain $\Omega = [x_a, x_b] \times [y_a, y_b]$ where $[x_a, x_b] = [-x_0, x_0]$ corresponds to the ring width. As the analytical texture is supposed to be periodic in the y-direction, $[y_a, y_b]$ corresponds to the width of one pattern.
At x_a and x_b the pressure boundary condition is 0 and a periodic condition is used in the y direction: $p(x, y_a) = p(x, y_b)$.

Working in a coordinate system linked to the piston ring, the mean velocity is $-v_p(t)/2$ where $v_p(t)$, the piston ring velocity, is computed as follows:

$$v_p(t) = \frac{s\omega}{2}\cos(\omega t)(1 + \frac{sin(\omega t)}{\sqrt{\frac{c^2}{r^2} - \cos^2(\omega t)}}) \tag{6.4}$$

where s is the stroke, $r = s/2$, ω is the rotational speed and c the con-rod length.

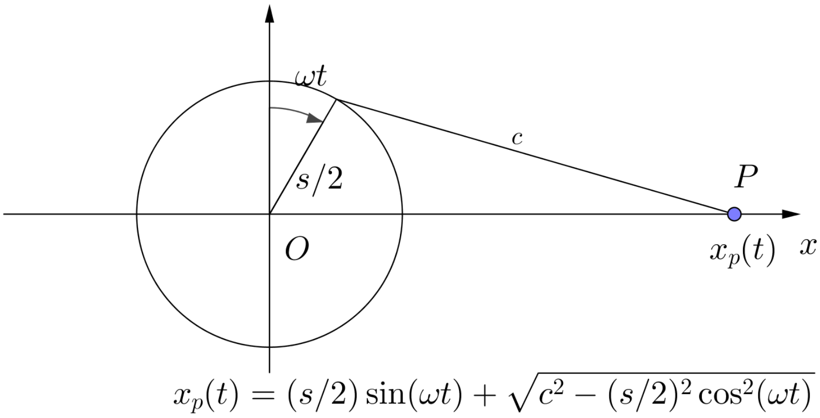

Figure 6.1: Piston position.

6.2.1 Dimensionless equations

The dimensionless parameters are chosen as follows:
Dimensionless coordinates: $X = x/x_0$, $Y = y/x_0$.
Dimensionless film height: $H(X,Y) = h(x,y)/h_0$ with $h_0 R_x = x_0^2$ where R_x is the ring radius of curvature.
Dimensionless time: $T = t/t_0$ with $t_0 = 1/\omega$ where ω is the crankshaft rotational speed.
Dimensionless pressure: $P(X,Y) = p(x,y)/p_0$ with $p_0 = (12\eta x_0^2)/(t_0 h_0^2)$.
Dimensionless load carrying capacity: $W = w/(p_0 x_0^2)$.
Dimensionless mean velocity: $U_m(T) = u_m(t)t_0/x_0 = -0.5 v_p(t)t_0/x_0$.
Dimensionless indent depth: $A = a/h_0$.
Dimensionless distance between grooves: $D = d/x_0$.
Dimensionless groove width between grooves: $\Lambda = \lambda/x_0$.

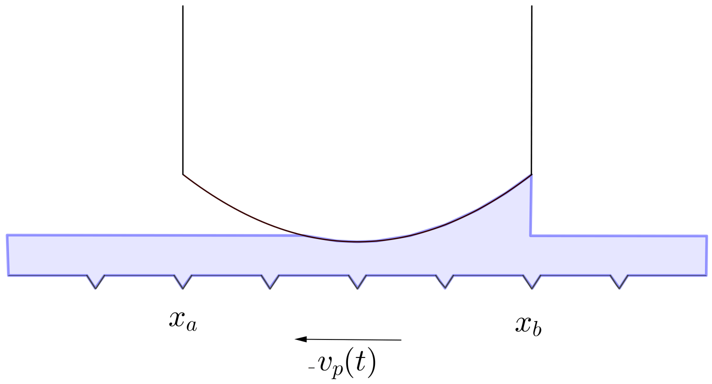

Figure 6.2: Piston ring and grooved liner cross section.

With these dimensionless variables the dimensionless Reynolds equation reads:

$$\frac{\partial}{\partial X}(H^3\frac{\partial P}{\partial X})+\frac{\partial}{\partial Y}(H^3\frac{\partial P}{\partial Y})-U_m(T)\frac{\partial H}{\partial X}-\frac{\partial H}{\partial T}=0 \text{ and } P>0 \quad (X,Y)\in\Omega_1 \tag{6.5a}$$

$$P=0 \quad (X,Y)\in\Omega_2 \tag{6.5b}$$

with the following dimensionless boundary conditions:

$$P=0 \quad \text{if} \quad X=X_a \quad \text{or} \quad X=X_b \tag{6.6a}$$

$$P(X,Y_a)=P(X,Y_b). \tag{6.6b}$$

The calculation domain is $[-X_a,X_b]\times[-Y_a,Y_b]=[-1,1]\times[-0.5/\sin(\alpha),0.5/\sin(\alpha)]$.
The dimensionless geometry is

$$H(X,Y,T)=H_m(T)+\frac{X^2}{2}+\Phi(X-2TU_m(T),Y)$$

Figure 6.3) shows the dimensionless groove pattern that defines the liner roughness. The dimensionless distance D_1 between two nodes in the X-direction will sometimes be used. It is equal to $D/\cos(\alpha)$ where D is the dimensionless distance between grooves. The force balance equation reads:

$$\iint_{[X_a,X_b]\times[Y_a,Y_b]} P(X,Y,T)\,\mathrm{d}X\,\mathrm{d}Y=W_0, \quad \forall T. \tag{6.7}$$

6.2.2 Relaxation process

The initial Alcouffe based code is adapted in order to satisfy the force balance equation. This is done by changing $H_m(T)$. As this only induces low frequency errors, it is sufficient to change it on the coarsest grid. On the coarsest grid, a few relaxations of the Reynolds equation are performed to obtain a new approximation of the pressure. Afterwards $H_m(T)$ is updated by relaxing the

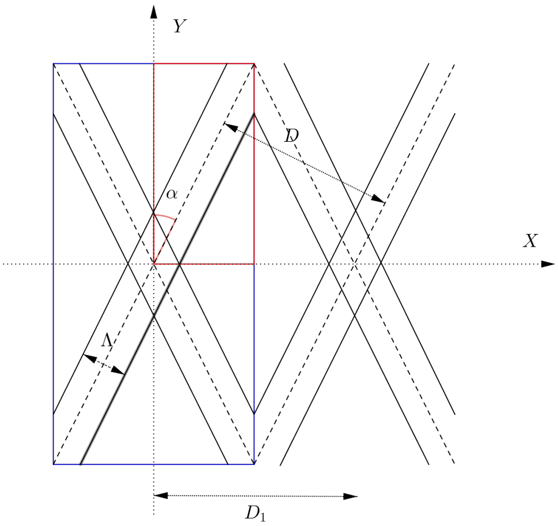

Figure 6.3: Cross hatched groove pattern

force balance equation and some extra relaxations of the Reynolds equation are performed in order to get a coarse grid estimate of the pressure with the new geometry. It is important to note that changing H_m induces changes of the whole geometry. Therefore all Reynolds equation coefficients on all grids have to be modified as well as all the operators just after updating H_m. Besides at each new time step, the geometry also changes because of the displacement of the piston ring and all coefficients and operators need being computed again. Only V-cycles are used. The Reynolds equation is relaxed as before. For the force balance equation we proceed as described in the dry contact chapter of [5]. At time T the discretized force balance equation on the grid of level k reads:

$$h_x h_y \sum_i \sum_j P_{i,j}^k = g^k. \tag{6.8}$$

On the finest grid $g^k = W_0$. The Full Approximation Scheme (FAS) is used. The force balance equation residual reads:

$$rg^k = g^k - h_x h_y \sum_i \sum_j P_{i,j}^k \tag{6.9}$$

where h_x and h_y are the discretization steps in the X and Y directions on the grid k. The right hand side of the balance equation on the grid $k-1$ is given by:

$$g^{k-1} = H_x H_y \sum_I \sum_J P_{I,J}^{k-1} + I_k^{k-1} rg^k. \tag{6.10}$$

where H_x and H_y are the discretization steps in the X and Y directions on the grid $k-1$. As rg^k is a scalar, its restriction to the next coarse grid $I_k^{k-1} rg^k$ is rg^k. Henceforth

$$g^{k-1} = H_x H_y \sum_I \sum_J P_{I,J}^{k-1} + rg^k = H_x H_y \sum_I \sum_J P_{I,J}^{k-1} + g^k - h_x h_y \sum_i \sum_j P_{i,j}^k. \tag{6.11}$$

Using the Moes-Venner relation that relates the mean velocity, the load and the minimum film thickness, $\Delta H_m(t)/H_m(t)$ is proportional to $-\Delta W/W$ and H_m^k is modified of $-\omega rg^k/g^k$ on the coarsest grid. The coefficient ω is an under-relaxation factor that has to be tuned according to various factors and in particular to the velocity.

6.3 Convergence and code validation.

Since the solution, from one time step to the next, varies little, only V(2,1)-cycles are used without FMG. The coarsest grid grid has 5 points in the X-direction that is to say that on the coarsest grid $h_x = (X_b - X_a)/4$ and the number of points in the Y-direction is chosen so that $h_x \approx h_y$. The time step has to be chosen sufficiently small in order to get a convergent code. In our model the dimensionless mean velocity which is half the piston ring velocity roughly varies in the range $[-27, 27]$. The time step h_t was chosen to be at least $0.05 * h_x$ where h_x is the fine grid space step in the sliding direction. Each time a level is added h_x and h_y, the 2 space steps, are divided by 2 and therefore the calculation time for each relaxation is multiplied by 4. Besides the time step is divided by 2 and henceforth the computation time on the same period is multiplied by 8. As the time step is rather small and because the problem has to be solved at least over a complete engine cycle, it is necessary to find a good compromise between accuracy and the total number of grids and the time step. We also need sufficiently many points on the finest grid to correctly capture the grooves. We also need to optimize the number of V-cycles per time step. The most important changes in H_m will take place at the beginning of each time step and once H_m is stabilized, the Reynolds equation converges more efficiently. It will be shown that 5 V-cycles will suffice to get a reasonable accuracy. Besides there are some numerical errors that are more important at high velocities and that are non existent when the piston velocity is close to 0 due to the number of grooves that pass through the contact during the time step. With more grids the oscillations diminish. But as will be shown, the results that are obtained with only 7 levels are quite acceptable.

In the smooth case no problems are encountered. Our code is validated by comparison with a semi-analytical solver developed by Martin Denni, based on Jeng [76] and Taylor [81] works. The parameters values are taken from Taylor [81]:

Bore radius	44.95 mm
Con-rod length	154.0 mm
Stroke	78.70 mm
Crankshaft rotational speed	2500 rpm
Piston ring tension	171 kPa
Ring width	1.5 mm
Ring radius of curvature	100 mm
Oil viscosity	6.676 mPa.s

Table 6.1: Chosen piston ring characteristics

These values will be kept in the subsequent evaluations. The effects of the variation of temperature on the oil viscosity are not taken into account although in section 6.5.1 some results are presented to show how it affects the minimum film thickness. The trial groove geometries are shown in figures 6.4. The dimensionless calculation domain Ω is $[-1,1] \times [-D/(2\sin(\alpha), D/(2\sin(\alpha)]$, the distance between grooves is respectively $D = \cos(\alpha), 0.5\cos(\alpha), 0.25\cos(\alpha)$ for the three geometries shown in figure 6.4. The angle α is the angle between the grooves and the Y-axis. In our first tests, it is equal to 15°.

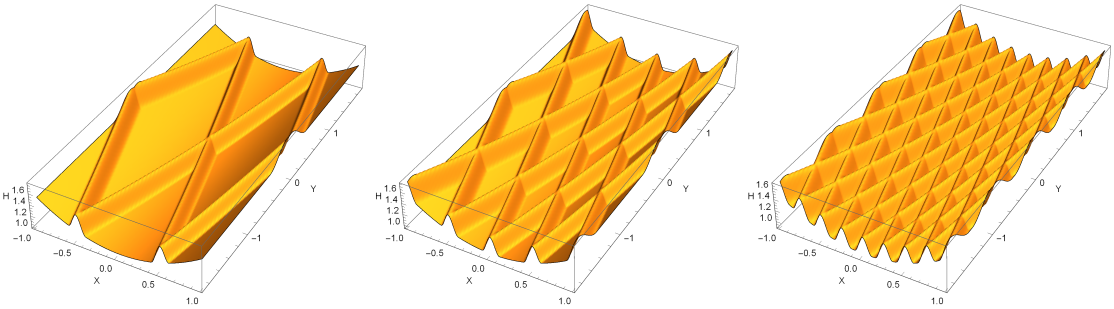

Figure 6.4: Groove geometry, low density (left), medium (middle), high (right).

Only the fully flooded case is studied. In this problem, cavitation does not occur near top and bottom dead center where minimum film thickness is found (see Figure 6.5. At TDC and BDC, the pressure is not zero as can be seen in Figures 6.5 (b) and (e) although the maximum pressure is lower than for other crank angles. Pressure is more evenly distributed at those points. Close to TDC and BDC, pressures in grooves is far from 0. More precisely, there is no cavitation in a range of 5° around top and bottom dead centers. A posteriori, this justifies the use of the non flow conserving algorithm.

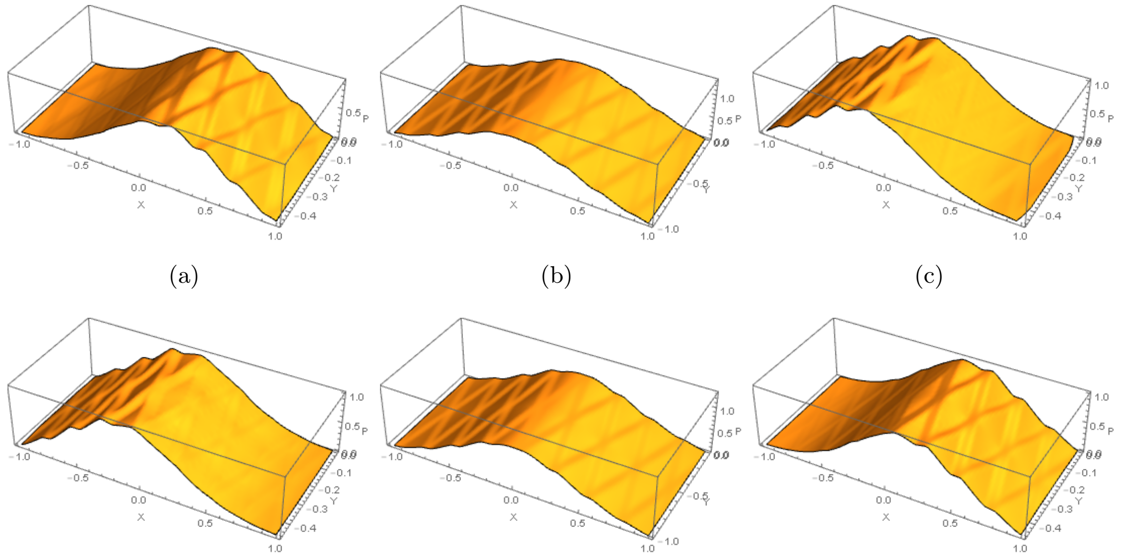

(a) (b) (c)

(d) (e) (f)

Figure 6.5: For $D = 0.25$, $A = 0.3$, $\Lambda = 0.1$, positive (> 0) pressure at crank angle: (a) 87.5°, (b) 90° (TDC), (c) 92.4°, (d) 267°, (e) 270° (BDC), (f) 272.4°.

6.4 Optimization of the computational time

The computational time is a real challenge for this type of problem. As mentioned before, because of the periodicity in the Y-direction the problem is solved on $[-1, 1] \times [-D/(2\sin(\alpha), D/(2\sin(\alpha)]$ and the time step h_y in the Y-direction is chosen to be almost equal to h_x, the time step in the X-direction. For a groove angle $\alpha = 15°$ and $D = 0.25\cos(\alpha)$ or $D_1 = 0.25$ where D_1 represents the distance between two groove nodes in the sliding direction, with 8 levels, 10 V-cycles per time step and 100 time steps, about 6 minutes are needed to perform the calculation. Choosing the time step h_t as $0.05h_x$ where h_x is the space step on the finest level, 64339 time steps are need to solve the problem over 2 engine cycles. It amounts to a total time of about 61 hours. Five V-cycles will be sufficient as will be shown in section 6.4.3, the computing time can be reduced to about 31 hours. If one more level is added, the number of points on the fine grid is multiplied by 4 while the number of time steps is multiplied by 2. Therefore the total time is multiplied by 8. When D is multiplied by 2, the total time is also multiplied by 2.

6.4.1 Time step influence

Some calculations have been performed on 7 levels for three different time steps, $h_t = 0.05h_x$, $0.02h_x$ and $0.01h_x$ for the third geometry (figure 6.4) with grooves of depth $A = 0.3$ and width $\lambda = 0.2$. Figure 6.6 shows the mean dimensionless velocity and the resulting minimum film thickness.

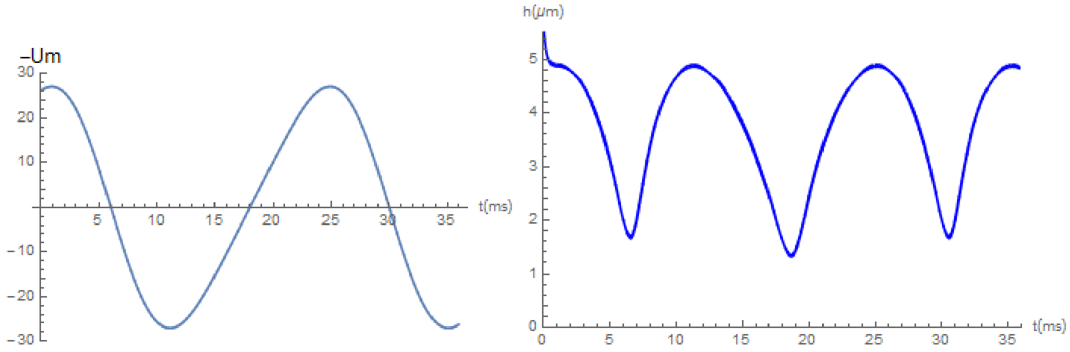

(a) (b)

Figure 6.6: On 7 levels, for $A = 0.3$, $D_1 = 0.25$ and $\Lambda = 0.2$ (a) Mean velocity, (b) Minimum film thickness.

Zooming on the extrema of the minimum film thickness, many oscillations can be noted. The film oscillates more for high velocities than for low velocities since it depends on the number of grooves entering the contact during the considered time step. In figure 6.7, three time steps are considered. The three resulting curves over an engine cycle are shown together. Afterwards, for the three chosen time steps, we zoom on what happens in the vicinity of a maximum, in the vicinity of a minimum and when the mean velocity is almost zero. The differences between the three curves around the minima do not exceed 0.2% in the vicinity of the minimum and 0.8% near the maximum. It may be noticed that the minima do not coincide with a zero velocity. Near the points where the velocity vanishes, oscillation disappear and the three curves are very close to each other. Besides the error does not propagate. Henceforth a time step of $0.05h_x$ is considered sufficient.

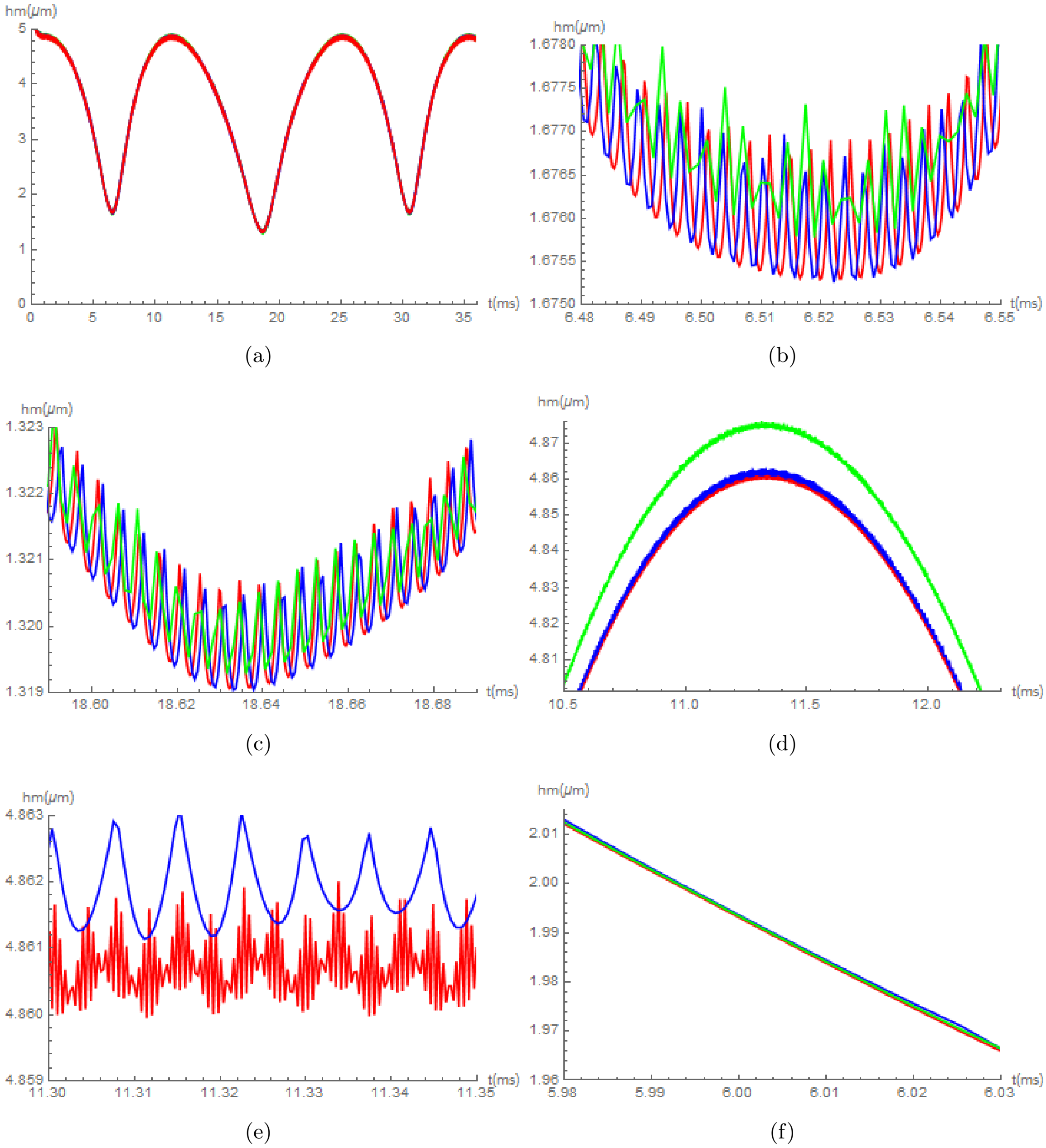

(a) (b)

(c) (d)

(e) (f)

Figure 6.7: 7 levels, $A = 0.3$, $D_1 = 0.25$, $\Lambda = 0.2$, in green $h_t = 0.05h_x$, in blue $h_t = 0.02h_x$, in red $h_t = 0.01h_x$ (a) over an engine cycle (b) zoom around TDC (c) zoom around BDC (d) zoom around the first maximum (e) closer to the first maximum (f) velocity almost 0.

6.4.2 Number of levels: influence of the space step

The space discretization was studied. Results between 7 and 8 levels were compared for $h_t = 0.02h_x$. In figure 6.8, it can be observed that in the neighborhood of minima, the oscillations diminish and the average value of the minimum film thickness varies less than 0.1%. There is a larger difference around the maxima but still very small and corresponding to the discretization error and again the oscillations diminish. These numerical effects do not seem to interfere with the overall film thickness.

The influence of the number of levels was also considered by assuming a constant velocity and compared on level 7, 8, 9 and 10. For a complete engine cycle, in order to study those effects 15 V-cycles per time step were considered, the computation time becomes huge for 10 levels and is already consequent with 9 levels. For a dimensionless mean velocity around 26.2 (close to its maximum value at mid-stroke) computations were performed on these 4 levels. Stabilized results are shown in figure 6.9. The oscillations diminish with the number of levels and the difference between the mean values of each curve correspond to the discretization error. The main frequencies are related to the passing grooves while the others come from time and space discretization. They vanish with finer meshes.

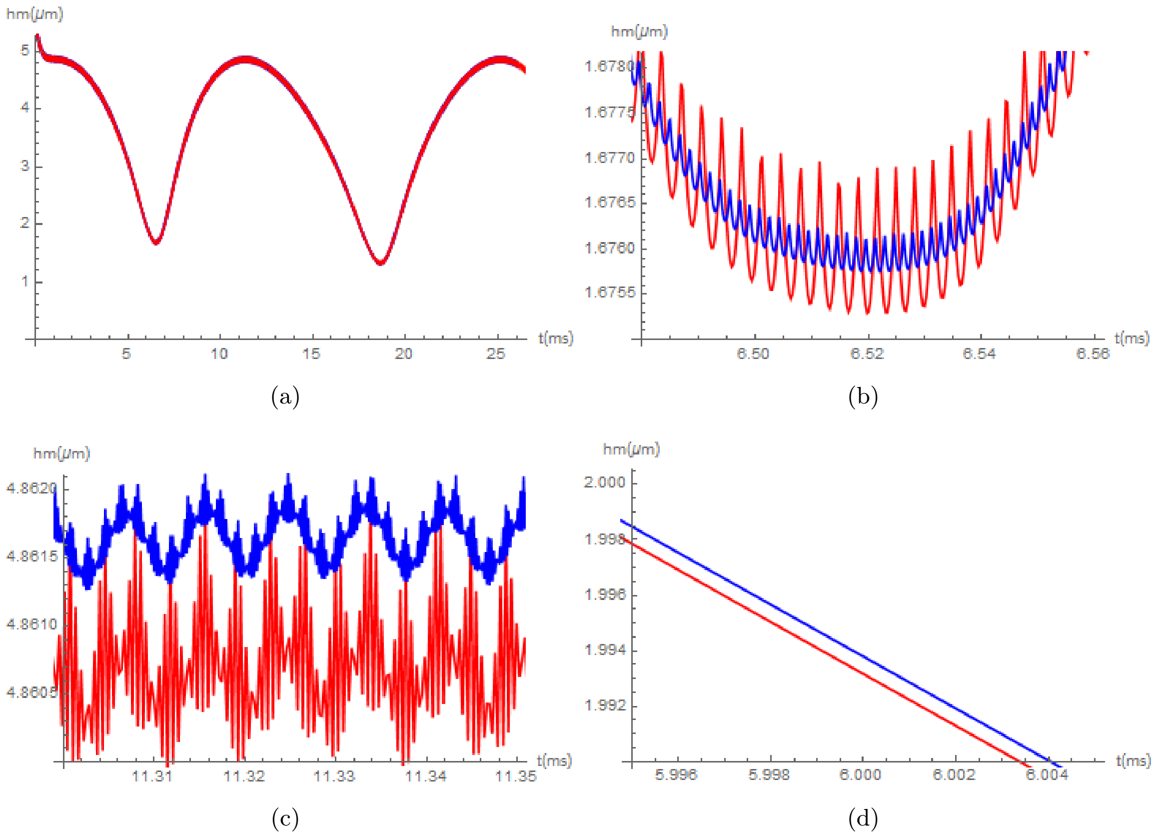

(a) (b)

(c) (d)

Figure 6.8: In red 7 levels, in blue 8 levels; $A = 0.3$, $D_1 = 0.25$, $\Lambda = 0.2$, $h_t = 0.02h_x$ (a) over an engine cycle (b) zoom around the first minimum (c) zoom around the first maximum (d) velocity close to 0.

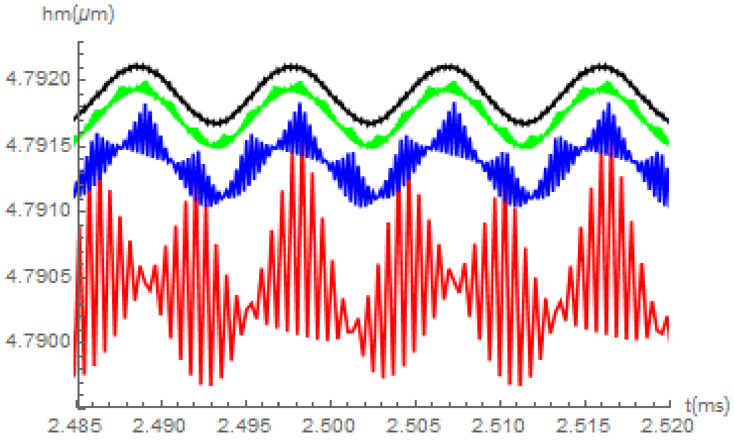

Figure 6.9: Zoom on $H_m(t)$ at high speed,$A = 0.3$, $D_1 = 0.25$, $\Lambda = 0.2$, $h_t = 0.01h_x$. In red: 7 levels, in blue: 8 levels, in green: 9 levels, in black: 10 levels.

6.4.3 Number of V-cycles

Because of the computational time the number of V-cycles also need to be minimized. As can be seen in Figure 6.10, the curves for 10 and 20 V-cycles coincide while a less than 0.1% difference can be observed for 5 and 10 V-cycles near minima. Henceforth, 5 V-cycles per time step may be sufficient.

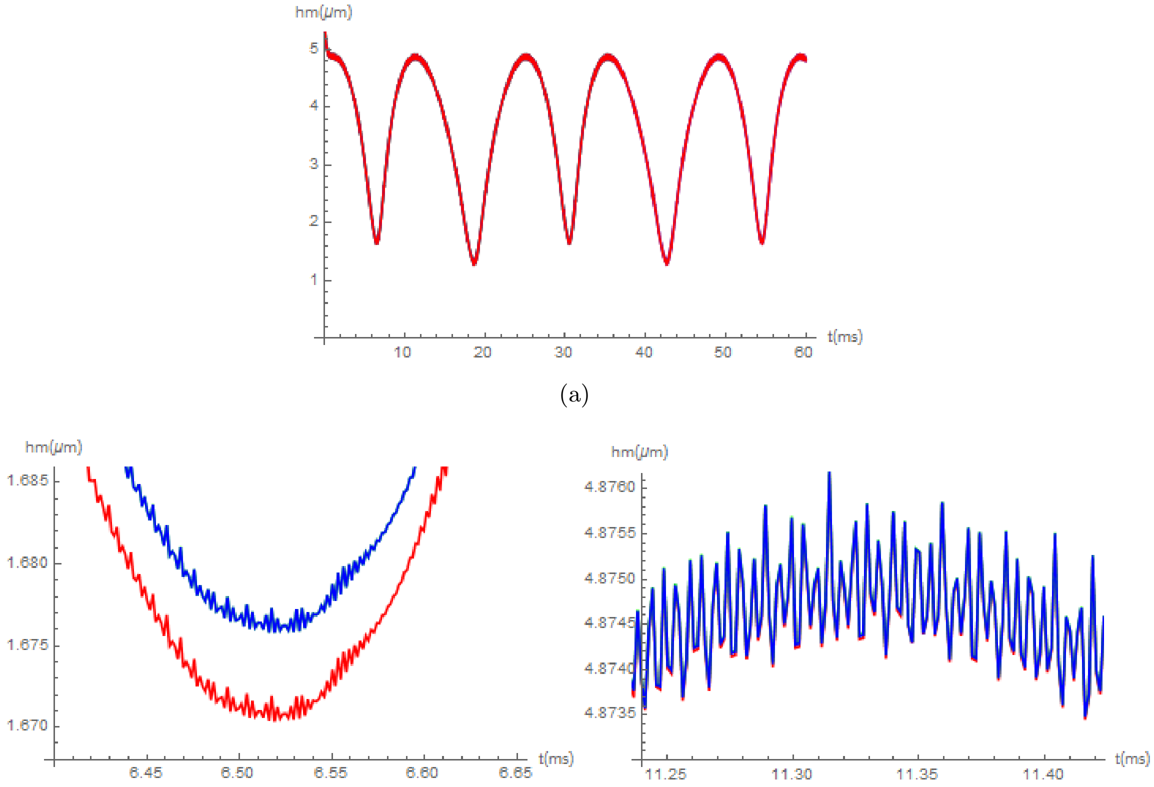

(a)

(b) (c)

Figure 6.10: 7 levels, $A = 0.3$, $D_1 = 0.25$, $\Lambda = 0.2$, $h_t = 0.05h_x$, in red ncy=5, in green ncy=20, in blue ncy=10, (a) over two engine cycles (b) zoom around the first minimum (TDC), (c) zoom around the first maximum.

6.5 Minimum film thickness

In all the curves showing the minimum film thickness h_m or the associated dimensionless value H_m as a function of time, the first time steps must not be considered because of important numerical errors. The range of values of the time t for the curves over an engine cycle has been chosen to avoid those points.

6.5.1 Temperature

In order to study the influence of the various geometry parameters, it was decided not to account for the temperature influence. However, some calculations were performed assuming a linear variation of the temperature between the bottom dead center and the top dead center. In the smooth case the minimum film thickness is evaluated at constant temperature 125°C, with a BDC liner temperature of 100°C and a TDC liner temperature of 150°C and finally with a BDC liner temperature of 90°C and a TDC liner temperature of 160°C. Results are shown in figure 6.11. The viscosity is calculated by the Vogel equation:

$$\eta(\theta) = \kappa \exp(\frac{\theta_1}{\theta_2 + \theta}) \tag{6.12}$$

where θ is the temperature. The chosen values of the parameters κ, θ_1 and θ_2 depends on the chosen oil. For SAE 15W-40 oil, $\kappa = 0.0292$ mPa.s, $\theta_1 = 1424.3$°C and $\theta_1 = 137.2$°C.

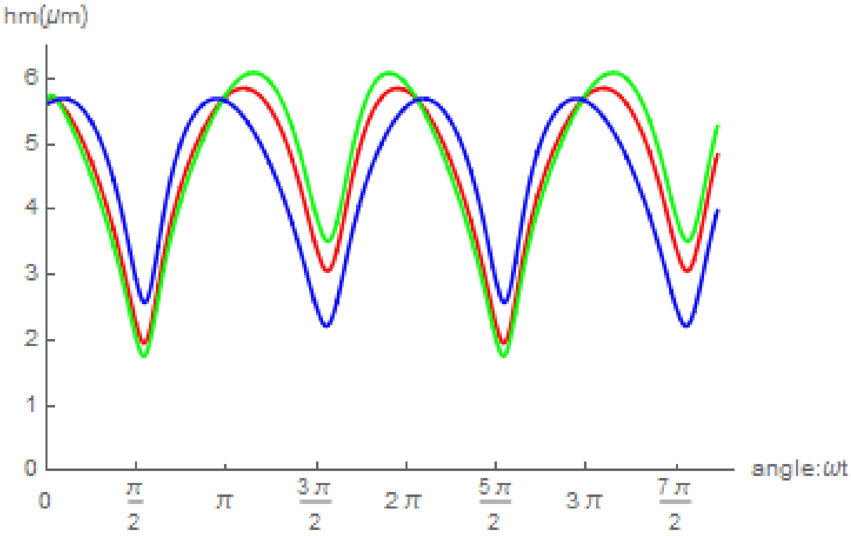

Figure 6.11: Smooth case, in blue constant temperature 125°C, in red BDC 100°C and TDC 150°C, in green BDC 90°C and TDC 160°C.

It may be noticed that the three curves intersect at the same point which corresponds to the mean temperature obtained for angles that are multiples of π that is to say at mid-stroke since a linear variation of the temperature was chosen. It can be seen that for the constant temperature, the minimum film thickness is higher at TDC (angle $\pi/2$ modulo 2π) than at BDC (angle $3\pi/2$

modulo 2π). The piston ring acceleration at TDC is roughly three times the acceleration at BDC. The velocity varies more rapidly near the TDC. Its maximum value is obtained for an angle slightly above 0 mod π and its minimum for an angle slightly less than $\pi/2$ mod π(see Figure 6.12). It implies that, at constant temperature, there is less time for the oil to be squeezed out and thus the minimum film thickness is higher near TDC than near BDC. However, when the temperature effect is considered, the viscosity becomes much lower at TDC than at BDC (see Figure 6.12). As the minimum film thickness is proportional to ηV, it becomes lower at TDC. The variations of η are much more important around the BDC than around the TDC. This explains why the difference between the maxima in Figure 6.11 for non constant temperature are more important than for minima.

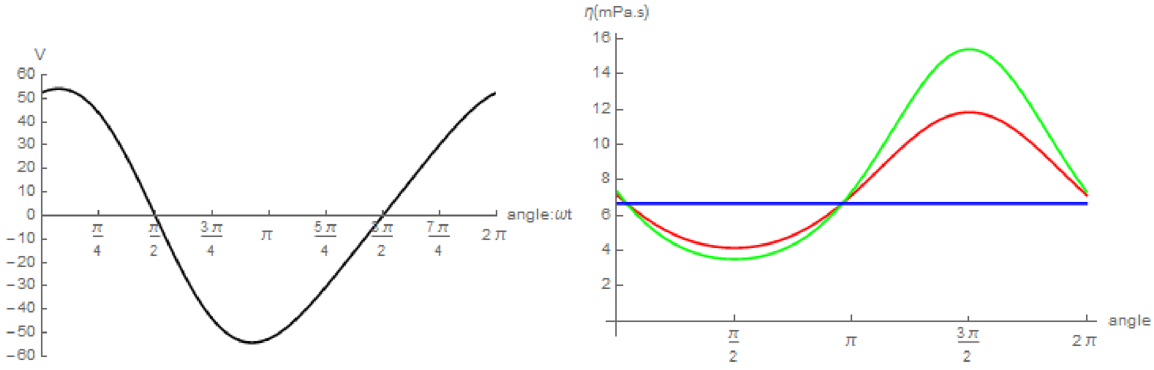

(a) (b)

Figure 6.12: (a) Dimensionless piston velocity (b) Variations of η over an engine cycle, in blue constant temperature 125°C, in red temperature varies from 100°C to 150°C and in green from 90° to 160°C.

In the sequel, we work at constant temperature and henceforth the minimum film thickness is minimum at BDC instead of TDC.

6.5.2 Geometrical parameter influence: part 1

- **Distance between grooves**
  The distance between grooves is $D = D_1 \cos(\alpha)$ where D_1 is the distance between two groove nodes in the sliding direction. This distance D or D_1 is directly related to the groove surface ratio. This ratio can be approximated by $2\Lambda/D$. The exact formula is $\Lambda/D(2 - \Lambda/D)$. The variation of D and also of the groove width indicates the influence of the groove density on the behavior of the minimum film thickness during an engine cycle. Studying Figures 6.13 (or 6.14 which is basically the same), a number of observations can be made. The difference $\Delta H = Hm(t) - Hs(t)$ where $h_s(t)$ is the smooth minimum film thickness at time t, approximately remains constant. Besides, when D is divided by 2 the difference with the smooth case is doubled. It seems then to have roughly a linear behavior in $1/D$. The ratio λ/D should not become too large to keep this linearity. It may

be noticed that the minimum film thickness is only significantly reduced at a high groove density.

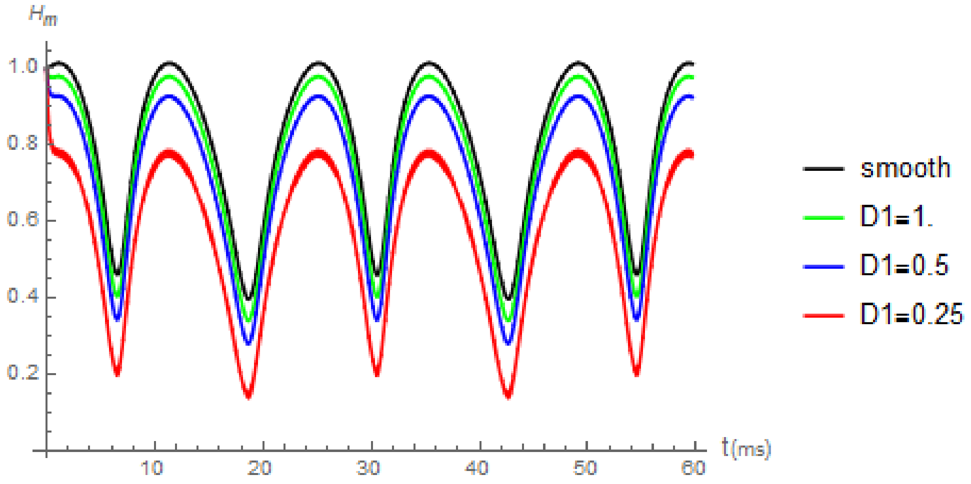

Figure 6.13: Influence of the distance between grooves on $H_m(t)$ for $A = 0.5$, $\Lambda = 0.2$, $\alpha = 15°$, $h_t = 0.05h_x$.

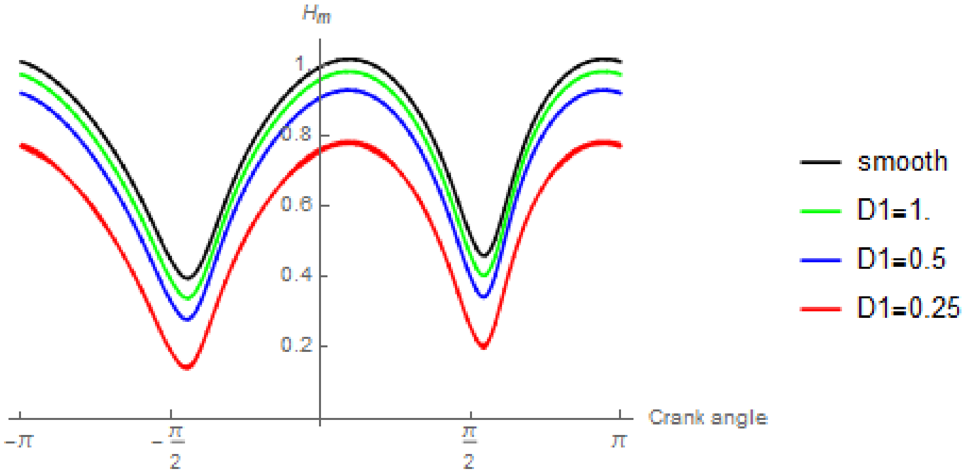

Figure 6.14: Influence, over an engine cycle, of the distance between grooves on H_m for $A = 0.5$, $\Lambda = 0.2$, $\alpha = 15°$, $h_t = 0.05h_x$.

- **Influence of the groove depth**
  The load is inversely proportional to the minimum film thickness. The groove depth causes pressure losses and therefore losses of load carrying capacity. Henceforth the deeper the grooves, the lower the minimum film thickness, as observed in Figures 6.15 or 6.16. Here, it seems that the distance to the smooth case is roughly doubled when the groove depth is doubled. For the considered depth values (in the range $[0.02, 0.5]$, a linear behavior is

observed. The depth is also related to the groove volume and the oil quantity they can contain.

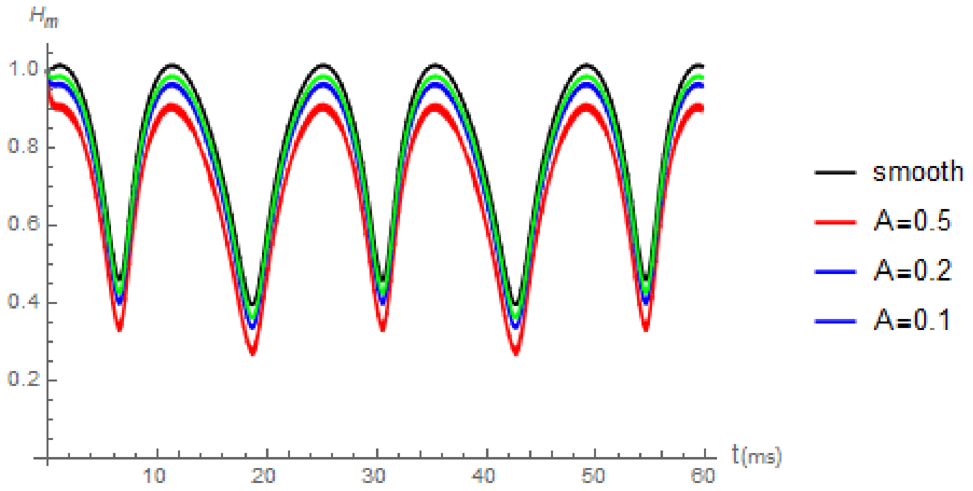

Figure 6.15: Influence of the groove depth on $H_m(t)$ for $D_1 = 0.25$, $\Lambda = 0.1$, $\alpha = 15°$, $h_t = 0.05h_x$.

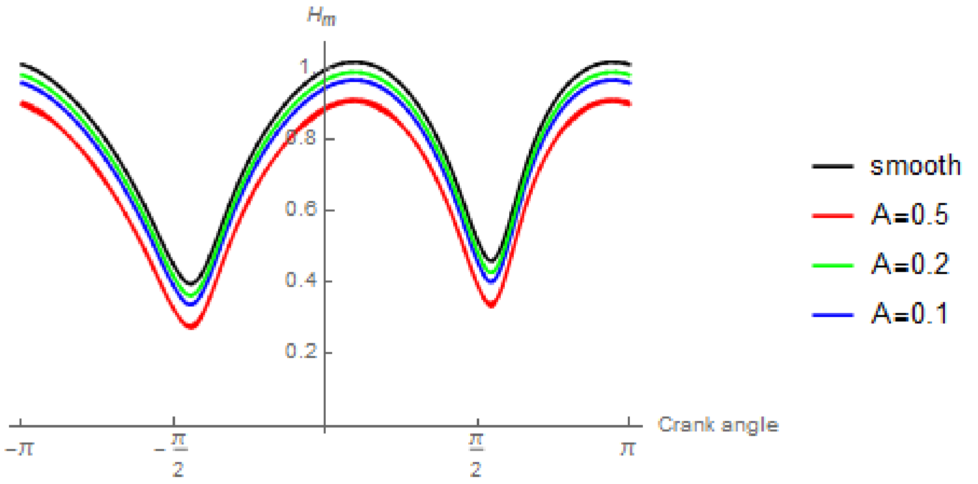

Figure 6.16: Influence, over an engine cycle, of the groove depth on H_m for $D_1 = 0.25$, $\Lambda = 0.1$, $\alpha = 15°$, $h_t = 0.05h_x$.

- **Influence of the groove width**
  The groove width affects the groove density, its volume and the region where there are pressure losses and henceforth LCC losses. The wider the grooves are, the lower the minimum film thickness is. Here too a linear decrease compared to the smooth case can be observed in Figures 6.17 or 6.18.

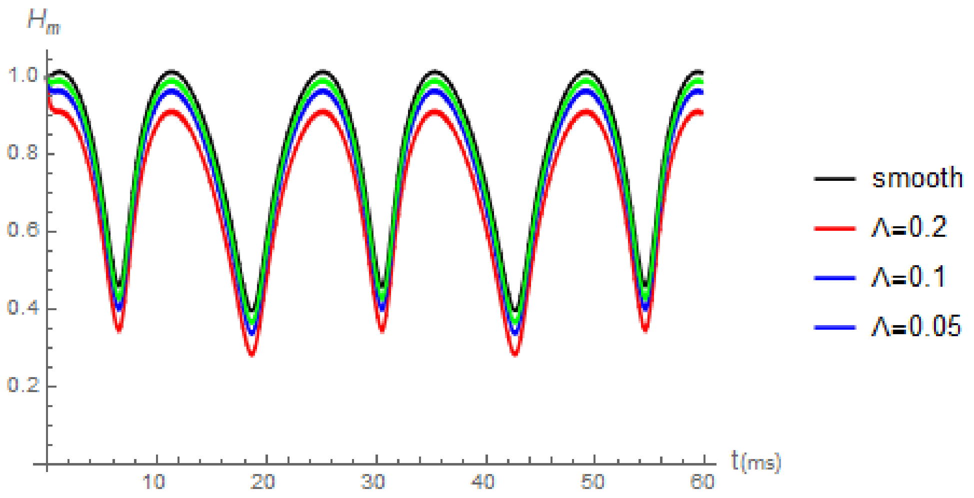

Figure 6.17: Influence of the groove width on $H_m(t)$ for $D_1 = 0.25$, $A = 0.2$, $\alpha = 15°$, $h_t = 0.05h_x$.

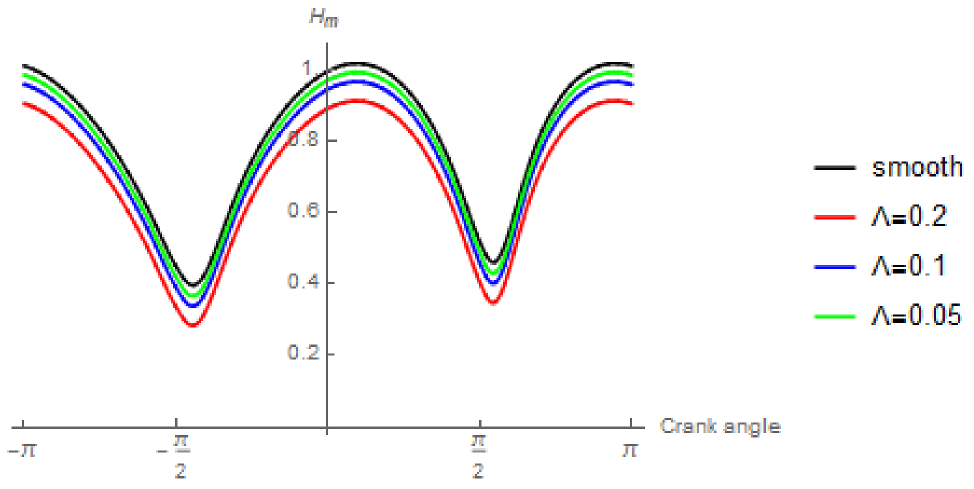

Figure 6.18: Influence, over an engine cycle, of the groove width on H_m for $D_1 = 0.25$, $A = 0.2$, $\alpha = 15°$, $h_t = 0.05h_x$.

- **Influence of the groove angle**
  Figures 6.19 and 6.20 show that for small values, the angle influence is not very significant. It becomes more important for larger values. For a given D_1, as the distance between grooves is $D = D_1 \cos(\alpha)$, the angle influence the groove density through its cosine. For small angles α, $\cos(\alpha) \doteqdot 1 - \alpha^2/2$ and therefore it hardly impacts the D value. This is less true for bigger angles. For the 3 angles that were used in the calculations, we get the following values: $\cos(10°) \approx 0.985$, $\cos(15°) \approx 0.966$ and $\cos(25°) \approx 0.906$.

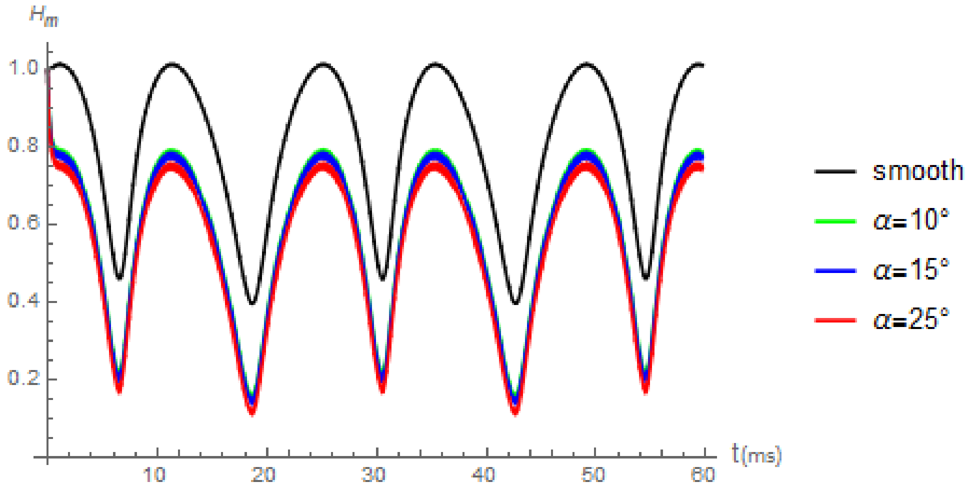

Figure 6.19: Influence of the groove angle on $H_m(t)$ for $D_1 = 0.25$, $A = 0.5$, $\Lambda = 0.2$, $h_t = 0.05h_x$.

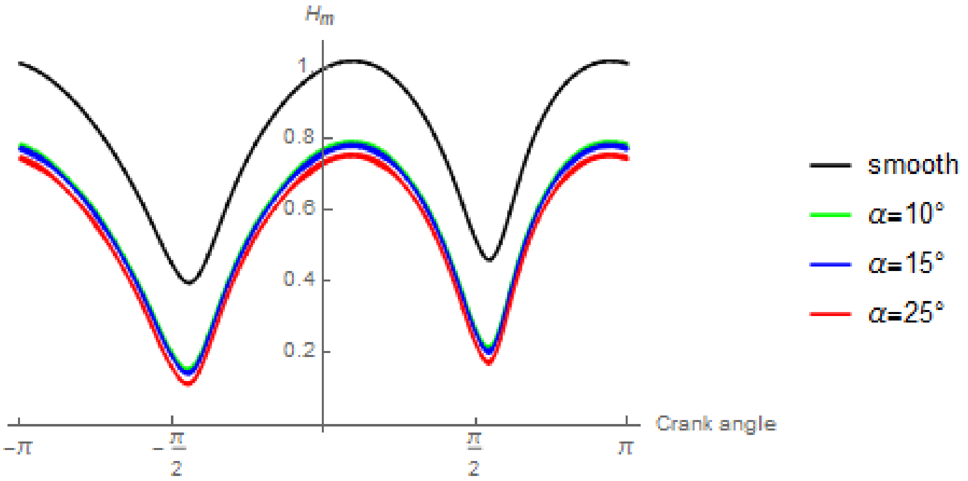

Figure 6.20: Influence, over an engine cycle, of the groove angle on H_m for $D_1 = 0.25$, $A = 0.5$, $\Lambda = 0.2$, $h_t = 0.05h_x$.

6.5.3 Geometrical parameter influence: part 2

The trends presented in the above section are illustrated for some particular parameter values in a more quantitative way. Calculations were performed for the smooth case, for three angles: $\alpha = 10°, 15°, 25°$, for three distances: $D_1 = 1.0, 0.5, 0.25$ and for the values of groove depth and width given in Table 6.2.

For the angle $\alpha = 15°$, calculations were also performed for $D_1 = 0.125$. For $\Lambda = 0.2$, results are not considered since then, the distance between grooves is smaller than the groove width. By looking at the figures of section 6.5.2, it seems that the difference $\Delta H = H - Hs$ between the

$\Lambda = 0.02$	$\Lambda = 0.05$	$\Lambda = 0.1$	$\Lambda = 0.2$
$A = 0.05$	$A = 0.05$	-	-
$A = 0.1$	$A = 0.1$	$A = 0.1$	-
-	$A = 0.2$	$A = 0.2$	$A = 0.2$
-	-	$A = 0.5$	$A = 0.5$

Table 6.2: Chosen values of groove depth A and groove width Λ.

average film thickness H over an engine cycle with the smooth case Hs is inversely proportional to the distance between grooves D, proportional to their width Λ. At first sight it seemed it was also proportional to the groove depth A. The linearity with respect to the width seems to be correct as shown in Figures 6.21 and 6.23 since for a given depth and a given distance the values of $\Delta H/\Lambda$ coincide. But it is not so true for the depth. It seems more exact to say it is proportional to $\approx A^{0.8}$ as shown in Figures 6.22 and 6.24. These figures also illustrate the linearity in $1/D$. For deep grooves $A = 0.5$ the linearity in $1/D$ fails for $D = 0.25$ that is to say for a high groove density. In Figures 6.23 and 6.24, the lines that appear on these figures are deduced from the fit given below.

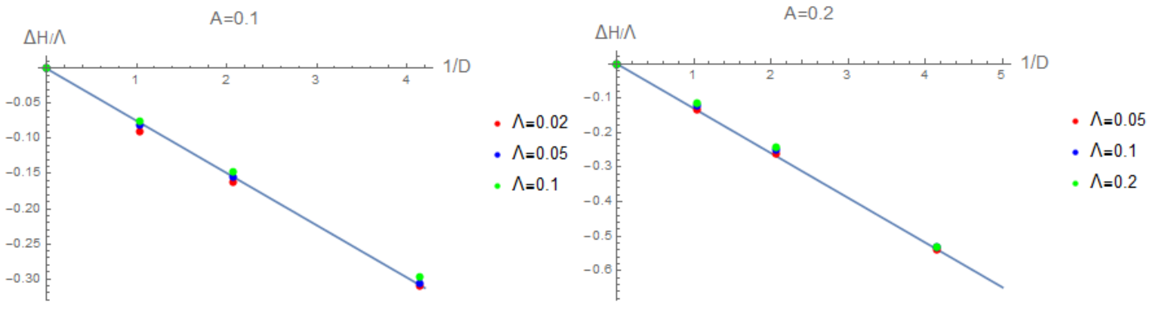

(a) (b)

Figure 6.21: $\Delta H/\Lambda$ with $\Delta H = H - Hs$, average film difference with the smooth case, as a function of $1/D$ for $\alpha = 15^\circ$, $h_t = 0.05h_x$, 8 levels. (a) $A = 0.1$, (b) $A = 0.2$.

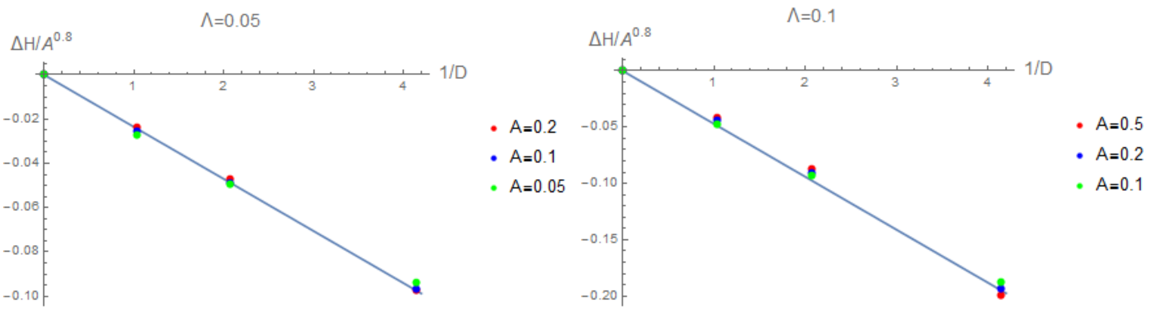

(a)

(b)

Figure 6.22: $\Delta H/A^{0.8}$ with $\Delta H = H - Hs$, average film difference with the smooth case, as a function of $1/D$ for $\alpha = 15°$, $h_t = 0.05h_x$, 8 levels. (a) $\Lambda = 0.05$, (b) $\Lambda = 0.1$.

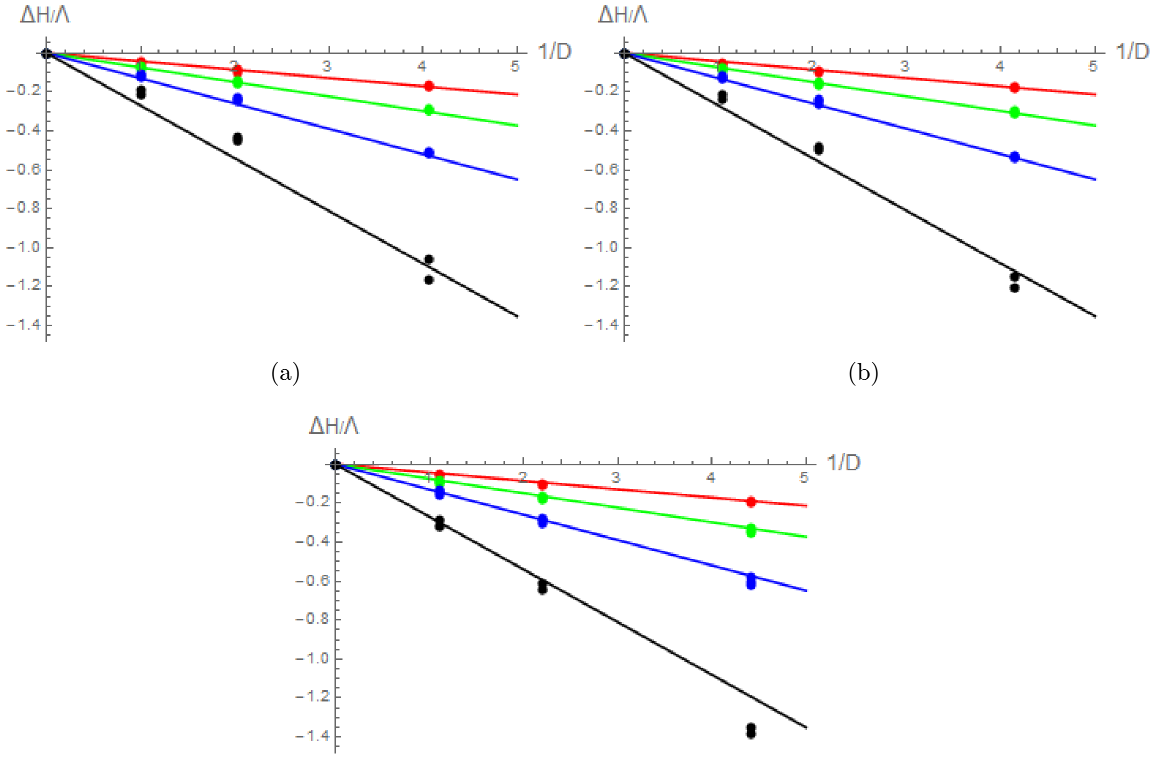

(a)

(b)

(c)

Figure 6.23: $\Delta H/\Lambda$ with $\Delta H = H - Hs$, average film difference with the smooth case, as a function of $1/D$ for $h_t = 0.05h_x$, 8 levels, in red $A = 0.05$, in green $A = 0.1$, in blue $A = 0.2$, in black $A = 0.5$ (a) $\alpha = 10°$, (b) $\alpha = 15°$, (c) $\alpha = 25°$.

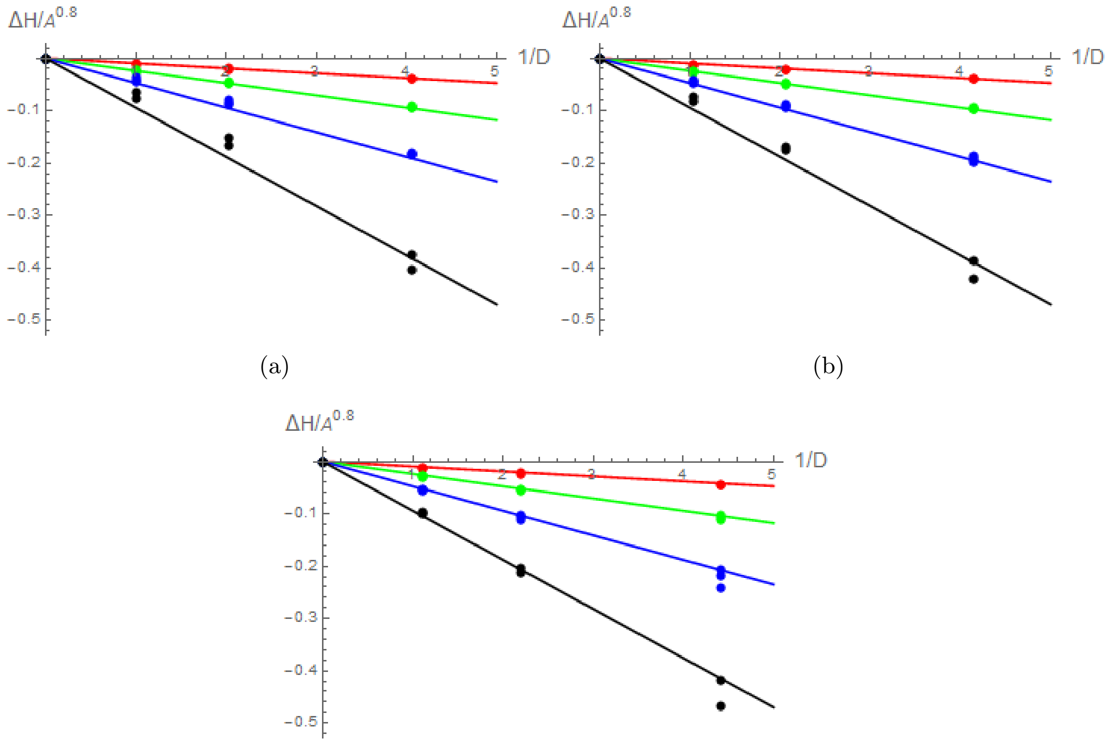

(a)

(b)

(c)

Figure 6.24: $\Delta H/A^{0.8}$ with $\Delta H = H - Hs$, average film difference with the smooth case, as a function of $1/D$ for $h_t = 0.05h_x$, 8 levels, in red $\Lambda = 0.02$, in green $\Lambda = 0.05$, in blue $\Lambda = 0.1$, in black $\Lambda = 0.2$ (a) $\alpha = 10°$, (b) $\alpha = 15°$, (c) $\alpha = 25°$.

In Figure 6.25, all data is represented as a function of $A^{0.8}\Lambda/D$. The linearity seems less valid when $A^{0.8}\Lambda/D$ is large. Using logarithmic scale as shown in Figure 6.26, we obtain a nearly linear behavior. A linear fit of those points is given by the function $\phi(t) = -0.873466 - 0.965134t$ but if we impose the t coefficient to be one (to get a linear dependence of the form γt for the initial data), we obtain a fit with $\psi(t) = -0.754821 - t$. This line is shown in Figure 6.26. It leads to the following approximation of$\Delta H = H - Hs \approx -0.470095A^{0.8}\Lambda/D$. It is shown in Figure 6.25. Further calculations should be performed to define the limits of this linear trend.

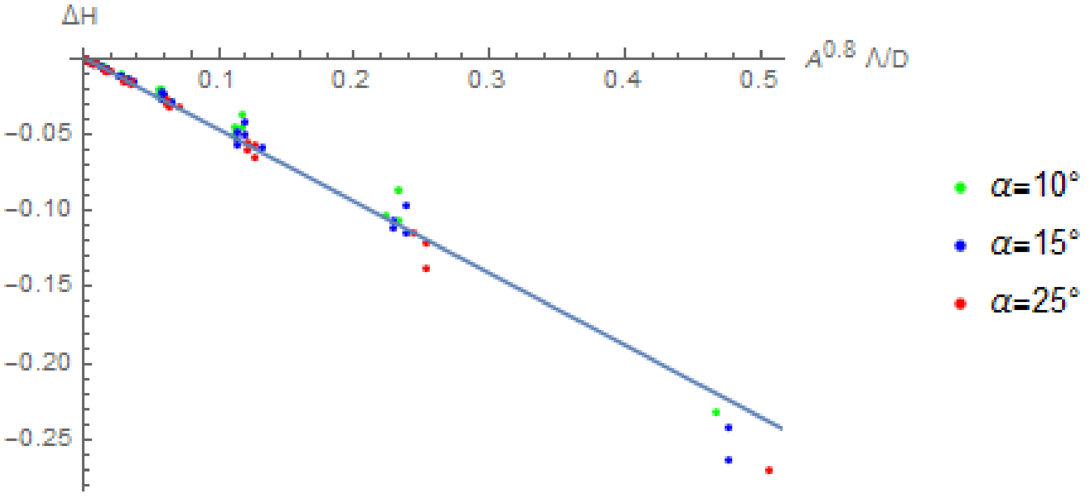

Figure 6.25: Average film thickness difference $Hs - H$ as a function of $A^{0.8}\Lambda/D$, $h_t = 0.05h_x$, 8 levels and the function $-0.47A^{0.8}\Lambda/D$.

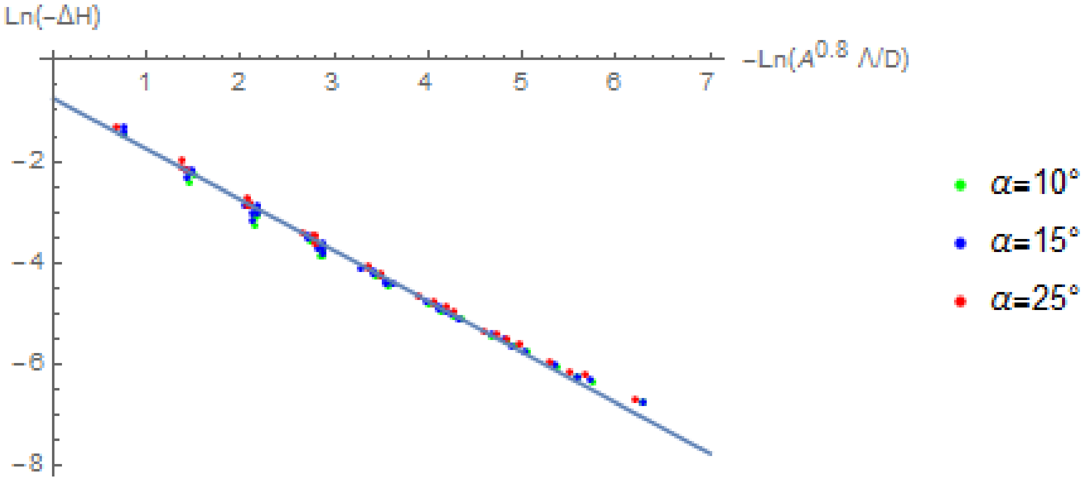

Figure 6.26: $\ln(Hs - H)$ as a function of $-\ln(A\Lambda/D)$ fitted by $f(t) = -0.754821 - t$, $h_t = 0.05h_x$, 8 levels.

6.6 Conclusion

In this chapter the Alcouffe based algorithm developed in the first chapter for the stationary case was completed to include the transient term $\partial H/\partial T$ and used to study, in the PRLC hydrodynamic contact, the influence of the groove parameters for a cross hatched liner on the variations of the minimum film thickness along an engine cycle. The temperature was assumed to be constant although it is easy to include temperature variations in the code. The flow conserving algorithm was not used because in the vicinity of the top and bottom dead center no cavitation occurs and it would have increased the computational time. With our choices this time remains reasonable and should allow further calculations to get a better prediction of the system behavior. The grooves cause a film reduction which is nearly constant over the engine cycle. The film reduction at mid-stroke is rather similar to the film reduction at TDC or BDC. For the range of parameters studied, the influence on the average minimum film thickness was close to linear in $1/D$, A or rather $A^0.8$ and Λ. Linear best fits were found. Our results seem to show a linear behavior of the average film thickness difference $Hs - H$ as a function of $A^{0.8}\Lambda/D$.

Conclusion

In order to improve engine performance and respect the various environmental norms that are now imposed to constructors, it is possible to act on the piston lubrication. Our efforts mostly focused on the piston-ring cylinder liner contact in the hydrodynamic regime. To optimize the lubricant film thickness in order to reduce friction and limit oil consumption, textured surfaces are used. Their geometrical parameters such as configuration, shape, density, volume, ... have to be studied in order to determine a good compromise. Besides the rings geometries are different: parabolic for the top ring or flat for the oil control ring and there are submitted to various conditions depending on their function and position. Because of the experimental study cost and the extent of the problem, it is worth investing in theoretical studies. Because of the required number of calculation points and eventually of time steps for transient problems, multigrid techniques constitute a good option for solving such problems. They are efficient convergence accelerators. However multigrid techniques necessitate a good representation of the target grid problem on coarse grid otherwise they fail.

For the PRCL textured contact, the coefficient of the equation to be solved are highly varying and therefore it is not possible to use a standard geometrical multigrid algorithm as in [5]. An algebraic multigrid algorithm would be a possibility but there are not as efficient in terms of calculation time as a geometrical algorithm. A more robust geometrical multigrid code has been written. It is based on ideas developed by Alcouffe et al. [4] and adapted to the Reynolds equation. All interpolation and restriction operators as well as the coarse grid operators have been coded and explained. The cavitation free boundary was also accounted for.

The obtained code having a much better coarse grid representation than the standard geometrical multigrid algorithm proved to be much more robust. Its efficiency in terms of convergence was demonstrated and it was shown that in spite of the numerous additive stencil calculations, the computing time is only doubled. As memory was not an issue, memory management was not optimized. By taking a closer look to the stencil coefficients, as some are repeated from one step to the next one, it could probably be improved.

The code was validated by comparison with a 1D analytical model and used to study the influence of groove geometrical parameters for a parabolic geometry with a cross-hatched pattern. The influence of the groove position was also studied. Only small groove angles where considered. It was seen that the groove shape has a minor influence while groove depth, density and position are more important factors. Further calculations should be done to better investigate the groove angle influence.

At this stage flow conservation was not considered. For a parabolic geometry it was not very important because although non physical pressure generation appears at the contact outlet, they are very small and do not considerably affect the trends.

However to study the influence of a geometry consisting of dimples for a contact between parallel surfaces with application to a flat ring such as an oil control ring, having a flow conserving algorithm became crucial. It proved to be a difficult task and only a semi-satisfying solution has been obtained. A new relaxation scheme based on the physics of the phenomenon has been written. Coarse grid interpolation and restriction were more difficult since we needed operators for the pressure and the oil film that could not be built in the same way. Finally a solution was adopted by putting the wedge term in the right hand side of the equation. This way, a code was obtained that converges for all starvation conditions for highly varying geometry. Unfortunately, its convergence rate is not fully satisfactory. A difficulty at film formation or re-formation was hard to overcome. At this frontier there are discontinuities in the Couette and Poiseuille flow while Alcouffe et al.'s ideas where based, in our problem, on a continuity of the Poiseuille flow. Many attempts have been made and some are presented in an appendix but this point still requires further work. A promising way may be the use of the $p - \theta$ formulation of the Elrod-Adams problem where p is the pressure and $\theta = hoil/h$ the cavity fraction. It leads to solving a system of the form $G(p, \theta) = 0$ where G is a C^1 function of p and θ (see [36]). This was not tried and is maybe the next step for improving our code.

The flow conserving code was applied to the study of dimple influence for the lubrication of parallel surfaces and possible use for the oil control ring. Without texture no load carrying capacity can be generated. In particular the dimple position in the contact was studied. It was shown that the loss of pressure when the texture lies in the outlet is less than the gain when it is located in the inlet. The influence of the dimple parameters, of the ambient pressure on the load carrying capacity was also studied. It was noted that the parameter influence is stronger for an inlet texture than for an outlet one.

Finally, the transient term of the Reynolds equation was added to our code. It implies many stencil re-calculations at each time step and each time the minimum film thickness is updated. It was used to study the variations of the minimum film thickness along an engine cycle in the lubrication of a parabolic ring and a cross-hatched groove liner. The temperature was assumed to be constant and the ring tension too. Variations of those 2 parameters could have easily been introduced. We did not use the flow conserving algorithm because in the vicinity of TDC and BDC, where the minimum film thickness is lowest, no cavitation occurs. Considering the number of time steps that were necessary, the present flow conserving algorithm would need a substantial increase in computation time. We were able to deduce a curve fitted formula for the average film thickness difference with the smooth case in terms of groove parameters.

Perspectives:

- Further calculations with the existing code in order to more thoroughfully study the influence of texture on lubrication and confirm, or not, certain observed trends.
- Adapt and use our codes on real textured surfaces.
- Adapt Alcouffe et al.'s ideas to elastohydrodynamic lubrication.
- Pursue investigation to get a more robust flow conserving code and in particular try the $p - \theta$ method([36]).

Bibliography

[1] Holmberg Kenneth. and Erdemir Ali. Global impact of friction on energy consumption, economy and environment. *FME Transactions*, 43:181–185, 2015. (Cited on page 6.)

[2] Heywood J. B. .H. *Internal combustion Engine Fundamentals*. Mc Graw Hill, 1988. (Cited on page 8.)

[3] Wong Victor W. and Tung Simon C. Overview of automotive engine friction and reduction trends – Effects of surface, material and lubricant-additive technologies. *Springerlink.com open access, Friction*, 4:1–28, 2016. (Cited on pages 8 and 10.)

[4] Alcouffe R. E., Brandt A., Dendy J. E., and Painter J. W. The multi–grid method for the diffusion equation with strongly discontinuous coefficients. *SIAM J. Sci. Stat. Comput.*, 2:430–454, 1981. (Cited on pages 9, 11, 13, 23, 95, 119 and 134.)

[5] Venner C. H. and Lubrecht A. A. *Multilevel methods in lubrication*. Elsevier, 2000. Tribology Series, Vol. 37. (Cited on pages 10, 11, 12, 30, 31, 37, 39, 98 and 119.)

[6] Biboulet N. and Lubrecht A. A. Analytical solution for textured piston ring - cylinder liner contacts (1D analysis). *Tribology International, Elsevier*, 96:269–278, 2016. (Cited on pages 10, 44, 45, 46, 47 and 137.)

[7] Fedorenko R. P. A relaxation method for solving elliptic difference equations. *USSR Computational Math. and Math. Phys.*, 1:1092–1096, 1962. (Cited on page 12.)

[8] Fedorenko R. P. The speed of convergence of one iterative process. *USSR Computational Math. and Math. Phys.*, 4:227–235, 1964. (Cited on page 12.)

[9] Brandt A. 1984 multigrid guide, lightly revised 2011.
URL= http://www.wisdom.weizmann.ac.il/ achi/. (Cited on pages 12 and 23.)

[10] Briggs W., Henson V., and McCormick S. *A multigrid tutorial – Second edition*. SIAM, 2000. (Cited on pages 12, 23 and 154.)

[11] Elrod H.G. A Cavitation Algorithm. *ASME J. of Lub. Tech*, pages 350–354, 1981. (Cited on pages 24, 53 and 72.)

[12] Elrod H.G. and Adams M.L. A computer program for Cavitation and Starvation Problems. *Proceedings of the 1st Leeds-Lyon Symposium on Tribology*, pages 37–41, 1974. (Cited on pages 24, 53 and 72.)

[13] Ma M. T., Sherrington I., and Smith E. H. Analysis of lubrication and friction for a complete piston-ring pack with an improved oil availability model Part 1: circumferentially uniform film. *Proc.ImechE Part J: Engineering Tribology*, 211(1):1–15, 1997. (Cited on page 43.)

[14] Ma M. T., Sherrington I., Smith E. H., and Grice N. Development of a detailed model for piston-ring lubrication in IC engines with circular and non-circular cylinder bores. *Tribology international*, 30(11):779–788, 1997. (Cited on page 43.)

[15] Mishra P. C., Rahnejat H., and King P. D. Tribology of the ring-bore conjunction subject to a mixed regime of lubrication. *Proc.ImechE Part J: Engineering Tribology*, 223(4):987–998, 2009. (Cited on page 43.)

[16] Chen H. Modeling of liner finish effects on oil control ring lubrication in internal combustion engines based on deterministic method. *Mechanical Engineering - Master's degree, URL=http://hdl.handle.net/1721.1/44872*, 2008. (Cited on page 43.)

[17] Grabon W., Pawlus P., and Sep J. Tribological characteristics of one-process and two-process cylinder liner honed surfaces under reciprocating sliding conditions. *Tribology international, Elsevier*, 43(10):1882–1892, 2010. (Cited on page 43.)

[18] Bouassida H. *Lubricated piston ring cylinder liner contact: influence of the liner microgeometry*. PhD thesis, INSA Lyon, 2014. (Cited on page 43.)

[19] Pascovici M.D., Cicone T., Fillon M., and Dobrica M.B. Analytical investigation of a partially textured parallel slider. *Proceedings of the Institution of Mechanical Engineers, part J: Journal of Engineering Tribology*, 223(8):151–158, 2009. (Cited on page 43.)

[20] Tala-Ighil N., Fillon M., and Maspeyrot P. Effect of textured area on the performances of a hydrodynamic journal bearing. *Tribology international, Elsevier*, 44(3):211–219, 2011. (Cited on pages 43, 73 and 79.)

[21] Dobrica M.B., Fillon M., Pascovici M.D., and Cicone T. Optimizing surface texture for hydrodynamic lubricated contacts using a mass-conserving numerical approach. *Proceedings of the Institution of Mechanical Engineers, part J: Journal of Engineering Tribology*, 224:737–750, 2010. (Cited on pages 43 and 73.)

[22] Rahmani R., Mirzaee I., Shirvani A., and Shirvani H. An analytical approach for analysis and optimization of slider bearings with infinite width parallel textures. *Tribology International, Elsevier*, 43:737–750, 2010. (Cited on page 43.)

[23] Organisciack M. *Optimisation de la microgéométrie des chemises des moteurs à combustion interne.* PhD thesis, INSA Lyon, 2007. (Cited on page 43.)

[24] Dimkovski Z., Anderberg C., Ohlsson R., and Rosén B.-G. Characterisation of worn cylinder liner surfaces by segmentation of honing and wear scratches. *Wear, Elsevier*, 41:40–46, 2010. (Cited on page 43.)

[25] Cabanettes F., Dimkovski Z., and Rosén B.-G. Roughness variations in cylinder liners induced by honing tools' wear. *Precision engineering, Elsevier*, 41:40–46, 2015. (Cited on page 43.)

[26] Imai N. and Kato T. Effects of texture patterns on hydrodynamic and mixed lubrication characteristics. *Proceedings of the Institution Of Mechanical Engineers, part J- Journal of Engineering Tribology*, 227:898–904, 2013. (Cited on page 43.)

[27] Liu L. and Tian T. Modeling piston ring-pack lubrication with consideration of ring structural response. *SAE Technical Paper Series*, (2005-01-1641):40–46, 2005. (Cited on page 43.)

[28] Bouassida H., Biboulet N., Sainsot P., and Lubrecht A.A. Piston ring load carrying capacity: influence of cross-hatching parameters. *Proceedings of the Institution Of Mechanical Engineers, part J- Journal of Engineering Tribology*, 228:642–648, 2014. (Cited on page 43.)

[29] Biboulet N., Bouassida H., and Lubrecht A.A. Cross hatched texture influence on the load carrying capacity of oil control rings. *Tribology International*, 82:12–19, 2015. (Cited on page 43.)

[30] Patir N. and Cheng H.S. An average flow model for determining effects of three-dimensional roughness on partial hydrodynamic lubrication. *Transactions of the ASME, Journal of tribology*, 100:12–17, 1978. (Cited on page 43.)

[31] Bayada G., Martin S., and Vasquez C. An average flow model of the Reynolds roughness including a mass-flow preserving cavitation model. *Transactions of the ASME, Journal of tribology*, 127:793–802, 2005. (Cited on pages 43, 53 and 73.)

[32] Almqvist T. and Dasht J. 'the homogenization process of the reynolds equation describing compressible liquid flow. (Cited on page 43.)

[33] Sahlin F., Almqvist T., Larsson R., and Glavatskih S. Rough surface flow factors in full film lubrication based on a homogenization technique. *Tribology International, Elsevier*, 40(6):325–333, 2011. (Cited on page 43.)

[34] Ausas R., Ragot P., Leiva J., Jai M., Bayada G., and Buscaglia G. The impact of the cavitation model in the analysis of microtextured lubricated journal bearings. *Transactions of the ASME, Journal of tribology*, 129:868–875, 2007. (Cited on pages 53 and 72.)

[35] Giacopini M., Fowell M. T., Dini D., and Strozzi A. A mass-conserving complementarity formulation to study lubricant films in the presence of cavitation. *Transactions of the ASME, Journal of tribology*, 132:041702–1–041702–12, 2010. (Cited on pages 53, 73 and 74.)

[36] Woloszynski T., Podsiadlo P., and Stachowiak G. W. Efficient solution to the cavitation problem in hydrodynamic lubrication. *Tribology letters, Springer*, 58(1), 2015. (Cited on pages 53, 69, 74, 120 and 155.)

[37] Qiu Y. and Khonsari M. M. On the prediction of cavitation in dimples using a mass-conservative algorithm. *Transactions of the ASME, Journal of tribology*, 131:041702–1–041702–11, 2009. (Cited on pages 53 and 73.)

[38] Etsion I., Halperin G., Brizmer V., and Kligerman Y. Experimental investigation of laser textured parallel thrust bearings. *Tribology Letters*, 17(2):295–300, 2004. (Cited on page 72.)

[39] Kligerman Y., Etsion I., and Shinkarenko A. Improving tribological performance of piston rings by partial surface texturing. *Transactions of the ASME, Journal of tribology*, 127:632–638, 2005. (Cited on page 72.)

[40] Brizmer V., Kligerman Y., and Etsion I. A laser surface textured parallel thrust bearing. *Tribology Transactions*, 46:397–403, 2003. (Cited on page 72.)

[41] Etsion I., Kligerman Y., and Halperin G. Analytical and experimental investigation of laser-textured mechanical seal faces. *Tribology Transactions*, 42(3):511–516, 1999. (Cited on pages 72 and 94.)

[42] Ryk G., Kligerman Y., and Etsion I. Experimental investigation of laser surface texturing for reciprocating automotive components. *Tribology Transactions*, 45(4):444–449, 2002. (Cited on pages 72 and 94.)

[43] Etsion I. and Halperin G. A laser surface textured hydrostatic mechanical seal. *Tribology Transactions*, 45(3):430–434, 2002. (Cited on page 72.)

[44] Tonder K. Hydrodynamics effects of taylored inlet roughness: extended theory. *Tribology International, Elsevier*, 37:137–142, 2004. (Cited on page 72.)

[45] Wakuda M., Yamauchi Y., Kanzaki S., and Yasuda Y. Effect of surface texturing on friction reduction between ceramic and steel materials under lubricated sliding contact. *Wear, Elsevier*, 254:356 – 363, 2003. (Cited on page 72.)

[46] Vladescu S.-C., Olver A.V., Pegg I.G., and Reddyhoff T. The effects of surface texture in reciprocating contacts - An experimental study. *Tribology International, Elsevier*, 82:28–42, 2015. (Cited on pages 72 and 94.)

[47] Lu P., Wood R.J.K., Gee M.G., Wang L., and Pfleging W. The friction reducing effect of square-shaped surface textures under lubricated line-contacts - An experimental study. *Lubricants*, 4(3):26, 2016. (Cited on page 72.)

[48] Tomanik E. Modeling the hydrodynamic support of cylinder bore and piston rings with laser textured surfaces. *Tribology International, Elsevier*, 59:90–96, 2013. (Cited on pages 72, 79 and 94.)

[49] Fowell M. T., Olver A.V., Gosman A.D., Spikes H.A., and Pegg I. Entrainment and inlet suction: two mechanisms of hydrodynamic lubrication in textured bearings. *Transactions of the ASME, Journal of tribology*, 129:336–347, 2007. (Cited on pages 72 and 79.)

[50] Fowell M. T., Medina S., Olver A.V., Spikes H.A., and Pegg I.G. Parametric study of texturing in convergent bearings. *Tribology International, Elsevier*, 52:7–16, 2012. (Cited on page 72.)

[51] Pascovici M.D., Cicone T., and Fillon M. andDobrica M.B. Analytical investigation of a partially textured parallele slider. *Proceedings of the Institution of Mechanical Engineers, part J: Journal of Engineering Tribology*, 223(2):151–158, 2009. (Cited on page 72.)

[52] Rahmani R., Shirvani A., and Shirvani H. Optimization of partially textured parallel thrust bearings with square-shaped micro-dimples. *Tribology Transactions*, 50:3:401–406, 2007. (Cited on page 72.)

[53] Jakobsson B. and Floberg L. The finite journal bearing considering vaporization. *Transactions of Chalmers University of Technology,*, Guthenburg, Sweden, Report 190, 1957. (Cited on page 72.)

[54] Olsson K.O. Cavitation in dynamically loaded bearing. *Transactions of Chalmers University of Technology*, Guthenburg, Sweden, Report 380, 1965. (Cited on page 72.)

[55] D. Vijayaraghavan and T. G. Keith Jr. Development and Evaluation of a Cavitation Algorithm. *Tribology Transactions*, 32(2):225–233, 1989. (Cited on page 73.)

[56] Bertocchi L., Dini D., Giacopini M., Fowell M. T., and Baldini A. Fluid film lubrication in the presence of cavitation: a mass-conserving two-dimensional formulation for compressible, piezoviscous and non-Newtonian fluids. *Tribology International, Elsevier*, 67:61–71, 2013. (Cited on page 73.)

[57] Ausas R., Jai M., Ciuperca I., and Buscaglia G. Conservative one-dimensional finite volume discretization of a new cavitation model for piston-ring lubrication. *Tribology international, Elsevier*, 57:54–66, 2013. (Cited on page 73.)

[58] Profito F.J., Giacopini M., Zachariadis D.C., and Dini D. A General Finite Volume Method for the Solution of the Reynolds Lubrication Equation with a Mass-Conserving Cavitation Model. *Tribology Letters*, 60, 2015. (Cited on page 73.)

[59] Sahlin F., Glavatskih S., Almqvist T., and Larsson R. Two-dimensional CFD-analysis of micro-patterned surfaces in hydrodynamic lubrication. *Transactions of the ASME, Journal of tribology*, 127:96–102, 2005. (Cited on page 73.)

[60] Menon Dileep P., Anil P.M., and Kulkarni Prakash S. An analysis on the influence of oil pocket shape and distribution on the reduction of friction in hydrodynamic lubrication. *17th Annual CFD Symposium*, 2015. (Cited on page 73.)

[61] Dobrica M.B. and Fillon M. About the validity of Reynolds equation and inertia effects in textured sliders of infinite width. *Proceedings of the Institution of Mechanical Engineers, part J: Journal of Engineering Tribology*, 223(1):69–78, 2009. (Cited on page 73.)

[62] Cupillard S., Glavatskih S., and Cervantes M.J. Computational fluid dynamic analysis of a journal bearing with surface texturing. *Proceedings of the Institution Of Mechanical Engineers, part J- Journal of Engineering Tribology*, 222(4):97–107, 2007. (Cited on page 73.)

[63] Cupillard S., Cervantes M.J., and Glavatskih S. Pressure buildup mechanism in a textured inlet of a hydrodynamic contact. *Transactions of the ASME, Journal of tribology*, 130(4):021701–1–021701–10, 2008. (Cited on page 73.)

[64] Shen Cong and Khonsari M.M. On the magnitude of cavitation pressure of steady-state lubrication. *Tribology Letters*, 51:153–160, 2013. (Cited on page 73.)

[65] Shen Cong and Khonsari M.M. Effect of dimple's internal structure on hydrodynamic lubrication. *Tribology Letters*, 52:415–430, 2013. (Cited on page 74.)

[66] Shen Cong and Khonsari M.M. Numerical optimization of texture shape for parallel surfaces under unidirectional and bidirectional sliding. *Tribology International, Elsevier*, 82:1–11, 2015. (Cited on page 74.)

[67] Shen Cong and Khonsari M.M. The effect of laser machined pockets on the lubrication of piston ring prototypes. *Tribology International, Elsevier*, 101:273–283, 2016. (Cited on pages 74, 79 and 94.)

[68] Gherca A.R., Maspeyrot P., Hajjam M., and Fatu A. Influence of texture geometry on the hydrodynamic performances of parallel bearings. *Tribology Transactions*, 56:3:321–332, 2013. (Cited on page 74.)

[69] Gherca A.R., Fatu A., Hajjam M., and Maspeyrot P. Effects of surface texturing in steady-state and transient flow conditions: two-dimensional numerical simulation using a mass-conserving cavitation model. *Proceedings of the Institution Of Mechanical Engineers, part J- Journal of Engineering Tribology*, 229(4):505–522, 2015. (Cited on page 74.)

[70] Medina S., Fowell M.T., Vladescu S.-C., Reddyhoff T., Pegg I., Olver A.V., and Dini D. Transient effects in lubricated textured bearings. *Proceedings of the Institution Of Mechanical Engineers, part J- Journal of Engineering Tribology*, 229(4):523–537, 2015. (Cited on pages 74 and 94.)

[71] Ryk G. and Etsion I. Testing piston rings with partial laser surface texturing for friction reduction. *Wear, Elsevier*, 261:792–796, 2006. (Cited on pages 79 and 94.)

[72] Etsion I. and Sher E. Improving fuel efficiency with laser surface textured piston rings. *Tribology International*, 42:542–547, 2009. (Cited on page 79.)

[73] Castleman R.A. A hydrodynamic theory of piston ring lubrication. *Journal of applied physics*, 7(9):364–367, 1936. (Cited on page 93.)

[74] Eilon S. and Saunders A. A study of piston-ring lubrication. *Proceedings of the Institution of Mechanical Engineers*, 171(1):427–462, 1957. (Cited on page 93.)

[75] Furuhuhama S. A dynamic theory of piston-ring lubrication. *Bulletin of JSME*, 2(7):423–428, 1959. (Cited on page 93.)

[76] JengY. R. Theoretical analysis of piston-ring lubrication part I: fully flooded lubrication. *Tribology transactions*, 35(4):696–706, 1992. (Cited on pages 93 and 99.)

[77] JengY. R. Theoretical analysis of piston-ring lubrication part II: starved lubrication and its application to a complete ring pack. *Tribology transactions*, 35(4):707–714, 1992. (Cited on page 93.)

[78] Priest M., Dowson D., and Taylor C.M. Predictive wear modeling of lubricated piston rings in a diesel engine. *Wear, Elsevier*, 231:89–101, 1999. (Cited on page 94.)

[79] Tian T., Wong V.W., and Heywood J. A piston ring-pack film thickness and friction model for multigrade oils and rough surfaces. *SAE Technical Paper*, 962032, 1996. (Cited on page 94.)

[80] Akalin O. and Newaz G.M. Piston ring-cylinder Bore friction modeling in mixed lubrication regime: part I - analytical results. *Journal of Tribology*, 123:211–218, 2001. (Cited on page 94.)

[81] Taylor R. I. Squeeze film lubrication in piston rings and reciprocating contacts. *Proc.ImechE Part J: Engineering Tribology*, 229(8):977–988, 2015. (Cited on pages 94, 95 and 99.)

[82] Spencer A., Almqvist T., and Larsson R. A semi-deterministic texture-roughness model of the piston ring-cylinder liner contact. *Proceedings of the Institution of Mechanical Engineers, part J- Journal of Engineering Tribology*, 225:994–1002, 2011. (Cited on page 94.)

[83] Vladescu S.-C., Ciniero A., Tufail K., Gangopadhyay A., and Reddyhoff T. Looking into a laser textured piston ring-liner contact. *Tribology International, Elsevier*, 115:140–153, 2017. (Cited on pages 94 and 95.)

[84] Vladescu S.-C., Medina S .and Olver A.V., Pegg I.G., and Reddyhoff T. Lubricant film thickness and friction force measurements in a laser surface textured reciprocating line contact simulating the piston-ring liner pairing. *Tribology International, Elsevier*, 98:317–329, 2016. (Cited on page 94.)

[85] Gherca A.R., Fatu A., Hajjam M., and Maspeyrot P. Influence of surface geometry on the hydrodynamic performances of parallel bearings in transient flow condition. *Tribology Transactions*, 56:953–967, 2013. (Cited on page 94.)

[86] Biboulet N., Bouassida H., Cavoret J., and Lubrecht A.A. Determination of fundamental parameters for the cross-hatched cylinder liner micro-geometry. *Proc.ImechE Part J: Engineering Tribology*, 213(3):293–301, 2014. (Cited on page 94.)

[87] Kwak Do Y.. and Lee Jun S. Multigrid algorithm for the cell-centered finite difference method II: discontinuous coefficient case. *Applied Mathematics and Computation*, 105(1):77–85, 1999. (Cited on page 150.)

Appendices

Appendix A

Algorithm complements

A.1 Alcouffe discretization of the term σU

To complete the volume discretization described in chapter 1, section 1.4 and although in our applications the function σ will be zero and therefore we had skip this part, we account here for the integral of $\sigma(x, y)U(x, y)$ over a cell. With the notations of that section:

$$\iint_\Delta \sigma(x,y)U(x,y)\,\mathrm{d}x\mathrm{d}y \approx U_{i,j} \iint_\Delta \sigma(x,y)\,\mathrm{d}x\mathrm{d}y \approx C_{i,j}U_{i,j} \tag{A.1}$$

with

$$C_{i,j} = \frac{1}{4}(h_{i-1}k_{j-1}\sigma_{i-\frac{1}{2},j-\frac{1}{2}} + h_i k_{j-1}\sigma_{i+\frac{1}{2},j-\frac{1}{2}} + h_{i-1}k_j\sigma_{i-\frac{1}{2},j+\frac{1}{2}} + h_i k_j \sigma_{i+\frac{1}{2},j+\frac{1}{2}}) \tag{A.2}$$

Thus we obtain:

$$-A_{i,j+\frac{1}{2}}(U_{i,j+1}-U_{i,j})-A_{i,j-\frac{1}{2}}(U_{i,j-1}-U_{i,j})-B_{i+\frac{1}{2},j}(U_{i+1,j}-U_{i,j})-B_{i-\frac{1}{2},j}(U_{i-1,j}-U_{i,j})+C_{i,j}U_{i,j} = F_{i,j} \tag{A.3}$$

A priori, these formulas are only valid for an inner rectangle. They can be extended to the boundary rectangles by setting the functions f, σ and D to 0 outside Ω and adding to $C_{i,j}$ the following term $C'_{i,j}$:

$$C'_{i,j} = \begin{cases} 0 & \text{if } (i,j) \text{ is an inner point of } \Omega \\ \frac{k_{j-1}+k_j}{2}\gamma_{i,j} & \text{if } i = 0 \text{ or } i = i_{max} \\ \frac{h_{i-1}+h_i}{2}\gamma_{i,j} & \text{if } j = 0 \text{ or } j = j_{max} \end{cases}$$

Where $\gamma_{i,j}$ is the value of the function γ that was defined in section 1.3 at the node (i, j). Indeed, if for instance, we consider a left boundary cell as represented in figure C.11, remembering that the functions f, D, σ are set to 0 outside Ω. For $i = 0$, everything is unchanged (null functions outside Ω) except that now, $\int_{P_3}^{P_1} D\partial U/\partial x\,\mathrm{d}x\mathrm{d}y$ must be added to estimate $\iint_\Delta -\nabla(D\cdot\nabla U)\,\mathrm{d}x\mathrm{d}y$. On the segment $[P_1, P_3]$,

$$\nu(x,y)\cdot D(x,y)\nabla U(x,y) = (-1,0)\cdot(D\frac{\partial U}{\partial x}, D\frac{\partial U}{\partial y}) = -D\frac{\partial U}{\partial x} = \gamma(x,y)U(x,y)$$

Hence

$$\int_{P_3}^{P_1} D\frac{\partial U}{\partial x}\,\mathrm{d}x\mathrm{d}y = -\int_{P_1}^{P_3} D\frac{\partial U}{\partial x}\,\mathrm{d}x\mathrm{d}y \approx \gamma_{i,j}U_{i,j}\frac{k_{j-1}+k_j}{2}$$

which yields the expected result. Similar calculations can be performed on the other parts of the boundary of Ω.

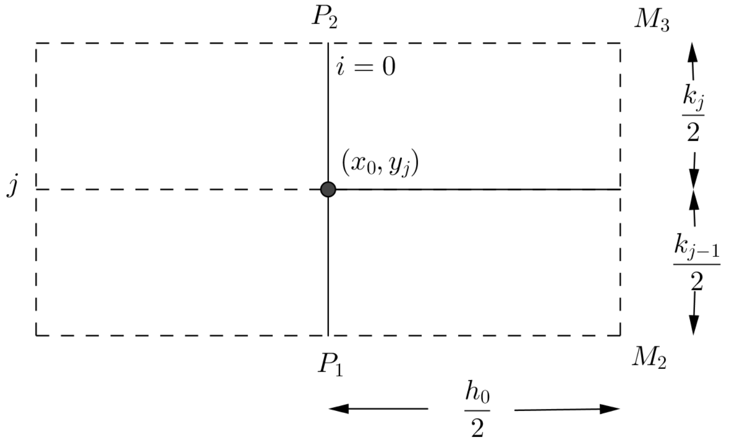

Figure A.1: Left Boundary cell

A.2 Coarse grid operator

Galerkin method: the operator L^{k-1} on grid $k-1$ is deduced from the fine grid operator by the following calculation rule:

$$L^{k-1} = I_k^{k-1}\, L^k\, I_{k-1}^k.$$

The stencil of this linear operator at the point (i_C, j_C) is determined by finding the image of basis function $u^{k-1} = e_{i_C,j_C}^{k-1}$. Remember that e_{i_C,j_C}^{k-1} is the coarse grid function that has the value 1 at node (i_C, j_C) and 0 elsewhere. To simplify the notations, the stencil of I_{k-1}^k at point (i_C, j_C) is denoted:

$$\begin{bmatrix} nw & n & ne \\ w & c & e \\ sw & s & se \end{bmatrix} \tag{A.4}$$

The stencil of L^k at the point (i, j) is denoted:

$$\begin{bmatrix} L_{nw}^k(i,j) & L_n^k(i,j) & L_{ne}^k(i,j) \\ L_w^k(i,j) & L_c^k(i,j) & L_e^k(i,j) \\ L_{sw}^k(i,j) & L_s^k(i,j) & L_{se}^k(i,j) \end{bmatrix} \tag{A.5}$$

The influence of $L^k\, I_{k-1}^k$ on $u^{k-1} = e_{i_C,j_C}^{k-1}$ extends to the 25 points of the fine grid k surrounding the point$(i_F, j_F) \equiv (i_C, j_C)$. The result of $I_{k-1}^k\, e_{i_C,j_C}^{k-1}$ is

$$\begin{bmatrix} 0 & 0 & 0 & 0 & 0 \\ 0 & nw & n & ne & 0 \\ 0 & w & c & e & 0 \\ 0 & sw & s & se & 0 \\ 0 & 0 & 0 & 0 & 0 \end{bmatrix} \tag{A.6}$$

The result of $L^k\, I^k_{k-1}\, e^{k-1}_{i_C,j_C}$ at the 25 points around (i_F, j_F) is then

$$\begin{bmatrix} t(0,4) & t(1,4) & t(2,4) & t(3,4) & t(4,4) \\ t(0,3) & t(1,3) & t(2,3) & t(3,3) & t(4,3) \\ t(0,2) & t(1,2) & t(2,2) & t(3,2) & t(4,2) \\ t(0,1) & t(1,1) & t(2,1) & t(3,1) & t(4,1) \\ t(0,0) & t(1,0) & t(2,0) & t(3,0) & t(4,0) \end{bmatrix} \tag{A.7}$$

Elsewhere its value is 0. Using the stencils of L^k, one has for instance:

$$\begin{aligned} t(0,0) &= sw \times L^k_{sw}(i_F{-}1, j_F{-}1) \\ t(0,1) &= sw \times L^k_{w}(i_F{-}1, j_F{-}1) + w \times L^k_{sw}(i_F{-}1, j_F) \\ t(0,2) &= sw \times L^k_{nw}(i_F{-}1, j_F{-}1) + w \times L^k_{w}(i_F{-}1, j_F) + nw \times L^k_{sw}(i_F{-}1, j_F+1) \\ t(0,3) &= w \times L^k_{nw}(i_F{-}1, j_F) + nw \times L^k_{w}(i_F{-}1, j_F+1) \\ t(0,4) &= nw \times L^k_{nw}(i_F{-}1, j_F+1) \\ t(1,0) &= sw \times L^k_{s}(i_F{-}1, j_F{-}1) + s \times L^k_{sw}(i_F, j_F{-}1) \\ &.... \\ t(2,2) &= sw \times L^k_{ne}(i_F{-}1, j_F{-}1) + s \times L^k_{n}(i_F, j_F{-}1) + se \times L^k_{nw}(i_F+1, j_F{-}1) \\ &\quad + w \times L^k_{e}(i_F-1, j_F) + c \times L^k_{c}(i_F, j_F) + e \times L^k_{w}(i_F+1, j_F) \\ &\quad + nw \times L^k_{se}(i_F-1, j_F+1) + n \times L^k_{s}(i_F, j_F+1) + ne \times L^k_{sw}(i_F+1, j_F+1) \\ &etc... \end{aligned} \tag{A.8}$$

Finally, the result of $I^{k-1}_k\, L^k\, I^k_{k-1}\, e^{k-1}_{i_C,j_C}$ gives the stencil of L^{k-1} at the point (i_C, j_C). The stencil coefficients are directly computed in the code by restriction of the function w^{k-1} whose values at the 25 fine grid points surrounding (i_C, j_C) are given in the table t and which are 0 at other points. As the equation has been integrated, the operator L^k represents the flow through a cell and therefore the restriction operator that is used here is J^{k-1}_k instead of I^{k-1}_k with J^{k-1}_k defined by stencil:

$$J^{k-1}_k = \begin{bmatrix} NW & N & NE \\ W & C & E \\ SW & S & SE \end{bmatrix} \tag{A.9}$$

It means that the normalizing factor $\frac{h_x h_y}{H_x H_y}$ is omitted. This factor is used for the restriction of functions but not for the restriction of flows. In our problem deduced from the Reynolds equation I^{k-1}_k will be used when coarsening the pressure while J^{k-1}_k will also be used when coarsening the right hand side of the equation. This way, a nine point operator is obtained. It stencil reads:

$$\begin{bmatrix} L^{k-1}_{nw}(i_C, j_C) & L^{k-1}_{n}(i_C, j_C) & L^{k-1}_{ne}(i_C, j_C) \\ L^{k-1}_{w}(i_C, j_C) & L^{k-1}_{c}(i_C, j_C)) & L^{k-1}_{e}(i_C, j_C) \\ L^{k-1}_{sw}(i_C, j_C) & L^{k-1}_{s}(i_C, j_C) & L^{k-1}_{se}(i_C, j_C) \end{bmatrix} \tag{A.10}$$

The calculations will be performed by the computer using the stencils of J^{k-1}_k at the corresponding point. For instance the value of $L^{k-1}_{sw}(i_C, j_C)$ is obtained with the stencil of the restriction

J_k^{k-1} at the point $(i_C{-}1, j_C{-}1)$ applied to the following table of values for the surrounding points:

$$\begin{bmatrix} 0 & t(0,1) & t(1,1) \\ 0 & t(0,0) & t(1,0) \\ 0 & 0 & 0 \end{bmatrix}$$

while the value of $L_c^{k-1}(i_C, j_C)$ is obtained with the stencil of the restriction J_k^{k-1} at the point (i_C, j_C) applied to the following table of values for the surrounding points:

$$\begin{bmatrix} t(1,3) & t(2,3) & t(3,3) \\ t(1,2) & t(2,2) & t(3,2) \\ t(1,1) & t(2,1) & t(3,1) \end{bmatrix}$$

A.3 Alcouffe Full multigrid interpolation

In the full multigrid code (FMG), a solution of the problem is computed on the coarse grid $k{-}1$, it is then interpolated to the grid k and this interpolation is used as an initialization of the solution on grid k. In [4], Alcouffe, Brandt, Dendy and Painter propose a new cubic interpolation that is also based on the continuity of $D\partial U/\partial x$ and $D\partial U/\partial y$. Although they note that classical cubic interpolation is sufficient which can be verified on our problem. Both were tried and it did not lead to significant improvement on the problems I studied.
Here too, we interpolate one direction at a time. For simplicity, only one variable is used. The coarse grid solution is denoted u_C and its fine grid interpolation is denoted by u.
The coarse grid values are simply injected and therefore $u(2i_C) = u_C(i_C)$
The coarse grid diffusion coefficients respectively between nodes -3 et -1 and nodes 1 and 3 are denoted by D_{-2} and D_2. The fine grid diffusion coefficients respectively between nodes -1 and 0, and nodes 0 and 1 are denoted by $d_{-1/2}$ and $d_{1/2}$ (see Figure A.2). Instead of looking for a polynomial P of degree 3 taking the same values as u at the nodes $-3, -1, 1, 3$, we impose conditions on its derivatives in order to account for the continuity of $D\partial U/\partial x$ and $D\partial U/\partial y$. More precisely:
$P'(x) = a_0 + a_1 x + a_2 x^2$ must verify

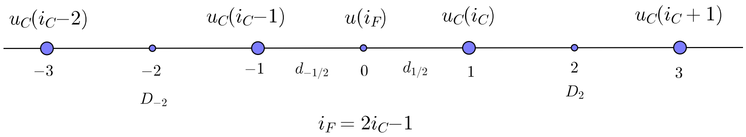

Figure A.2: Interpolation

$$\begin{aligned} &P'(-2) = D_{-2}\frac{u(i_F-1)-u(i_F-3)}{2} \quad && P'(2) = D_2\frac{u(i_F+3)-u(i_F+1)}{2} \\ &P'(-1/2) = d_{-1/2}\frac{u(i_F)-u(i_F-1)}{1} \quad && P'(1/2) = d_{1/2}\frac{u(i_F+1)-u(i_F)}{1} \end{aligned} \tag{A.11}$$

Eliminating a_0, a_1 and a_2 and using the injected values at coarse grid points, one obtains

$$\begin{aligned} u(i_F) = \frac{1}{8(d_{-1/2}+d_{1/2})}&(-D_{-2}u_C(i_C-2)+(8d_{-1/2}+D_{-2})u_C(i_C-1)+ \\ &(8d_{1/2}+D_2)u_C(i_C)-D_2u_C(i_C+1)) \end{aligned} \tag{A.12}$$

It may be noted that when the diffusion coefficients are equal to 1, the same formula as for usual cubic interpolation is obtained:

$$u(i_F) = \frac{1}{16}(-u_C(i_C-2)+9u_C(i_C-1)+9u_C(i_C)-u_C(i_C+1)) \tag{A.13}$$

Some care must be taken with the interpolation formula of fine grid points next to the boundaries. For instance, if $i_F = 1$, the interpolated value reads:

$$\begin{aligned} u(1) = \frac{1}{4(7d_{-1/2}+15d_{1/2})}&(28d_{-1/2}u_C(0)+(60d_{1/2}+21D_2)u_C(1)- \\ &(21D_2+5D_4)u_C(2)+D_4u_C(3)) \end{aligned}$$

Where D_4 is the coarse grid diffusion coefficient between the coarse grid nodes of indices 2 and 3.

APPENDIX B

Numerical values

B.1 Liner groove parameters

Examples of commonly encountered dimensional parameter values are given in Table B.1 with the corresponding range for the associated dimensionless value given in Table B.2 using the dimensionless calculation rules described in Chapter 3. These tables are quoted from [6].
For a viscosity $\eta = 0.01$Pa.s, a mean velocity $u_m = 4\,\mathrm{m/s}$, a minimum film thickness $h_0 = 3.\,\mu$m, a ring curvature radius $R = 0.1$m, the dimensionless pressure is $P = p/p_0$ with $p_0 = 29.2\,\mathrm{MPa}$.

	Min	Max
Radius r	1cm	1m $\rightarrow \infty$
Groove depth a	0.5μm	5μm
Groove width λ	5μm	50μm
Half contact width e	0.4 mm	1 mm
Minimum film thickness h_0	0.1μm	10μm

Table B.1: Groove dimensional parameters.

	Min	Max
Groove depth A	0.05	50
Groove width Λ	$1.6\,10^{-3}$	1.6
Half contact width E	0.13	31

Table B.2: Groove dimensionless parameters.

B.2 Dimple parameters

Examples of commonly encountered dimensional parameter values are given in Table B.3 with the corresponding range for the associated dimensionless value given in Table B.4 using the dimple radius and the clearance as dimensionless factors (see Chapter 5). For a viscosity $\eta = 0.01\,\mathrm{Pa.s}$, a mean velocity $u_m = 4\,\mathrm{m/s}$, a clearance $h_0 = 1.\,\mu$m and a radius $r = 12.5\,\mu$m, the dimensionless pressure is $P = p/p_0$ with $p_0 = 6\,\mathrm{MPa}$. In this case, our choice for the range of P_{amb} values yields the following range of values for $p_{amb} - p_{cav}$:

$$p_{amb} - p_{cav} \in [0.06\,\mathrm{MPa}, 0.3\,\mathrm{MPa}]$$

.

It can be noticed that for an ambient pressure $p_{amb} = 0.1\,\mathrm{MPa}$, the last value does not make sense. The operating conditions tell us what dimensionless results can be used.

	Min	Max
Dimple radius r	5μm	50μm
Dimple depth a	0.1μm	10μm
Half contact width x_0	0.1 mm	0.15 mm
Clearance h_0	0.1μm	1μm

Table B.3: Dimple dimensional parameters.

	Min	Max
Dimple depth A	0.1	10
Half contact width X_0	2.0	30.

Table B.4: Dimple dimensionless parameters.

Appendix C

Cell centered algorithm

C.1 Introduction

The convergence obtained in chapter 4 was not fully satisfactory, especially in the partially starved contacts for smooth surfaces. Besides, we did not manage to get a working multigrid code without including the wedge term in the left hand side of the equation. For these reasons, we realized that it might be better to first study and better understand a simpler case. Henceforth it was decided to consider a smooth surface, forgetting Alcouffe's algorithm and using simpler grids in order to focus on the present task. The fine grid relaxation scheme correctly describes the flow behavior on the finest grid. But it was difficult to transfer it to the coarse grids. The coarse flow representation was poor especially at the inlet meniscus and at the cavitation boundary. We also have to build the multigrid routines so that the flow is correctly represented on the coarse grids.

C.2 Grid description

The domain is divided in cells using regularly spaced straight lines that are parallel to the axes. In Figure C.1, a fine grid and the next coarser grid are shown with an indication of the cell numbering. In Figure C.2, the cell (i, j) is described. The pressure P will be evaluated at the cell center while the oil height is computed at the mid points of the right and left boundaries of the cell.

C.3 Relaxation scheme

C.3.1 Fine grid relaxation

Again using a volume discretization of equation 4.1, the flow through each cell boundary (see Figure C.3) is evaluated as follows:
- through the X-boundary between the cells (i, j) and $(i + 1, j)$, the flux $\Phi_X(i, j)$ is

$$\Phi_X(i,j) = hy \times Hoil(i,j) - b_{i,j}(P(i+1,j) - P(i,j))$$

where $b_{i,j}$ is a diffusion coefficient computed according to:

$$b_{i,j} = \frac{1}{2}(H^3(X_i, Y_j) + H^3(X_i, Y_{j-1}))\frac{h_x}{h_y}.$$

- through the Y-boundary between the cells (i, j) and $(i, j + 1)$, the flux $\Phi_Y(i, j)$ is

$$\Phi_Y(i,j) = -a_{i,j}(P(i,j+1) - P(i,j))$$

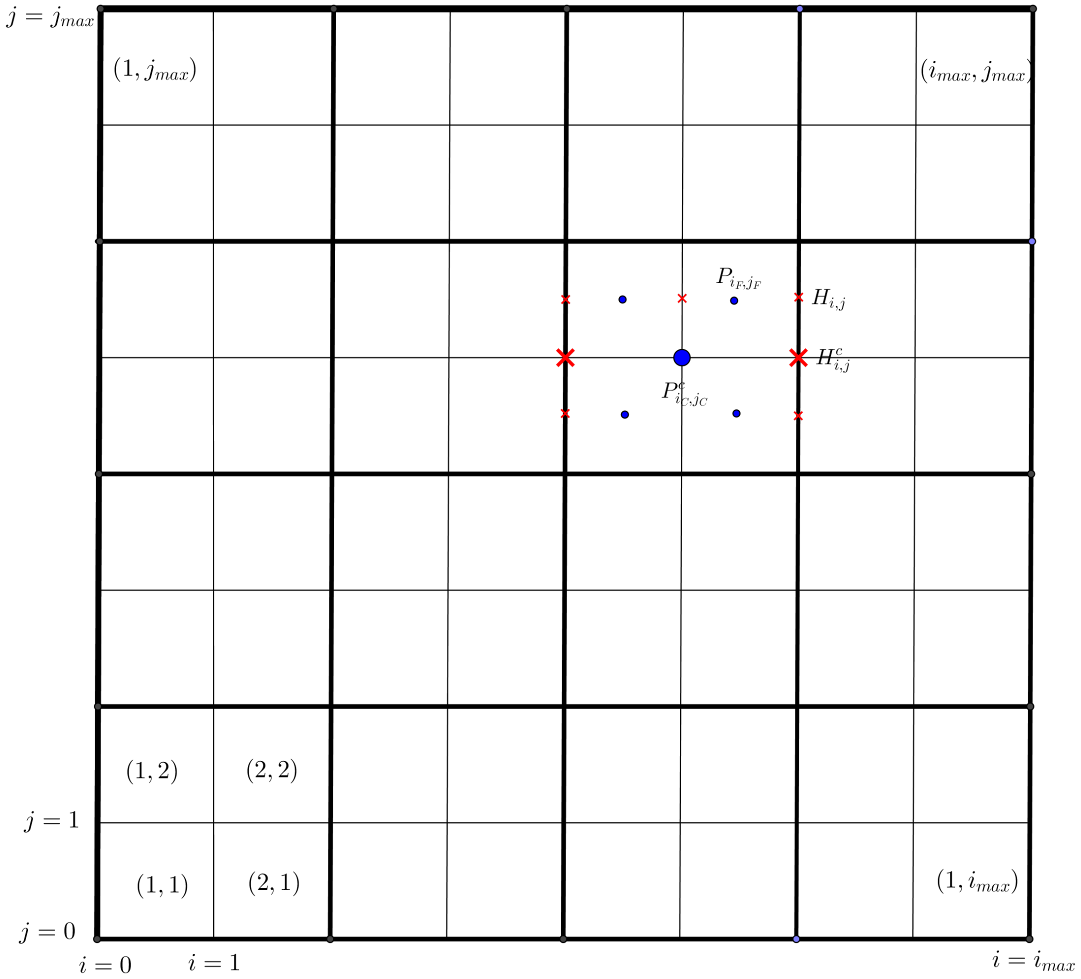

Figure C.1: Fine grid and next coarser grid

where $a_{i,j}$ is a diffusion coefficient computed by

$$a_{i,j} = \frac{1}{2}(H^3(X_i, Y_j) + H^3(X_{i-1}, Y_j))\frac{h_y}{h_x}.$$

The chosen relaxation process for the finest grid is adapted from the one that was described in Chapter 4. For each cell (i, j), the residual Δ of the discretized equation corresponds to the balance of the flows through the four cell boundaries. More precisely

$$\Delta = \Phi_X(i-1, j) - \Phi_X(i, j) + \Phi_Y(i, j-1) - \Phi_Y(i, j).$$

The relaxation process cancels the residual of the cell (i, j). It is also meant to properly describe the physical behavior of the lubricant. To conserve the flow especially at the cavitation or film re-formation boundaries, the relaxation has to change pressures and oil level under the correct conditions. It will be distributive on the oil level $Hoil$ to preserve a kind of ellipticity at least in

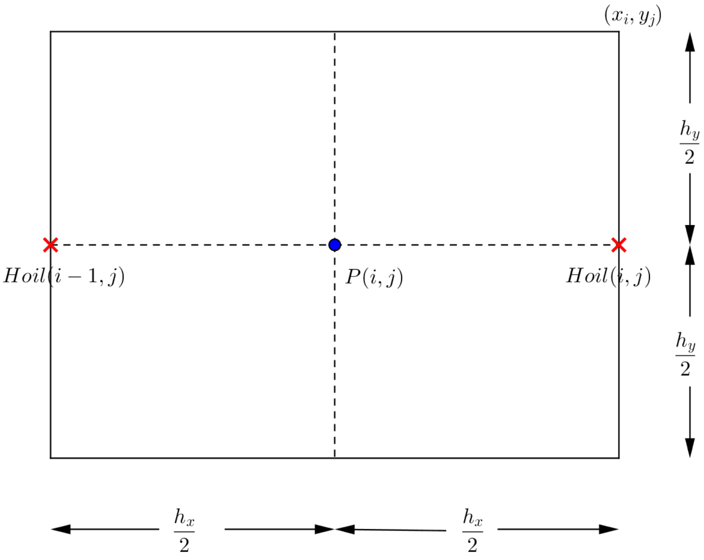

Figure C.2: Cell (i, j)

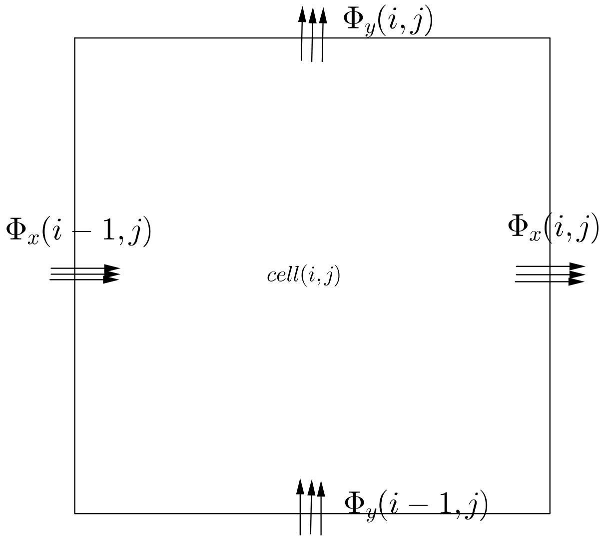

Figure C.3: Flow through the boundaries of the cell(i, j).

the X-direction in the cavitated zone which matters for multigrid efficiency. In the pressurized zone the oil film is complete. Henceforth, when the residual is positive, we first increase the oil level $Hoil(i + 1, j)$ by half the residual. If it reaches the maximum possible value, we increase the pressure to eliminate the remaining part of the residual otherwise the oil level $Hoil(i, j)$is diminished. When the residual is negative, we first decrease the pressure. If it becomes negative, we set it to zero and then change the oil film thickness on both sides of the cell.

- Evaluate the residual res at point (i, j)
- if $res > 0$
  - $Hoil_{i+1,j} \leftarrow Hoil_{i+1,j} + 0.5 * res/hy$
  - if $Hoil_{i+1,j} > H_{i+1,j}$
    - $Hoil_{i+1,j} = H_{i+1,j}$
    - Evaluate the remaining residual $res1$ at point (i, j)
    - $P_{i,j} \leftarrow P_{i,j} - res1/c_{i,j}$
  - else $Hoil_{i,j} \leftarrow Hoil_{i,j} - 0.5 * res/hy$
- if $res < 0$
  - $P_{i,j} \leftarrow P_{i,j} - res1/c_{i,j}$
  - if $P_{i,j} < 0$
    - $P_{i,j} = 0$
    - Evaluate the remaining residual $res2$ at point (i, j)
    - $Hoil_{i+1,j} \leftarrow Hoil_{i+1,j} + 0.5 * res2/hy$
    - $Hoil_{i,j} \leftarrow Hoil_{i,j} - 0.5 * res2/hy$
    - if $Hoil_{i,j} > H_{i,j}$ then $Hoil_{i,j} = H_{i,j}$

Where $c_{i,j} = -a_{i,j} - -a_{i,j-1} - -b_{i,j} - -b_{i-1,j} < 0$

C.3.2 Single grid results

In the smooth case the single grid relaxation process converges well and is mass conserving. It works with Dirichlet conditions on the four boundaries and $H(X, Y) = 1 + 0.5X^2 + 0.5Y^2$ or for a periodic code in Y with $H(X, Y) = 1 + 0.5X^2$ and Dirichlet condition on the 2 X-boundaries. The results presented in this section correspond to the periodic code. Similar results are obtained in the other case which are not presented here. The code was run on a 256 × 256 grid covering the domain $\Omega = [X_a, X_b] \times [Y_a, Y_b] = [-2, 2] \times [-2, 2]$.

The obtained code converges for any starvation condition:

- fully flooded with an initial oil level corresponding to the geometry H,
- fully flooded but an initial level of oil defined by $H_0 = 1.5$ lower that the geometry H and higher than the exit oil film level in fully flooded conditions,
- partially starved contact with an initial level of oil defined by $H_0 = 1.1$ lower than the exit oil film level in fully flooded conditions but higher the minimum of H which is 1,
- completely starved case with an initial level of oil $H_0 = 0.8$ less than the minimum of H.

The last case becomes obvious if the initial oil condition is chosen as $\min(H(X,Y),H_0)$ where H_0 is the initial film height on the line $X = X_a$. The resulting pressure and oil film height are shown in Figures C.4 and C.5 for the whole domain and in Figure C.6 for the central line.
As expected the film height becomes constant in the cavitated area. Besides, as expected, in the partially starved contact, the outcoming oil film thickness is equal to the initial value of the oil level. The flows were computed on each vertical line that is to say for constant Y and was found to be constant.

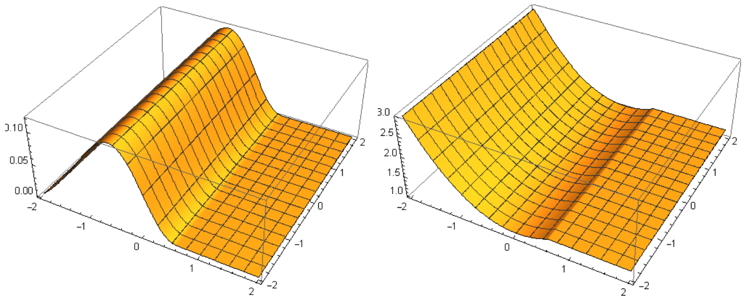

(a) (b)

Figure C.4: Pressure and oil level in the periodic case - Fully flooded contact - Single grid.

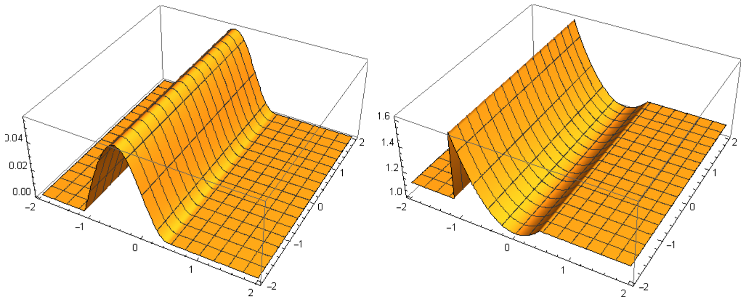

(a) (b)

Figure C.5: Pressure and oil level in the periodic case - partially starved contact - Single grid.

The evolution of the average residual in terms of the work units Wu can be seen in Figure C.7. The first two figures correspond to the fully flooded case but in the second one the initial film thickness is much lower than the geometry and therefore at the beginning a certain amount of work is needed to reach the fully flooded regime and this explains why the convergence is a little slower. In the last partially starved case, there are two main convergence difficulties associated with two free boundary problems at the inlet and at the outlet of the contact and this explains the slower convergence than in the fully flooded cases.

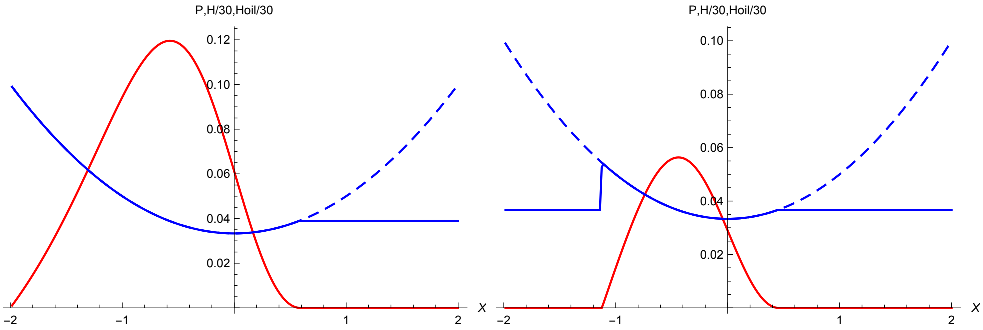

(a) (b)

Figure C.6: Pressure (red), geometry(dashed blue) and oil level (blue) on the central line $Y = 0$ in the periodic case - Single grid - (a) fully flooded contact, (b) partially starved contact

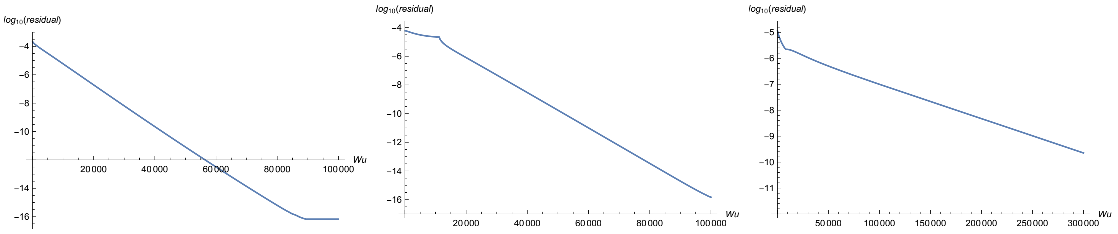

(a) (b) (c)

Figure C.7: Average residual as a function of the number of work units in the periodic case - Monogrid (a) fully flooded, (b) fully flooded with $H_0 = 1.5$ and (c) partially starved with $H_0 = 1.1$

A second geometry named ”wavy geometry” was considered. It is defined by $H(X, Y) = 1.5 + 0.5\cos(\pi X)$ (Figure C.8). This case enables us to verify that the single grid code behaves properly while entering pressurized areas or cavitated areas. Again, on one grid, the code converges but more slowly. Results for a fully flooded initial condition: $H_0 = H(X_a, Y)$ are shown in Figures C.8 on the whole domain and in Figure C.9 only on the central line. With this geometry the film height becomes constant in the X-direction after the first cavitation boundary then the oil film thickness is rebuilt in a way similar to the partially starved contact studied when $H(X, Y) = 1 + 0.5X^2$. At the second cavitation boundary the outcoming oil film thickness is equal to the value it has reached after it first cavitates. The flow on each line with constant Y is constant up to 5×10^{-6} which is of the order of the discretization error.

The evolution of the average residual in terms of the number of work units Wu can be seen in Figure C.10 (a). Here we may note that there are three main features that lead to convergence difficulties: the first cavitation, the entrance of the second contact and the second cavitation boundary which cause the convergence to slow down as shown in Figure C.10 (b).

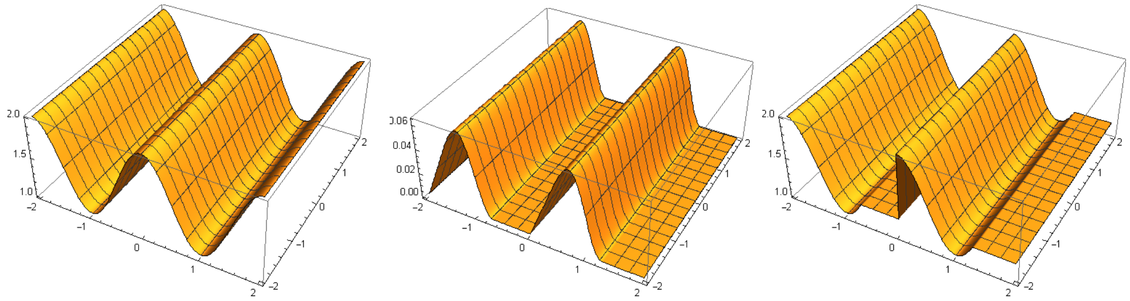

(a) (b) (c)

Figure C.8: (a) Geometry - (b) pressure - (c) oil level - periodic case - wavy geometry - single grid.

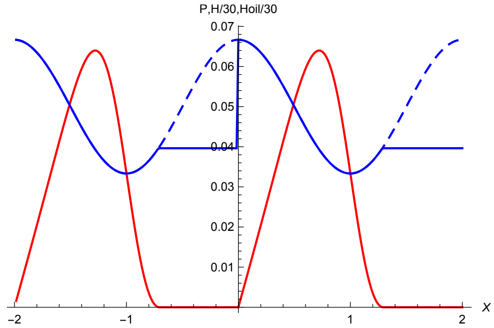

Figure C.9: Pressure (red), geometry(dashed blue) and oil level (blue) on the central line $Y = 0$ in the periodic case - wavy geometry - single grid.

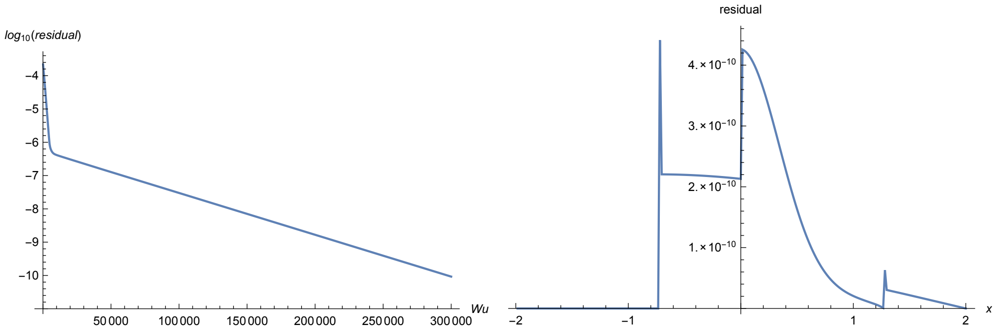

(a) (b)

Figure C.10: (a) Average residual as a function of the number of work units (b) Residual on the central line $Y = 0$ - periodic wave - single grid.

C.3.3 Coarse grid relaxation

It is important to have a good coarse grid representation of the flow through each coarse grid cell and adapt the relaxation scheme accordingly. In Figure C.11, a coarse grid cell made of four fine grid cells can be seen.

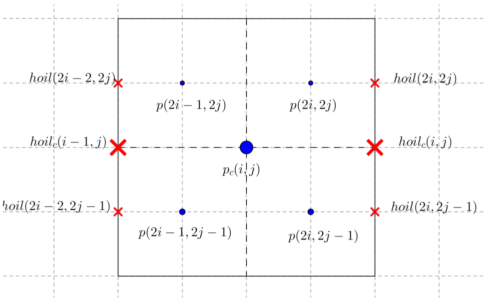

Figure C.11: Coarse grid cell (i, j) and the four associated fine grid cells

The flow can be decomposed into two parts on the vertical boundaries of the cells, the Couette flow defined as $\Phi_{C,X}(i,j) = hy \times Hoil(i,j)$ and the Poiseuille flow calculated by $\Phi_{P,X}(i,j) = -b_{i,j}(P(i+1,j) - P(i,j))$. According to the position of the cavitation boundary or of the entrance meniscus when dealing with the coarse grid, various cases are to be considered as shown for instance in Figure C.12. In this special case on the coarse grid the flow through the right vertical boundary calculated on the fine grid would involve a Poiseuille component because the coarse pressure at the cell center is positive. But this is not correct since at the cavitation boundary $\partial P/\partial X = 0$ and therefore there should be no Poiseuille flow through this coarse grid boundary. To try to remedy this, it was decided to associate a type T with each coarse grid vertical boundary to be able to account or not for the Poiseuille component according to the location of the coarse grid boundary. It was implemented as follows:

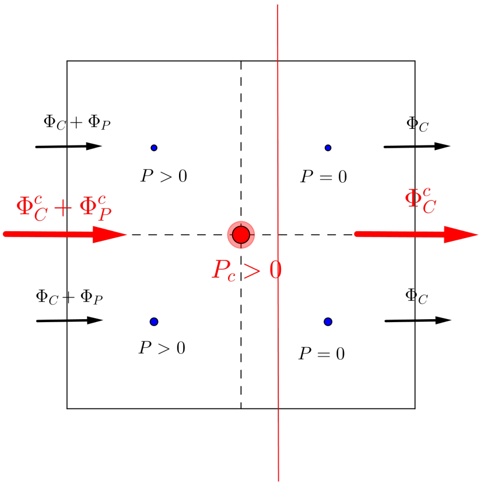

Figure C.12: Poiseuille and Couette flow through the vertical boundaries of a coarse cell (in red) and through the corresponding fine grid boundaries (in black) together with the cavitation boundary (red line).

In Figure C.13, we have represented in red the coarse grid boundary between the coarse cell

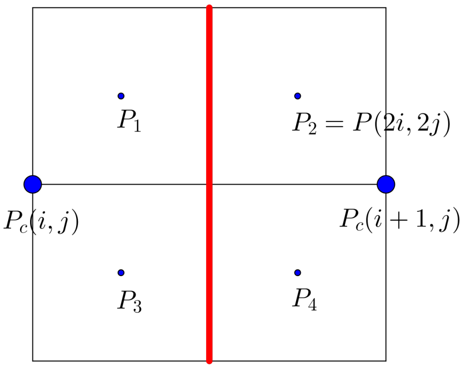

Figure C.13: Coarse grid boundary (i, j).

(i, j) and $(i + 1, j)$. The fine grid surrounding pressures are $P_1 = P(2i, 2j)$, $P_2 = P(2i + 1, 2j)$, $P_3 = P(2i, 2j - 1)$ and $P_4 = P(2i + 1, 2j - 1)$.

- $T = 0$ if $P_1 = P_2 = P_3 = P_4 = 0$ (Non pressurized zone, only Couette flow).
- $T = 1$ if $P_1 = P_3 = 0$ and $P_2 \geq 0, P_4 \geq 0$ with $P_2 > 0$ or $P_4 > 0$ (Inlet boundary).
- $T = 2$ if $P_2 = P_4 = 0$ and $P_1 \geq 0, P_3 \geq 0$ with $P_1 > 0$ or $P_3 > 0$ (Outlet boundary).
- $T = 3$ if $P_1 \geq 0, P_3 \geq 0$ with $P_1 > 0$ or $P_3 > 0$ and $P_2 \geq 0, P_4 \geq 0$ with $P_2 > 0$ or $P_4 > 0$ (Boundary in the pressurized zone).

The flows on the coarse grid are then computed according to the type of each piece of boundary. For types $1, 2$ or 3 we have a Couette and a Poiseuille flow.
On the coarse grids the relaxation process is slightly modified.
Call $T(i, j)$ the type of the (i, j) boundary.

- If $T(i - 1, j) = 3$ or $T(i, j) = 3$ or $T(i - 1, j) = 1$ or $T(i, j) = 2$, the cell (i, j) is relaxed as on the fine grid.
- If $T(i - 1, j) = 0$ and $T(i, j) = 1$, to account for the discontinuous behavoir of $Hoil$, the residual is only absorbed by $Hoil(i, j)$.
- Otherwise the residual is distributed between $Hoil(i - 1, j)$ and $Hoil(i, j)$.

Along the vertical boundaries, maybe a similar procedure will have to be adapted for the Dirichlet case.

C.4 Operators

C.4.1 Right hand side coarsening

For smooth surfaces, on each grid, it is sufficient to directly deduce them from the discretization of the equation 4.1 on the grid k. We have

$$Lu(k, P_k, H_k, Hoil_k) = F_k$$

with

$$Lu(k, P_k, H_k, Hoil_k, i, j) = \Phi_X(i-1, j) - \Phi_X(i, j) + \Phi_Y(i, j-1) - \Phi_Y(i, j).$$

On the finest grid, we have

$$F_k(i, j) = 0$$

and on the coarser grid F_k is computed so that it properly represents the flow equilibrium on each cell. On the grid $k-1$ next coarse grid to grid k, it is thus evaluated as follows:

$$F_{k-1}(i, j) = Lu(k-1, P_{k-1}, H_{k-1}, Hoil_{k-1}, i, j) + (rnw + rne + rsw + rse)$$

with

$$\begin{aligned}
rnw &= F_k(2i-1, 2j) - Lu(k, P_k, H_k, Hoil_k, 2i-1, 2j)\\
rne &= F_k(2i, 2j) - Lu(k, P_k, H_k, Hoil_k, 2i, 2j)\\
rsw &= F_k(2i-1, 2j-1) - Lu(k, P_k, H_k, Hoil_k, 2i-1, 2j-1)\\
rse &= F_k(2i, 2j-1) - Lu(k, P_k, H_k, Hoil_k, 2i, 2j-1)
\end{aligned}$$

C.4.2 Restriction operator

Two restriction operators have to be defined, one for the oil level $Hoil$ and one for the pressure P.

For the lubricant height, the natural choice is given, according to Figure C.11, by:

$$Hoil_c(i, j) = 0.5(Hoil(2i, 2j) + Hoil(2i, 2j-1)).$$

This choice is consistent with the flux representation on the coarse grid because if h_y is the height of the fine grid cell and H_y the one of the next coarser grid. The coarse grid variation of flow through the coarse cell (i, j) is given by:

$$\begin{aligned}
&H_y(Hoil_c(i, j) - Hoil_c(i-1, j))\\
&\quad = h_y(Hoil(2i, 2j) + Hoil(2i, 2j-1) - Hoil(2i-2, 2j) - Hoil(2i-2, 2j-1))\\
&\quad = h_y(Hoil(2i, 2j) - Hoil(2i-1, 2j) + Hoil(2i-1, 2j) - Hoil(2i-2, 2j))\\
&\quad + h_y(Hoil(2i, 2j-1) - Hoil(2i-1, 2j-1) + Hoil(2i-1, 2j-1) - Hoil(2i-2, 2j-1))
\end{aligned}$$

It corresponds exactly to the variation of the Couette flow through the 4 fine cells constituting the coarse grid cell. It will be done only outside the pressurized zone because otherwise it will lead to relaxation problems since it may not be equal to H inside the pressurized area.

For the pressure, the natural choice is given by a simple average (see Figure C.11):

$$P_c(i, j) = 0.25(P(2i-1, 2j) + P(2i, 2j) + P(2i-1, 2j-1) + P(2i, 2j-1)).$$

C.4.2.1 Interpolation operator

Again two interpolation operators have to be defined one for the oil level $Hoil$ and one for the pressure P. The simplest choice for $Hoil$ is given by the following interpolation operator I_{oil}. We define $Hoil = I_{oil}Hoil_c$ by:

$$Hoil(2i,2j) = Hoil(2i,2j-1) = Hoil_c(i,j)$$

and for the pressure,the following interpolation operator I_P defined by $P = I_P P_c$ with:

$$P(2i,2j) = P(2i,2j-1) = P(2i-1,2j) = P(2i-1,2j-1) = P_c(i,j).$$

It can be improved as follows by defining I_{oil} by:

$$\begin{aligned}
Hoil(2i,2j) &= 0.75Hoil_c(i,j) + 0.25Hoil_c(i,j+1)\\
Hoil(2i,2j-1) &= 0.75Hoil_c(i,j) + 0.25Hoil_c(i,j-1)\\
Hoil(2i-1,2j) &= 0.5(Hoil(2i,2j) + Hoil(2i,2j-1))\\
Hoil(2i-1,2j-1) &= 0.5(Hoil(2i,2j) + Hoil(2i,2j-1)).
\end{aligned}$$

For I_P, one can also take

$$\begin{aligned}
p(2i,2j) = P(2i,2j-1) &= 0.75P_c(i,j) + 0.25P_c(i+1,j)\\
P(2i-1,2j) = P(2i-1,2j-1) &= 0.75P_c(i,j) + 0.25P_c(i-1,j)
\end{aligned}$$

It has to be noted that the pressure correction interpolation has to be carried out only for the fine grids points already in pressure and the oil film correction interpolation is only performed in the non pressurized zone.

C.5 Difficulties

Here many difficulties are to be considered. We have a complementary problem with possibly several free boundaries. The pressure and the film height are not computed at the same points. This allows a precise description of the flow but may also lead to difficulties for finding the solution to the complementary problems.
For the starved case, the pressure remains zero. Everything goes very well. The flow representation on the coarse grid is exact.
For the other cases many difficulties can interfere with each other. It was noticed that it was probably better to refine the pressure only in the pressurized zone and for the oil level only outside the pressurized zone. In the coarsening steps, it was also better to coarsen the oil level only outside the pressurized zone otherwise it may be smaller than the geometry where it should not. But these modifications were not sufficient to obtain good convergence.
It was then decided to study a problem that does not cavitate. To achieve this we considered a flat geometry of height 1 with a shallow circular indent in the middle and to take an ambient pressure $P_0 > 0$. For a square domain $\Omega = [-2,2] \times [-2,2]$ and an indent of radius 1 and depth 0.2, we chose $P_0 = 0.05$ and we did a 2 level analysis to make sure that the pressure error was

smooth. The error is indeed smooth as shown in Figure C.14. Using a 32×32 coarse grid, we solve the problem on the fine grid up to an error of 10^{-7} then we add an artificial error to the pressure of magnitude 10^{-3}, coarsen it, solve the coarse grid problem, refine the coarse grid solution and perform 2 fine grid relaxations in order to eliminate the high frequencies errors that are induced by the interpolation process. and get a smooth error on P.

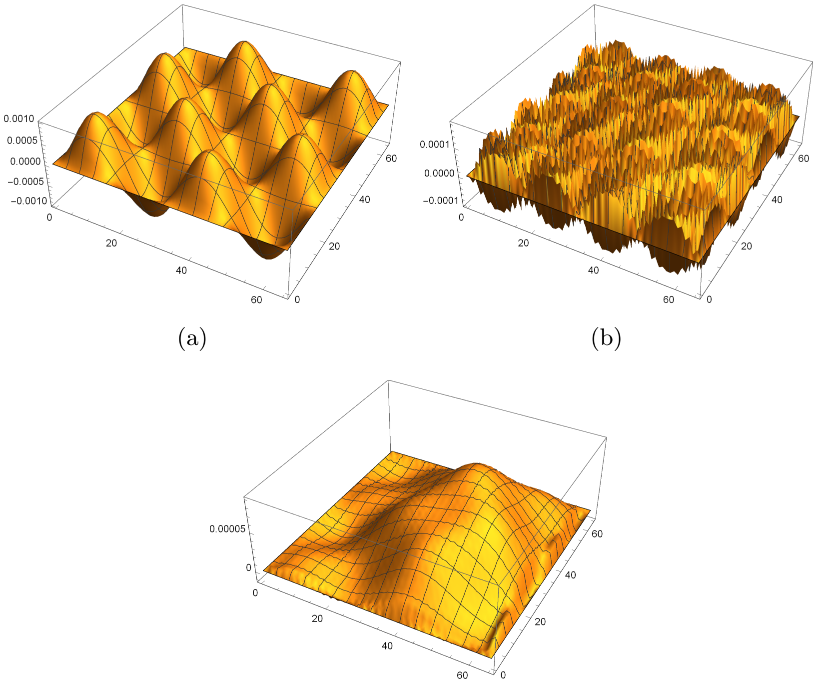

(a)

(b)

(c)

Figure C.14: Two level analysis: pressure error (a) after an artificial perturbation , (b) after solving the problem on the coarse grid and the interpolation to the fine grid (c) after 2 more relaxations on the fine grid

This was satisfactory. However a strange behavior of the residual was noticed. It became huge on the boundaries of the domain when relaxing the fine grid after the refining steps as shown in Figure C.15. As can be seen on this figure after the refining step, the residual vanishes inside the domain after a few fine grid relaxations but becomes and remains huge on the boundary. We found out that the cause might be a bad evaluation of the partial derivatives in p and henceforth of the flux on the boundaries of the domain. As we used a cell centered discretization for the pressure, the pressure was set to the ambient pressure p_0 outside the domain but to evaluate the partial derivatives on the boundary we must impose it to be p_0 on the boundary. For instance to evaluate $\partial p/\partial x$ at a point $(0, j)$, instead of using the general formula with $p(0, j) = p_0$ we must impose $p(0, j) = p_0 - \delta$ where $\delta = p(1, j) - p_0$ so that the average pressure is equal to the ambient pressure on the line $X = X_a$. Do Y. Kwak and Jun S. Lee mention this in [87].
This has improved the performance of the code in the fully flooded case, when the pressurized

zone touches one of the boundaries and when there is no cavitation we obtain good multigrid convergence.

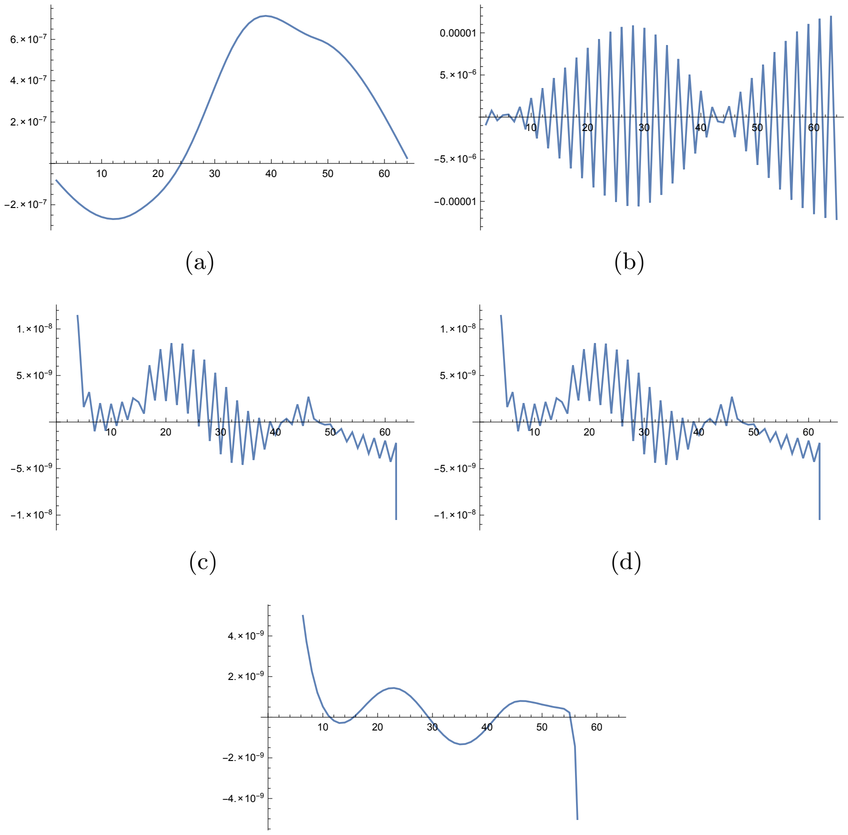

(a) (b)

(c) (d)

(e)

Figure C.15: Two level analysis: fine grid residuals on the line $Y = 0$ (a) solving the problem up to 10^{-7} with fine grid relaxations (b) after solving the problem on the coarse grid and the interpolation to the fine grid (c) after 1 more relaxation on the fine grid, (d) after 2 more relaxations on the fine grid, (e) after 10 more relaxations on the fine grid

C.6 Multigrid results: periodic code

C.6.1 1D periodic code

Because of the many problems that arose and whose source is not always easy to identify in multigrid, a preliminary semi-1D code was written. The domain Ω is a square $[-2, 2] \times [-2, 2]$, in the periodic case with a geometry H defined by $H(X, Y) = 1 + 0.5X^2$ and the flow in the Y-direction was not considered. The obtained code shows good convergence for every starvation condition: fully flooded, fully flooded but with initial level of oil 1.5, partially starved contact (initial level of oil: 1.1), and completely starved case (initial level of oil: 0.8). Since no pre-relaxation was used, because of the free boundaries at cavitation or in the inlet (in the case of partially starved condition), V-cycles with 10 relaxations per grid before each coarsening steps and 5 relaxations after each refining steps are used. The coarsest grid is 4×4 grid. Table C.1 shows the average residual per point that is obtained on levels $6, 7, 8$ and 9 using FMG with 10 V-cycles.

The table is obtained for an initial level of oil equal to the geometry outside the first vertical line. This explains why we also include the results for the completely starved case. The completely starved case is very quickly solved on the coarsest grid and the FMG interpolation already provides the exact solution to the next fine grid and so on. This is why very small residuals are rapidly obtained in this case. The convergence is slower for the partially starved contact, $Hoil(-2) = 1.1$, because in this case there are two free boundaries: in the inlet and in the outlet. In this case, however, using 15 V-cycles per level, we can get a final residual of $5\,10^{-13}$. Because of the FMG process for $Hoil(-2) = 1.5$, on the coarsest grid we rapidly get the fully flooded regime and therefore results are quite similar to the one obtained for the fully flooded case.

Film height on line $X = -2$	6 levels	7 levels	8 levels	9 levels
Fully flooded	$1.36\,10^{-14}$	$3.72\,10^{-15}$	$1.29\,10^{-16}$	$3.25\,10^{-15}$
$Hoil(-2) = 1.5$	$6.82\,10^{-14}$	$1.10\,10^{-14}$	$2.56\,10^{-15}$	$4.12\,10^{-15}$
$Hoil(-2) = 1.1$	$8.64\,10^{-10}$	$8.48\,10^{-10}$	$2.58\,10^{-11}$	$2.99\,10^{-12}$
$Hoil(-2) = 0.8$	$1.08\,10^{-19}$	$2.71\,10^{-20}$	$6.78\,10^{-21}$	$1.69\,10^{-21}$

Table C.1: FMG Residuals with 10 V(10,10,5)-cycles for the 1D smooth problem - Parabolic geometry

For the wave, $H(X, Y) = 1 + 0.1(1 + \cos(\pi x))$, it does not work as well. In this case we have several cavitated zones and therefore several convergence difficulties. Besides globally this surface is also flatter than the parabola: $|\partial H/\partial X| \leq 0.1\pi$. To get a partially starved contact, the initial oil level $Hoil(-2)$ on the line $X = -2$ should be between 1 and 1.0656.

In the fully flooded case with 9 levels, FMG with 20 V(10,10,5)-cycles the final residual is $1.30\,10^{-12}$. If $Hoil(-2) = 1.1$, the process converges to the fully flooded contact. After FMG with 20 V-cycles the obtained residual on level 9 is $9.73\,10^{-12}$ and the fully flooded regime is reached. After FMG with 50 V-cycles, it becomes $4.85\,10^{-18}$. Results can be seen in table C.2. In the fully flooded case with 9 levels, FMG with 20 V(10,10,5)-cycles the final residual is $1.30\,10^{-12}$. Of course the convergence is rather slower than with the parabolic geometry since there are more free boundaries.

Film height on line $X = -2$	6 levels	7 levels	8 levels	9 levels
Fully flooded	$2.44\,10^{-10}$	$6.65\,10^{-10}$	$2.12\,10^{-9}$	$3.96\,10^{-10}$
$Hoil(-2) = 1.1$	$1.40\,10^{-9}$	$1.22\,10^{-9}$	$1.09\,10^{-10}$	$9.09\,10^{-10}$
$Hoil(-2) = 1.05$	$8.31\,10^{-8}$	$4.25\,10^{-8}$	$5.39\,10^{-8}$	$9.59\,10^{-10}$

Table C.2: FMG Residuals with 10 V(10,10,5)-cycles for the 1D smooth problem - Wavy geometry

C.6.2 Periodic code, the Y-flow

The code was then modified to include the Poiseuille flow in the Y-direction. It was tested on the same domain with the same geometry and the same initial oil conditions. For the parabolic geometry, the convergence is slower. The convergence can be improved by choosing better interpolation operators but it seems to attain a certain accuracy and afterwards, it slows down. This was not the case without the Y-flow. One reason may be the lack of coupling in the Y-direction outside the pressurized zone. The results for the residual are shown in table C.3. Here again, the initial oil level is equal to the geometry outside the first vertical line.

Film height on line $X = -2$	6 levels	7 levels	8 levels	9 levels	10 levels
Fully flooded	$3.19\,10^{-10}$	$9.47\,10^{-11}$	$6.57\,10^{-12}$	$1.83\,10^{-12}$	$3.56\,10^{-13}$
$Hoil(-2) = 1.5$	$1.71\,10^{-9}$	$7.50\,10^{-10}$	$5.66\,10^{-11}$	$1.53\,10^{-11}$	$8.41\,10^{-12}$
$Hoil(-2) = 1.1$	$1.10\,10^{-9}$	$6.13\,10^{-8}$	$2.31\,10^{-9}$	$3.35\,10^{-11}$	$1.12\,10^{-11}$

Table C.3: FMG Residuals with 10 V(10,10,5)-cycles for the 1D smooth problem with Y-flow - Parabolic geometry

For the wave, $H(X,Y) = 1 + 0.1(1 + \cos(\pi x))$, Table C.4 gives the residual obtained with the FMG code and 10 V-cycles. On level 9, for $Hoil(-2) = 1.1$ with 20 V-cycles the residual becomes $1.67\,10^{-9}$ but it is not yet fully flooded and the inlet meniscus is not yet stabilized. With 50 V-cycles the residual becomes $6.24\,10^{-12}$ and it is fully flooded. On level 9, for $Hoil(-2) = 1.05$ with 20 V-cycles the residual becomes $7.75\,10^{-10}$, with 50 V-cycles it is $1.11\,10^{-11}$ and with 100 V-cycles it drops to $3.3\,10^{-14}$. With only 10 V-cycles, convergence results are more similar to the one obtained without the Y-flow than for the parabolic case. But in this case there are more free boundaries and it may hide the influence of the flow in the Y-direction. But when the number of cycles increases and the frontiers are more stabilized, here too the convergence is not as good as without the Y-flow.

Film height on line $X = -2$	6 levels	7 levels	8 levels	9 levels
Fully flooded	$1.20\,10^{-9}$	$6.26\,10^{-10}$	$5.88\,10^{-9}$	$4.46\,10^{-9}$
$Hoil(-2) = 1.1$	$6.97\,10^{-10}$	$3.66\,10^{-10}$	$3.68\,10^{-9}$	$1.32\,10^{-9}$
$Hoil(-2) = 1.05$	$9.33\,10^{-8}$	$2.49\,10^{-9}$	$4.30\,10^{-9}$	$2.93\,10^{-9}$

Table C.4: FMG Residuals with 10 V(10,10,5)-cycles for the 1D smooth problem with Y-flow - wave

C.6.3 Multigrid results: 2D code with Dirichlet conditions

The domain Ω is still the square $[-2,2] \times [-2,2]$. Now the geometry H is defined by $H(X,Y) = 1 + 0.5X^2 + 0.5Y^2$. The obtained code does not converge. Only the single grid algorithm and the fully starved multigrid algorithm converge. In the cavitated area the oil level has a non zero curvature in the Y direction and because there is no coupling in the Y-direction, the convergence becomes very hard around the cavitation boundary and afterwards in the cavitated area . Therefore semi-coarsening (see for instance [10]) may have to be considered. It was tried without success...

C.6.4 Residual and work units

The following pictures give the behavior of the residual in terms of work units for the periodic case with 2 geometries: periodic parabolic, $H(X,Y) = 1+0.5X^2$ and periodic wave, $H(X,Y) = 1.1 + 0.1\cos(\pi X)$, for the 1D code with or without Y-flow. For each case, 3 values of the initial oil level H_0 are given: fully flooded initial value, initial value that converges to the fully flooded regime and partially starved condition. The code was run on 8 levels, the coarse grid being a 4×4 grid for comparison with the single grid results of section C.3.2. FMG with 50 V(10,5)-cycles was used. The domain is $\Omega = [-2,2]\times[-2,2]$. In Figure C.16, the results without considering the Y-flow are shown. It converges well for the parabolic geometry and more difficultly in the case of the wavy geometry. When the number of free boundaries increases, convergence difficulties also increase. In Figure C.17, the Y-flow is considered and it can be seen that it slows down the convergence significantly as already mentioned. For the fully flooded regime when the initial oil level is lower that the geometry on the line $X = -2$, without Y-flow the convergence is very similar to the one obtained in the fully flooded case. It is less true with the Y-flow in the case of the parabolic geometry.

For the partially starved contact the obtained pressure and film thickness are shown in Figure C.18.

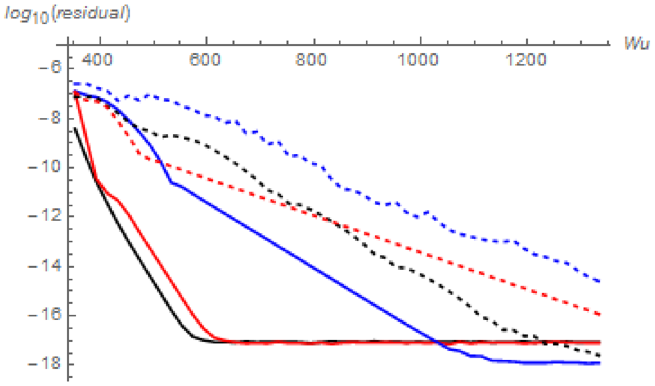

Figure C.16: Residual in terms of work units -No Y-flow- Full lines periodic parabolic geometry: fully flooded in black, $H_0 = 1.5$ in red and $H_0 = 1.1$ in blue - Dashed lines periodic wave : fully flooded in black, $H_0 = 1.1$ in red and $H_0 = 1.05$ in blue

C.7 Conclusion

At the film formation the continuity used by Alcouffe is not quite satisfactory because of the discontinuity of the film level and therefore of the Couette and Poiseuille flow even in the smooth

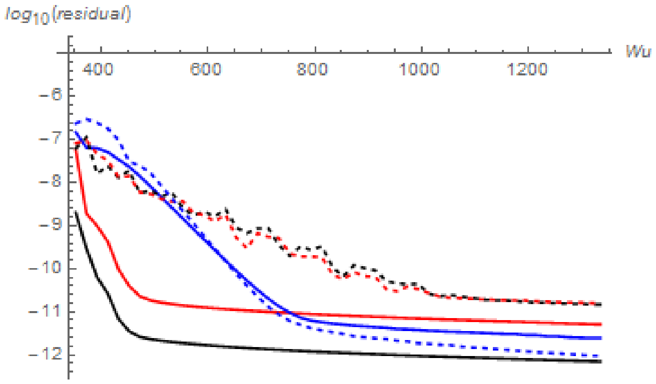

Figure C.17: Residual in terms of work units -With Y-flow- Full lines periodic parabolic geometry: fully flooded in black, $H_0 = 1.5$ in red and $H_0 = 1.1$ in blue - Dashed lines periodic wave : fully flooded in black, $H_0 = 1.1$ in red and $H_0 = 1.05$ in blue

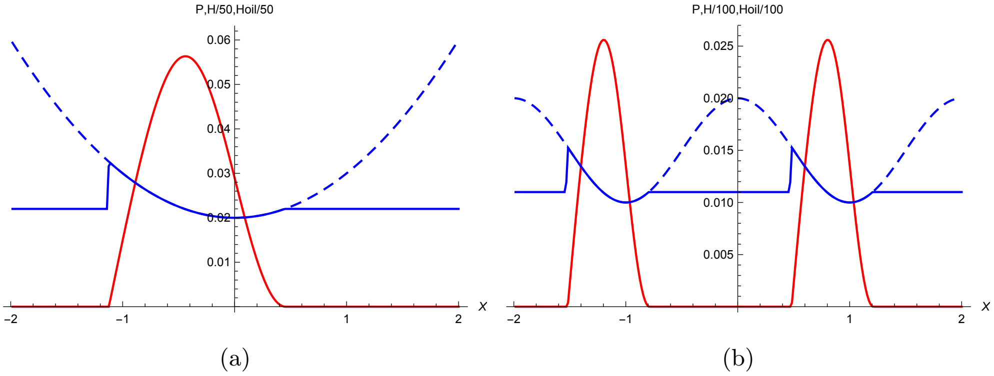

(a) (b)

Figure C.18: Pressure (red), geometry (dashed blue) and oil level (blue) on the central line $Y = 0$ (a) periodic parabolic geometry, $H_0 = 1.1$ (b) periodic wave, $H_0 = 1.05$

case. Coming back to a simple discretization we have tried to better account for the behavior of the flow through each cell in the relaxation process. We have also tried to obtain a better representation of the fine grid flow on the coarse grid. Special attention was given to the nature of the flow according to the position of the boundaries and a coarse grid relaxation was built accordingly. Maybe when coarsening the right hand side of the equation the Couette flow and the Poiseuille flow parts should also be distinguished. Besides no special attention was paid to the flow in the Y-direction and the lack of coupling in the non pressurized zone seems to be a problem and for a real 2D geometry such as $H(X,Y) = 1 + 0.5X^2 + 0.5Y^2$, we did not succeed at all. As already mentioned in Chapter 4, the use of the variable $P - \theta$ proposed in [36] could be a solution.

FOLIO ADMINISTRATIF

THESE DE L'UNIVERSITE DE LYON OPEREE AU SEIN DE L'INSA LYON

NOM : NOUTARY DATE de SOUTENANCE : 10 Novembre 2017

Prénoms : Marie-Pierre

TITRE :
A robust Reynolds solver for textured surfaces in the piston ring liner contact.

NATURE : Doctorat Numéro d'ordre : 2017LYSEI105

Ecole doctorale : EDA162: MEGA

Spécialité : Mécanique

RESUME :

Le contact Segment-Piston-Chemise (SPC) est essentiel pour la réduction des émissions de CO_2 et de polluants dans les moteurs automobile. Pour optimiser ces deux contraintes antagonistes, il est nécessaire d'étudier l'influence de la micro-géométrie afin de trouver de nouvelles architectures de ce contact.
L'étude expérimentale étant très coûteuse, il est impératif de pouvoir modéliser les performances du contact SPC. Les méthodes multigrilles permettent de réduire considérablement les temps de calcul. Pour le contact SPC, les méthodes multigrilles classiques perdent leur efficacité en présence de texture. Un nouvel algorithme, basé sur des idées développées par Alcouffe et al. a été conçu qui permet l'étude du contact hydrodynamique en présence de texturation importante. Il a été validé par comparaison avec un modèle analytique 1D, ses performances ont été étudiées et une première étude de l'influence des paramètres sur la portance pour une surface striée a été faite.
L'algorithme a ensuite été modifié pour imposer la conservation des flux. Un processus de relaxation plus proche de la physique du phénomène est utilisé. Le code obtenu n'atteint pas l'efficacité multigrille optimale. Cependant sa convergence est suffisamment rapide pour étudier l'influence de pores pour le segment plat et montrer l'importance d'une texturation partielle.
Pour finir, le terme transitoire de l'équation de Reynolds est pris en compte. Pour un segment parabolique et une chemise striée, l'influence des paramètres des stries (profondeur, largeur, distance et angle des stries) sur la variation moyenne de la hauteur de film par rapport à une surface lisse est analysée.

MOTS-CLÉS :
Multigrilles – Equation de Reynolds – Lubrification Hydrodynamique – Contact Segment Piston Chemise – Texturation.

Laboratoire (s) de recherche : LAMCOS

Directeur de thèse: Professeur A.A. LUBRECHT

Président de jury : Professeur A. Tanguy

Composition du jury :

Dini, Daniele	Professeur Imperial College London	Rapporteur
Fillon, Michel	Directeur de recherche Université de Poitiers	Rapporteur
Tian, Tian	Principal Research Engineer M.I.T. Boston	Examinateur
Tanguy, Anne	Professeur INSA Lyon	Examinatrice
Biboulet, Nans	Maître de Conférences INSA Lyon	Examinateur
Lubrecht, Antonius	Professeur INSA Lyon	Directeur de Thèse